CHAPTER FIVE

STRUCTURAL DETERMINATION OF THE NA/SI(111)1X1 SURFACE: SUBSTRATE BULK-TERMINATION AND ADSORPTION GEOMETRY

Abstract

It has been suggested from experimental and theoretical results[1-5] that the structure of the underlying Si for the Na/Si(111)1x1 interface is bulk-terminated, with Na adsorbed in high-symmetry sites on the surface. By using X-Ray Standing Waves (XSW) on both Si and Na core levels, we directly determine the geometry of this interface and find that the suggested bulk-terminated structure is correct. Surface-sensitive XSW data monitoring the Si 1s photopeak demonstrate a large change in the Si surface atomic positions for the Na/Si(111)1x1 surface compared to the clean 2x1 surface. In particular the coherent fraction of the XSW data increases upon Na adsorption, indicating the Si surface atoms are in positions similar to those in the bulk. From XSW data on the Na 1s photopeak along the (111) direction, we measure a Na adatom height of 1.981 ± 0.060 Å above the top layer of bulk-terminated Si, which

agrees with covalent bond lengths for threefold-coordinated symmetric adsorption sites. Triangulation of data from the (111) and (11$\bar{1}$) reflections indicates population of both threefold-filled and threefold-hollow adsorption sites. This bulk-terminated Na/Si(111)1x1 structure also is supported by changes in low-energy electron diffraction (LEED) and photoemission (PES) results as the Na coverage is increased from the clean cleaved Si(111)2x1 π-bonded chain surface through an intermediate 2x2 phase to the Na/Si(111)1x1 interface, which is seen from 0.58 monolayers (ML) Na up to the saturation coverage of 1 ML Na.

Introduction

The interest of many studies in alkali metal(AM)/semiconductor interfaces is related to its use as a simple model for other metal/semiconductor interfaces due to the AM atom's single valence electron and ordered adsorption on semiconductors. In addition, AM/semiconductor surfaces have practical applications related to the large reduction in the work function of the surface upon submonolayer AM adsorption and the creation of negative electron affinity (NEA) interfaces upon further oxidation of the interface[6-9]. Both the cleavable Si(111)2x1 and Si(111)7x7 wafer surfaces are well determined reconstructions. While the 7x7 reconstruction is achieved by annealing silicon to temperatures above 1000°C, the 2x1 reconstruction naturally occurs after cleaving along the (111) plane at room temperature. The 7x7 reconstruction is an absolute energy minimum of the Si(111) surface with a large activation barrier, while the π-bonded chain reconstruction of the 2x1 surface is metastable. The height of the energy barrier between the π-bonded chain reconstruction and the ideal bulk-terminated Si(111)1x1 surface is only 0.03 eV per surface atom[29], and can easily be overcome through AM overlayer adsorption. The cleaved 2x1 reconstruction of the cleaved Si(111) surface is well-suited to the geometrical technique of X-Ray Standing Waves as it has Si surface atoms distributed in fewer sites than does the 7x7 reconstruction, so structural parameters can be extracted more easily from standing wave data and changes in the Si structure with AM adsorption can be detected readily.

In their studies of adsorption of Na, K, and Cs on the cleaved Si(111) surface, Reihl *et al.* [1,10,11] found that the three AM's are not isoelectronic and have different LEED patterns at the saturation coverage of 1 ML. In particular, Na forms a semiconducting 1x1 interface at 1 ML [1], while Cs induces a $\sqrt{3}$x$\sqrt{3}$–R30° reconstructed semiconducting surface[10], and upon K adsorption the 2x1 reconstruction is maintained and the surface is metallic[11]. Our LEED studies of K and Cs adsorption [12,13] differ from these results, and the LEED patterns which

appear for Na, K, or Cs adsorption upon Si(111) still differ. For Na adsorption, Reihl *et al.* [1] found that the 2x1 LEED pattern of the cleaved Si(111) surface converts to a 1x1 LEED pattern at a Na coverage of 1/2 ML and the 1x1 pattern remains at the saturation Na coverage of 1ML. As described below, we also observe a 1x1 LEED pattern at saturation Na coverage on the cleaved Si(111) surface; however, we see an additional "2x2" phase at intermediate coverage. While this cleaved Na/Si(111) LEED "phase diagram" is more detailed than that seen by Reihl *et al.* [1], it is much less complex than the six LEED patterns seen for submonolayer potassium dosings[12]. Clearly atomic size and the specific AM adsorbed are important in the resulting interface structure. Due to its smaller size, Na atoms may adsorb more readily into sites on Si(111) than do K or Cs, and the simpler Na/Si(111) surface phase dosing progression suggests a simpler picture of the surface atomic geometry for smaller Na adatoms than for K or Cs.

A simple model of the saturation coverage Na/Si(111)1x1 surface is a bulk-termination of the Si(111) surface due to Na adsorption. Several total energy calculations [3-5] of the bulk-terminated Na/Si(111)1x1 surface at 1 ML coverage have been made. These calculations differ widely in the degree of charge transfer from Na to Si in bonding to the surface; however, all three calculations agree upon the threefold-coordinated adsorption sites as being most energetically favorable. In addition, through a simulation of annealing, Moullet *et al.* [4] determined the bulk-terminated 1x1 surface to be stabilized by Na adsorption at 1 ML coverage with the conversion from 2x1 occurring at 1/2 ML. The photoemission results of Reihl *et al.* [1] agree with the filled state dispersion of all three calculations; however, inverse photoemission agrees better with the unfilled states of Northrup[3] and Moullet *et al.* [4]. This agreement between theory and experiment for the Na/Si(111)1x1 interface suggest that the bulk-terminated model of the underlying Si surface is correct.

In this experiment, we apply multiple techniques to the saturation coverage Na/Si(111)1x1 interface in order to completely determine its atomic structure. In addition, we apply the backreflection X-Ray Standing Waves (XSW) technique[14-16,19-23,30,32,35-37] to the Na/Si(111)1x1 surface to determine the geometry of both the Na adatoms and the Si surface atoms. This results of previous experiments and structural calculations suggest a bulk-terminated Si surface underneath the Na overlayer for Na/Si(111), but by using surface-sensitive Si 1s XSW, we directly examine the geometrical structure of the Si substrate at the interface. The Si 1s yield XSW data confirm that a surface Si structural transition to a bulk-terminated surface occurs as the LEED pattern changes from 2x1 to 1x1. The Na 1s absorption XSW data for the (111)

reflection of Si quantify the Na atom height above the bulk diffracting planes to high precision. We compare the measured height to the height of adsorption sites on model surfaces, using a bond length equal to the sum of Na and Si covalent radii. We find the measured height matches that for high-symmetry adsorption sites on the bulk-terminated surface. Combining this data with the Na 1s XSW data for the $(11\bar{1})$ reflection in order to triangulate of Na adsorption site gives also results consistent with the lateral positions of adsorption sites on the bulk-terminated surface. A similar analysis using the measured Na adatom height and lateral triangulation rules out all adsorption sites on the π-bonded chain reconstruction, indicating the reconstruction has been removed for the Na/Si(111) surface. In addition, we observe core-level Na 2p and Si 2p as well as valence band photoemission (PES) spectra and LEED patterns with increasing Na coverage, and find PES and LEED support the structural conversion to a bulk-terminated surface as the LEED pattern becomes 1x1. With the ending surface structure determined, our coverage-dependent PES and LEED data provide details about the structural transition from the π-bonded chain reconstruction of the clean surface to the bulk-terminated surface at saturation Na coverage. The agreement of the independent techniques of PES and XSW determines the structure of the saturation coverage Na/Si(111)1x1 surface to be bulk-terminated with Na adsorbed in the high-symmetry sites described below.

Experimental

All experiments were performed inside a UHV chamber, with ~$4x10^{-11}$ torr base pressure. The pressure during dosing did not rise above $8x10^{-11}$ torr. Good vacuum was required during the experiment as room-temperature dosed alkali/semiconductor interfaces are very susceptible to contamination. In addition, the 2x1 reconstruction of clean Si(111) is metastable, and can convert to 1x1 with sufficient adsorption of oxygen and other contaminants. The Si(111) surface samples were cleaved *in situ* from *p*-type 5x5x12mm^3 crystalline Si bars of resistivity 26 Ω-cm using the anvil-and-hammer technique. The samples were cut and oriented in the chamber so that the top face is normal to the $(\bar{1}10)$ direction and the side faces are normal to the $(11\bar{2})$ direction. Before dosing, the quality of the cleaved surface was checked using LEED, and only surfaces with good single-domain 2x1 LEED patterns were studied. Sodium was evaporated upon the samples by resistively heating a well-outgassed SAES chromate getter. The distance from the Na getter to the Si(111) was optimized at ~3.8 cm to avoid heating of the sample surface from the evaporator while

limiting the required dosing time and pressure. Earlier experiments used a getter-to-sample distance of 0.8 cm and produced similar LEED and PES results. The cleaver, getter, cylindrical mirror analyzer (CMA), and LEED optics all are in the same analysis chamber. All of the data (LEED, work function difference, photoemission, and X-ray standing waves) were collected with the sample at room temperature.

The work function (WF) difference and photoemission spectroscopy (PES) measurements for sodium dosing progressions were taken on Beam Line 8-1 at the Stanford Synchrotron Radiation Laboratory (SSRL). The incident beam was monochromatized using 822.6 and 2400 line/mm toroidal grating monochromators (TGMs), and exit slits downstream of the TGM were set to 100μm in both vertical and horizontal directions. A double-pass CMA analyzed the photoelectron yield, and the sample surface was oriented at an angle of 45° from both the incident beam and the CMA axis. Sodium coverage was measured by integrating the Na 2p photopeak area (binding energy 30.5 eV), and the data were normalized to the incident photon flux, which was measured using a channeltron to collect electrons emitted from a thin Ni grid placed in the incident beam's path. Sodium coverage for a given dose is represented as the percentage of the Na 2p photopeak area achieved at the saturation coverage, which we define as one monolayer (1 ML). Further Na does not attach to a full Na layer at room temperature. The change in the secondary electron cutoff with sodium coverage provided WF difference data. The sample bias was -12.31 V for the cutoff measurements. The incident photon energy for Na 2p and Si 2p PES spectra were 77 eV and 145 eV, respectively, and the electron kinetic energies for the Si 2p spectra are close to the minimum of the "universal" escape depth curve. The photon energy for the valence band PES spectra and WF difference measurements was 65 eV. Throughout the dosing progression, no evidence of oxygen contamination (emission ~5 eV below the valence band maximum) was observed in the valence band (VB) spectra.

LEED photographs were taken for each Na dose as Na coverage was increased from the clean 2x1 through the intermediate 2x2 phase to the saturation coverage 1x1 surface. LEED patterns were imaged using a reverse-view LEED optics, which allowed a clear field of view. Photographs were taken near 45 eV beam energy with a 30 sec exposure time. The filament current was ~1 mA, and we tried to take pictures quickly to avoid electron beam damage to the surface. Clean Si(111) surfaces were checked for a good, single-domain 2x1 pattern before dosing was performed; the clean surface was photographed as well. Most LEED patterns observed appeared over a large beam energy range down to ~25 eV or below and over the entire sample. When the 2x1 LEED pattern did not appear over the entire sample, visible steps or roughness

on part of the surface explained the lack of a spatially continuous pattern. Each of the LEED patterns to be described below was also achieved by "one shot" dosing on the clean surface as well as appearing in a progression of sodium dosings.

X-ray Standing Wave (XSW) data were collected in the backreflection mode[14,19,21-23,30,35-37] using the same chamber and instrumentation as for the LEED and PES studies. The sample is aligned so that incident photons are normal to the (111) or $(11\bar{1})$ Bragg planes of Si and monochromatized using a pair of InSb(111) crystals on the soft X-ray beam line 3-3 (JUMBO) at SSRL. The sum of the incident and Bragg-reflected X-ray flux is monitored by amplifying the emission current of an Ni grid collected with a channeltron. Before collecting XSW data, a photoemission scan is taken to locate the photopeak of interest, either Na 1s or Si 1s at binding energies –1069.6 eV or –1839.3 eV, respectively. Then the XSW absorption yield of Na or Si atoms as a function of photon energy is monitored via the total counts at the photopeak with the CMA. The photopeak kinetic energy is tracked as the photon energy changes. Background standing wave scans are recorded slightly above the peak (higher kinetic energy) and the background XSW data are collected in a separate run immediately after the on-peak XSW data. The background XSW data reflect the bulk Si atomic positions as its main contribution is from Si photoelectrons or Auger electrons which have lost kinetic energy due to inelastic scattering. This background XSW yield also varies with photon energy and must be subtracted from the on-peak XSW yield to give the specific signal of interest. With the photon energy equal to the (111) backreflection energy of 1977 eV for Si, the Si 1s photoelectrons are highly surface sensitive, with a kinetic energy near the minimum of the universal curve. Total electron yield data are recorded concurrently by monitoring the amplified drain current from the sample.

Both (111) and $(11\bar{1})$ diffraction planes were used for backreflection XSW, and in most cases the XSW data set for one reflection were taken on the same surface immediately after taking the full data set for the other reflection. Oxygen contamination was checked periodically via O 1s photoemission, as reasonable valence band spectra were not available at this high photon energy. We tried to take the XSW data in as short an amount of time as possible to get reasonable fit results, in order to avoid contamination of the surface, which is highly susceptible to adsorption of oxygen and other contaminants. This accounts for the roughness of the XSW data presented. The (111) reflection is taken with the surface normal to the incident beam, while the $(11\bar{1})$ reflection has the sample turned towards the analyzer so the incident photons are at an angle of 70.53° with respect to the surface normal. In the horizontal plane, the CMA

axis is 90° from the incident photon and parallel to the bulk reflecting planes. The sample orientation for the $(1\bar{1})$ reflection may lead to the X-ray beam hitting the side of the sample, but it is unlikely for many photoelectrons from the sample side to reach the analyzer in our geometry. Any alkali metal atoms adsorbed on the side of the sample are assumed to be in disordered positions and to only reduce the coherent fraction of the $(1\bar{1})$ reflection standing wave data.

X-Ray Standing Waves

Introduction

We present the results of applying the backreflection X-Ray Standing Wave (XSW) technique [14-16,19-23,30,32,35-37] to the Na/Si(111)1x1 surface. We examine the structural changes in the Si substrate geometry between the clean reconstructed Si(111)2x1 and saturation coverage Na/Si(111)1x1 phases by comparing XSW data monitoring the Si 1s photoemission peak on the same surface before and after Na dosing. LEED data for the 1x1 surface cannot definitively determine whether the 1x1 periodicity reflects a bulk-terminated Si(111) surface, or the periodicity of the Na overlayer alone, with an underlying reconstructed Si surface. In order to determine if the Si surface structure changes, an element-specific and surface-sensitive technique is required. XSW is a technique fulfilling these requirements which provides a direct quantitative determination of atomic positions, rather than the indirect determination of surface structural changes from electronic changes in photoemission data. The Si 1s XSW data confirm a bulk-termination of the Si surface, and using the bulk-terminated surface structure, we determine Na adsorption positions through XSW data monitoring the Na 1s photemission peak. By looking at the (111) and $(1\bar{1})$ Bragg reflections, we can determine the Na adatom height above the Si surface and the Na lateral registry, respectively. As Woicik *et al.* [30] have done for the Ag/Si(111) $\sqrt{3}$x$\sqrt{3}$-R30° interface, we use both adsorbate and substrate XSW to completely determine the surface structure.

XSW Principles

The backreflection version of the X-Ray Standing Wave (XSW) technique[14,19-23,30,35-37] utilizes synchrotron radiation by keeping the sample angle fixed and varying the photon energy in a region about the Bragg energy of a Si

crystal diffraction plane oriented normal to the incident X-rays. Near the Bragg condition, the incident beam is reflected by the bulk Si crystal lattice, and the superposition of incident and reflected X-rays forms a standing wave which both penetrates the crystal and extends out past the crystal surface. The phase of the standing wave, and therefore the position of its intensity extrema with respect to the crystal diffraction plane, changes with photon energy for the fixed-angle technique. By monitoring the X-ray absorption of adsorbate or substrate atoms as a function of incident photon energy in the Bragg region, an absorption profile is measured which is characteristic of the atomic position, relative to the bulk diffracting plane position of the substrate crystal. The coherent distance D_c and the coherent fraction f_c of the absorbing atoms are determined by fitting the absorption profile to the equation

$$Y(E) / Y_0 = 1 + R(E) + 2 f_c \sqrt{R(E)} \cos(\nu(E) - 2\pi D_c) \qquad (1)$$

where Y_0 is the background absorption yield away from the Bragg reflection, and R(E) and ν(E) are the magnitude and phase of the reflectivity and are functions of photon energy E. In the case of single-site adsorption, the coherent distance D_c corresponds to the distance of the absorbing atom from the diffracting plane divided by the diffraction plane spacing (3.135 Å for the (111) planes of Si). This distance is only known to within a multiple of this diffraction plane spacing, since D_c is only unique modulo 1; however, reasonable assumptions about bond length and geometry determine whether the true value is less or more than one diffraction plane spacing. The coherent fraction f_c is equal to the fraction of adsorbing atoms situated in the site; the remaining fraction $(1 - f_c)$ of atoms are disordered and their contribution to the interference term (last term of the above equation) averages to zero. Thermal disorder in the absorbing atoms also reduces the coherent atoms by a Debye-Waller factor $e^{-2\pi^2\sigma_H^2}$, where σ_H^2 is related to the atomic vibration amplitude in the direction of the reflection H. In the case of multiple sites of the absorbing atoms, each site *i* contributes an interference term, with the weight of each term determined by the relative populations $f_{c,i}$ and the phase of each term given by the distance $D_{c,i}$ of the site from the diffracting plane; the fraction $1 - \Sigma f_{c,i}$ corresponds to the fraction of atoms in disordered positions. The bulk structure of Si has two inequivalent atom positions for the (111) and $(11\bar{1})$ reflections due to the bilayer structure along these directions. In this manner, the bulk Si atoms located 1/8 of a plane spacing above and below the (111) or $(11\bar{1})$ diffraction plane contribute the terms

$$2\,(1/2)\sqrt{R(E)}\cos(\nu(E)-2\pi(\pm 1/8)) \qquad (2)$$

to the adsorption profile, which can be combined to give

$$2\,(1/\sqrt{2})\sqrt{R(E)}\cos(\nu(E)-2\pi(1)) \qquad (3)$$

Si atoms in different bilayers are located the same distance from the nearest bulk diffraction plane and thus have the same contribution to the overall absorption profile. Thus the absorption profile of bulk Si atoms along the (111) and $(11\bar{1})$ reflections can be fit to a single standing wave with $D_c = 1$ and $f_c = 1/\sqrt{2} = 0.707$. This bulk profile can be measured via total yield or the electron yield of the off-peak background, which is dominated by inelastically scattered electrons. These electrons are produced within a substrate depth much less than the extinction depth of the photons. "Hot" electrons also do not contribute to the total and background yields at the low photon energy of the backreflection condition[21]. The total yield and background XSW data for all the data sets presented here agreed within error bars with the expected values for the bulk atomic structure ($D_c = 1$, $f_c = 0.707$), which is an internal check of the XSW data.

The (111) reflection measures the normal component of adatom surface positions (i.e. height above the substrate), while the coherent distance from the $(11\bar{1})$ reflection is predominantly the surface lateral component of adatom positions along the $(1\bar{1}2)$ direction, although there is still a component of $(11\bar{1})$ normal to the surface. On the cleaved Si(111) surface, the $(1\bar{1}2)$ direction corresponds to the direction perpendicular to the π-bonded chains of the clean Si(111)2x1 surface, provided the LEED pattern of the clean surface is single-domain and in the horizontal direction for our sample orientation. Both the (111) and $(11\bar{1})$ reflections are used in the Na 1s photoemission yield XSW to determine the Na adatom position.

The XSW photoemission yield data are fit to the standing wave equation in order to determine the coherent distance D_c and fraction f_c as fit parameters. First, the reflectivity is fit to the theoretical lineshape convoluted with a Gaussian in order to determine the Gaussian energy width due to the monochrometer and the peak offset from the calculated Bragg energy. The background XSW data are subtracted from the on-peak data to give the variation of the photopeak height versus photon energy. The background data are multiplied by a constant before subtraction to adjust the background yield to its value underneath the photopeak. A straight line is fit to the tails of the subtracted XSW data (outside the Bragg condition) and the standing wave

equation is multiplied by the equation for this line to produce a possible fit to the data. The fit is offset in energy and convoluted with the Gaussian energy distribution determined from the reflectivity data. The best fit is chosen through a least-squares technique, and the error bars listed reflect where the χ^2 value is doubled from its minimum value.

Substrate XSW: Si 1s Data

XSW using surface-sensitive photoabsorption yield previously has been used to determine the substrate reconstruction of a number of surfaces, as well as the position of the substrate surface atoms beneath the adatoms[21-23,30,36]. The Si 1s XSW data for the clean Si(111)2x1 and Na/Si(111)1x1 surfaces, along the (111) direction normal to the surface, are shown in Figure 5.1. We used the same sample surface to look at the Si 1s standing waves before and after saturation Na dosing onto the clean cleaved Si(111)2x1 surface. The size of the absorption feature is considerably larger for the Na/Si(111)1x1 surface data than for the clean Si(111)2x1 surface data, although the lineshape is very similar. As the coherent fraction scales nearly linearly with the amplitude of modulation of the absorption feature, we observe a large increase in the coherent fraction f_{111} from 0.503±0.052 for the clean 2x1 surface to 0.641±0.092 for the 1x1 surface. Our error bars are generous, since one can see directly from Figure 5.1 the dramatic increase in the size of the absorption modulation.

At the photon energy for Si(111) backreflection (1977 eV), the Si 1s kinetic energy is highly surface sensitive. Assuming an escape depth of 7.2 ± 1.6 Å as determined from the kinetic energy of photoemitted Si 1s electrons and the "universal curve" for Si[28] and performing an angular integral over the CMA acceptance cone, we find the contribution from the topmost bilayer was 63% across most of our models, with the second bilayer contributing 20% and the bulk Si contributing the remaining 17%. Thus the contribution of bulk Si atoms to the total signal must be considered. As mentioned above, atoms in multiple positions along the Bragg reflection will decrease the overall coherent fraction of the data. If the Si(111) surface atoms are in different positions than the Si bulk atoms relative to the bulk (111) diffracting plane position, the Si 1s XSW data will have a coherent fraction which is reduced to bulk coherent fraction of $f_c = 0.707$, due to the interference of bulk and surface contributions with different phases (distances). A bulk-terminated surface nominally will have surface atoms in the same positions as bulk Si and should have a coherent fraction near the bulk value. Therefore an increase in the coherent fraction of the (111) XSW data for the

Na/Si(111)1x1 surface relative to the known reconstructed Si(111)2x1 surface demonstrates the bulk termination of the surface.

Table 5.1 gives the measured values of coherent distance D_c and fraction f_c from the Si 1s XSW data for the (111) reflection as well as simulated standing wave results from model bulk-terminated and π-bonded chain reconstruction models of the Si(111) surface. The bulk-terminated model has an unrelaxed surface and two sets of positions of the Si atoms for the π-bonded chain model were tested[25,27]. For the simulated data, the standing wave contributions of the atoms in each bilayer were summed and the bilayer sums were weighted by their contribution to photoemission due to the escape depth, in order to sum over all Si atoms. The magnitude and phase of this overall sum correspond the coherent fraction and distance, respectively, of the resulting simulated standing wave. The (111) reflection probes Si distances normal to the surface, which includes the height of the surface Si atoms above the rest of the substrate. The match of the measured and simulated coherent distances is good for both the clean Si(111)2x1 and Na/Si(111)1x1 surfaces; the negative distance for the simulated π-bonded chain data results from an overall contraction of the outer bilayer in this reconstruction. The measured increase in coherent fraction from the clean Si(111)2x1 surface to the saturation coverage Na/Si(111) surface is in excellent agreement with the corresponding increase from the π-bonded reconstructed surface to the bulk-terminated surface. Both measured coherent fractions are decreased by 0.06 from their simulated counterparts; this reduction is explained by thermal and steric disorder on the real surface, an effect which the simulations do not address. This reduction can also arise from deviations in the true Si surface positions relative to the model positions, e.g. the outer bulk-terminated Si position has relaxed or contracted due to interaction with the Na overlayer.

The large increase in the size of the absorption for the Si 1s XSW data, which is related to the coherent fraction, demonstrates large changes in the Si surface atom positions upon conversion of Si(111)2x1 to Na/Si(111)1x1. The Si surface structure for Na/Si(111)1x1 is different from the π-bonded chains of the clean surface. The relative surface and bulk Si atom positions with respect to the bulk diffracting planes produces interference between their contributions to the XSW signal and determine the coherent fraction of the Si 1s XSW data. The interference is more constructive for the bulk-terminated surfaces than for any reconstructed surface since Si surface atoms are at nominally bulk positions; this results in the largest coherent fraction and the largest feature in the standing wave data for the bulk-terminated surface. Thus the large increase in feature size from the Si 1s XSW data determines that the Si surface structure

is bulk-terminated for Na/Si(111)1x1. In addition, the data from both the clean Si(111)2x1 and Na/Si(111)1x1 surfaces match the simulated data from for the well-determined π-bonded chain and bulk-terminated models of the surface, respectively. In the following sections, we will use this bulk-terminated Si structure determined quantitatively from XSW to determine the Na adsorption position on the surface with Na 1s XSW as well as investigate signatures of the bulk-termination in our photoemission and LEED measurements.

Adsorbate XSW: Na 1s Data

Figure 5.2 depicts the bulk-terminated Si(111) surface, along with the locations of the three possible high-symmetry Na adsorption sites for Na/Si(111)1x1, namely the atop (T_1), threefold filled (T_4), and threefold hollow (H_3) sites. Adsorption in the atop (T_1) symmetry site results in a single bond to the underlying top layer Si atom. The threefold filled (T_4) and threefold hollow (H_3) site involve bonding of the adatom to three top layer Si atoms, and the sites differ in whether it is above the second layer Si atom (T_4) or not (H_3). XSW data monitoring the Na 1s photoemission peak for the (111) Bragg reflection quantify the Na adatom height above the bulk-terminated Si surface. This height is compared to reasonable Na-Si bond lengths given by the sum of the Si and Na covalent radii. The triangulation of the adatom position given by the combination of the XSW data from the (111) and (11$\bar{1}$) reflections also helps to determine the adsorption geometry.

Table 5.2 lists the results of the Na 1s XSW data for (111) (normal) and (11$\bar{1}$) (near lateral) reflections. The high coherent fraction $f_{111} = 0.842 \pm 0.130$, which is an average over most of the 1x1 surface samples, indicates the Na adatoms are all at one height regardless of their lateral position on the surface. The coherent distance D_{111} is equal to the height of the Na adatom above the (111) diffraction plane, in units of the diffraction plane spacing (3.135 Å). For the 1x1 case, $D_{111} = 0.757 \pm 0.019$ corresponds to a height of 1.981 ± 0.060 Å above the unrelaxed bulk-terminated top Si layer. This distance is too short for the Na adatom to be in the atop T_1 symmetry site, as the Na-Si covalent distance is 2.65 Å; however, both of the threefold symmetry sites (H_3 and T_4) of the bulk-terminated surface are candidates, as the bond lengths for the measured height would be 2.973 Å and 2.765 Å, respectively, from the unrelaxed top Si layer. In their theoretical models of bulk-terminated Na/Si(111)1x1, both Northrup [3] and Moullet *et al.* [4] calculated a long Na-Si bond length (Northrup 2.71 Å; Moullet 2.99 Å for H_3, 2.93 Å for T_4) close to our bond lengths for the measured

height. Both also found the atop T_1 site to be energetically unfavorable. The H_3 and T_4 symmetry sites are within 0.12 eV of each other for both theoretical models, suggesting both sites are viable. This site energy difference is considerably less than the 0.3 eV site energy difference for Northrup's calculation for Al adsorption on the Al/Si(111) $\sqrt{3}$x$\sqrt{3}$-R30° interface[31], for which the T_4 site is favored but the calculated surface state bands are very similar for H_3 and T_4 geometries. The reasonable bond lengths for both of these sites derived from the measured D_{111} also support the bulk-termination of the Na/Si(111)1x1 surface structure.

In order to determine the lateral position of the Na adatom, we triangulate the (111) standing wave data with the $(11\bar{1})$ standing wave data. This is important for the 1x1 surface, since both H_3 and T_4 sites are possible from the (111) data and from bulk-terminated models. Triangulation XSW results from multiple Bragg reflections has successfully determined adatom registry for several interfaces[16,32]. Assuming a fixed Na atom height of $D_{111} = 0.757 \pm 0.019$, the Na/Si(111)1x1 (111) and $(11\bar{1})$ reflection data triangulate the Na adatoms at a position $x = 0.57 \pm 0.10$, which is between the H_3 ($x = 0.67$) and T_4 ($x = 0.33$) sites (Figure 5.2(a)). x is given in units of the Si(111) surface lateral periodicity in the $(11\bar{2})$ direction, which is 3.326 Å, and the origin is chosen at the lateral position of the T_1 site. Comparing the fits to the Na 1s yield XSW data of Figure 5.3, the size of the absorption feature is 26% of the background level for the (111) direction, while for $(11\bar{1})$ the feature size is 10%. Thus the coherent fraction f_c is much higher for the (111) direction normal to the surface than in the $(11\bar{1})$ direction. The very low $(11\bar{1})$ coherent fraction $f_{11\bar{1}} = 0.270 \pm 0.155$ suggests lateral disorder or multiple adsorption sites. The largely differing coherent fractions for adsorbate standing waves in the (111) and $(11\bar{1})$ directions has previously seen by Vlieg *et al.* [32] for the Ag/Si(111) $\sqrt{3}$x$\sqrt{3}$-R30° interface. In that work, the low $(11\bar{1})$ fraction was seen on several samples and matched well with a honeycomb-chained trimer (HCT) model of the surface. Although the adsorbate was well-ordered in the model, the differing $(11\bar{1})$ distances for the three atoms in the trimer caused their contributions to the overall signal to interfere destructively. In addition, room temperature dosing also may allow some adatoms to sit in disordered positions laterally as well and lower the coherent fraction in this direction, although the heights of these disordered atoms above the surface is similar to adatoms in the high symmetry sites. If the Na adsorbed in a single site, the measured coherent distance would place the adatom at a non-symmetric site which is clearly energetically unfavorable; the low coherent fraction also rules out single-site adsorption. In the case of adsorption into two equally populated sites, the coherent distance is the average distance of the two adatom sites

from the diffraction planes. Since the standing wave data triangulate near the midpoint between the H_3 and T_4 sites (x = 0.50), this suggests nearly equal populations of H_3 and T_4 sites on the Na/Si(111)1x1 surface. Since the triangulated lateral position x is closer to the H_3 position, there may be more Na adatoms in the H_3 site than the T_4 site, suggesting H_3 is slightly more favorable energetically. From the (111) and (11$\bar{1}$) standing wave coherent distances we propose that Na adsorbs on the bulk-terminated surface in nearly equal populations of the H_3 or T_4 site. The adsorption could be in patches that contain only H_3 adsorption or T_4 adsorption or the site adsorption could be mixed locally. A SEXAFS experiment looking for the Na-Na distance would determine the local order, although detecting 1 ML of Na at a photon energy near the K edge (1070.8 eV) would be difficult. The number of dangling bonds on the Si(111) surface sets a saturation coverage at 1 ML regardless of the local site distribution. With one atom in a H_3 or T_4 site per unit cell the coverage is 1 ML and the LEED pattern is 1x1.The difference in the (111) and (11$\bar{1}$) coherent fractions fits this model, as Na is at a similar height above the surface in both the H_3 and T_4 sites but has different lateral position, resulting in a higher f_{111} than $f_{11\bar{1}}$. In addition, the models of Moullet *et al.* [4] and Northrup[3] suggest the H_3 and T_4 sites both may be occupied due to similar site adsorption energies.

As an alternative model of Na/Si(111)1x1 we also tested multiple Na adsorption sites upon the Si(111)2x1 π-bonded surface of Pandey [24], with Si atomic positions taken from Himpsel *et al.* [25]. In this case, the observed 1x1 LEED pattern of the Na/Si(111)1x1 surface would originate from the Na overlayer and not the reconstructed Si surface underneath. Out of several possible adsorption sites, only one matched the data with a reasonable bond length and triangulated position; however filling all such sites would only put 1/2 ML Na on the surface. The triangulated position also does not match a substitutional site in the Si surface bilayer, which is a site proposed for models of the Na/Al(111)2x2 surface [26]. For these reasons and the better fit of Na sites on the bulk-terminated model to the measured triangulation, we conclude that the Na 1s XSW data support the model of Na adsorption in a combination of H_3 and T_4 sites on an underlying bulk-terminated Si substrate for Na/Si(111)1x1.

Results of Other Techniques

Work Function Measurements

The work function difference $\Delta\Phi$, measured from changes in the secondary electron cutoff energy, decreases linearly with Na coverage through saturation of the Na 2p photopeak area (Figure 5.4). The value of the work function decrease at saturation coverage is $\Delta\Phi_{sat} = -2.91 \pm 0.10$ eV, which is averaged over four samples. Of these samples, only the sample in Figure 5.4 had a minimum before the saturation of the Na 2p photopeak was reached. A second sample had the work function plateau between 82% and 100% of Na 2p photopeak saturation with no increase at saturation, while for the other samples the lowest work function was at saturation coverage. This value of $\Delta\Phi_{sat}$ is in reasonable agreement with Reihl's value of $\Delta\Phi_{sat} = -2.7$ eV [1]. However, Reihl observed an actual work function minimum which he defined as 1 ML, and increase of the work function after further dosing was attributed to contamination. In addition, both our and Reihl's results are consistent with Northrup's calculated Na $\Delta\Phi_{sat} = -2.7$ eV for a bulk-terminated 1x1 surface[3].

LEED

Figure 5.5 is a diagram of the surface phases observed with LEED as a function of Na coverage for four cleaved Si(111) samples at room temperature. The points in the diagram represent observed coverages at which the corresponding LEED pattern was seen. The horizontal bars indicate outer limits on the coverage for the surface phases as determined from multiple dosing runs. These bars are drawn at points halfway between consecutive doses, and the dosing run chosen for the limit is the one for which the width of the coverage range is maximized. These "surface phase diagrams" indicate overlapping coverage limits for several phases; this overlap is seen in the observed coverage data points as well as in the estimated coverage limits. The overlap can be explained by differing dosing conditions between sample as described below; however, it also is possible that the details of steps, defects, etc. on the initial surface may also affect the transition Na coverages. Figure 5.6 shows photographs of the LEED patterns corresponding to the three surface structural phases.

Four Na dosing runs were performed on cleaved Si(111) surfaces. The LEED patterns for the first two dosing runs, represented by X's and crossed squares in Figure 5.5, were observed with a standard forward-view LEED optics and no photographs were taken, while the other two samples were from a later experiment and, using the reverse-view LEED, their LEED patterns were photographed. In addition, the evaporator-to-sample distance for the earlier experiment was 0.8 cm, while it was 3.8

cm for the later experiment, which may account for overlapping coverage data points across the phase transitions of Figure 5.5.

Our LEED study demonstrates the existence of three surface structural phases for Na/Si(111) at different Na coverages. In the results below, F_{Na} is the Na coverage represented as the fraction of Na 2p peak area relative to saturation coverage. In order of increasing Na coverages, the phases were the following:

1. For $0.00 \leq F_{Na} \leq 0.43$, the 2x1 pattern observed for the clean surface is maintained (Figure 5.6(a)). Initial LEED patterns were single-domain (X's and crossed squares), two-domain (O's), and one-domain with weak second and third domains (triangles).

2. For $0.26 \leq F_{Na} \leq 0.81$ and for three of the samples, a phase we label "2x2" is seen (Figure 5.6(b)). It is possible that this pattern is three-domain 2x1, which appears identical to 2x2. The corresponding clean surfaces had only one or two strong 2x1 domains (see #1 above).

3. For $0.58 \leq F_{Na} \leq 1.00$, the LEED pattern reverts to 1x1, and remains 1x1 up to saturation coverage (Figure 5.6(c)).

In addition to these three surface structural phases, some samples exhibited additional transitional LEED patterns at Na coverages between neighboring phases. These patterns were a combination of a strong 1x1 pattern with weak second-order spots in a 2x1 or 2x2 formation. One of the samples (represented by X's) showed no 2x2 phase but only the transitional "1x1 with weak 2x1" pattern. Another sample (crossed squares) had two regions with different domain orientations of the 2x1 pattern on the clean surface, and at $F_{Na} = 0.53$, one region was a 2x2 phase while the other showed the "1x1 with weak 2x1" pattern. We believe that the appearance of these transitional LEED patterns depend on the details of the initial cleaved surface structure.

The common elements of the "surface phase diagrams" of all four samples are the retention of the 2x1 LEED pattern for low Na coverage and the conversion to a 1x1 phase at saturation coverage. The conversion of the LEED pattern of the room temperature Na/Si(111) surface to 1x1 near 1/2 ML and up to 1 ML agrees with the previous results of Reihl *et al.* [1]. However, they do not report observing a 2x2 phase at intermediate coverage. The low-coverage 2x1 LEED pattern suggests Na adsorption upon the π-bonded reconstruction of the clean Si(111)2x1 surface while the saturation 1x1 pattern indicates a change in the periodicity of the Na overlayer and/or Si substrate to match the bulk periodicity. The details of the surface structure at intermediate Na

coverage are somewhat unclear because of the different patterns seen on different samples in this coverage range. In addition, the "2x2" LEED pattern could also be interpreted as three domains of a 2x1 pattern. If the "2x2" pattern is 3-domain 2x1, this indicates Na adsorption triggers long-range reordering of the single-domain π-bonded Si chains of the clean surface to produce domains of chains pointing in all three equivalent directions. On the other hand if the pattern is indeed 2x2, a Si(111) surface reconstruction different from the clean surface reconstruction is required. One set of Si 1s standing wave data was taken on the "2x2" phase which is similar to the data for the clean surface, indicating similar Si atomic heights and a reconstructed Si surface. However, these data do not provide lateral position information to differentiate between 2x2 and 3-domain 2x1 structures. The PES spectra for "2x2" phase described below are similar to those for the Na-dosed single-domain 2x1 phase, suggesting that this phase may be three-domain 2x1. The fact that the 1x1 pattern always is seen at saturation Na coverage as well as the changes described below in the PES spectra for the 1x1 surface led us to undertake a study of the atomic geometry of Na/Si(111)1x1 using X-ray standing waves.

Photoemission: Na 2p, Si 2p and Valence Band

Three dosing runs for the Na/Si(111) interface were done on Beam Line 8-1 at SSRL. LEED and photoemission were used to characterize the surface after each Na dosing. As seen from Figure 5.5, the four runs produced a similar phase diagram, characterized by a 2x1 phase at low coverages, a 2x2 transition phase around F_{Na} ~ 0.5, followed by a 1x1 phase up to saturation coverage. As we describe below, the photoemission spectra of each of these phases are distinct from one another. Mangat *et al.* [2] conducted a similar photoemission study with emphasis on the amount of charge transfer in the Na-Si bond. In our study, we link changes in the LEED patterns with coverage to the photoemission spectra, and emphasize the structural changes in the underlying Si surface that can be inferred from photoemission.

Figure 5.7 shows the Na 2p peak lineshape (photon energy 77 eV) as Na coverage increases from 0 to 100% Na 2p area saturation. Not shown in Figure 5.7 are two wide loss peaks at 2.4 eV and 5.0 eV lower energy, which may be 1- and 2-plasmon loss peaks; for this paper we focus on changes in the photopeak itself. The peak for the first dose, which retains the 2x1 LEED pattern of the clean surface, is about twice the width of the peak at high coverage (~1.0 eV vs. ~0.55 eV full width at half-maximum), indicating the existence of multiple photopeak components. These

separate components become more visible as coverage is increased and the LEED pattern becomes 2x2. This suggests more than one adsorption site and/or disordered adsorption for the low- and intermediate-coverage Na/Si(111)2x1 and 2x2 surfaces. The structure of the 2x2 surface is such that the higher binding energy sites are less numerous on the 2x2 surface than the lower binding energy sites. As the LEED pattern changes to 1x1, the Na 2p peak narrows dramatically and shifts to higher binding energy. The reduction in number of Na 2p components suggests a simplification of the Na adsorption geometry to fewer adsorption sites of similar energy and possibly a change in the underlying Si substrate structure. One possible Si(111) surface with high symmetry and a 1x1 LEED pattern is the bulk-terminated surface. Both Northrup [3] and Moullet *et al.* [4] model the Na/Si(111)1x1 surface as bulk-terminated and find a stable configuration with Na adsorbed in the threefold hollow site (H_3) or threefold filled site (T_4). Our proposed model derived from the standing wave data suggests both sites are occupied. As these models predict only a 0.1 eV difference in adsorption energy between the sites, the two Na 2p components one would expect for a two-site model are very close in energy and may combine to give the narrow photoemission peak observed. The width of the peak is still 0.2 eV larger than our experimental resolution. In contrast, the difference in adsorption energies for Na should be greater for the two chain atom sites of the π-bonded chain reconstruction, as evidenced by the large difference in the corresponding Si 2p component binding energies discussed below. This larger difference in site adsorption energies as well as additional adsorption sites produce a wider overall Na 2p lineshape for the 2x1 and 2x2 surfaces.

The progression of the Si 2p lineshape (photon energy 145 eV) with increasing Na coverage is depicted in Figure 5.8. For all samples, the overall shape of the Si 2p peak for Na dosings corresponding to the 2x1, 2x2, and 1x1 LEED patterns are similar for dosings with the same LEED pattern, and different for the three different LEED patterns. This indicates different geometrical and bonding arrangements of surface Si atoms for the 2x1, 2x2, and 1x1 phases.

The Si 2p lineshape was fit using Voigt functions for several component doublet peaks, along with an integrated background. Figures 8(a)-(d) show the results of these fits for the clean 2x1 and Na-dosed 2x1, 2x2 and 1x1 surfaces, respectively. We use an experimental Gaussian width of 0.38 eV, a spin-orbit splitting of 0.605 eV and a branching ratio of 2, which are the same values Woicik *et al.*. [18] used in their fit of Si 2p data from the clean Si(111)2x1 surface, for which the lineshape of the component was determined by examining the Si 2p spectrum of Si(111) covered with an overlayer of Ge. The Lorentzian width was allowed to vary at first to find the best

fit and then fixed at the best value of 0.07 eV for all the components in order to determine their energies. Four components were required to fit the clean surface Si 2p peak in Figure 5.8(a), with peak position results similar to those of Woicik *et al.*. [18]. The component peak positions and areas for the clean and Na-dosed surfaces are given in Table 5.3. The component labeled B is assigned to bulk Si atoms, while components S1 through S3 are surface components which are assigned to different atom in the π-bonded chain reconstruction of the Si(111) surface. We adopt the component assignments of Woicik *et al.*. [18], where S1 corresponds to the outermost of the two buckled chain atoms, S2 corresponds to the other chain atom, and S3 corresponds to the two atoms directly bonded to these chain atoms and the atoms in the second bilayer. The relative weights of the surface and bulk peaks varies with dosage and corresponding LEED pattern. Note that the kinetic energy chosen for the photoelectrons is highly surface sensitive, with up to 65% of the total Si 2p peak area coming from Si atoms in the top two bilayers of the surface.

After the first Na dose, $F_{Na} = 0.18$, there are still three surface components as for the clean surface, and the relative weights of the surface peaks S1 and S2 are similar to those for the clean surface spectrum. However, the energies of the components shift slightly, with the chain components S1 and S2 moving to higher kinetic energy and S3 to lower kinetic energy. The direction of the shift of the chain components S1 and S2 suggests electron transfer to these Si chain atoms due to Na bonding. The bonding of Na to the chain atoms is also supported by the growth of components S1 and S2 with increasing coverage. This Na-Si bonding to the chain influences the second layer Si atoms as well, as seen by the shift in component S3. From the electronegativity difference of 0.97 between Na and Si, an energy shift of 0.75-0.80 eV is predicted by the empirical relationship of Himpsel *et al.* between electronegativity and Si 2p core level shifts[33]. The shift in component S1 is significantly less than the predicted shift, suggesting only partial donation from the Na to the Si. The shift is similar at higher coverages, suggesting the nature of the Na-Si bond is not fully ionic at any coverage but remains covalent. The overall Si 2p lineshape for the first Na dose is similar to that of the clean 2x1 surface with the exception of the high kinetic energy shoulder due to component S1. This suggests that the underlying Si surface structure for the Na-dosed 2x1 phase is similar to that for the clean surface. This is expected, since at this low Na coverage large parts of the surface should remain uncovered.

As Na coverage is increased into the 2x2 LEED phase, more of the spectral weight moves to the sides of the lineshape, indicating an increase in the relative areas of both surface components S1 and S2. The shoulder at high kinetic energy shows a

definite increase from the spectra for the first Na dose. This increase is due to further Na-Si bonding to both chain atoms. The kinetic energies of the surface components relative to the bulk for the second Na dose (F_{Na} = 0.53, Figure 5.8(c)) are within 0.04 eV of their values for the second dose (F_{Na} = 0.18, Figure 5.8(b)), indicating not much charge redistribution as the surface becomes 2x2. The similar energies suggest the Si bonding arrangement for the 2x2 phase is similar to that for the clean and Na-dosed 2x1 surfaces. This similarity could also indicate that the surface may have a long-range transition from one to three domains of 2x1 chains as suggested by LEED results.

At the high coverages corresponding to the Na/Si(111) 1x1 phase, the number of components required to fit the Si 2p lineshape well reduces from four to two. Figure 5.8(d) shows the Si 2p lineshape at saturation coverage, F_{Na} = 1.00, which is composed of a bulk component of 64% total peak area and a single surface peak at +0.36 eV kinetic energy relative to the bulk. The relative weight of the surface and bulk components matches that for the reported Si 2p spectrum of the Sb/Si(111) surface[34], for which 1 ML of Sb is bonded to the 1 ML of Si surface atoms, which confirms the 1 ML Na coverage for the surface. This peak is in a similar position to the S1 peak, although the energy shift is 0.07 eV less than at lower Na coverages. This suggests charge transfer back to the Na overlayer as Na-Na interactions become more important at high coverage. This reduction in charge transfer near 1 ML coverage is a general characteristic of AM adsorption on semiconductor and metal surfaces[9]. Comparing the total Si 2p lineshapes for the Na-dosed surfaces, the shoulder on the high kinetic energy side for the lower coverage surfaces (Figures 8(b)-(c)) has disappeared for the saturation coverage Na 1x1 surface (Figure 5.8(d)), because of the reduction in the size of the shift of component S1. Also, the dip between the spin-orbit components of the overall lineshape are more pronounced, indicating the removal of lower kinetic energy components S2 and S3. The existence of only one surface component indicates a more symmetric arrangement of Si atoms with fewer inequivalent Si sites than for the lower coverage Na/Si(111) surfaces. The increased weight of the bulk peak is consistent with the sum of the contributions for the bulk and second bilayer components B and S3 for the lower coverage surfaces, indicating that the second bilayer atoms revert to their bulk-terminated positions. This supports the idea of a bulk-terminated Si(111) surface underneath the Na overlayer, with the surface component corresponding to the Si atoms in the topmost layer which are bonded to the Na adatoms. The removal of two of the surface components related to the π-bonded chain structure suggests the chain collapses for the 1x1 phase. The reduction of surface components for the 1x1 surface also was seen in the Na 2p photoemission data of

Figure 5.7. Both Na 2p and Si 2p photoemission data support the reduction of the number of inequivalent Si surface atoms through reversion to a bulk-terminated structure, as well as indicating that the bulk-terminated surface is more stable than the low-coverage chain surface since Na 2p and Si 2p surface binding energies increase for the bulk-terminated surface.

Changes are also seen in the valence band photoemission spectra with increasing Na adsorption, particularly in the 4 eV region below the valence band maximum. Valence band spectra (photon energy 65 eV) from 0% to 100% Na saturation are presented in Figure 5.9. This photon energy produces high surface sensitivity in the valence band spectra, as is seen by the large surface state peak at the top of the valence band for the clean surface.

A large peak grows near the top of the valence band with increasing Na coverage (see Figure 5.9). This peak also exhibits a shift to higher binding energy as Na coverage increases from lower coverage phase to the saturation coverage 1x1 surface. For the clean 2x1 surface, the peak at the top of the valence band corresponds to surface π states from the chain atoms of the reconstructed surface. After the first Na dose, this peak remains; as the LEED remains 2x1 after this dose, the peak still can be attributed to a π-bonded chain structure. Through the intermediate coverages for which the LEED pattern is 2x2, the energy of this peak remains constant while its absolute intensity increases. Here more Na adatoms are supplying electrons to the state at the energy of this peak, and the increase of the peak area confirms its assignment as an Na-Si bonding peak. The similar energy position of this peak and overall shape of the valence band spectrum compared to the first dose suggest that the 2x2 and Na-dosed 2x1 surfaces have a similar bonding arrangement, and that perhaps the observed 2x2 LEED pattern actually is the combination of three 2x1 domains. As the LEED pattern converts to 1x1 and Na coverage increases to saturation, the valence band peak's corresponding increase and saturation confirms that it reflects electrons in a Na-Si chemical bond. However, upon converting to the 1x1 surface, the peak shifts dramatically to a binding energy 0.6 eV greater than the original Si surface state of the clean surface. This large shift of the Na-Si bonding peak, when correlated with the reduction of the number of components in the Na 2p and Si 2p spectra, suggests a large change in the atomic arrangement of the Na and Si atoms involved in the Na-Si bond for the 1x1 surface as compared to that of the 2x1 and 2x2 surfaces.

This prominent Na-Si bonding feature of the Na/Si(111)1x1 valence band spectrum was observed in angle-integrated photoemission by Reihl *et al.* [1], and they investigated the dispersion of this peak on the Na-saturated surface using angle-

resolved photoemission (ARPES). As our analyzes averages over a large angular cone, we would expect a state which disperses in angle to appear as a broad peak in our valence band spectrum. However, the observed peak is quite sharp (0.5 eV wide compared to our 0.38 eV instrumental resolution), indicating that the Na-Si bonding state has little angular dispersion and therefore is localized. This suggests that for 1 ML saturation coverage of Na on the surface, Na-Na interactions are small and an metallic overlayer does not form. The ARPES results of Reihl *et al.* [1] also revealed a band that was fairly flat 0.5 eV below the valence band maximum for the parts of the Brillouin zone where it did not coincide with the bulk bands. The surface also was semiconducting. These measurements, as well as angle-resolved inverse photoemission mappings of empty surface bands, coincide with the calculated bands of Northrup [3] and of Moullet *et al.* [4] who both use a bulk-terminated model of the surface. The observed filled band is derived from a Na 3s - Si 3p bond between the bulk-terminated top Si layer and Na adatoms in either a threefold filled (T_4) or threefold hollow (H_3) site. These are the same two sites which share Na adsorption in our model of the Na/Si(111)1x1 surface derived from the Na 1s standing wave data.

Through Na dosing on the cleaved Si(111) surface, we see the removal of the surface state of the π-bonded Si chains at the top of the valence band and its replacement by a narrow Na-Si bonding state also at the top of the valence band but at higher binding energy. This state matches a localized bonding state in bulk-terminated models of the Na/Si(111) 1x1 surfaces, and changes in the Na 2p and Si 2p photoemission also indicate structural change for the 1x1 surface compared to lower coverage surfaces. The photoemission data corroborate our model of the Na/Si(111)1x1 surface derived from Si 1s and Na 1s standing wave data, namely a bulk-terminated Si(111) surface with Na adsorbed in both threefold filled (T_4) and threefold hollow (H_3) sites.

Conclusion

By increasing sodium coverage through dosing on cleaved Si(111) at room temperature, the LEED pattern of the Na/Si(111) surface converts from the 2x1 pattern of the clean surface and low Na coverages to a previously unreported "2x2" phase at intermediate Na coverage, and 1x1 at the saturation Na coverage of one monolayer (1 ML). We observe changes in the Na 2p, Si 2p, and valence band photoemission spectra corresponding to each of the three main LEED phases of this phase diagram. In particular, we conclude that the underlying Si substrate of the Na/Si(111)1x1 surface has a bulk-terminated and not a π-bonded chain or other reconstructed structure, and

that Na adsorbs in similar population on the threefold-hollow (H_3) and threefold-filled (T_4) symmetry sites of the bulk-terminated Si surface. This conclusion is supported by these five observations:

1. The surface-sensitive Si 1s XSW absorption yield profile along the (111) reflection for the clean Si(111)2x1 and Na-dosed Si(111) 1x1 surfaces match the predicted XSW profiles for the π-bonded chain reconstructed and bulk-terminated surface geometries, respectively. In particular, the large increase in the amplitude of the XSW absorption feature for the 1x1 surface as compared to the 2x1 surface demonstrates that the 1x1 surface structure has changed from the π-bonded chain reconstruction and that the surface atoms are close to the corresponding extended bulk positions.
2. Na 1s absorption yield XSW along the (111) and (11$\bar{1}$) reflections select the H_3 site of the bulk-terminated 1x1 surface as the most viable. The measured H_3 Na-Si distance of 2.97 $\pm$ 0.04 Å for a bulk-terminated surface matches the H_3 Na-Si distance of 2.99 Å from Moullet *et al.* [4]. The measured height of the Na adatoms above the unrelaxed bulk-terminated Si surface is 1.981 $\pm$ 0.060 Å. Na also populates the energetically similar T_4 site, since the Na average lateral position triangulates between the H_3 and T_4 sites. All but one of the Na adsorption sites upon a π-bonded chain surface gave unreasonable bond lengths, and this site did not triangulate with the (11$\bar{1}$) reflection Na 1s XSW data.
3. The energy width of the Na 2p photoemission peak decreases as the Na/Si(111)1x1 surface is formed, indicating reductions in the number of peak components and in the energy difference between these components. This suggests fewer Na adsorption sites and a more symmetric surface structure than the original π-bonded reconstructed surface.
4. The number of components (surface plus bulk) required to fit the Si 2p PES spectra decreases from four to two as the Na/Si(111)1x1 surface is formed, so the underlying Si surface structure is simpler on the 1x1 surface than on the 2x1 surface. The number of inequivalent Si surface atoms is reduced, which is the case for conversion from the π-bonded chain surface to the bulk-terminated surface.
5. The 1x1 phase exhibits a large Na-Si bonding peak in the valence band PES spectrum which is shifted to 0.6 eV higher binding energy than the clean 2x1 surface state. This peak is consistent with the Na-Si bonding band 0.5 eV below the valence band maximum calculated for the bulk-terminated Na/Si(111)1x1 surface by Northrup [3] and Moullet *et al.* [4].

The combination of X-Ray Standing Waves and photoelectron spectroscopy is a powerful method to find complementary atomic and electronic structural data, and both techniques support a bulk-terminated model of the underlying Si surface for Na/Si(111)1x1. The π-bonded chain reconstruction of the cleaved Si(111) surface is removed at saturation Na coverage. With this determination of the surface structure of Na/Si(111)1x1, we investigate the changes in electronic and atomic structure of the cleaved Si(111) surface with increasing Na coverage and through the structural transition to 1x1 near 0.6 ML Na, using the work function difference, PES, and LEED measurements. The work function monotonically decreases with increasing Na coverage with a minimum of $\Delta\Phi_{sat} = -2.91 \pm 0.10$ eV near or at saturation (1 ML Na) in agreement with the measurements of Reihl *et al.* [1] and the calculation of Northrup[3]. The LEED pattern remains 2x1 up to 0.4 ML Na, where the previously unreported "2x2" pattern is observed, and then converts to 1x1 at 0.6 ML Na and remains 1x1 up to saturation at 1 ML Na. Si 1s XSW data from the 2x2 surface indicate the surface is still reconstructed, but it is not determined whether the "2x2" phase is a new reconstruction or a sodium-induced long-range change in the orientation of the π-bonded chains from one to three equivalent domains. However, the similarity of the Si 2p and valence band photoemission data for the Na-dosed 2x1 and 2x2 surfaces suggests the π-bonded reconstruction remains. Analysis of the three surface and one bulk component of the Si 2p photoemission spectra indicate Na attaches to the dangling bonds to Si buckled chain atoms, but at all coverages the amount of charge transfer from Na to Si indicated by the surface component energy shifts is less than expected from considering the difference in electronegativity between Na and Si. This suggests covalent bonding between Na and Si at all coverages, and Na-Na overlayer interactions are weak at saturation coverage due to the localized nature of the sharp Na-Si bonding peak observed in the valence band spectra.

[1] B. Reihl, S. L. Sorensen, R. Dudde and K.O. Magnusson, Phys. Rev. B 46 (1992) 1838.

[2] P. S. Mangat, P. Soukiassian, Y. Huttel and Z. Hurych, J. Vac. Sci. Tech. B 12 (1994) 2694.

[3] J. E. Northrup, J. Vac. Sci. Tech. A 4 (1986) 1404.

[4] I. Moullet, W. Andreoni and M. Parrinello, Surface Science 269-270 (1992) 1000.

[5] S. Ossicini, C. Arcangeli, and O. Bisi, Phys. Rev. B 42 (1990) 7671.

[6] R. U. Martinelli and D. G. Fisher, Proc. IEEE 62 (1974) 1339.

[7] J. D. Levine, Surf. Sci. 34 (1973) 90.

[8] B. Reihl, M. Erbudak and D. M. Campbell, Phys. Rev. B 19 (1979) 6358.

[9] H. P. Bonzel, A. M. Bradshaw and G. Ertl, Eds., Physics and Chemistry of Alkali Metal Adsorption (Elsevier, Amsterdam, 1989).

[10] K. O. Magnusson and B. Reihl, Phys. Rev. B 39 (1989) 10456.

[11] B. Reihl and K. O. Magnusson, Phys. Rev. B 42 (1990) 11839.

[12] E. J. Nelson, T. Kendelewicz, P. Liu, and P. Pianetta, Surf. Sci. 380 (1997) 365.

[13] E. J. Nelson, T. Kendelewicz, P. Liu, and P. Pianetta, in preparation.

[14] D. P. Woodruff, Prog. Surf. Sci. 57 (1998) 1.

[15] P. L. Cowan, J. A. Golovchenko, and M. F. Robbins, Phys. Rev. Lett. 44 (1980) 1680.

[16] J. A. Golovchenko, J. R. Patel, D. R. Kaplan, P. L. Cowan, and M. J. Bedzyk, Phys. Rev. Lett. 49 (1982) 560 .

[17] B. Reihl, S. L. Sorensen, R. Dudde, and K. O. Magnusson, Surf. Sci. 269-270 (1992) 1005.

[18] J. C. Woicik, P. Pianetta, and T. Kendelewicz, Phys. Rev. B 40 (1989) 12463.

[19] B. W. Batterman and H. Cole, Rev. Mod. Phys. 36 (1964) 681.

[20] J. Zegenhagen, Surf. Sci. Rep. 18 (1993) 199.

[21] J. C. Woicik, T. Kendelewicz, K. E. Miyano, P. L. Cowan, C. E. Bouldin, B. A. Karlin, P. Pianetta and W. E. Spicer, Phys. Rev. Lett. 68 (1992) 341.

[22] T. Kendelewicz, J. E. Klepeis, J. C. Woicik, S. H. Southworth, C. Mailhiot, M. van Schilfgaarde, M. Methfessel, A. Herrera-Gómez, and K. E. Miyano, Phys. Rev. B 51 (1995) 10774.

[23] T. Kendelewicz, P. Liu, G. E. Brown, Jr. and E. J. Nelson, Surf. Sci. 395 (1998) 229.

[24] K.C. Pandey, Phys. Rev. Lett. 47 (1981) 1913.

[25] F. J. Himpsel, P. M. Marcus, R. Tromp, I. P. Batra, M. R. Cook, F. Jona, and H. Liu, Phys. Rev. B 30 (1984) 2257.

[26] J. Burchhardt, M. M. Nielsen, D. L. Adams, E. Lundgren, J. N. Andersen, C. Stampfl, M. Scheffler, A. Schmalz, S. Aminpirooz and J. Haase, Phys. Rev. Lett. 74 (1995) 1617.

[27] H. Sakama, A. Kawazu, and K. Ueda, Phys. Rev. B 34 (1986) 1367.

[28] C. M. Garner, I. Lindau, C. Y. Su, P. Pianetta, and W. E. Spicer, Phys. Rev. B 19 (1979) 3944.

[29] J. E. Northrup and M. L. Cohen, Phys. Rev. Lett. 49 (1982) 1349.

[30] J. C. Woicik, T. Kendelewicz, S. A. Yoshikawa, K. E. Miyano, G. S. Herman, P. L. Cowan, P. Pianetta and W. E. Spicer, Phys. Rev. B 53 (1996) 15425.

[31] J. E. Northrup, Phys. Rev. Lett. 53 (1984) 683.

[32] E. Vlieg, E. Fontes, and J. R. Patel, Phys. Rev. B (1991) 7185.

[33] J. Himpsel, B. S. Meyerson, F. R. McFeely, J. F. Morar, A. Taleb-Ibrahimi, and J. A. Yarmoff, in: Photoemission and Absorption Spectrosopy of Solids and Interfaces with Synchrotron Radiation, Vol. 108 of the Proceedings of the International School of Physics "Enrico Fermi", Varenna (Italy), 1988, M. Campagna and R. Rosei Eds. (North-Holland, Amsterdam, 1990), pp. 203-236.

[34] J. C. Woicik, T. Kendelewicz, K. E. Miyano, C. E. Bouldin, P. L. Meissner, P. Pianetta, and W. E. Spicer, Phys. Rev. B 43 (1991) 4331.

[35] J. C. Woicik, T. Kendelewicz, A. Herrera-Gómez, K. E. Miyano, P. L. Cowan, C. E. Bouldin, P. Pianetta, and W. E. Spicer, Phys. Rev. Lett. 71 (1993) 1204.

[36] J. C. Woicik, T. Kendelewicz, A. Herrera-Gómez, A. B. Andrews, B. S. Kim, P. L. Cowan, K. E. Miyano, C. E. Bouldin, B. A. Karlin, G. S. Herman, J. L. Erskine, P. Pianetta, and W. E. Spicer, J. Vac. Sci. Tech. A 11 (1993) 2359.

[37] J. C. Woicik, T. Kendelewicz, K. E. Miyano, P. L. Cowan, C. E. Bouldin, B. A. Karlin, P. Pianetta, and W. E. Spicer, Phys. Rev. B 44 (1991) 3475.

Table 5.1. Si 1s XSW data and comparison to Si(111) surface structural models

Surface	Reference	D_{111}	f_{111}	Notes
1x1 Bulk-terminated		0.000	$1/\sqrt{2} = 0.707$	
2x1 π-bonded chain	Ref. 25	–0.0215	0.577	
2x1 π-bonded chain	Ref. 27	–0.0178	0.557	
Na/Si(111) 1x1	Expt. data	+0.030±0.022	0.641±0.092	same sample as 2x1 clean
2x1 clean	Expt. data	0.000±0.016	0.503±0.052	

Table 5.2. Na 1s X-ray Standing Wave (XSW) Results

Reflection	Number of Samples	Coherent Distance D_c (plane spacings)	Coherent Distance D_c (Å)	Coherent Fraction f_c
(111)	5	0.757 ± 0.019	2.37 ± 0.06	0.842 ± 0.130
$(11\bar{1})$	1	0.657 ± 0.093	2.06 ± 0.29	0.270 ± 0.155
Lateral position x in $(11\bar{2})$ dir.		0.571 ± 0.099	1.90 ± 0.33	Between H_3 and T_4 sites

Table 5.3. Si 2p photoemission surface component fit results - see Figure 5.8

F_{Na} (ML)	Bulk (B) fraction of total area	S1 kinetic energy rel. to bulk (eV)	S1 fraction of total area	S2 kinetic energy rel. to bulk (eV)	S2 fraction of total area
0.00	0.34	+0.34	0.15	-0.65	0.04
0.18	0.34	+0.43	0.10	-0.61	0.07
0.53	0.33	+0.42	0.19	-0.57	0.12
1.00	0.64	+0.36	0.36		

F_{Na} (ML)	S3 kinetic energy rel. to bulk (eV)	S3 fraction of total area
0.00	-0.19	0.47
0.18	-0.28	0.49
0.53	-0.25	0.33
1.00		

Table 5.4. Na Adsorption Site Analysis Using Na 1s XSW data

Na Site for 1x1 Bulk-terminated Model, Fig. 8(a)	Na-Si Distance Using (111) XSW Data	Reasonable Bond Length?	Lateral Match?	Possible Site?
Threefold hollow H_3	2.97 Å	Yes	Yes	YES
Threefold filled T_4	2.76 Å	Yes	Yes	YES
Atop T_1	1.98 Å	No	No	NO

Figure 5.1. Surface-sensitive Si 1s XSW data for the clean Si(111)2x1 and Na/Si(111)1x1 surfaces, for the (111) backreflection (normal to the surface).

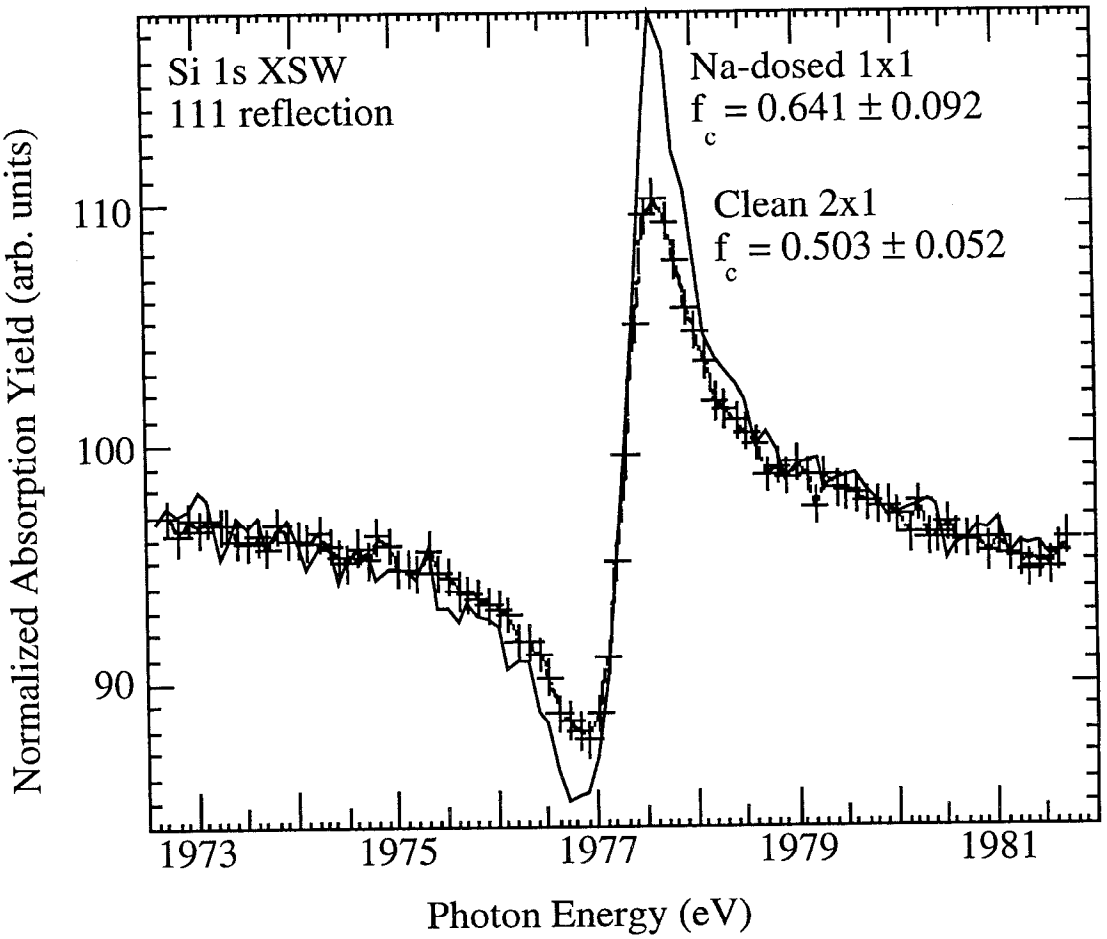

Figure 5.2. The bulk-terminated Si(111) surface, in both top and side views. The locations of the three possible high-symmetry Na adsorption sites for Na/Si(111)1x1 are indicated, namely the atop (T_1), threefold filled (T_4), and threefold hollow (H_3) sites.

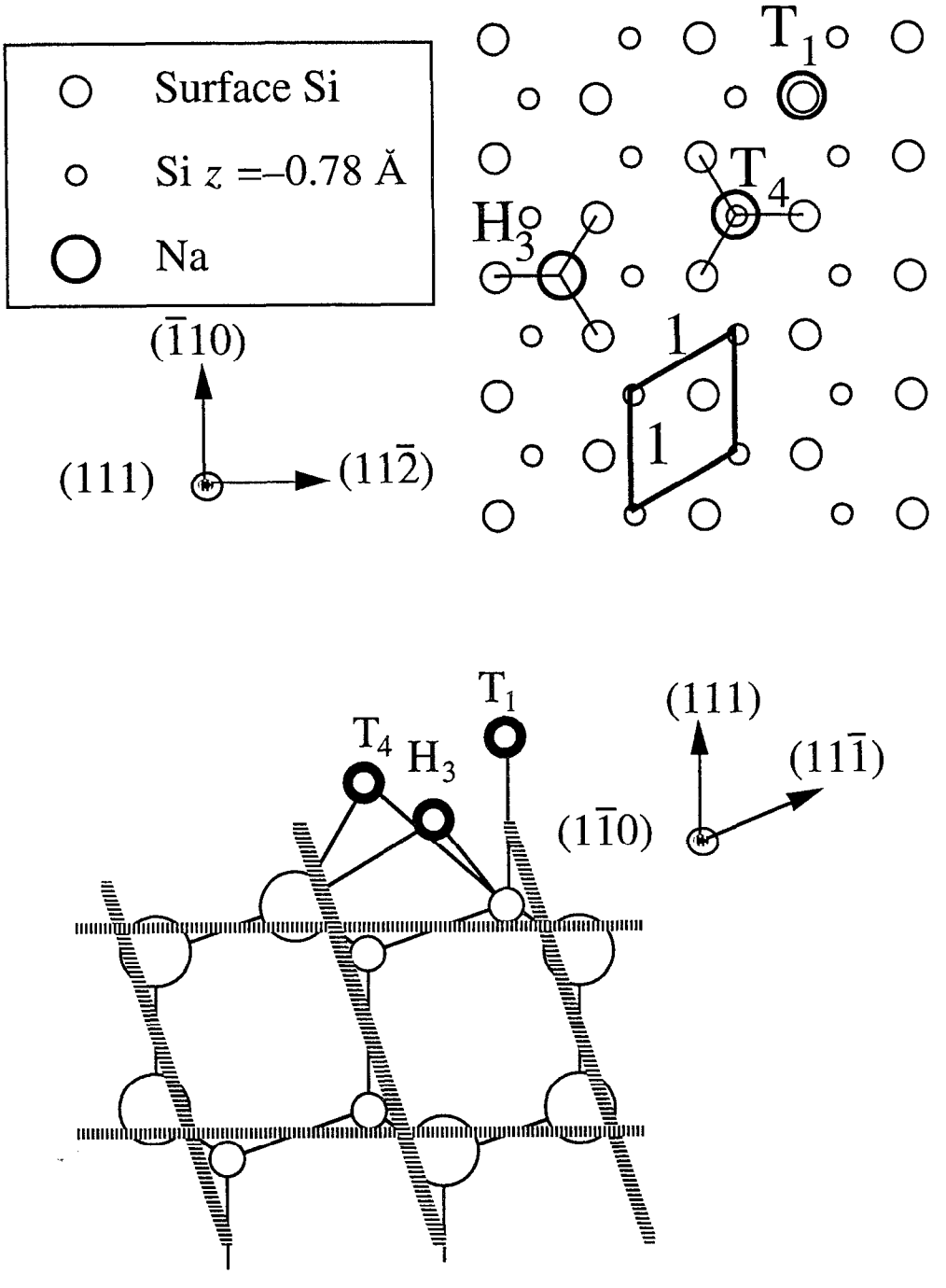

Figure 5.3. Na 1s XSW data for the Na/Si(111)1x1 interface, for the (111) (normal to the surface) and (11$\bar{1}$) (mostly lateral to surface) reflections of Si.

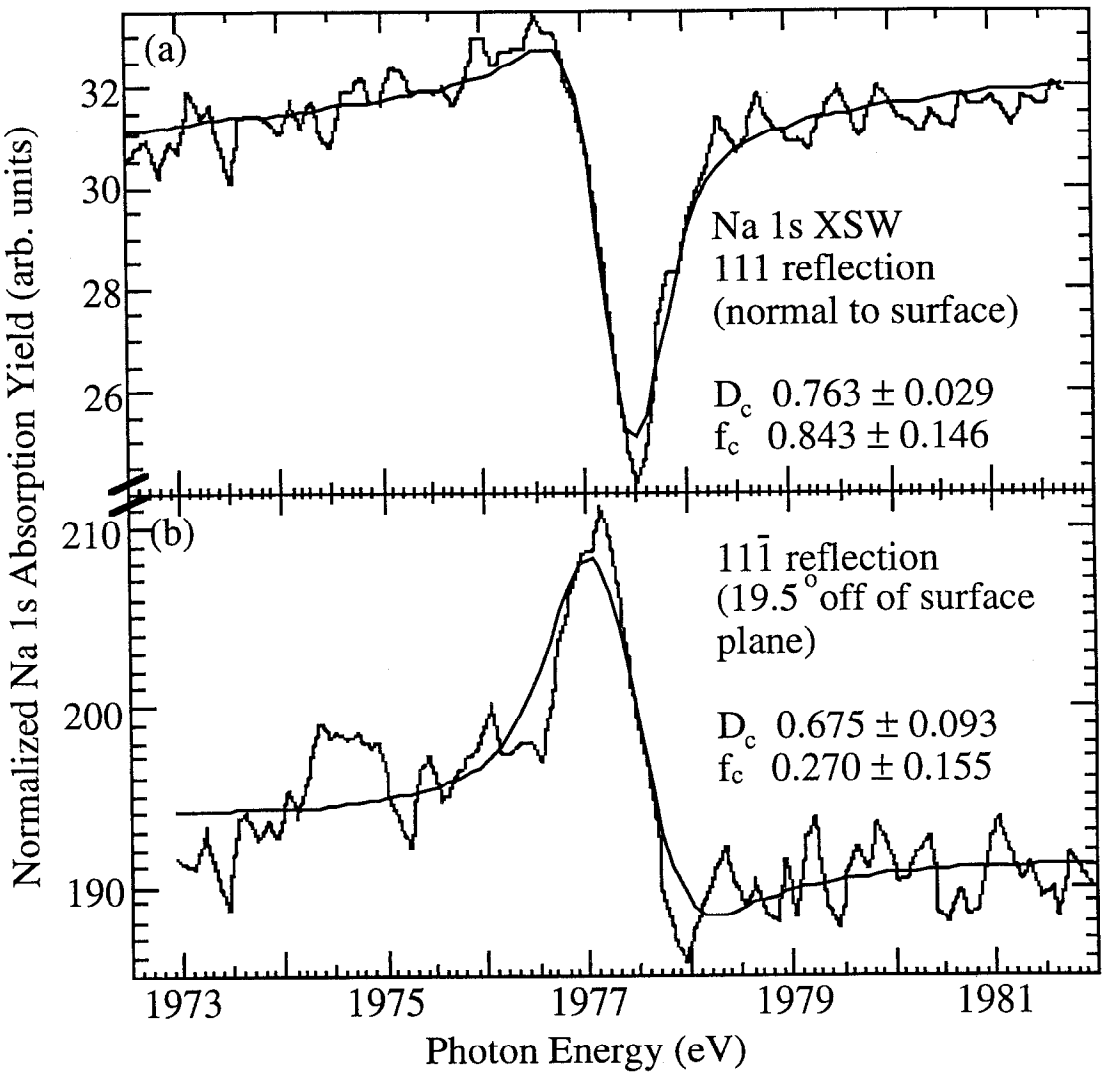

Figure 5.4. Work function difference (relative to the value for the clean Si(111) 2x1 surface) versus % Na 2p photopeak area saturation for room temperature Na dosing on Si(111).

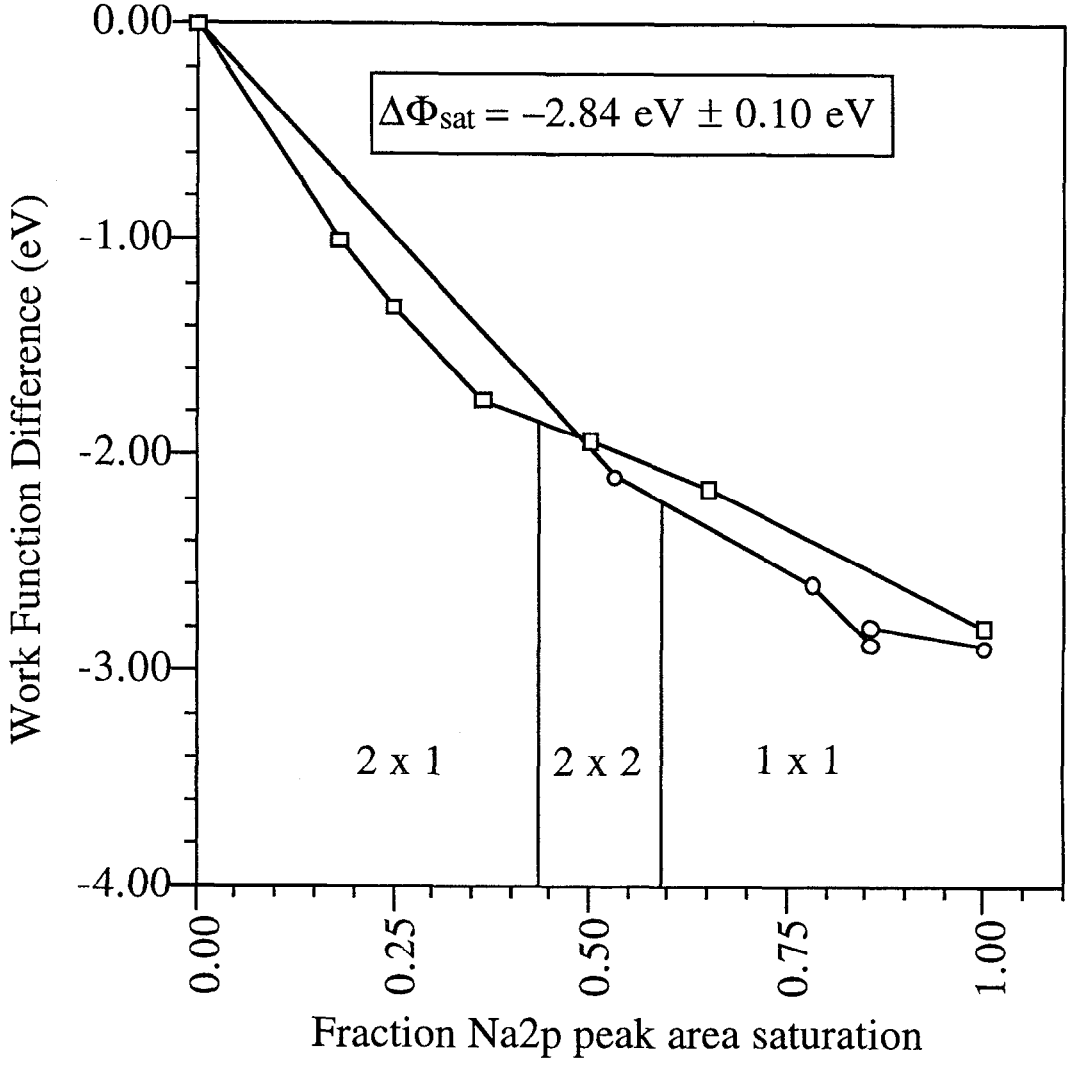

Figure 5.5. "Surface phase diagram" of observed LEED patterns for the Na/Si(111) interface as a function of Na coverage (% Na 2p photopeak area saturation) for room temperature Na dosing.

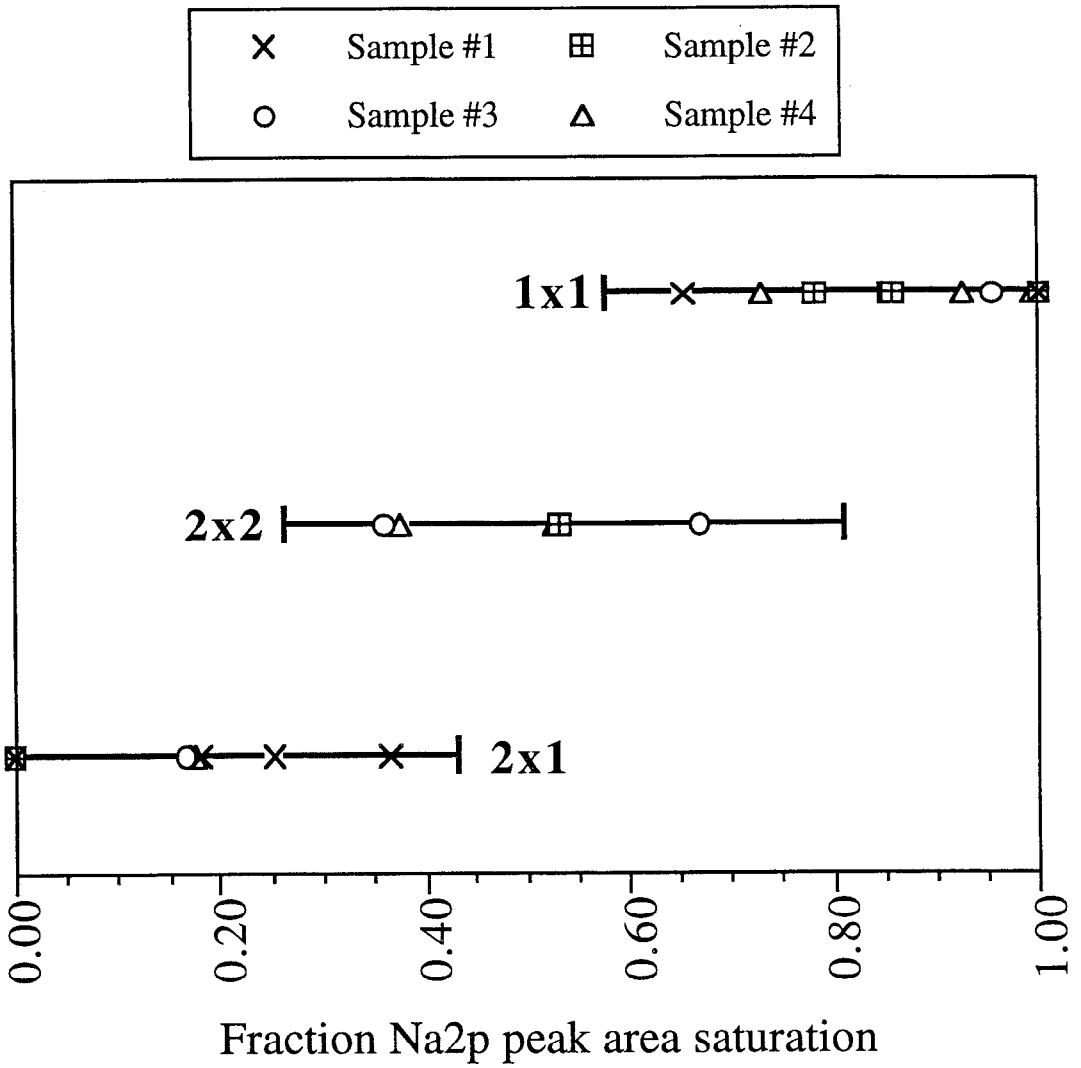

Figure 5.6. Photographs of the three LEED patterns observed with increasing Na coverage for the room temperature Na/Si(111) interface. (a) 2x1 (b) 2x2 (c) 1x1 (pattern at saturation Na coverage).

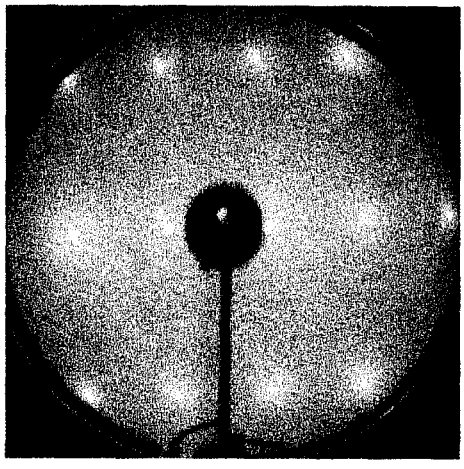

(a) 2 x 1
0% to 43% of Na 2p
area saturation
Beam energy 46.3 eV

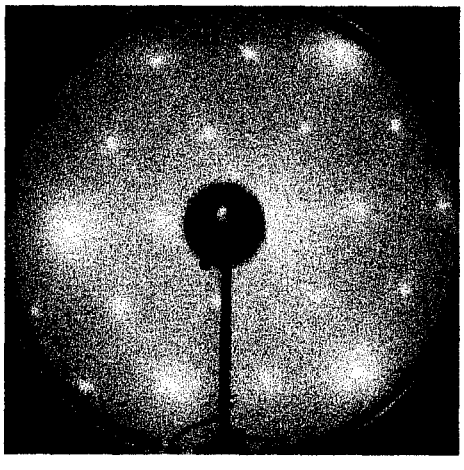

(b) 2 x 2
43% to 59% of Na 2p
area saturation
Beam energy 45.0 eV

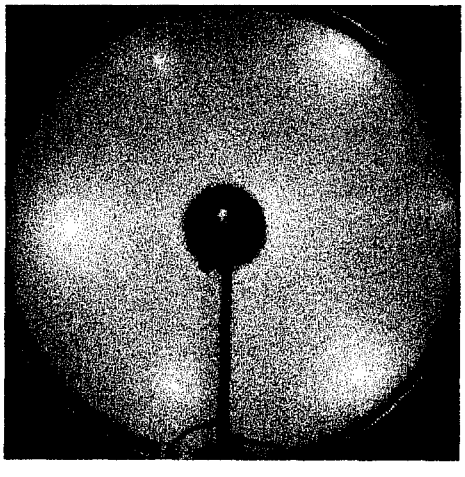

(c) 1 x 1
59% to 100% of Na 2p
area saturation
Beam energy 45.0 eV

Figure 5.7. Na 2p core-level photoemission spectra for the Na/Si(111) interface as Na coverage is increased. The observed LEED pattern at each coverage is indicated. Photon energy is 77 eV.

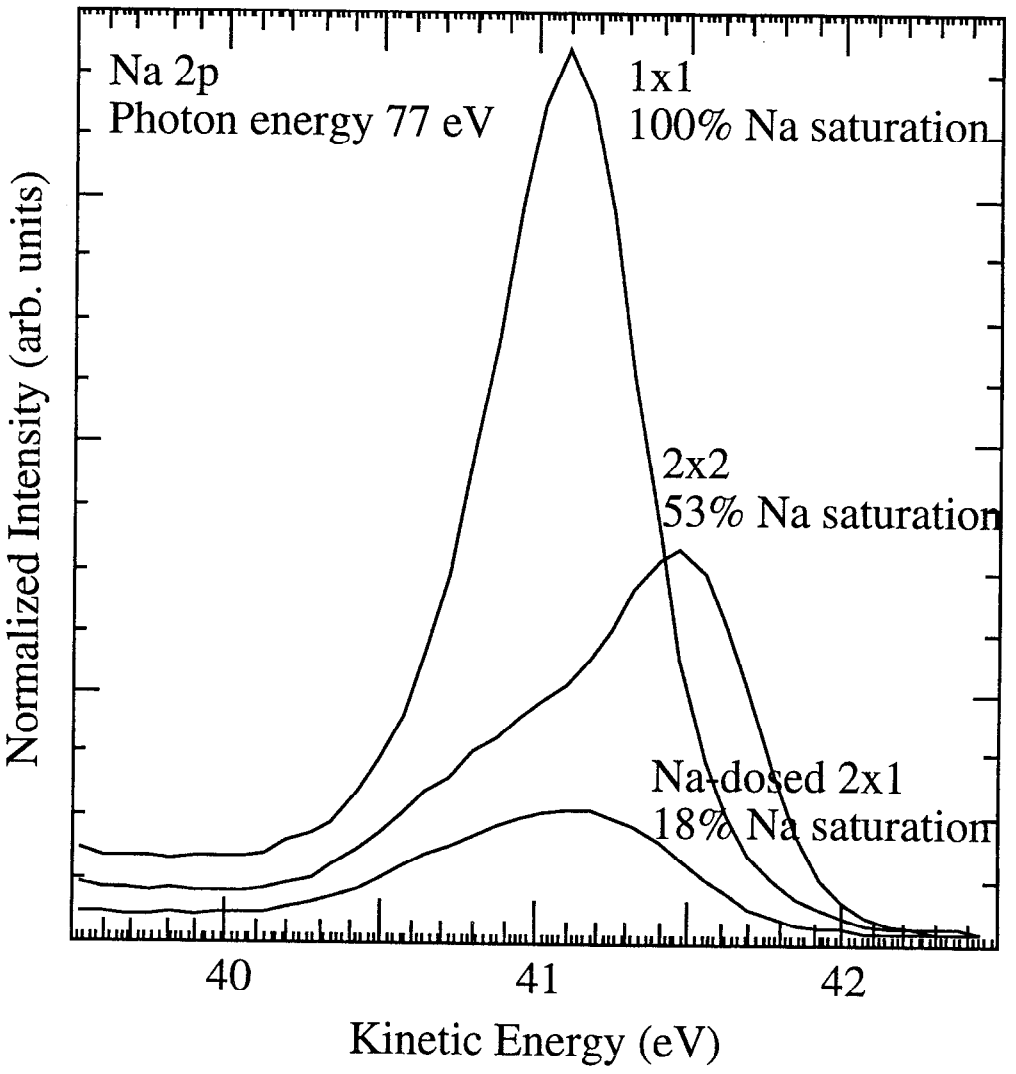

Figure 5.8. Surface-sensitive Si 2p core-level photoemission spectra for the Na/Si(111) interface as Na coverage is increased. The observed LEED pattern at each coverage is indicated. Photon energy is 145 eV. Also indicated are the bulk (B) and surface (S1-S3) components of the best fit to the Si 2p lineshape.

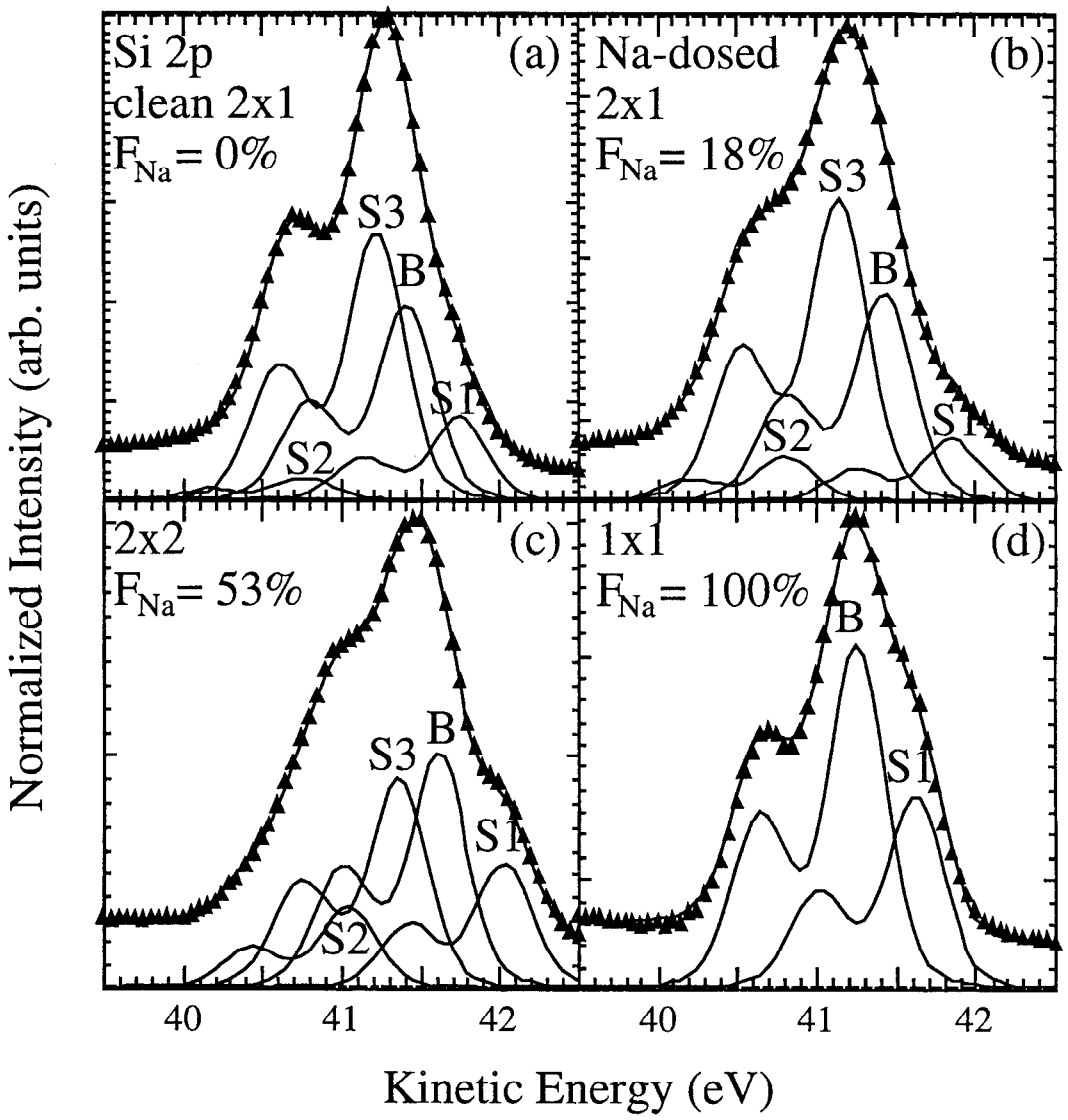

Figure 5.9. Photoemission spectra of the valence band region for the Na/Si(111) interface as Na coverage is increased. The observed LEED pattern at each coverage is indicated. Photon energy is 65 eV. Note the growing peak at the top of the valence band and the dramatic shift of this peak as the surface becomes 1x1.

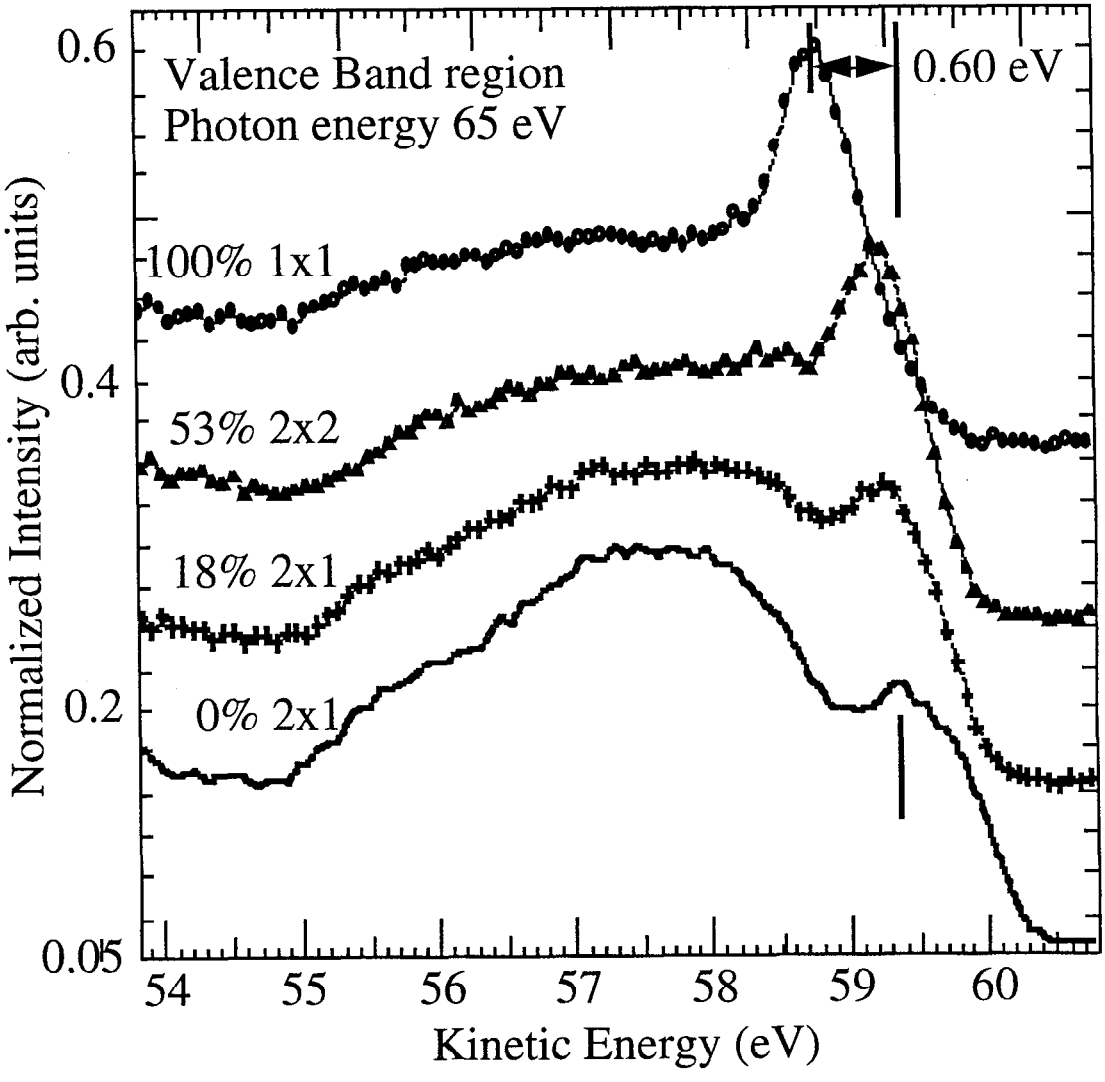

CHAPTER SIX

STRUCTURAL DETERMINATION OF THE CLEAVED CS/SI(111) $\sqrt{3}$x$\sqrt{3}$–R30^{o} INTERFACE: RETENTION OF THE SUBSTRATE PI-BONDED CHAIN STRUCTURE AND ADSORPTION GEOMETRY

Abstract

The atomic geometry of the cleaved Cs/Si(111) $\sqrt{3}$x$\sqrt{3}$–R30^{o} interface at 1/3 ML Cs coverage is determined through a combination of the techniques of backreflection X-ray standing waves, low-energy electron diffraction, photoelectron spectroscopy, and secondary-electron cutoff measurements. Unlike the structure of other metal/Si(111) $\sqrt{3}$x$\sqrt{3}$–R30^{o} interfaces, Cs interacts weakly with the Si substrate and does not destroy the reconstruction of the clean surface. X-ray standing wave data from the 111 and 11$\bar{1}$ reflections indicate that Cs adsorbs in two equivalent high-coordination sites on either side of the π-bonded Si chains. The resulting unit cell is $2\sqrt{3}$x$\sqrt{3}$–R30^{o}; however, a kinematic simulation shows the LEED pattern to be $\sqrt{3}$x$\sqrt{3}$–R30^{o} over the observed energy range.

Introduction

Determining the atomic structure of alkali metal / semiconductor interfaces is an important part of understanding the process of alkali adsorption. Due to the alkali metal's single valence electron, the interaction between the alkali adsorbate and semiconductor substrate might be expected to be simple at first glance. However, experiments have shown that the resulting interface structure and electronic properties depend upon the initial surface structure, alkali coverage, alkali adatom size, and the relative strength of adsorbate-substrate versus adsorbate-adsorbate interactions. For example, in their studies of adsorption of Na, K, and Cs upon the cleaved Si(111) surface, Reihl *et al.* [1,2,3] found that these alkali are not isoelectronic and have different LEED patterns at saturation coverage.

The adsorption of Cs upon the cleaved Si(111)2x1 surface has been studied previously with conflicting results. On one side is the experimental work of Tochihara *et al.* [4,5] and the complementary band structure calculation of Ishida *et al.* [6]. Through core-level Cs 4d photoemission spectroscopy, Tochihara *et al.* observe a plasmon loss peak at 100% Cs saturation coverage which does not appear at 40% Cs saturation coverage and suggest a transition to a metallic overlayer occurs at 50% Cs saturation coverage[4]. Valence-band photoemission results indicate the π-bonding state of the Pandey-chain reconstruction[7] of the clean Si(111)2x1 surface is stable to Cs adsorption up through saturation coverage. In addition, a peak attributed to a Cs 6s-like state can be seen in the difference spectra of the valence band at different coverages. Ishida *et al.* [6] used these results to model the surface bands of a Cs/Si(111)2x1 surface with Cs adsorbed in a high-coordination site on top of a buckled π-bonded Si chain structure. The resulting band structure shows little modification to the bonding π-band relative to the clean surface, while the Cs 6s band of a Cs overlayer and the antibonding π^*-band hybridize to form a new surface band which is partially filled and therefore metallic at saturation coverage. The interaction between Cs and Si is weak, and the π-bonded chain structure of the clean surface remains underneath a metallic Cs overlayer at high coverages.

On the other side, Magnusson and Reihl[3] performed a study of Cs adsorbed on the cleaved Si(111) surface using low-energy electron diffraction (LEED) and angle-resolved inverse photoemission spectroscopy. They also measured the lowering of the work-function with increasing Cs coverage due to alkali-Si dipole formation, and found that at the minimum of the work function, a well-ordered $\sqrt{3}x\sqrt{3}$–R30° LEED pattern is observed. Angle-resolved inverse photoemission spectroscopy on the lowest unoccupied state showed no Fermi level crossing, so the surface is semiconducting.

The π-bonded chains of the underlying Si surface are claimed to be removed by the Cs adsorption, because a √3x√3–R30° arrangement of adsorbate atoms usually occurs upon a bulk-terminated Si(111) surface.

The cleaved Cs/Si(111)√3x√3–R30° interface is different from other √3x√3–R30° interfaces in several ways. First, the Cs/Si(111)√3x√3–R30° pattern is formed after room temperature dosing, while most other √3x√3–R30° interfaces require annealing. Previously studied √3x√3–R30° interfaces also are formed upon an initial Si(111)7x7 wafer surface, while the Cs/Si(111)√3x√3–R30° is formed upon the cleaved Si(111)2x1 surface. The 7x7 structure is an absolute energy minimum of the Si(111) surface, while the 2x1 reconstruction forms spontaneously upon room temperature cleaving and is a local minimum of surface energy. The energy required to convert the Si(111)2x1 surface to a bulk-terminated 1x1 structure is 0.36 eV per surface atom on the clean surface[8]. This energy often is overcome by overlayer adsorption, and for this reason the bulk-terminated surface frequently is chosen as the starting point of structural models on the Si(111) surface. We previously have found[9] that Na adsorption destroys the π-bonded chain structure and bulk-terminates the surface at saturation coverage, and Batra *et al.* [10] have found that a bulk-terminated K/Si(111) surface has 0.3 eV lower total energy than a K/Si(111) surface with an underlying π-bonded chain structure. However, the Cs atomic radius is considerably larger than that of Na or K and previous results suggest the strength of the Cs-Si interactions is weaker from those for Na and K, and may be insufficient to convert the π-bonded chain surface to a bulk-terminated structure.

While a bulk-terminated Si surface seems a natural choice for the model of the Cs/Si(111)√3x√3–R30° interface, not all √3x√3–R30° interfaces on Si(111) have an underlying bulk-terminated surface. In particular, the Ag/Si(111)√3x√3–R30° interface was found to have a extra top layer of Si in honeycomb chained trimers (the HCT model)[11-12], with Ag adsorbed in a site bridging neighboring Si trimers. In this case the √3x√3–R30° LEED pattern is created by both the substrate and adsorbate structure. However, in most cases the √3x√3–R30° LEED pattern is created by the adsorbate overlayer geometry on top of a bulk-terminated Si structure. Al, Ga, and In all adsorb in the threefold-coordinated filled (T_4) high-symmetry site[13-15], while Sb trimerizes in a "milk stool" geometry centered on the same T_4 site[16]. The coverage to produce a √3x√3–R30° interface also varies with the adsorbate. Al, Ga, and In/Si(111)√3x√3–R30° interfaces appear at 1/3 ML, while Sb and Pd[17] form √3x√3–R30° interfaces at 1 ML, where "1 ML" is one monolayer, corresponding to one adatom per Si surface atom. Bi forms √3x√3–R30° interfaces at both 1/3 ML and 2/3

ML with different adsobate geometries on the bulk-terminated Si(111) surface. As seen from the discussion above, the Cs coverage of the Cs/Si(111)$\sqrt{3}$x$\sqrt{3}$–R30° interface is disputed.

In this paper we examine the Cs/Si(111)$\sqrt{3}$x$\sqrt{3}$–R30° interface in further detail using the techniques of backreflection X-ray standing waves, low-energy electron diffraction, photoelectron spectroscopy, and secondary-electron cutoff (work function difference) measurements. In this way we resolve the apparently contradicting previous results by determining the true Cs coverage for the Cs/Si(111)$\sqrt{3}$x$\sqrt{3}$–R30° interface and suggesting a new structural model for the surface based upon the precise structural information provided by X-ray standing waves. This model is novel in that it maintains the π-bonded Si chain structure underneath the Cs overlayer. Cs adsorbs in a two-site geometry which has a 2$\sqrt{3}$x$\sqrt{3}$–R30° unit cell, but the Cs overlayer produces a $\sqrt{3}$x$\sqrt{3}$–R30° LEED pattern over the observed energy range. The retention of the π-bonded chain structure for the Si(111) substrate is supported by our photoemission and LEED data and surface-sensitive X-ray standing wave data probing surface Si positions. The photoemission data agree with that of Tochihara *et al.* [4-5] and suggests a weak interaction between Cs and Si for the Cs/Si(111)$\sqrt{3}$x$\sqrt{3}$–R30° interface.

Experimental

All experiments were performed inside a UHV chamber, with ~$4\text{x}10^{-11}$ torr base pressure. The pressure during dosing did not rise above $8\text{x}10^{-11}$ torr. Good vacuum was required during the experiment as room-temperature dosed alkali/semiconductor interfaces are very susceptible to contamination. The Si(111) surface samples were cleaved *in situ* from *p*-type 5x5x12mm^3 crystalline Si bars of resistivity 26 Ω-cm using the anvil-and-hammer technique. The samples were cut and oriented in the chamber so that the top face is normal to the $(\bar{1}10)$ direction and the side faces are normal to the $(11\bar{2})$ direction. Before dosing, the quality of the cleaved surface was checked using LEED, and only surfaces with good single-domain 2x1 LEED patterns were studied. Cesium was evaporated upon the samples by resistively heating a well-outgassed SAES chromate getter. The distance from the Cs getter to the Si(111) was optimized at ~3.8 cm to avoid heating of the sample surface from the evaporator while limiting the required dosing time and pressure. The cleaver, getter, cylindrical mirror analyzer (CMA), and LEED optics all are in the same analysis chamber. All of the data were collected with the sample at room temperature.

The work function (WF) difference and photoemission spectroscopy (PES) measurements for sodium dosing progressions were taken on Beam Line 8-1 at the Stanford Synchrotron Radiation Laboratory (SSRL). The incident beam was monochromatized using 822.6 and 2400 line/mm toroidal grating monochromators (TGMs), and exit slits downstream of the TGM were set to 100μm in both vertical and horizontal directions. A double-pass CMA analyzed the photoelectron yield, and the sample surface was oriented at an angle of 45° from both the incident beam and the CMA axis. The change in the secondary electron cutoff with sodium coverage provided WF difference data. The sample bias was -12.31 V for the cutoff measurements. The incident photon energy for Cs 4d and Si 2p PES spectra were 77 eV and 145 eV, respectively, and the electron kinetic energies for the Si 2p spectra are close to the minimum of the "universal" escape depth curve. Photoemission data were normalized to the incident photon flux, which was measured using a channeltron to collect electrons emitted from a thin Ni grid placed in the incident beam's path. The photon energy for the Cs 5p and valence band PES spectra and WF difference measurements was 65 eV. Throughout the dosing progression, no evidence of oxygen contamination (emission ~5 eV below the valence band maximum) was observed in the valence band (VB) spectra.

LEED photographs were taken for each Cs dose to check the quality of the clean single-domain 2x1 and Cs-dosed $\sqrt{3}x\sqrt{3}$–R30° interfaces. LEED patterns were imaged using a reverse-view LEED optics, which allowed a clear field of view. Photographs were taken at several beam energies with a 30 sec exposure time. The filament current was ~1 mA, and we tried to take pictures quickly to avoid electron beam damage to the surface. Most LEED patterns observed appeared over a large beam energy range down to ~25 eV or below and over the entire sample. The $\sqrt{3}x\sqrt{3}$–R30° LEED pattern also was produced during a separate experiment in which we invested the progression of the LEED pattern with increasing cesium coverage, and appeared at similar Cs coverage to the "one shot" dosings used for the X-ray standing wave experiments.

X-ray Standing Wave (XSW) data were collected in the backreflection mode[18-26] using the same chamber and instrumentation as for the LEED and PES studies. The sample is aligned so that incident photons are normal to the (111) or $(11\bar{1})$ Bragg planes of Si and monochromatized using a pair of InSb(111) crystals on the soft X-ray beam line 3-3 (JUMBO) at SSRL. The sum of the incident and Bragg-reflected X-ray flux is monitored by amplifying the emission current of an Ni grid collected with a channeltron. Before collecting XSW data, a photoemission scan is taken to locate the photopeak of interest, either Cs 3d or Si 1s at binding energies –740.5 eV or –1839.3

eV, respectively. Then the XSW absorption yield of Cs or Si atoms as a function of photon energy is monitored via the total counts at the photopeak with the CMA. The photopeak kinetic energy is tracked as the photon energy changes. Background standing wave scans are recorded slightly above the peak (higher kinetic energy) and the background XSW data are collected in a separate run immediately after the on-peak XSW data. This background XSW yield reflects inelastically scattered bulk electrons and also varies with photon energy, and is subtracted from the on-peak XSW yield to give the specific signal of interest. With the photon energy equal to the (111) backreflection energy of 1977 eV for Si, the Si 1s photoelectrons are highly surface sensitive, with a kinetic energy near the minimum of the universal curve. Total electron yield data are recorded concurrently by monitoring the amplified drain current from the sample.

Both (111) and (11$\bar{1}$) diffraction planes were used for backreflection XSW, and in most cases the XSW data set for one reflection were taken on the same surface immediately after taking the full data set for the other reflection. Oxygen contamination was checked periodically via O 1s photoemission, as reasonable valence band spectra were not available at this high photon energy. We tried to take the XSW data in as short an amount of time as possible to get reasonable fit results, in order to avoid contamination of the surface, which is highly susceptible to adsorption of oxygen and other contaminants. This accounts for the roughness of the XSW data presented. The (111) reflection is taken with the surface normal to the incident beam, while the (11$\bar{1}$) reflection has the sample turned towards the analyzer so the incident photons are at an angle of 70.53° with respect to the surface normal. In the horizontal plane, the CMA axis is 90° from the incident photon and parallel to the bulk reflecting planes.

Coverage Determination

The cesium coverage of the Cs/Si(111)$\sqrt{3}$x$\sqrt{3}$–R30° interface is critical to selecting a correct structural model. We determined this coverage as part of a cesium dosing progression experiment. At incremental cesium coverages on the same surface, Cs 4d, Cs 5d, Si 2p, valence band, and secondary electron cutoff photoemission spectra and LEED patterns were taken. The coverage was increased until the Cs 4d photopeak area saturated. Cesium coverage was measured by integrating the Cs 4d photopeak area (binding energy Cs $4d_{3/2}$ 79.8 eV and Cs $4d_{5/2}$ 77.5 eV), normalized to the incident photon flux. Cesium coverage for a given dose is represented as the

percentage of the Cs4d photopeak area achieved at the saturation coverage. The progression includes eight distinct LEED patterns from the clean surface to saturation Cs dosing, which will be discussed elsewhere. Averaging over three samples in three separate experimental runs, the $\sqrt{3}x\sqrt{3}$–R30° LEED pattern occurred between 56% and 88% of saturation coverage. As there were finite dosing steps, these limits are halfway between the observed coverage for $\sqrt{3}x\sqrt{3}$–R30° LEED pattern and the neighboring patterns. The observed $\sqrt{3}x\sqrt{3}$–R30° LEED patterns occurred between 65% and 83% of saturation coverage.

The Cs/Si(111) interface work function difference from the clean surfacewas measured from differences the secondary electron cutoff. Figure 6.1 plots work function difference as a function of coverage, which is represented as the percentage of Cs 4d peak area saturation. The work function is minimized at 93% saturation coverage at a value of -3.56 ± 0.10 eV, in agreement with the value of -3.7 eV measured by Magnusson and Reihl[3] for the cleaved Cs/Si(111) interface. Above this coverage, the work function begins to increase. Magnusson and Reihl[3] plot work function difference versus Cs dosing time. They interpreted the work function minimum as the saturation of Cs coverage and observed the $\sqrt{3}x\sqrt{3}$–R30° LEED pattern in the region of this minimum. They attributed the increase in the work function past the minimum to an oxidation effect. However, their work does not utilize a direct probe of Cs coverage such as Cs 4d photopeak area. Our interpretation of the work function minimum is that it occurs at slightly less than saturation coverage. At saturation coverage (upper spectrum in Figure 6.2), the Cs 4d photopeak shows a low-energy plasmon loss tail which can be attributed to a metallic overlayer. Therefore the increase in work function at saturation coverage is due to a weakening of the Cs-Si dipole strength as charge is returned from the Cs-Si bond to the metallic Cs overlayer. The region in which we observe the $\sqrt{3}x\sqrt{3}$–R30° LEED pattern is right before the work function minimum, which is consistent with the observation of Magnusson and Reihl [3]. The Cs 4d photoemission peak for Cs/Si(111)$\sqrt{3}x\sqrt{3}$–R30°, which is the lower spectrum in Figure 6.2, is the highest Cs coverage which does not have the metallic low-energy tail. So for Cs/Si(111)$\sqrt{3}x\sqrt{3}$–R30° the metallic overlayer has not yet formed, which is consistent with Magnusson and Reihl's determination that the interface is semiconducting[3].

Magnusson and Reihl[3] assign the $\sqrt{3}x\sqrt{3}$–R30° interface to a saturation coverage of 1 ML Cs. However, Cs is a very large atom, with a metallic radius of 2.62 Å. Thus a metallic hcp overlayer of Cs, which may be expected at saturation coverage, has a Cs-Cs distance of 5.24 Å. The distance between Si surface atoms on the bulk-

terminated Si surface is the second-nearest-neighbor distance, 3.48 Å. Therefore, the number of monolayers at saturation coverage, defined as the number of Cs atoms for each surface Si atom, is $(3.48 \text{ Å} / 5.24 \text{ Å})^2 = 0.54$ ML. The $\sqrt{3}x\sqrt{3}$–R30° interface, observed from 56% to 88% of saturation coverage, corresponds to 0.30 to 0.48 ML. Thus we assign a coverage of 1/3 ML to our model of the Cs/Si(111)$\sqrt{3}x\sqrt{3}$–R30° interface, although the LEED pattern may persist at coverages up to 1/2 ML.

Photoemission and LEED Results

As discussed in the introduction, the 2x1 π-bonded chain reconstruction is formed spontaneously upon cleaving the (111) face of Si. This structure, first proposed by Pandey[7], consists of Si zig-zag chains along the $[\bar{1}10]$ direction, with π-bonding between the top chain atoms and a dangling bond at each top chain atom. The side view consists alternating 5-fold and 7-fold chain atoms, which evolve from the 6-fold rings of the bulk-terminated surface through a pathway described by Northrup and Cohen[8] which has an energy barrier of 0.03 eV per surface atom from the 1x1 to 2x1 surface. The clean 2x1 surface is metastable, 0.36 eV per surface atom lower in energy than the bulk-terminated surface[8] but 0.04 eV per surface atom higher in energy than the absolute energy minimum, the 7x7 reconstruction[27]. However, the 7x7 cannot be acheived at room temperature due to the large rearrangement of Si surface atoms. In contrast, the 2x1 reconstruction pathway involves the breaking and reforming of one Si-Si bond, with no missing Si atoms. It can be reverted to the bulk-terminated structure through the adsorption of a sufficiently reactive atom, and among alkalis Na has been shown to bulk-terminate the surface at saturation coverage[1,9]. However, our photoemission and LEED data demonstrate that Cs does not interact strongly enough with the surface Si to bulk-terminate the surface, and the underlying Si surface of the Cs/Si(111)$\sqrt{3}x\sqrt{3}$–R30° interface retains the π-bonded chain structure.

The valence band photoemission spectra of the clean Si(111)2x1 and Cs/Si(111)$\sqrt{3}x\sqrt{3}$–R30° surfaces are compared in Figure 6.3. The clean surface spectrum displays the π-bonding surface state peak at the top of the valence band which is characteristic of the π-bonded chain reconstruction. This peak remains in the $\sqrt{3}x\sqrt{3}$–R30° surface spectrum; in addition, spectral weight has been added to the valley between the surface state peak and the rest of the valence band. Tochihara *et al.* [4] had similar valence band spectra, and when subtracting the Cs-dosed and clean spectra, they found the increased spectral weight formed a peak which increased with

Cs coverage and developed a metallic loss feature at coverages near saturation. They assign this peak to a Cs 6s-like bonding band, and the calculation of Ishida *et al.* [6] confirms this assignment and that the Cs 6s and π^* antibonding band of the Si chains overlap in parts of the surface Brioullin zone. They also find the π-bonding band of the chain reconstruction to survive the Cs adsorption. Since the peak corresponding to the clean 2x1 π-bonding surface state remains for the Cs/Si(111)$\sqrt{3}$x$\sqrt{3}$–R30° interface, we conclude the π-bonded chain surface remains underneath a Cs overlayer that determines the $\sqrt{3}$x$\sqrt{3}$–R30° LEED pattern.

Si 2p and Cs 4d spectra (not depicted) also support the retention of the π-bonded chains. Both the Si 2p and Cs 4d lineshapes do not change significantly from their shapes for the Cs/Si(111) surface with 20% saturation Cs coverage. The low-coverage surface shows a LEED pattern with strong 2x1 spots and additional $\sqrt{7}$x$\sqrt{7}$–R19° spots, and at such a coverage the π-bonded chain reconstruction should remain with Cs decorating the surface. The Si 2p takes a 4-component fit corresponding to a bulk and three surface components, while the Cs 4d has one wide (0.77 eV Gaussian width) component at all Cs coverages up to and including that for Cs/Si(111)$\sqrt{3}$x$\sqrt{3}$–R30°. At higher coverages up to saturation, the Cs 4d lineshape develops a plasmon loss peak -1.1 eV kinetic energy below the main peak, which is consistent with the core-level photoemission work of Tochihara *et al.* [5]. Since the lineshapes do not change from that for the low-coverage Cs/Si(111) surface where Cs decorates the underlying π-bonded chain, the Cs 4d and Si 2p photoemission spectra also support the retention of the π-bonded chain underneath the Cs overlayer for Cs/Si(111)$\sqrt{3}$x$\sqrt{3}$–R30°.

The neighboring LEED patterns for Cs coverages above and below the $\sqrt{3}$x$\sqrt{3}$–R30° LEED pattern (Figure 6.4(b)) also suggest an underlying direction to the Si surface structure. The lower-coverage pattern, seen from 37% to 77% saturation Cs coverage, is a combination of 2x1 and $\sqrt{3}$x$\sqrt{3}$–R30° LEED patterns (Figure 6.4(a)). This pattern could indicate patches of bare silicon 2x1 and Cs-covered $\sqrt{3}$x$\sqrt{3}$–R30° on the surface, but could also be due to a $\sqrt{3}$x$\sqrt{3}$–R30° Cs overlayer of not enough Cs coverage to damp out the 2x1 pattern from an underlying Si chain. While this pattern is not conclusive on its own, the LEED pattern following the $\sqrt{3}$x$\sqrt{3}$–R30° LEED pattern also shows the directionality of the original 2x1 clean surface. This complicated-looking zig-zag pattern (Figure 6.4(c)) can be separated into two domains of a $\sqrt{3}$x2 or $\begin{pmatrix} 2 & 0 \\ 1 & 2 \end{pmatrix}$structure. The pattern clearly has a mirror plane about the vertical $[\bar{1}10]$ axis. However, the missing third domain makes the symmetry of the overall pattern twofold,

not threefold as one would expect from the bulk-terminated Si surface or an adsorbate overlayer reconstruction on a bulk-terminated surface.

This reduced symmetry is due to the underlying π-bonded chain, which restricts the adsorption geometry of the Cs for this pattern. Since the patterns at coverages above and below the $\sqrt{3}x\sqrt{3}$–R30° LEED pattern have reduced symmetry and suggest and underlying π-bonded Si chain structure, it is reasonable to assume that the $\sqrt{3}x\sqrt{3}$–R30° LEED pattern reflects the Cs overlayer structure and that the π-bonded chain is retained underneath but does not contribute significantly to the LEED pattern. The LEED pattern will be discussed further below in the presentation of our model for the Cs/Si(111)$\sqrt{3}x\sqrt{3}$–R30° interface.

X-ray Standing Wave Results: Cs 3d Absorption Yield

The backreflection version of the X-Ray Standing Wave (XSW) technique[18-26] utilizes synchrotron radiation by keeping the sample angle fixed and varying the photon energy in a region about the Bragg energy of a Si crystal diffraction plane oriented normal to the incident X-rays. Near the Bragg condition, the incident beam is reflected by the bulk Si crystal lattice, and the superposition of incident and reflected X-rays forms a standing wave which both penetrates the crystal and extends out past the crystal surface. The phase of the standing wave, and therefore the position of its intensity extrema with respect to the crystal diffraction plane, changes with photon energy for the fixed-angle technique. By monitoring the X-ray absorption of adsorbate or substrate atoms as a function of incident photon energy in the Bragg region, an absorption profile is measured which is characteristic of the atomic position, relative to the bulk diffracting plane positions of the substrate crystal. The coherent distance D_c and the coherent fraction f_c of the absorbing atoms are determined by fitting the absorption profile to the equation

$$Y(E)/Y_0 = 1 + R(E) + 2 f_c \sqrt{R(E)} \cos(\nu(E) - 2\pi D_c) \qquad (1)$$

where Y_0 is the background absorption yield away from the Bragg reflection, and R(E) and ν(E) are the magnitude and phase of the reflectivity and are functions of photon energy E. In the case of single-site adsorption, the coherent distance D_c corresponds to the distance of the absorbing atom from the diffracting plane divided by the diffraction plane spacing (3.135 Å for the (111) planes of Si). The coherent fraction f_c is equal to the fraction of adsorbing atoms situated in the site; the remaining

fraction $(1 - f_c)$ of atoms are disordered and their contribution to the interference term (last term of the above equation) averages to zero. Thermal disorder in the absorbing atoms also reduces the coherent atoms by a Debye-Waller factor $e^{-2\pi^2\sigma_H^2}$, where σ_H^2 is the mean squared atomic vibration amplitude in the direction of the reflection H. In the case of multiple sites of the absorbing atoms, each site *i* contributes an interference term, with the weight of each term determined by the relative populations $f_{c,i}$ and the phase of each term given by the distance $D_{c,i}$ of the site from the diffracting plane; the fraction $1 - \Sigma f_{c,i}$ corresponds to the fraction of atoms in disordered positions. For the specific case of equal populations of atoms in two different absorbing atom positions, the coherent distance D_c is equal to the average atom position, and the coherent fraction is related to the spread in the two atom positions $D_{c,1}$-$D_{c,2}$ by the equation

$$f_c = \cos(\pi(D_{c,1}-D_{c,2})) \qquad (2)$$

Thus, if the two atoms are separated by half a diffraction plane spacing, their contributions to the standing wave absorption yield are exactly out of phase and cause the coherent fraction to vanish, and the absorption yield matches the sum of incident and reflected intensities, 1+R(E).

The (111) reflection measures the normal component of adatom surface positions (i.e. height above the substrate), while the coherent distance from the $(11\bar{1})$ reflection is predominantly the surface lateral component of adatom positions along the $(1\bar{1}2)$ direction. On the cleaved Si(111) surface, the $(1\bar{1}2)$ direction corresponds to the direction perpendicular to the π-bonded chains of our single-domain clean Si(111)2x1 surfaces. By considering the data from both reflections, the Cs adsorption site positions can be triangulated.

The bulk Si profile can be measured via total yield or the electron yield of the off-peak background, which is dominated by inelastically scattered electrons. These electrons are produced within a substrate depth much less than the extinction depth of the photons. "Hot" electrons also do not contribute to the total and background yields at the low photon energy of the backreflection condition[21]. The total yield and background XSW data for all the data sets presented here agreed within error bars with the expected values for the bulk atomic structure (D_c= 1, f_c = 0.707), which is an internal check of the XSW data.

Cs 3d absorption yield XSW data for the (111) and $(11\bar{1})$ reflections are given in Figure 6.5 for the Cs/Si(111)$\sqrt{3}$x$\sqrt{3}$–R30° interface, along with the best fits to the data. The resulting coherent distance and fractions of the fits for each reflection were reproducible over multiple samples. The coherent distance and fraction values,

averaged over two samples, is given in Table 6.1. The best fit is chosen through a least-squares technique, and the error bars listed reflect where the χ^2 value is doubled from its minimum value.

For the (111) reflection normal to the surface, the coherent distance of 0.952 ± 0.042 corresponds to a Cs height of 2.98 ± 0.13 Å above the bulk diffraction plane. For an unrelaxed bulk-terminated Si surface model, this height corresponds to a reasonable Cs-Si distance of 3.52 Å for the threefold symmetry sites on the surface (H_3 and T_4). However, the Cs-Si distance of 2.59 ± 0.13 Å for an atop geometry (T_1) is far too short relative to the sum of covalent radii, ruling out a single-coordination geometry. As we shall see in our model below, the measured Cs height is reasonable for adorption sites on a π-bonded-chain reconstructed Si(111) surface.

In the case of single-site adsorption, the $(11\bar{1})$ reflection and (111) reflection coherent distances can be triangulated to determine the Cs adsorption site position. For a bulk-terminated surface model for the Cs/Si(111)$\sqrt{3}$x$\sqrt{3}$–R30° interface, this triangulation places the Cs adsorption site close to the atop geometry (T_1). However, the Cs-Si distance determined by the (111) reflection distance alone rules out this geometry. In addition, for single-site adsorption we would expect a $(11\bar{1})$ coherent fraction close to 1, but the measure fraction is much less than 1. The bulk-terminated atop geometry has been shown to be energetically unfavorable for K and Na adsorption on the Si(111) surface[28-30], so it is reasonable to assume that this is not the preferred geometry for Cs. Instead, the threefold-cordinated sites are preferred. However, models of the Cs $\sqrt{3}$x$\sqrt{3}$–R30° overlayer using only threefold-coordinated sites (H_3 and T_4) on the bulk-terminated surface cannot reproduce a XSW triangulation near the atop geometry. Along with the photoemission and LEED results described above, the conflicting XSW results of the measured height and lateral triangulation rule out a bulk-terminated model for the underlying Si surface for Cs/Si(111)$\sqrt{3}$x$\sqrt{3}$–R30°.

The lower coherent fraction in the $(11\bar{1})$ direction also indicates multiple Cs sites with different lateral registry or lateral disorder on the surface. The higher (111) coherent fraction suggests that multiple Cs sites would have similar heights above the Si(111) surface. Vleig *et al.* had a similar, repeatable decrease in the $(11\bar{1})$ coherent fraction relative to the (111) coherent fraction for the Ag/Si(111)$\sqrt{3}$x$\sqrt{3}$–R30° interface, and they successfully modelled the surface with Ag in a triangular arrangement on top of a honeycomb-chained-trimer (HCT) reconstructed Si(111) surface. The inequivalent lateral positions of the three Ag atoms in the triangle reduced the $(11\bar{1})$ coherent fraction, while the (111) fraction was equal to 1 within error bars, indicating the Ag were all at the same height above the surface. The Cs coherent fraction for the vertical

(111) reflection is 0.641 ± 0.165, significantly lower than 1. We assert that the reduction of the (111) coherent fraction is almost completely due to the thermal motion of Cs, which is weakly bound to the Si as seen from photoemission. Using the equation $f_{c,themal} = e^{-2\pi^2\sigma_H^2}$, where σ_H^2 is the mean squared atomic vibration amplitude normalized to the diffraction plane spacing, the measured coherent fraction corresponds to a mean squared amplitude of 0.22 ± 0.11 Å^2. Unfortunately, no published Debye-Waller factors exist for Cs/Si(111), but fits to surface X-ray diffraction data on the Cs/Cu(001) interface [31] give a mean squared vibration amplitude between 0.18 Å^2 and 0.29 Å^2, which matches our amplitude for Cs/Si(111) assuming the reduction in the coherent fraction is mostly thermal in origin. A similar thermal reduction factor of about 0.7 should be expected for the $(11\bar{1})$ coherent fraction; however, the measured fraction is 0.371 ± 0.108, indicating further reduction due to multisite Cs adsorption or Cs static lateral disorder. Cs static disorder can be ruled out due to the long-range ordered implied by the good $\sqrt{3}x\sqrt{3}$–R30° LEED pattern; therefore, Cs adsorbs in multiple sites upon the Si(111) surface.

Cs/Si(111)$\sqrt{3}x\sqrt{3}$–R30° Interface Structural Model

Our PES, LEED, and Cs 3d XSW data place restrictions on a structural model for the Cs/Si(111)$\sqrt{3}x\sqrt{3}$–R30° interface. This model should have an underlying π-bonded Si chain structure, and a Cs overlayer arranged to form a $\sqrt{3}x\sqrt{3}$–R30° LEED pattern with multiple Cs adsorption sites. Our proposed structural model fulfulling these requirements is depicted in Figure 6.6. As seen in the top view Cs is adsorbed in two equivalent sites, labelled Cs1 and Cs2, which correspond approximately to the centers of the two tilted hexagons of the buckled Si(111) π-bonded chain stucture. Each Cs adatom satisfies the dangling bonds of two Si top chain atoms with a Cs-Si distance of 3.78 Å. This bond length was chosen to match the measured value of 3.79 ± 0.04 Å for low-coverage Cs overlayers on the Si(111)7x7 surface[32]. The Cs atoms in both sites also are 3.78 Å away from a second layer Si chain atom, and 4.11 Å away from the top chain Si atom in the neighboring chain. Thus the Cs coordination is at least threefold, and location at the hexagon centers could increase the bond coordination further. This tendency towards higher coordination has been seen for both the K/Si(111) and Na/Si(111) surfaces[9, 28-30]. As the bond lengths and coordination environment are quite similar for the two Cs sites, we expect the PES core-level shift for the two sites to be quite similar. The measured PES spectra only

show one Cs 4d component, but the large width of the peak makes the occupation of two energetically similar Cs sites reasonable.

This model was based upon structural models of the Cs/GaAs(110) surface, which are further based upon STM results on Cs/GaAs(110) [33]. These models depict Cs lining up along and bonding with the GaAs chains. However, Cs bonds to only one side of the chain due to the inequivalence of Ga and As. For Si(111)2x1 the two Si atoms in the buckled top chain are not identical, but they are more similar than Ga and As, which may allow Cs to bond on both sides of the π-bonded chain in sites Cs1 and Cs2. The fact that Cs zig-zags instead of lining up along the $[\bar{1}10]$ direction may be in order to reduced to Cs-Si dipole-dipole repulsion; if the Cs were lined up, the Cs-Cs distance would be reduced. In addition, Cs atoms in a line would not produce a "$\sqrt{3}$x3/2" rectangular overlayer unit cell and corresponding LEED pattern, which is not observed, and the Cs adatoms would all have the same lateral registry and would produce a $(11\bar{1})$ coherent fraction much closer to 1 than the measured value of 0.371 ± 0.108. The zig-zag two-site Cs overlayer structure in Figure 6.6 lowers the coherent fraction, and matches the observed LEED pattern when modelled kinematically as described in the section below. The lateral Cs position of Cs1 (see side view) is very similar to that of the model of Ishida *et al.*[6], and site Cs2 is its reflection onto the other side of the buckled chain.

The model was created in several steps, starting with the height and lateral triangulation of the Cs from the Cs XSW results. Using a two-site model as descibed above, the coherent distance matches the average site position, while the coherent fraction is related simply to the spread in the two site positions. With the two nearly equivalent sites in Figure 6.6, the assumption of equal population of both sites is reasonable. The Cs sites were then set so they matched the Cs XSW data, with Debye-Waller coherent fraction reduction factors of 0.64 and 0.74 in the (111) and $(11\bar{1})$ directions, respectively. The intersection of the measured (111) and $(11\bar{1})$ coherent distances is therefore at the midpoint between the two Cs sites. Next, the positions of the Si atoms were taken from the clean Si(111)2x1 buckled-chain surface model of Himpsel *et al.* [34], which is a form of the original Pandey π-bonded chain model [7]. The upper and lower chain Si positions and the Si position in the next bilayer underneath were allowed to vary, while the deeper Si bilayers were kept fixed at bulk values. The upper and lower chain Si positions were varied to make the closest Cs-Si distance equal to 3.78 Å while Si-Si distance were kept between 2.31 Å and 2.39 Å, and the underlayer Si was relaxed to maintain Si-Si bond lengths as well. The side view depicts the differences between the Si chain structure for the Cs-covered surface

(squares) and clean Si(111)2x1 surface (diamonds). The Si structure for Cs/Si(111) amounts an average shift of the Si x positions by 0.45 Å, and an increase in the top chain Si buckling to 0.50 Å (the clean surface buckling is 0.38 Å). In reality, the lateral shift probably is less than this since the deeper layers are not fixed in position. However, the buckling of the chain is required to match the measured $(11\bar{1})$ coherent distance. An unbuckled chain would put the average Cs lateral position at the center of the lower Si chain and would shift the average Cs position by 0.7 Å from the measured average position. This variation procedure did not use an energy minimization procedure; however, since Si-Si bond lengths were unchanged and the resulting structure is not far from the original clean 2x1 surface, the proposed model should be close to an energy minimum of the surface.

Surface-sensitive X-ray standing wave data monitoring the Si 1s photopeak intensity also indicate that the Si surface for the Cs/Si(111)$\sqrt{3}$x$\sqrt{3}$–R30° interface is reconstructed. The data were taken in the backreflection configuration for the (111) reflection of Si, and measures the height distributions of the Si atoms normal to the surface. Because at the (111) backreflection energy of 1977 eV the Si 1s photelectron kinetic energy is near the minimum of the "universal curve", the monitored Si 1s yield has a large component from the first few atomic layers of the Si crystal. Table 6.1 shows the results of fits to Si 1s XSW data for the Cs/Si(111)$\sqrt{3}$x$\sqrt{3}$–R30° interface, as well as measured values for the clean 2x1 surface, and the Na/Si(111)1x1 interface, which we have shown is bulk-terminated in Chapter 5. All three samples have similar coherent distances; this is because in all three models the Si atoms straddle the bulk diffracting planes and the average position is close to on the plane. This is not the case for honeycomb-chain trimer (HCT) and Seiwatz chain surfaces, because these surfaces are missing the Si top layer, so the largest surface contribution has a position below the bulk diffracting plane, and the coherent distance of the Si 1s signal is significantly less than 1. The coherent fraction for the Cs/Si(111)$\sqrt{3}$x$\sqrt{3}$–R30° interface is in between that for the clean Si(111)2x1 and bulk-terminated Si(111) surfaces, and equal to both within the error bars. The increase in coherent fraction for the Cs-covered surface may be a result of the relaxation of the underlying Si π-bonded chain surface and does not necessarily indicate bulk-termination; the increase in coherent fraction for the bulk-terminated Na/Si(111)1x1 compared to the clean 2x1 surface is larger than the corresponding increase for Cs/Si(111)$\sqrt{3}$x$\sqrt{3}$–R30° interface. The Si 1s XSW data are not inconsistent with the propsed π-bonded chain model but it is also not inconsistent with a bulk-terminated Si(111) surface; it does rule out missing top layer (MTL) reconstructions. MTL reconstructions are also ruled out by the fact that the

Cs/Si(111)$\sqrt{3}$x$\sqrt{3}$–R30° interface is created at room temperature, and there is not enough energy involved in adsorption to remove the top layer of Si.

The sum of the equal contributions from the two Cs positions in the model fit the Cs 3d X-ray standing wave results exactly, and Si positions were adjusted from the clean Si(111)2x1 positions to conserve Si-Si bond lengths and keep the Cs-Si bond length at the previously measured value of 3.78 Å [32]. As described in the next section, a Cs height difference of Δz = 0.10 Å needed to successfully emulate the LEED pattern. This height difference was included in the model as another constraint. However, the Debye-Waller factors were chosen from reasonable values in the literature, and varying these values will affect the coherent fraction, with a corresponding change in the spread of the two Cs positions to compensate. The errors in the Cs model positions are set by reasonable variation of these Debye-Waller factors, with a larger error in the lateral Cs positions since LEED results do not constrain the lateral registry of the Cs atoms with respect to the underlying Si(111) surface.

Kinematic Simulation of LEED Pattern for Cs/Si(111)$\sqrt{3}$x$\sqrt{3}$–R30° Model

While the above model matches the Cs 3d XSW data for the (111) and (11$\bar{1}$) reflections as well as the lack of change in the Cs 4d and Si 2p PES spectra and in the π-bonding surface state with increasing coverage, the top view of the model does not have a $\sqrt{3}$x$\sqrt{3}$–R30° unit cell. A parallellogram can be drawn between 4 neighboring Cs adatoms which has a shape similar to the $\sqrt{3}$x$\sqrt{3}$–R30° unit cell, but the angle between the sides of the parallelogram is 78.8° instead of 60°; in addition, it does not repeat along the [$\bar{1}$10] direction due to the zig-zag structure of the chains. The true unit cell is 2$\sqrt{3}$x$\sqrt{3}$–R30°, with the shorter unit vector across the chains in the [11$\bar{2}$] direction. The cell hold both Cs adatom sites. Along the [$\bar{1}$10] direction, one of the Cs sites is on the edge of the unit cell, while the other is exactly half the unit cell width from the edge. As a result, the 2$\sqrt{3}$ spots of the LEED pattern will have complete destructive interference assuming the two Cs sites are at the same height, and the $\sqrt{3}$ spots along the [$\bar{1}$10] direction will have complete constructive interference, making the LEED pattern appear to be $\sqrt{3}$x$\sqrt{3}$–R30°. However, along the mirrored [10$\bar{1}$] and [0$\bar{1}$1] directions, one of the Cs atoms is partially along the unit cell compared to the other, reducing the overall intensity to 50% of the $\sqrt{3}$x$\sqrt{3}$–R30° spots relative to the intensity of the $\sqrt{3}$x$\sqrt{3}$–R30° spots along [$\bar{1}$10] in the kinematic approximation. The observed LEED pattern shows little intensity difference between the three $\sqrt{3}$x$\sqrt{3}$–R30° directions, and no 2$\sqrt{3}$ spots between 40 and 140 eV. In order to match the observed

LEED behavior we must introduce a height difference between the two Cs sites. We model the spots using the kinematic approximation. The quality of this approximation has been shown to be questionable for LEED measurements on most surfaces, with full dynamical calculations needed to predict LEED intensities in most cases[35]. The kinematic approximation assumes single scattering from the topmost atomic layer only, ignoring multiple scattering effects due to the large interaction of low energy electrons and most materials. A Cs overlayer, however, having a much larger size and atomic number Z than the underlying Si, should be the predominant scatterer of low energy electrons, and the probability of multiple scattering should be reduced for heavy Cs atoms due to the high probability of inelastic scattering. Thus, in the case of Cs/Si the kinematic approximation is closer to being correct than on most surfaces. In this approximation, the intensities of the spots are proportional to the square of the structure factor $F_{h_1h_2}$, given by the following sum over all atoms j in the surface unit cell:

$$F_{h_1h_2} = \sum_j f_j \exp\left[2\pi i(h_1x_j + h_2y_j + (1+\cos\phi)z_j / \lambda)\right] \qquad (3)$$

$F_{h_1h_2}$ is the structure factor for the LEED spot with indices (h_1, h_2) in the directions of the surface reciprocal unit vectors, while x_j and y_j are the components of lateral position of atom j along the primitive unit vectors of the surface in real space. z_j is the height of the atom, λ is the wavelength of the electron beam, and ϕ is the angle between the diffracted beam and the surface normal. f_j is the atomic scattering factor of atom j, and in the kinematic approximation, only the Cs overlayer atoms are summed over. The spot intensity varies with beam energy through the wavelength and takeoff angle, and the frequency of this variation is related to differences in the vertical atom heights Δz. For $\Delta z = 0$, there is no energy variation of the spots, and as mentioned above, the pattern appears $\sqrt{3}x\sqrt{3}$–R30°, but the spots have different intensities along the $[\bar{1}10]$ and $[10\bar{1}]$ directions. For Δz greater than 0.15 Å using two Cs sites in the structure factor, the LEED pattern varies too quickly within the 40-140 eV energy range to reproduce the observed LEED behavior. The spot intensity versus beam energy (I-V) curves for the best value of $\Delta z = 0.10$ Å is given in Figure 6.7, along with a drawing of the cooresponding LEED spots in the pattern. With this choice of Δz, the intensity of the $2\sqrt{3}$ spots (labelled X) remains below 30% of the intensity for full constructive interference throughout the observed energy range. On a few samples at higher energies, we saw faint traces of these $2\sqrt{3}$ spots. Also, the $\sqrt{3}x\sqrt{3}$–R30° spots along the $[\bar{1}10]$ (labelled A) and $[10\bar{1}]$ (labelled B) directions have intensities within 25% of each other from 40-140 eV, which is a resaonable discrepancy within the adequacy of

the kinematic approximation and the detectable intensity variations of the LEED fluorescent screen. This difference in Cs heights of 0.10 Å has been incorporated in our Cs/Si(111)$\sqrt{3}$x$\sqrt{3}$–R30° structural model, and suggests buckling of an underlying chain, since the LEED pattern for an unbuckled chain ($\Delta z = 0$) does not match the observed pattern. The lowering of the Cs 3d XSW (111) coherent fraction due to this height difference is less than 1%, confirming our assertion that the low (111) coherent fraction is almost entirely due to thermal effects.

Conclusion

We have investigated the coverage, bonding, and atomic structure of the Cs/Si(111)$\sqrt{3}$x$\sqrt{3}$–R30° interface, formed by room temperature dosing of 1/3 ML Cs on a cleaved Si(111)2x1 surface. At a Cs coverage of 1/3 ML, the work function is near its minimum but the Cs 4d photopeak area has not saturated, indicating the $\sqrt{3}$x$\sqrt{3}$–R30° pattern does not occur at saturation coverage but slightly before. The neighboring LEED patterns at higher and lower coverages exhibit a twofold symmetry indicate retention of the π-bonded chains of the clean cleaved Si(111) surface under an ordered Cs overlayer. In addition, the lack of change in the Si 2p and Cs 4d spectral lineshapes with increasing Cs coverage as well as the retention of the π-bonding surface state at the top of the valence band further support the underlying Si structure of Cs/Si(111)$\sqrt{3}$x$\sqrt{3}$–R30° being the same as the clean Si(111)2x1 reconstruction. The retention of the chains also indicates a weak Cs-Si interaction.

X-ray standing wave data monitoring the Cs adsorption yield contradict models of a bulk-terminated Si(111) surface under the Cs $\sqrt{3}$x$\sqrt{3}$–R30° overlayer, as the triangulation of the coherent distance of the (111) and (11$\bar{1}$) reflections points to the atop (T_1) high-symmetry adsorption site of the bulk-terminated surface, but the (111) coherent distance alone indicates that the corresponding Cs height and bond length to Si are too short. The lower coherent fraction along the (11$\bar{1}$) direction than along (111) also indicates multiple Cs sites, also contradicting high-symmetry adsorption.

Our proposed model for the Cs/Si(111)$\sqrt{3}$x$\sqrt{3}$–R30° interface has Cs adsorption in two nearly equivalent sites on either sites of the retained π-bonded chain Si(111) surface reconstruction. The selection of two site position increases the Cs-Cs distance and reduces the dipole-dipole repulsion energy. Within the kinematic approximation appropriate for high-Z overlayers, the LEED pattern created by the Cs atoms in this model is $\sqrt{3}$x$\sqrt{3}$–R30° within the observed energy range. Unlike what one might expect from monovalent Cs, the adatoms are highly coordinated to Si atoms,

yet they are weakly interacting with the Si surface, as the reconstruction is not destroyed. This is quite different from the case of Na/Si(111)1x1, where the Na atoms bulk-terminate the Si(111) surface upon adsorption; however, in that case the Na also are threefold-coordinated. As thermal effects at room temperature are not enough to change the Si(111) surface structure, the strength of the alkali-Si interaction and the corresponding interface geometry mainly depend on the alkali atomic size. Cs and Na are on opposite ends of the scale of alkali atomic radii, with Cs being very large. At 1/3 ML the Cs atomic radii in neighboring sites are close to overlapping but do not do so, and adding further Cs causes the overlayer to metallize and further weaken the Cs-Si interaction. Thus, the Cs/Si(111)$\sqrt{3}$x$\sqrt{3}$–R30° interface is near a semiconductor-to-metal transition of the surface, and the lack of change in Si 2p, Cs 4d, and the surface state valence photoemission through the transition (beyond the formation of plasmon loss peaks) as well as LEED results suggest that the electronic transition is not accompanied by a corresponding structural transition in the interface. It will be interesting to see how an intermediate size alkali such as K will interact with the clean Si(111)2x1 surface and affect the interface geometry under the energetic constraint of room temperature adsorption.

References

[1] B. Reihl, S. L. Sorensen, R. Dudde and K.O. Magnusson, Phys. Rev. B 46 (1992) 1838.

[2] B. Reihl and K. O. Magnusson, Phys. Rev. B 42 (1990) 11839.

[3] K. O. Magnusson and B. Reihl, Phys. Rev. B 39 (1989) 10456.

[4] H. Tochihara, M. Kubota, M. Miyao, and Y. Murata, Surf. Sci. 158 (1985) 497.

[5] H. Tochihara, M. Kubota, and Y. Murata, Solid State Comm., 57 (1986) 437.

[6] H. Ishida, K. Terakura, M. Tsukada, Solid State Comm., 59 (1986) 365.

[7] K. C. Pandey, Phys. Rev. Lett. 47 (1981) 1913.

[8] J. E. Northrup and M. L. Cohen, Phys. Rev. Lett. 49 (1982) 1349.

[9] E. J. Nelson, T. Kendelewicz, J. C. Woicik, P. Liu, and P. Pianetta, to be published.

[10] I. P. Batra and S. Ciraci, Phys. Rev. B, 37 (1988) 8432.

[11] J. C. Woicik, T. Kendelewicz, S. A. Yoshikawa, K. E. Miyano, G. S. Herman, P. L. Cowan, P. Pianetta and W. E. Spicer, Phys. Rev. B 53 (1996) 15425.

[12] E. Vlieg, E. Fontes, and J. R. Patel, Phys. Rev. B (1991) 7185.

[13] J. E. Northrup, Phys. Rev. Lett. 53 (1984) 683.

[14] R. E. Martinez, E. Fontes, J. A. Golovchenko, Phys. Rev. Lett. 69 (1992) 1061.

[15] J. C. Woicik, T. Kendelewicz, A. Herrera-Gómez, K. E. Miyano, P. L. Cowan, C. E. Bouldin, P. Pianetta, and W. E. Spicer, 71 (1993) 1204.

[16] J. C. Woicik, T. Kendelewicz, K. E. Miyano, P. L. Cowan, C. E. Bouldin, B. A. Karlin, P. Pianetta, and W. E. Spicer, Phys. Rev. B 44 (1991) 3475.

[17] K. Akiyama, K. Takayanagi, and Y. Tanishiro, Surf. Sci. 205 (1988) 177.

[18] D. P. Woodruff, Prog. Surf. Sci. 57 (1998) 1.

[19] B. W. Batterman and H. Cole, Rev. Mod. Phys. 36 (1964) 681.

[20] J. C. Woicik, T. Kendelewicz, K. E. Miyano, P. L. Cowan, C. E. Bouldin, B. A. Karlin, P. Pianetta and W. E. Spicer, Phys. Rev. Lett. 68 (1992) 341.

[21] T. Kendelewicz, J. E. Klepeis, J. C. Woicik, S. H. Southworth, C. Mailhiot, M. van Schilfgaarde, M. Methfessel, A. Herrera-Gómez, and K. E. Miyano, Phys. Rev. B 51 (1995) 10774.

[22] T. Kendelewicz, P. Liu, G. E. Brown, Jr. and E. J. Nelson, Surf. Sci. 395 (1998) 229.

[23] J. C. Woicik, T. Kendelewicz, S. A. Yoshikawa, K. E. Miyano, G. S. Herman, P. L. Cowan, P. Pianetta and W. E. Spicer, Phys. Rev. B 53 (1996) 15425.

[24] J. C. Woicik, T. Kendelewicz, A. Herrera-Gómez, K. E. Miyano, P. L. Cowan, C. E. Bouldin, P. Pianetta, and W. E. Spicer, Phys. Rev. Lett. 71 (1993) 1204.

[25] J. C. Woicik, T. Kendelewicz, A. Herrera-Gómez, A. B. Andrews, B. S. Kim, P. L. Cowan, K. E. Miyano, C. E. Bouldin, B. A. Karlin, G. S. Herman, J. L. Erskine, P. Pianetta, and W. E. Spicer, J. Vac. Sci. Tech. A 11 (1993) 2359.

[26] J. C. Woicik, T. Kendelewicz, K. E. Miyano, P. L. Cowan, C. E. Bouldin, B. A. Karlin, P. Pianetta, and W. E. Spicer, Phys. Rev. B 44 (1991) 3475.

[27] G.-X. Qian and D. J. Chadi, Phys. Rev. B 35 (1987) 1288.

[28] J. E. Northrup, J. Vac. Sci. Tech. A 4 (1986) 1404.

[29] I. Moullet, W. Andreoni and M. Parrinello, Surface Science 269-270 (1992) 1000.

[30] F. Huaxiang and Y. Ling, Surf. Sci. Lett. 250 (1991) L373.

[31] H. L. Meyerheim, W. Moritz, H. Schulz, P. J. Eng, and I. K. Robinson, Surf. Sci. 331-333 (1995) 1422.

[32] D. R. Batchelor and D. A. King, Chem. Phys. Lett. 186 (1991) 19.

[33] P. N. First, R. A. Dragoset, J. A. Stroscio, R. J. Celotta, and R. M. Feenstra, J. Vac. Sci. Tech. A 7 (1989) 2868.

[34] F. J. Himpsel, P. M. Marcus, R. Tromp, I. P. Batra, M. R. Cook, F. Jona, and H. Liu, Phys. Rev. B 30 (1984) 2257.

[35] G. Ertl and J. Küppers, Low Energy Electrons and Surface Chemistry, Weinheim: Verlag Chemie, 1974, pp. 129-192.

Table 6.1. X-ray Standing Wave Results for the Cs/Si(111)$\sqrt{3}$x$\sqrt{3}$–R30° Interface

	Number of samples	Coherent Distance D_c	Coherent Fraction f_c
Cs 3d XSW			
(111) reflection	2	0.952 ± 0.042	0.641 ± 0.165
(11$\bar{1}$) reflection	2	0.231 ± 0.048	0.371 ± 0.108
Si 1s XSW			
(111) reflection	1	1.011 ± 0.016	0.590 ± 0.063

Figure 6.1. Work function difference (relative to the clean Si(111)2x1 surface) as a function of Cs coverage, which is represented as the percentage of Cs 4d peak area saturation. The observed LEED patterns are also indicated.

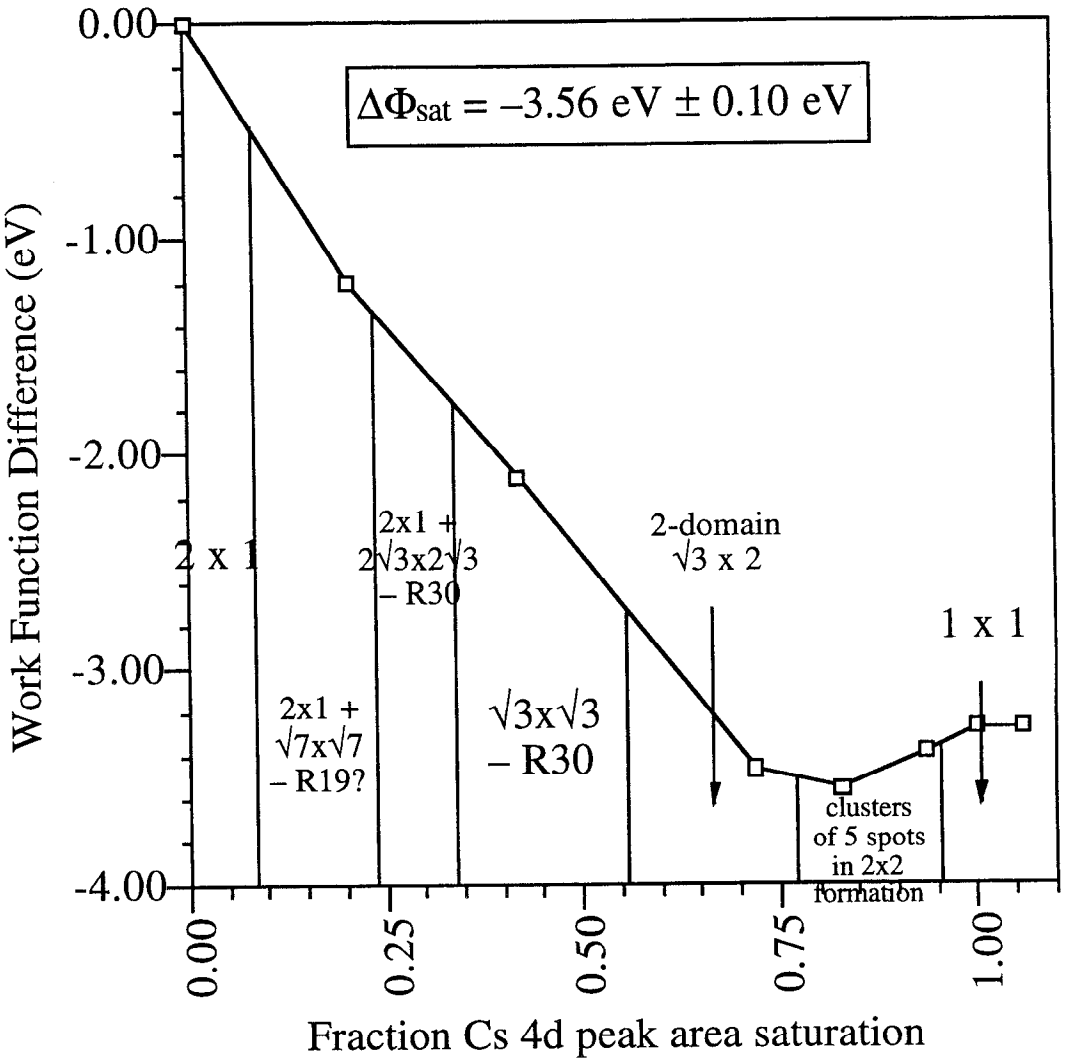

Figure 6.2. Cs 4d core-level photoemission spectra for the Cs/Si(111) interface as Cs coverage is increased by room temperature dosing. Photon energy is 120 eV. Note the metallic loss tail at higher Cs coverages.

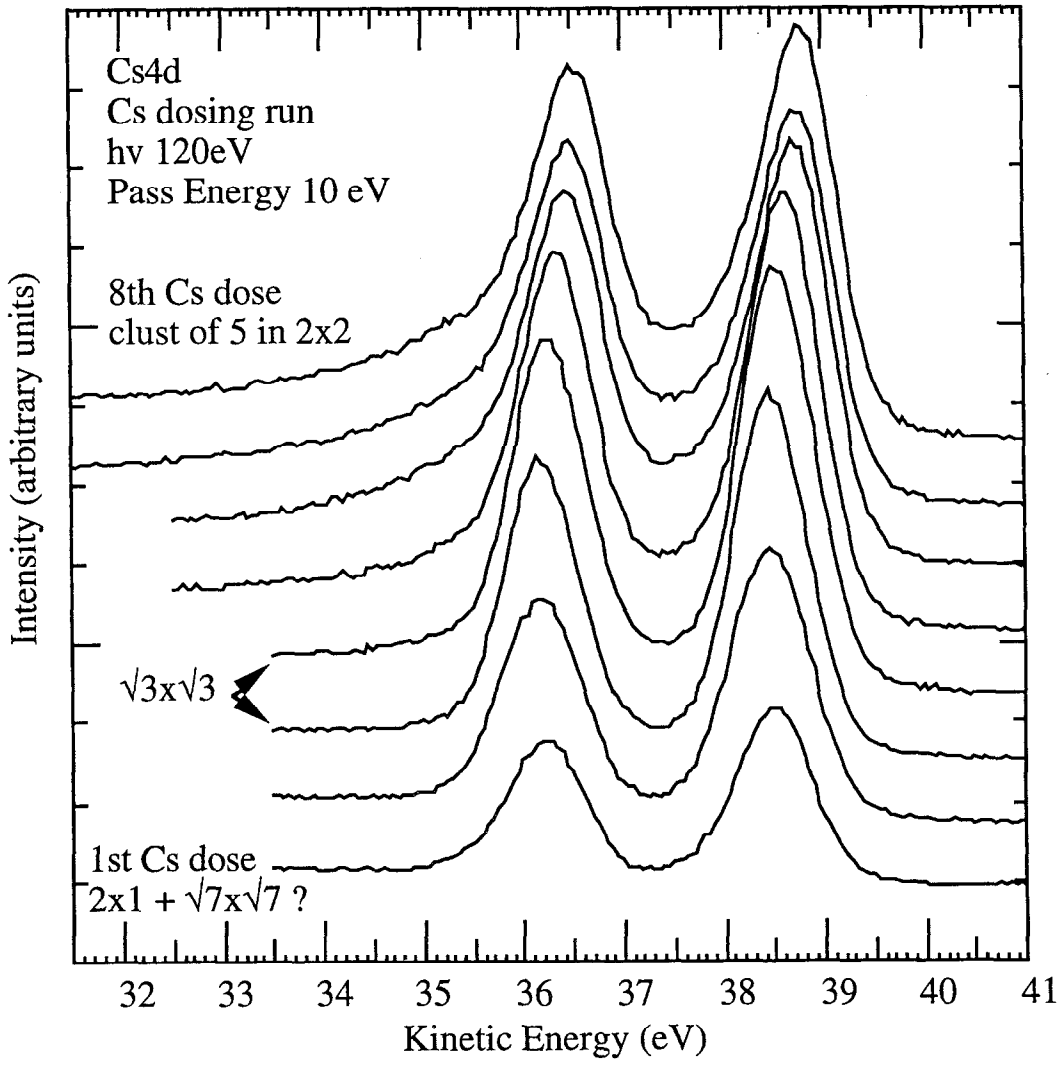

Figure 6.3. Photoemission spectra of the valence band region for the Cs/Si(111) interface as Cs coverage is increased by room temperature dosing. Photon energy 65 eV.

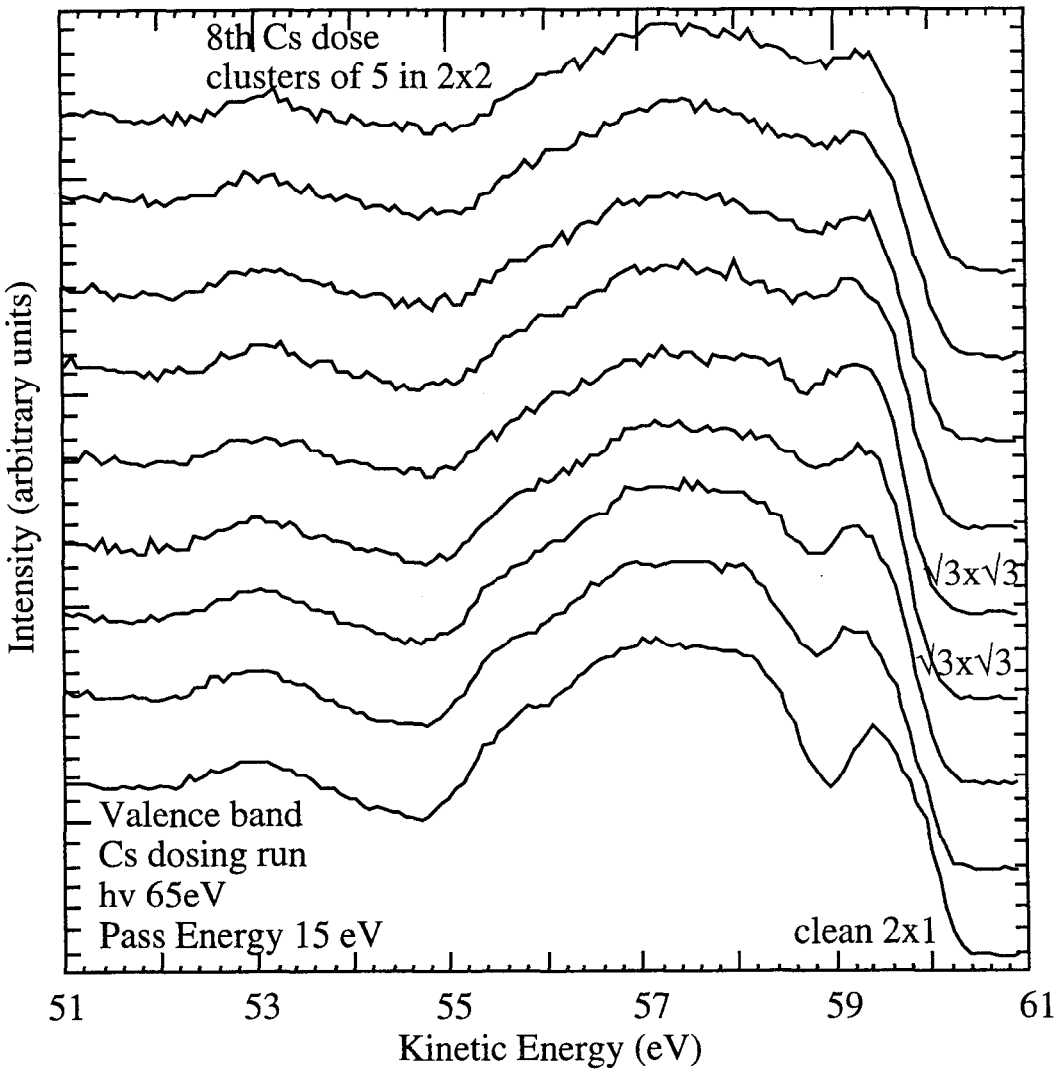

Figure 6.4. Photographs of the LEED patterns observed on the Cs/Si(111) interface in the Cs coverage range surrounding the $\sqrt{3}x\sqrt{3}$–R30° phase. The three LEED patterns are (a) 2x1 + $\sqrt{3}x\sqrt{3}$–R30° (b) $\sqrt{3}x\sqrt{3}$–R30° (c) 2-domain $\sqrt{3}x2$.

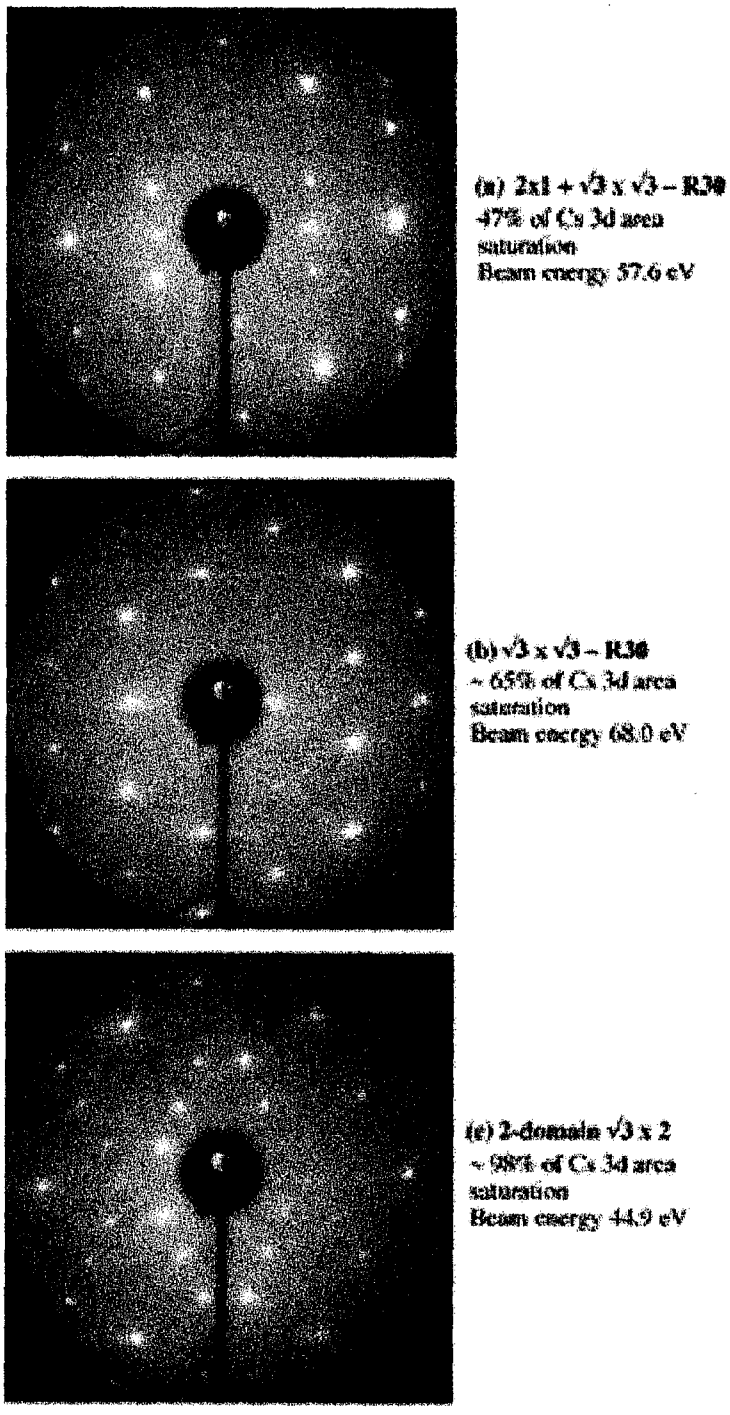

Figure 6.5. Cs 3d XSW data for the Cs/Si(111)$\sqrt{3}$x$\sqrt{3}$–R30° interface, for the (111) (normal to the surface) and (11$\bar{1}$) (mostly lateral to surface) reflections of Si.

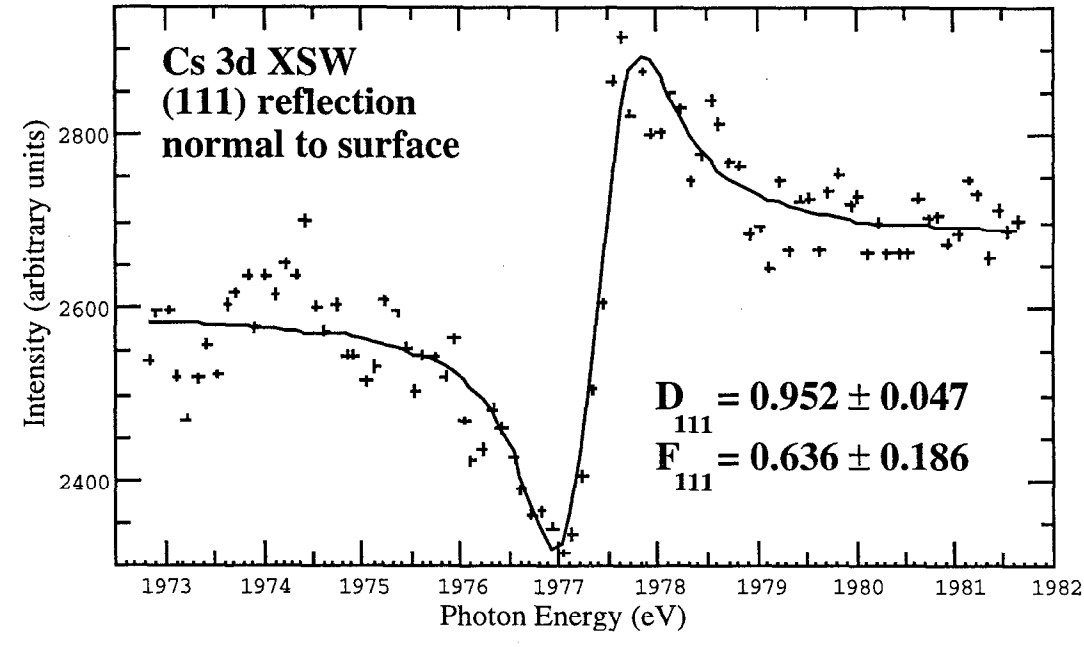

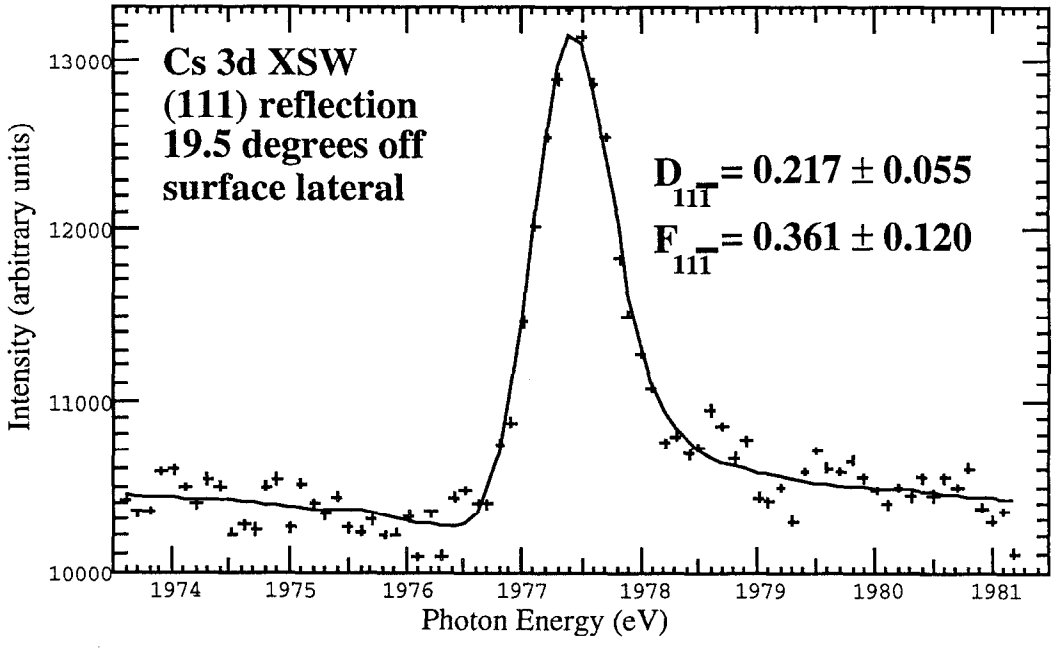

Figure 6.6(a). (a) Top (111) plane view of the proposed two-site model of the Cs/Si(111)$\sqrt{3}$x$\sqrt{3}$–R30° interface. The surface unit cell is 2$\sqrt{3}$x$\sqrt{3}$–R30° and the two atoms that make up the cell are indicated.

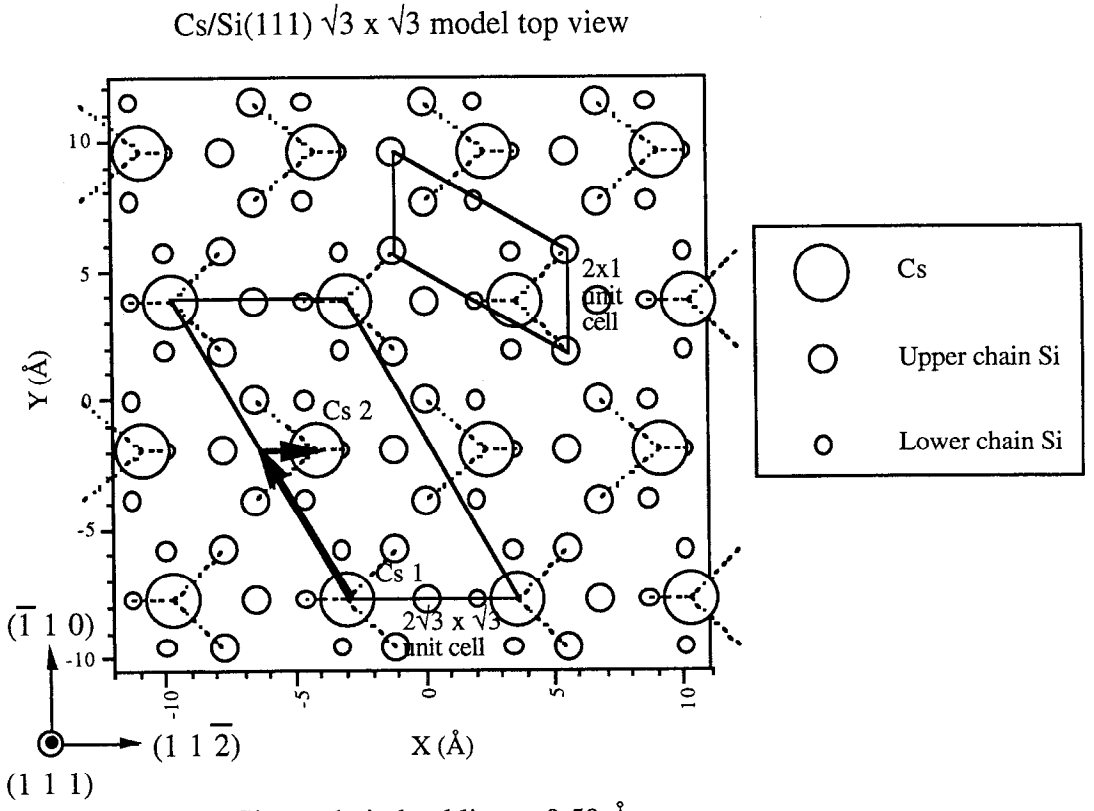

Si top chain buckling = 0.50 Å
lateral shift of Si layers = +0.45 Å
Cs1-Cs2 delta z = 0.10 Å
111 Debye-Waller = 0.64
111bar Debye-Waller = 0.74
Cs-Si bond length = 3.78 Å
Cs-Si bond length to next chain = 4.11 Å

Figure 6.6(b). (b) Side $(1\bar{1}0)$ plane view of the proposed two-site model of the Cs/Si(111)$\sqrt{3}$x$\sqrt{3}$–R30° interface. The surface unit cell is 2$\sqrt{3}$x$\sqrt{3}$–R30° and the two atoms that make up the cell are indicated.

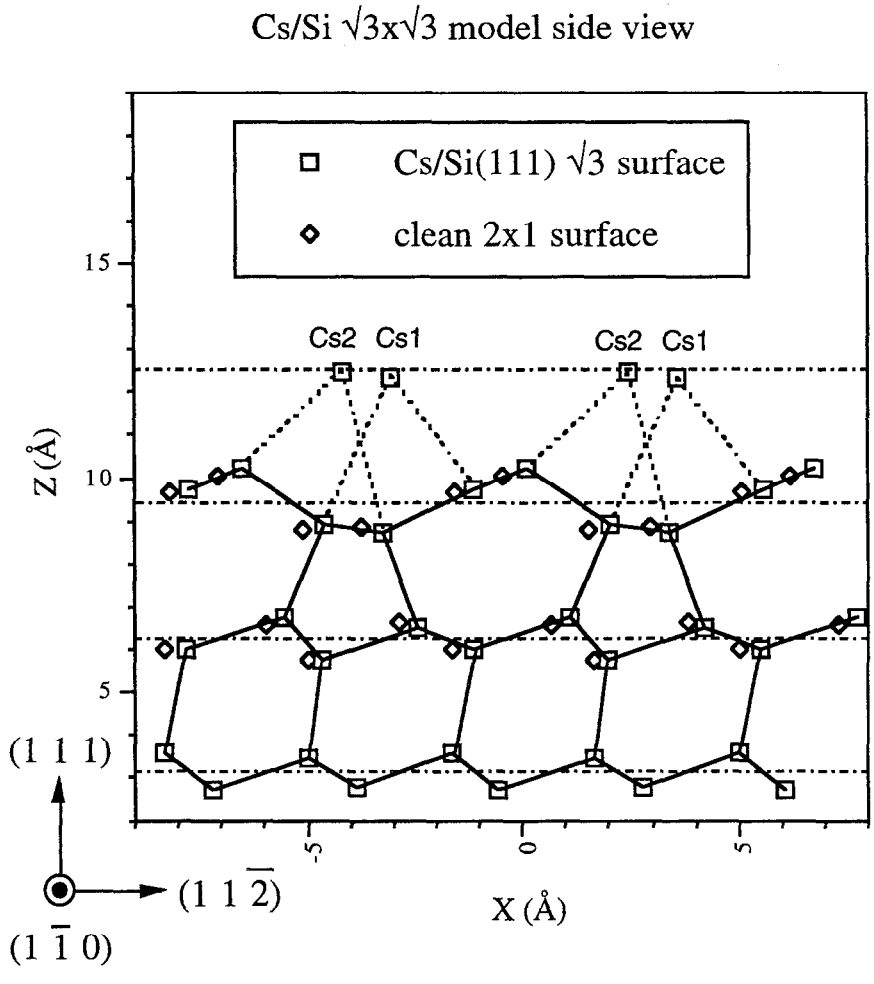

Si top chain buckling = 0.50 Å
lateral shift of Si layers = +0.45 Å
Cs1-Cs2 delta z = 0.10 Å
111 Debye-Waller = 0.64
111bar Debye-Waller = 0.74
Cs-Si bond length = 3.78 Å

Figure 6.7. Plot of kinematic LEED spot intensities versus beam energy for the proposed model of the Cs/Si(111)$\sqrt{3}$x$\sqrt{3}$–R30° interface. The $\sqrt{3}$x$\sqrt{3}$–R30° spots A and B are observed in equal intensity over the energy range 40-150 eV while the $2\sqrt{3}$x$\sqrt{3}$–R30° spot is not observed below 100 eV.

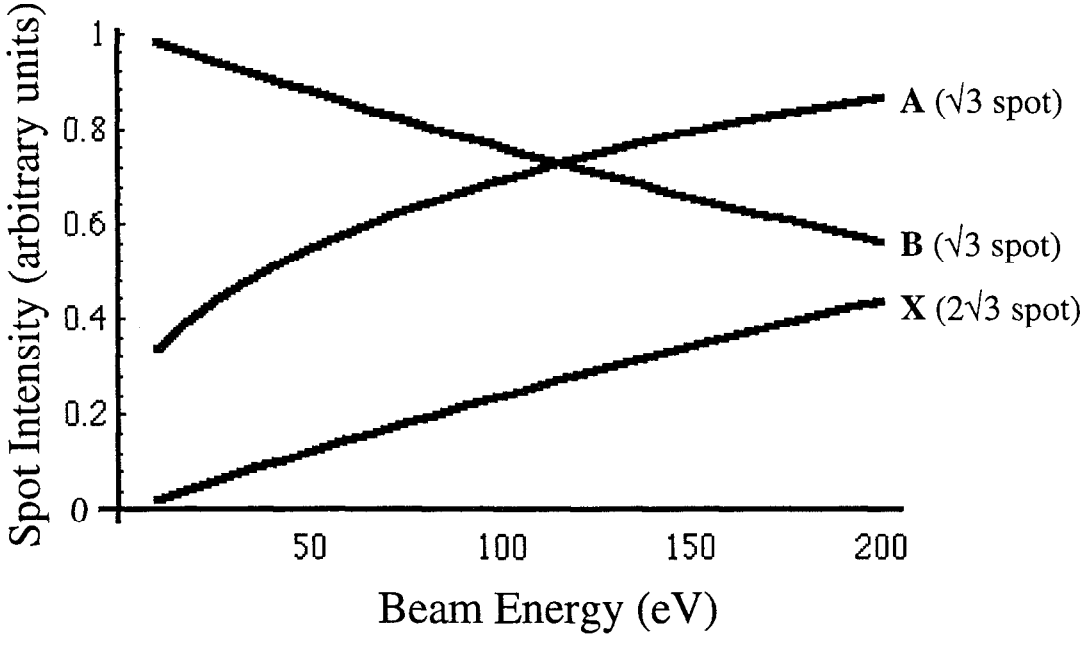

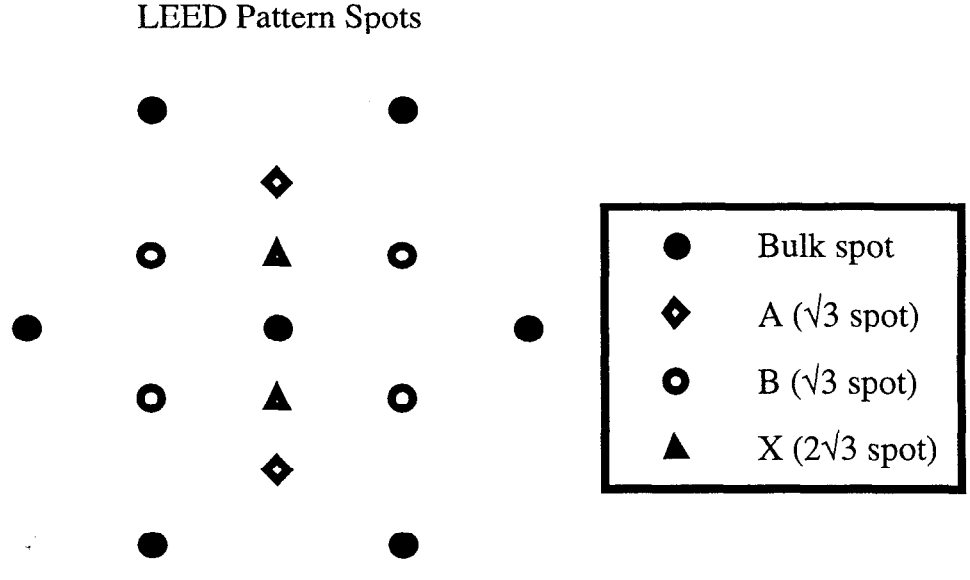

CHAPTER SEVEN

X-RAY STANDING WAVE ANALYSIS OF THE CLEAVED NA/SI(111)3X1 AND K/SI(111)3X1 INTERFACES: TEST AND COMPARISON OF THREE PROPOSED STRUCTURAL MODELS

Abstract

The X-ray standing wave technique provides a direct determination of adatom position as well as providing information about the structure of the underlying Si surface reconstruction. We apply X-ray standing waves to the annealed 1/3 monolayer Na/Si(111)3x1 and K/Si(111)3x1 surfaces. Using these results and reasonable bond lengths, we evaluate the various proposed structural models of the 3x1 reconstruction. Na standing wave data are found to match both the missing top layer Seiwatz-chain model and the recent "honeycomb-chain channel" model of channels alternating with fivefold and sixfold Si rings. However, the results for K were found only to fit the Seiwatz-chain model well. In addition, we investigate a recently discovered room temperature K/Si(111)3x1 surface reconstruction at 2/3 monolayer coverage for

cleavable Si(111). For this surface, K adsorbs onto a modified Pandey-chain structure with 3x1 periodicity.

Introduction

The structure of the alkali metal / Si(111) 3x1 surface has been under contention for many years. The 3x1 reconstruction is reported to form upon Si(111) after metal adsorption and annealing for all of the alkali metals (Li, Na, K, Rb, Cs), as well as for Ag and Mg[1-3]. Very similar 3x1 low-energy electron diffraction (LEED) I-V curves have been observed for Li, Na, Ag, and Mg, suggesting the 3x1 pattern is produced by a common substrate reconstruction and not solely by the metal overlayer. This conclusion is supported further by similar scanning tunneling microscopy (STM) and surface core-level shift (SCLS) results for these four metals[4-8]. K appears to have the same substrate structure as the other alkali metals; however, no direct comparison of experimental results between K and Na or Li has been made. Angle-resolved photoemission studies (ARUPS) have been made on Li/Si(111)3x1 and K/Si(111)3x1[8-9].

Unfortunately, the inability of LEED and STM to differentiate between adsorbate and substrate atom contributions to the signal inhibits its use as a tool to determine exact atomic structure. It is also true that STM measures the position of electronic states and not atoms per se, so it may be incorrect to assign atomic positions to STM spot positions. In addition, SCLS and ARUPS study the atomic structure indirectly, through the electronic structure resulting from a given structural model. Previous studies of the *M*/Si(111)3x1 surfaces (*M* = Ag, Mg, alkali metals) have relied on these four techniques as well as density-functional theory (DFT) total-energy calculations of structural models. These studies have narrowed the possible *M*/Si(111)3x1 surface structure to three structural models of differing levels of agreement with data, as discussed below. However, none of the models has been clearly ruled out through these techniques. It is clear that a more direct structural probe of this interface is required to resolve the 3x1 surface structure.

The X-ray standing wave (XSW) technique [10-22] is a natural choice of technique to directly study the atomic structure of these surfaces. By monitoring adatom or Si core-level absorption yield in the energy range of strong Bragg reflection, one can determine atomic positions with elemental specificity and high precision. Significant changes in the lineshape of the yield can be seen for changes in atomic position of 5% of the diffraction plane spacing, about 0.15 Å. As X-ray standing

waves measures the distance of the absorbing atom from the diffracting planes, measurements along the (111) and $(11\bar{1})$ planes can be used to determine adatom height above the surface and lateral position, respectively. By triangulating the adatom position and putting this position into a structural model, we can determine if the structural model is reasonable from the bond lengths of the adatom to the Si surface atoms. In addition, by taking surface-sensitive (photoelectron energy ~135 eV) X-ray standing wave data using the Si 1s photoemission yield for the (111) reflection normal to the surface, we can determine an "average" height and vertical spread of the top layer Si atoms. While the number of different Si surface atom positions prohibits individual atom position determination using a single reflection, the Si 1s X-ray standing wave data can distinguish between a missing-top-layer structure, and a structure which is closer to the bilayer structure of the π-bonded Pandey-chain Si(111)2x1 surface and of the bulk-terminated surface.

The three models of the *M*/Si(111)3x1 are depicted in Figure 7.1. The models differ in the number of top layer Si atoms and in the ordering of the Si rings in the side $(1\bar{1}0)$ projection. The first model (Figure 7.1(a)) is known as the Seiwatz-chain or missing top layer (MTL) model and consists of an Si top chains with channels between neighboring chains. The chain is often modeled as buckled, and dangling bonds extend out from the two chain atoms as well as vertically from the channel Si atom [23-25]. The side view shows a fivefold Si ring with one third the bulk periodicity, and we label this model "500500" for that reason, with "0" indicating a missing ring. Following this convention, the second model (Figure 7.1(b)) is labeled "560560". This model has been called the "missing Pandey-chain" model [25-26] and the "honeycomb chain-channel" model [27] and is the most recently introduced in the literature. This "560560" alkali/Si(111)3x1 model is extended from a Ag/Si(111)3x1 model suggested by Collazo-Davila, Grozea, and Marks[28], and consists of a channel as well as honeycomb-like top Si layer in which one of the two atoms near the center of the honeycomb adopts an sp^2 geometry and donates electronic charge to the neighboring honeycomb atom next to the channel. As a result, there is a single dangling bond off atom on the other side of the hexagon and over the channel. Adsorption sites bridge neighboring honeycomb chains in threefold coordination, a geometry similar to that of Ag in the Ag/Si(111)$\sqrt{3}$x$\sqrt{3}$–R30° honeycomb-chained trimer (HCT) surface[21-22]. Both "500500" and "560560" models for the 3x1 surface have structural units similar to the HCT model for $\sqrt{3}$x$\sqrt{3}$–R30° surface, which is reasonable since both Ag/Si(111)3x1 and Ag/Si(111)$\sqrt{3}$x$\sqrt{3}$–R30° are experimentally observed

structures[29]. In addition, both "500500" and "560560" models are missing top layer (MTL) models, with a single surface layer of Si atoms.

This is in contrast to the model of Figure 7.1(c), which we label the "567567" model and is also known as the extended Pandey chain model[24-25,30]. This model is based upon the Pandey-chain model [31] of the clean Si(111)2x1 surface reconstruction, which spontaneously forms upon cleaving a Si crystal along the (111) plane. In our notation, this 2x1 model would be "575757" and consists of a bilayer of upper and lower Si chains; in addition, the upper chain typically is buckled. The "567567" model inserts a sixfold ring between each fivefold-sevenfold ring pair to produce the 3x1 periodicity. Dangling bonds come from the upper chain atoms as well as the atom atop the sixfold ring. The "567567" model has a surface Si bilayer and the same number of Si surface atoms as the cleaved 2x1 surface reconstruction. This difference between the "567567" and the two "missing top layer" models will be relevant in our analysis of the Si 1s XSW data and the model for the room-temperature dosed K/Si(111)3x1 surface.

All three of these models are in reasonable agreement with the current set of published data for the M/Si(111)3x1 surface. The surface's semiconducting properties and surface passivation are accounted for by each of the models. Si 2p surface core level shifts are similar for all three models. However, the measured ARUPS surface band structure for Li/Si(111)3x1 and K/Si(111)3x1 are not matched well by the "567567" model in parts of the surface Brillouin zone, while the "500500" agreement is better[8-9]. On the other hand, the buckling of the chain in the "500500", as well as the lateral position of the two chain atoms, does not agree well with the spacing of spots in the double rows observed in STM images. These double rows are attributed to Si-adsorbate bonding states and not adsorbate atoms; earlier studies assumed the spots were due to adsorbate atoms, which made the adsorbate coverage 2/3 ML[5] instead of the experimentally confirmed 1/3 ML[6]. The "567567" and "560560" models have better agreement with the STM images. Currently the "560560" model looks the most promising, at least for Na/Si(111)3x1, as it agrees with surface X-ray diffraction (SXRD) results for the Li/Si(111)3x1 and Na/Si(111)3x1 surfaces[26]. SXRD is a more direct structural probe which can determine Si atom positions with multiple reflections; however, it still lacks elemental specificity. The "560560" model also is in reasonable agreement with STM and ARUPS[27] for Li/Si(111)3x1.

Experimental

All experiments were performed inside a UHV chamber, with ~$3x10^{-11}$ torr base pressure. The pressure during dosing did not rise above $7x10^{-11}$ torr, and during annealing the pressure remained below $9x10^{-11}$ torr. Good vacuum was required during the experiment as room-temperature dosed alkali/semiconductor interfaces are very susceptible to contamination. The cleaver, getter, cylindrical mirror analyzer (CMA), and LEED optics all are in the same analysis chamber. All Si(111) surface samples were cleaved *in situ* from $5x5x12mm^3$ crystalline Si bars of using the anvil-and-hammer technique. Standing wave measurements were made both on *p*-type Si of resistivity 26 Ω-cm, and *n*-type Si of resistivity 1-10 Ω-cm, with no difference in the results. Using cleaved surfaces removed the necessity to prepare the clean sample by flashing at high temperature, as required for 7x7, since the clean 2x1 reconstruction is readily formed by room temperature cleaving. The samples were cut and oriented in the chamber so that the top face is normal to the $(\bar{1}10)$ direction and the side faces are normal to the $(11\bar{2})$ direction.

3x1 surfaces were prepared both by annealing a saturation-coverage dosed surface and by room-temperature dosing to less than saturation coverage. Samples were pre-annealed before cleaving to avoid significant outgassing during the post-dosing anneal. Before dosing, the quality of the cleaved surface was checked using LEED, and only surfaces with good 2x1 LEED patterns were studied. Sodium or potassium was evaporated upon the samples by resistively heating a well-outgassed SAES chromate getter. The distance from the Cs getter to the Si(111) was optimized at ~3.8 cm to avoid heating of the sample surface from the evaporator while limiting the required dosing time and pressure. The samples were dosed to saturation coverage at room temperature, with a typical dosing time of 8 minutes broken into two 4-minute sessions to keep the pressure low. Saturation coverage surfaces exhibit a 1x1 LEED pattern; however, this was not checked for most samples as the saturation coverage surface is very susceptible to oxygen contamination. The saturation-dosed sample then was resistively heated right after dosing, and the temperature was monitored using a typical chromel-alumel thermocouple. The temperature was kept above 580°C for 5-10 min, and the peak temperature ranged from 600°C to 660°C. Upon cooling, the LEED pattern becomes 3-domain 3x1 for both the Na/Si(111) and K/Si(111) surfaces, as photographed in Figure 7.2. Some Na/Si(111)3x1 samples exhibited a stronger LEED contribution from the domain along the original clean 2x1 domain direction, as seen in Figure 7.2(b). Then all of the data were collected with the sample at room temperature. The 3x1 pattern also can be formed by dosing the sample while it is hot; however, the dosing time is increased as well as the pressure, which increased the risk of

contamination. Once formed, the 3x1 surface is resistant to oxygen contamination, as checked by O 1s photoemission before and after each XSW run. This passivation effect has been reported in earlier works[32], and is remarkable considering that alkali metals often act as catalysts for oxidation of Si surfaces for other surface reconstructions and adsorbate coverages.

The room-temperature (RT) dosed K/Si(111)3x1 surface was formed by dosing potassium on the cleaved Si(111)2x1 surface for 2.5 to 3.0 min. The resulting LEED pattern is single-domain 3x1, as seen in Figure 7.3(a), with the 3x1 domain direction the same as that of the clean 2x1 surface. Figure 7.3(b) shows a 2-domain 3x1 structure, which formed after dosing a clean 2-domain 2x1 surface. As reported elsewhere[33], the directionality and twofold symmetry of the single-domain 3x1 LEED pattern and those at higher and lower potassium coverages suggests the underlying Si structure retains the π-bonded chains of the clean Si(111)2x1 surface. The lower coverage surface has spots which split and migrate from the 2x1 positions to the 3x1 positions with increasing coverage suggesting mixed regions of 2x1 and 3x1 chains within the coherence length of the LEED electron beam. The higher coverage pattern in 2-domain $\sqrt{3}$x2 and maintains the twofold symmetry of the 3x1 and clean 2x1 surfaces. The RT-dosed pattern only occurs for potassium dosing; no RT dosed Na/Si(111)3x1 pattern was observed over the entire Na coverage range from zero to one monolayer (see Chapter 4).

As a check on the alkali metal coverage of the surface, photoemission data were taken near 2000 eV photon energy just before starting XSW data acquisition. Figures 7.4(a) and 7.4(c) show the Na 2p and K 3p photopeaks, respectively, for the saturation coverage 1x1 surface and the various 3x1 surfaces. By comparing the area of the photopeaks and assuming a saturation coverage near one monolayer, the area of the alkali core-level peak for the annealed Na/Si(111)3x1 and K/Si(111)3x1 is 1/3 ML or less. However, the coverage of the RT-dosed K/Si(111)3x1 photopeak is considerably larger than that of the annealed K/Si(111)3x1 surface. The room-temperature dosed K/Si(111)3x1 surface is at a coverage closer to 2/3 ML, and in a separate study we did at photon energy 65 eV over three room-temperature potassium-dosed samples, we found the RT-dosed K/Si(111)3x1 surface appeared over a coverage range of 0.40-0.68 ML. In our model diagrams below we assume a coverage of 1/3 ML and 2/3 ML, for the annealed and RT-dosed alkali/Si(111)3x1 surfaces, respectively. Our comparison of the models to the XSW data considers the alkali coverage more exactly. In addition, the width of the Na 2p peak in Figure 7.4(b) is larger for the 3x1 surface than for the 1x1 surface. This suggests multiple components in the Na 2p peak for the

3x1 surface with similar energies and supports a multi-site model for the Na/Si(111)3x1 surface. The K 3p data all exhibit similar widths for the different coverages. As multiple sites must be occupied on a reconstructed surface at higher coverages, this similarity in peak widths suggests the annealed K/Si(111)3x1 surface also has adatoms in multiple positions with respect to the Si substrate.

X-ray Standing Wave (XSW) data were collected in the backreflection mode[10-17, 21] using the same chamber and instrumentation as for the LEED and photoemission spectroscopy (PES) measurements. The sample is aligned so that incident photons are normal to the (111) or (11$\bar{1}$) Bragg planes of Si and monochromatized using a pair of InSb(111) crystals on the soft X-ray beam line 3-3 (JUMBO) at SSRL. The sum of the incident and Bragg-reflected X-ray flux is monitored by amplifying the emission current of an Ni grid collected with a channeltron. Before collecting XSW data, a photoemission scan is taken to locate the photoemission or Auger peak of interest, either the Na 1s or Si 1s photopeaks at binding energies –1070.8 eV or –1839.3 eV, respectively, or the K LMM Auger peak at 245 eV kinetic energy. Then the XSW absorption yield of Na, K, or Si atoms as a function of photon energy is monitored via the total counts at the peak with a double-pass cylindrical mirror analyzer (CMA). For photoemission peaks kinetic energy is tracked as the photon energy changes, while for Auger peaks the kinetic energy is kept constant with changing photon energy. Background standing wave scans are recorded slightly above the peak (higher kinetic energy) and the background XSW data are collected in a separate run immediately after the on-peak XSW data. This background XSW yield reflects inelastically scattered bulk electrons and also varies with photon energy, and is subtracted from the on-peak XSW yield to give the specific signal of interest. With the photon energy equal to the (111) backreflection energy of 1977 eV for Si, the Si 1s photoelectrons are highly surface sensitive, with a kinetic energy near the minimum of the universal curve. Total electron yield data are recorded concurrently by monitoring the amplified drain current from the sample.

Both (111) and (11$\bar{1}$) diffraction planes were used for backreflection XSW, and in most cases the XSW data set for one reflection were taken on the same surface immediately after taking the full data set for the other reflection. Oxygen contamination was checked periodically via O 1s photoemission, as reasonable valence band spectra were not available at this high photon energy. We tried to take the XSW data in as short an amount of time as possible to get reasonable fit results, in order to avoid contamination of the surface, which is still susceptible to contamination over the time frame of an 8-hour XSW run. This and the small peak height produced by 1/3 ML or

2/3 ML of alkali atoms accounts for the roughness of the XSW data presented. Several samples did not become contaminated even after 24 hours of data collection, confirming the passivation of the annealed alkali/Si(111)3x1 surface. The (111) reflection is taken with the surface normal to the incident beam, while the $(11\bar{1})$ reflection has the sample turned towards the analyzer so the incident photons are at an angle of 70.53° with respect to the surface normal. In the horizontal plane, the CMA axis is 90° from the incident photon and parallel to the bulk reflecting planes.

XSW explanation

The backreflection version of the X-Ray Standing Wave (XSW) technique[10-17, 21] utilizes synchrotron radiation by keeping the sample angle fixed and varying the photon energy in a region about the Bragg energy of a Si crystal diffraction plane oriented normal to the incident X-rays. Near the Bragg condition, the incident beam is reflected by the bulk Si crystal lattice, and the superposition of incident and reflected X-rays forms a standing wave which both penetrates the crystal and extends out past the crystal surface. The phase of the standing wave, and therefore the position of its intensity extrema with respect to the crystal diffraction plane, changes with photon energy for the fixed-angle technique. By monitoring the X-ray absorption of adsorbate or substrate atoms as a function of incident photon energy in the Bragg region, an absorption profile is measured which is characteristic of the atomic position, relative to the bulk diffracting plane positions of the substrate crystal. The coherent distance D_c and the coherent fraction f_c of the absorbing atoms are determined by fitting the absorption profile to the equation

$$Y(E)/Y_0 = 1 + R(E) + 2 f_c \sqrt{R(E)} \cos(\nu(E) - 2\pi D_c) \qquad (1)$$

where Y_0 is the background absorption yield away from the Bragg reflection, and R(E) and $\nu(E)$ are the magnitude and phase of the reflectivity and are functions of photon energy E. In the case of single-site adsorption, the coherent distance D_c corresponds to the distance of the absorbing atom from the diffracting plane divided by the diffraction plane spacing (3.135 Å for the (111) planes of Si). The coherent fraction f_c is equal to the fraction of adsorbing atoms situated in the site; the remaining fraction $(1 - f_c)$ of atoms are disordered and their contribution to the interference term (last term of the above equation) averages to zero. Thermal disorder in the absorbing atoms also reduces the coherent fraction by a Debye-Waller factor $e^{-2\pi^2\sigma_H^2}$, where σ_H^2

is the mean squared atomic vibration amplitude in the direction of the reflection H. In the case of multiple sites of the absorbing atoms, each site *i* contributes an interference term, with the weight of each term determined by the relative populations $f_{c,i}$ and the phase of each term given by the distance $D_{c,i}$ of the site from the diffracting plane; the fraction $1 - \Sigma f_{c,i}$ corresponds to the fraction of atoms in disordered positions. For the specific case of equal populations of atoms in two different absorbing atom positions, the coherent distance D_c is equal to the average atom position, and the coherent fraction is related to the spread in the two atom positions $D_{c,1}$-$D_{c,2}$ by the equation

$$f_c = \cos(\pi(D_{c,1}-D_{c,2})) \qquad (2)$$

Thus, if the two atoms are separated by half a diffraction plane spacing, their contributions to the standing wave absorption yield are exactly out of phase and cause the coherent fraction to vanish, and the absorption yield matches the sum of incident and reflected intensities, 1+R(E).

The bulk Si profile can be measured via total yield or the electron yield of the off-peak background, which is dominated by inelastically scattered electrons. These electrons are produced within a substrate depth much less than the extinction depth of the photons. "Hot" electrons also do not contribute to the total and background yields at the low photon energy of the backreflection condition[20]. The total yield and background XSW data for all the data sets presented here agreed within error bars with the expected values for the bulk atomic structure ($D_c = 1$, $f_c = 0.69$), which is an internal check of the XSW data. A coherent fraction of $f_c = 0.707$ for the bulk signal arises from equal populations of Si atoms located 1/8 of a plane spacing above and below the (111)-like diffraction planes. This fraction is further reduced to $f_c = 0.69$ by the Debye-Waller factor for bulk Si at room temperature.

The (111) reflection measures the normal component of adatom surface positions (i.e. height above the substrate), while the coherent distance from the $(11\bar{1})$ reflection is predominantly the surface lateral component of adatom positions along the $(11\bar{2})$ direction. On the cleaved Si(111) surface, the $(11\bar{2})$ direction corresponds to the direction perpendicular to the π-bonded chains of our single-domain clean Si(111)2x1 surfaces. By considering the data from both reflections, the alkali metal adsorption site positions can be triangulated.

As there are three equivalent directions for Si chain formation and alkali adsorption on the Si(111) surface, the contribution of each of the three domains observed in the LEED pattern for annealed M/Si(111)3x1 surfaces must be considered in our XSW data analysis. In addition, the results of the triangulation as well as the

existence of multiple adsorption sites with similar energetics in the models necessitates consideration of multiple sites in our analysis. The details of each of these two effects upon the XSW data as well as their implications upon the possible models can be derived from the more general definition of the coherent distance and fraction as the phase and amplitude of the absorbing atom structure factor. The structure factor F_H for the reciprocal lattice vector **H** is defined by the equation

$$F_H \equiv f_{c,H} e^{2\pi i D_{c,H}} = e^{-2\pi^2 \sigma_H^2} \sum_j f_{j,H} e^{2\pi i D_{j,H}} \qquad (3)$$

$D_{j,H}$ is the distance of absorbing atom j from the diffracting plane divided by the diffracting plane spacing $1/|\mathbf{H}|$, $f_{j,H}$ is the fractional population of atoms j, and the sum is over all absorbing atoms, where the index j separates atoms with different relative positions $D_{j,H}$. The Debye-Waller factor $e^{-2\pi^2\sigma_H^2}$ is given explicitly and reflects the component of thermal motion of absorbing atoms normal to the diffracting plane; this term is real and contributes only to the coherent fraction $f_{c,H}$. This expression for F_H is similar to the crystal structure factor for X-ray diffraction. However, the usual atomic scattering factor seen for X-ray diffraction is not present, because the XSW technique uses energy discrimination to select a specific photoemission or Auger peak. This insures that all of the absorbing atoms are of the same element, so the atomic scattering factor is factored out of the sum. If the real part of the above equation (3) is taken, we find the relationship between the sum of the contributions of the individual sites' cosine-like interference terms and the overall coherent fraction and distance of the third term of equation (1).

From the above equation, the coherent distance can be interpreted as a phase-averaged distance of all the absorbing atoms from the diffracting plane, and the coherent fraction represents the extent of constructive or destructive interference among the signals for the different atom populations. In the case of the adatoms, the different distances $D_{j,H}$ of the absorbing atoms arise from multiple sites and from the mapping of the adatom position into three equivalent domains. The three-domain mapping will not affect the (111) coherent distance or fraction as the adatom height above the surface is the same for the three domains. However, the simulated $(11\bar{1})$ data can be quite different for single-domain versus three-domain adsorption models, with the same adatom position relative to the Si chains in each domain. The two extremes of this "three-domain effect" are given in Figure 7.5 for the bulk-terminated Si(111) surface. The mapping of the adsorption site into three domains is given by a two 120° rotations about a top layer Si surface atom. Figure 7.5(a) shows the constructive case, where the

adatom is located on a high-symmetry site. In this case the rotations map the site to a lateral position which has the same distance from the $(11\bar{1})$ plane as the first domain. The coherent distance is equal to the distance of the first domain atom, and the coherent fraction is 1. Figure 7.5(b) shows the destructive case, where the first domain atom is displaced 1.92 Å along the $(\bar{1}10)$ direction from a high-symmetry site. The 120° rotations puts the adsorption site in the other two domains at the same distance from the $(11\bar{1})$ planes, but this distance differs by exactly half a plane spacing from the $(11\bar{1})$ distance for the first domain atom. Assuming equal populations of atoms in all three domains, the contribution of the first domain atom exactly cancels that from one of the two other domains. The overall coherent distance is equal to that of the atoms in the two rotated domains, and the coherent fraction is 1/3. For this adsorption geometry, the single-domain case would have a coherent distance which differs from the three-domain coherent distance by half a diffraction plane spacing, producing distinctly different XSW absorption profiles.

For ease of calculation, we represent the $(11\bar{1})$ distance for atoms in the two 120°-rotated domains into two other domains by taking the distances of the first domain atom from the $(\bar{1}11)$ and $(1\bar{1}1)$ planes. In other words,

$$\left(f_{c,11\bar{1}}\, e^{2\pi i D_{c,11\bar{1}}}\right)_{3\text{-domain}} = \frac{e^{-2\pi^2\sigma_H^2}}{3}\left(e^{2\pi i D_{11\bar{1}}} + e^{2\pi i D_{1\bar{1}1}} + e^{2\pi i D_{\bar{1}11}}\right) \qquad (4)$$

This is equivalent to rotating the first domain adatom site 120° into the other two domains, as the intersection of $(\bar{1}11)$ and $(1\bar{1}1)$ planes with the surface plane are rotated from the intersection of the $(11\bar{1})$ plane with the surface plane by 120°. Figures 7.5(c) and 7.5(d) shows the results for the constructive and destructive cases using this technique, and they are the same as from rotation of the adatom site into three domains and taking the $(11\bar{1})$ distance for all three domains. With the choice of coordinate system in Figure 7.5, i.e. x along $(11\bar{2})$, y along $(\bar{1}10)$, and z along (111), the distances from the various diffracting planes is given by these four equations:

$$
\begin{aligned}
d_{111} &= \frac{z}{3.135\ \text{Å}} \\
d_{11\bar{1}} &= \frac{x}{3.326\ \text{Å}} + \frac{1}{3}\left(\frac{z}{3.135\ \text{Å}}\right) \\
d_{1\bar{1}1} &= -\frac{1}{2}\left(\frac{x}{3.326\ \text{Å}}\right) - \frac{y}{3.84\ \text{Å}} + \frac{1}{3}\left(\frac{z}{3.135\ \text{Å}}\right) + \frac{3}{4} \\
d_{\bar{1}11} &= -\frac{1}{2}\left(\frac{x}{3.326\ \text{Å}}\right) + \frac{y}{3.84\ \text{Å}} + \frac{1}{3}\left(\frac{z}{3.135\ \text{Å}}\right) - \frac{1}{4}
\end{aligned}
\tag{5}
$$

x, y, and z are given in Å, and all the resulting distances are normalized by the (111) diffraction plane spacing of 3.135 Å. The origin was chosen so the positions of bulk Si atoms give the correct distances of +1/8 or -1/8 (modulo 1) relative to all the diffracting planes. x, y, and z correspond to the first domain adatom position, for which the only possible y values are y=0 Å and y=1.92 Å. Since the distances are only unique to modulo the diffraction plane spacing (i.e. modulo 1 in our normalization) and with this restriction on y values , it can be shown that

$$
d_{1\bar{1}1} = d_{\bar{1}11} \tag{6}
$$

where were refer to the distance to the closest diffracting plane. Thus the last two of the three terms in equation (5) are equal. Since the non-(111) reflections are almost in the surface plane, the dependence of the distances of all three reflections upon adatom height z is the same and is smaller than their dependence on x and y.

As the three domains contribute signals with different distances from the $(11\bar{1})$ plane for a given adsorbate lateral position (with the exception of the high-symmetry sites), the overall coherent fraction will be reduced from the corresponding fraction for a single-domain surface model, and the coherent distance also will be different. Figure 7.5(e) shows the possible values of $D_{11\bar{1}}$ and $f_{11\bar{1}}$ for a single-site, model when it is rotated into three equal domains, assuming a height corresponding to D_{111} = 1.04. When the measured XSW data for the $(11\bar{1})$ reflection do not fit points on this curve, it is reasonable to assume multiple-site adsorption in the structural model. In addition, even in the case of high-symmetry sites, multiple adsorbate sites will produce a $(11\bar{1})$ distance between the contributing sites and a reduced coherent fraction. All of the models suggest alternative bonding sites with slightly higher (<0.1eV) energies than the preferred site[24-25]. Combining these two factors with the Debye-Waller contribution can cause quite low coherent fractions. As a result, a well-ordered multi-domain and/or

multi-site surface may be mistaken for a highly disordered surface upon initial analysis of $(11\bar{1})$ XSW data. In our case, the quality of the 3x1 LEED patterns in addition to the repeatability of the XSW data led us to consider the annealed 3-domain alkali/Si(111)3x1 and room temperature dosed K/Si(111)3x1 surfaces as well ordered despite the relatively low $(11\bar{1})$ coherent fractions.

Si 1s XSW data for the (111) Bragg reflection

At the photon energy for Si(111) backreflection (1977 eV), the Si 1s kinetic energy is highly surface sensitive. The escape depth of photoemitted Si 1s electrons at this photon energy is 7.2 ± 1.6 Å as determined from the electron kinetic energy of ~135 eV and the "universal curve" for Si [34]. By performing an angular integral over the CMA acceptance cone for our sample-analyzer geometry, we find the contribution from the topmost Si bilayer was 63±9%, with the second bilayer contributing 20±2% and the bulk Si contributing the remaining 17±7%. Here the error bars reflect the change in percentages as the escape depth is varied within its own error bars. This assumes a full top bilayer of Si as in the "567567" model (Figure 7.1(c)), but for the missing top layer "500500" and "560560" models (Figures 7.1(a)-(b)), the overall contribution of each Si layer is also weighted by the number of atoms in each layer. Therefore, the contribution of bulk Si atoms to the total signal is significant. As mentioned above, atoms in multiple positions along the Bragg reflection will decrease the overall coherent fraction of the data. If the Si(111) surface atoms are in different positions than the Si bulk atoms relative to the bulk (111) diffracting plane position, the Si 1s XSW data will have a coherent distance and fraction which are different from the bulk values of $D_c = 1$ and $f_c = 0.707$, due to the interference of bulk and surface contributions with different phases (distances). A bulk-terminated surface nominally will have surface atoms in the same positions as bulk Si and should have a coherent fraction near the bulk value.

Table 7.1 gives the measured values of coherent distance D_c and fraction f_c from the Si 1s XSW data for the (111) reflection as well as simulated standing wave results from the various reconstruction models of the Si(111) 3x1 surface. The bulk-terminated model has an unrelaxed surface, while the Si atom positions for the 3x1 reconstructions were taken from density-functional theory calculations[24-26]. For the simulation of XSW data for each of these models, the third bilayer was fixed at the bulk Si positions. The standing wave contributions of the atoms in each bilayer to the (111) XSW structure factor were summed and the bilayer sums were weighted by their

contribution to photoemission due to the escape depth and weighted by the relative number of atoms in each layer, in order to sum over all Si atoms. The magnitude and phase of this overall structure factor correspond the coherent fraction and distance, respectively, of the resulting simulated standing wave.

The (111) reflection probes Si distances normal to the surface, i.e. the height of the surface Si atoms above the rest of the substrate. The simulated results are different for each of the structural models. The missing top layer "560560" and "500500" models have similar coherent distance, as do the "567567" and bulk-terminated models; however, the missing top layer models have a distance about 0.05 plane spacings lower than the other models, which have a full surface Si bilayer. This is because the missing top layer models do not have atoms at the height of the top half of the Si bilayer, i.e. near +1/8 plane spacings above the diffracting plane. The average height of the surface layer of the "500500" and "560560" models is 0.83 and 0.88 plane spacings from the (111) plane, respectively, which corresponds to the lower half of the Si bilayer in the bulk-terminated and "567567" models. As the surface layer contributes 63% of the total signal, with the remaining 37% close to the bulk bilayer structure with a distance near 1 plane spacing, the total signal for the missing top layer models has an intermediate coherent distance near 0.95. This difference of 0.05 plane spacings is significant, as error bars on the Si coherent distances are on the order of 0.01 plane spacing due to the good counting statistics of this data (the overlayer data, which has a considerably weaker peak to monitor, has correspondingly larger error bars). The Si 1s XSW data are quite similar for both the annealed Na/Si(111)3x1 and K/Si(111)3x1, which confirms previous findings that these surfaces have the *same* underlying Si reconstruction, independent of the alkali adsorbate. The room-temperature dosed K/Si(111)3x1 surface has a larger coherent distance, indicating its reconstruction is *different* from the annealed (Na,K)/Si(111)3x1 surfaces. Figure 7.6 displays the XSW data for the 3x1 surfaces, and the similarities and differences between the data can be seen. Comparing the data with our simulated data, the best match is the "500500" model for the annealed 3x1 surface, and the "567567" model for the room-temperature dosed K/Si(111)3x1 surface. While the "560560" model also has a reduced coherent distance D_{111} near the annealed 3x1 measured value, and the bulk-terminated model had a coherent distance near 1 like the room-temperature dosed 3x1 data, both the "560560" and bulk-terminated model simulated data have coherent fractions f_{111} which are significantly higher than the measured values. For the bulk-terminated model, the surface Si positions match the bulk Si positions exactly and produce the bulk coherent fraction of 0.707. The "560560" model consists of a very flat hexagonal surface layer,

with all the surface Si atoms at very similar height relative to the diffracting plane. The top layer contribution to the overall signal has a coherent fraction of 0.99. When combined with the bulk layer contribution, the overall coherent fraction is 0.79, which is larger than the bulk Si coherent fraction of 0.707. The coherent fraction is directly related to the size of the standing wave feature, as can be determined from equation (1). If the Si surface for the 3x1 surface matched the "560560" model, the measured feature of the Si 1s XSW signal would be larger than that for the bulk signal, which is measured through the total yield or off-peak background yield. However, the measured feature is smaller than that for the bulk Si signal, ruling out both the "560560" and bulk-terminated models. The overall coherent fractions for the "500500" and "567567" models are less than the bulk value of 0.707, due to the differences between surface and bulk atom heights relative to their nearest (111) diffracting planes. The "500500" model has one-third of the top layer Si atoms that the "567567" model does, so the surface contribution to the overall signal is less for the "500500" model, and therefore the coherent fraction is closer to the bulk value (higher) for "500500" than for "567567". Thus, from the Si 1s XSW data alone, we have determined the most probable surface reconstructions for the annealed (Na,K)/Si(111)3x1 and room-temperature dosed K/Si(111)3x1 surfaces, namely the "500500" (Seiwatz chain) and "567567" (extended Pandey chain) models, respectively. The difference between the annealed and room-temperature dosed K/Si(111)3x1 surface structures also is supported by the thermal energy required to remove a top layer of Si atoms and produce an MTL reconstruction. However, because of the model dependence and the need to consider the bulk contribution to the overall signal for Si 1s XSW, we also take adsorbate XSW data. The adsorbate (111) and $(11\bar{1})$ reflection data can triangulate the adatom position, and they provide a more direct structural test which can be combined with the Si 1s XSW data to confirm the underlying Si structure.

Na 1s and K LMM XSW Data

Table 7.2 presents the coherent distances and fractions from fits to the (111) and $(11\bar{1})$ XSW reflection data for Na and K absorption on the alkali/Si(111)3x1 surfaces. Sample data are presented in Figure 7.7. The noisiness of the data is due to the low number of counts in the Na 1s and K LMM peaks for a coverage of 1/3 or 2/3 ML and the limitation of the data collection time to ~8 hours to avoid contamination of the surface. For this reason data were collected on multiple samples for both reflections and all surfaces.

As a first step to determining the adsorbate geometry, the height of the adsorbate atom above a bulk-terminated Si(111) surface can be determined readily from the (111) coherent distance D_{111}. Table 7.3 shows the alkali-Si bond length if the alkali adatom was bonded to a high-symmetry site on the bulk-terminated surface at a height corresponding to the measured coherent distance D_{111}. The final column gives the sum of alkali and Si covalent radii as an estimate of a reasonable bond length to compare against. The Na-Si bond lengths are all too long if one assumes D_{111}=1.168, and too short if D_{111}=0.168. This suggests that there are no vertical bonds between Na and the Si surface. This would be the case for a adsorption site which satisfies a lateral dangling bond from a chain structure, as in the missing top layer "500500" and "560560" models. The bond lengths for the annealed K/Si(111)3x1 also are too long or too short depending on the adsorption site chosen. The threefold sites have K-Si bond lengths of 3.65 Å, which could be reduced by some Si surface relaxation or reconstruction to produce a K-Si bond of reasonable length. This suggests that there is a K-Si bond with a significant vertical component for the annealed K/Si(111)3x1 surface, unlike the sodium case. The K-Si bond length for the threefold-coordinated sites on the room-temperature K/Si(111)3x1 surface is about 3.35 Å, which is in reasonable agreement with the sum of covalent radii 3.20 Å, and is less than the range of bond lengths of 3.40 to 3.53 Å found in DFT calculations of the surface[24-26]. So a bulk-terminated model of the room-temperature dosed K/Si(111)3x1 surface is reasonable from considering the (111) data alone. However, a bulk-terminated surface is threefold symmetric and should not produce an ordered single-domain 3x1 structure at 2/3 ML coverage, especially when 1/3 ML of bonds would be left unsaturated. The directionality of the LEED pattern as well as the previous discussion about the Si 1s XSW data indicate the Si surface is reconstructed, and that the "567567" (extended Pandey chain) surface is a likely model. As both the bulk-terminated and "567567" models have a surface Si bilayer, we would expect the K-Si bond lengths to the "567567" surface to be similar to the bond lengths to a bulk-terminated surface, and the K adatom geometry will be in positions analogous to the threefold-coordinated sites of the bulk-terminated surface. While the assumption of a bulk-terminated surface for any of the 3x1 surfaces is not valid as indicated by LEED and Si XSW results, the bulk-terminated bond lengths from the measured (111) distance provide an estimate of bond lengths on the reconstructed surface, as well as suggesting which adatom-Si bonding arrangements are probable for the 3x1 surfaces.

The $(11\bar{1})$ reflection XSW data for Na and K adatom absorption yields also provide preliminary information on acceptable adsorption sites for surface structural

models. The $(11\bar{1})$ coherent fractions are equal to or significantly less than the (111) coherent fraction for all three surfaces studied. This indicates that the adatoms all have similar heights above the surface, but their lateral registry with respect to the $(11\bar{1})$ plane is not all the same due to multiple-domain and/or multi-site adsorption. In addition, the $(11\bar{1})$ coherent distance for the annealed Na 3x1 and annealed K 3x1 surfaces differ by 0.245 ± 0.103, indicating the geometry of the Na and K adsorption sites could be considerably different. This was also seen in the (111) bond-length analysis, and indicates the importance of the alkali adatom size in determining the best adsorption site. Table 7.4 lists the measured $(11\bar{1})$ coherent distances $D_{11\bar{1}}$ and the corresponding values for the high-symmetry sites of the bulk-terminated surface, calculated using equation (5) and the measured (111) coherent distance for z. The measured coherent distances are in between those for the high-symmetry sites, which indicates that the adsorbate lateral position does not correspond to the high-symmetry site lateral positions, and/or that multiple sites are populated which produce a phase-averaged position between the high-symmetry sites. This intermediate lateral position as well as the low $(11\bar{1})$ coherent fraction make necessary the consideration of multi-domain, multi-site models for all three surfaces.

Structural Models of the Na/Si(111)3x1 and K/Si(111)3x1 Surfaces

In the models we present below, we did not have a means of performing theoretical total-energy calculations, so we used Si atomic positions in the literature for each of the model surfaces as a starting point. In each case, these starting atomic positions correspond to the minimization of the total surface energy using density-functional theory calculations[24-26]. The calculations of the missing top layer ("500500" and "560560") models have two bilayers of Si plus the Si surface layer, while the "567567" (extended Pandey chain) model consists of the surface bilayer plus one underlying Si bilayer. These are the Si atoms whose position was allowed to vary. An additional Si bilayer was added to each model and fixed at the bulk Si positions, and defines the position of the (111) and $(11\bar{1})$ diffracting planes. After establishing the starting Si positions, the adatoms were placed at positions whose height matched the (111) coherent distance, and lateral positions were selected to produce reasonable bond lengths to one or two Si surface chain atoms, while keeping in agreement with the $(11\bar{1})$ coherent distance and fraction after adding the contributions from multiple domains and/or sites. The changes in bond lengths, adsorbate (111) and $(11\bar{1})$ coherent distance and fraction, and Si 1s (111) coherent distance and fraction with

changes in model atom positions were all monitored using a desktop spreadsheet program. Some preference was given to matching the adatom $(11\bar{1})$ distance and fraction, and some Si-Si bonds were rotated to give the correct alkali-Si bond lengths while maintaining the Si-Si distance. This usually resulted in small (<0.5 Å) shifts in the top Si layer lateral positions and changes in the vertical buckling of the Si chains. The "500500" model has Si atomic positions identical to those in Ref. [24] for the Na/Si(111)3x1 surface, and very small shifts (<0.1 Å) for the K/Si(111)3x1. Bond rotations were on the order of 10^{o} or less from the starting bond angles from DFT calculations[24]. When multiple adsorption sites were required to match the $(11\bar{1})$ data, two sites were chosen with similar coordination and bonding environments, either by having both sites on the same Si surface, or in the case of buckled chain reconstructions, using an adsorption site and its corresponding site on the opposite-buckled surface. The similarity of the two selected sites was required by the lack of visible multi-component structure in the Na 2p and K 3p photoemission peaks for the surfaces, and the similarity also agrees with the assumption of equal populations of both sites. However, as discussed above, the width of the photopeaks for these surfaces suggests multiple adsorption sites, although the energy difference is small enough to avoid a shoulder in the peak. We also operate under the assumption that changes in total energy from Si-Si bond rotation are less costly than changes in the Si-Si bond length, so our final surface models still should be near the total energy minimum.

Using the information about the underlying surface determined by the Si 1s XSW and (111) reflection adsorbate XSW, we perform the more complicated analysis of the $(11\bar{1})$ XSW reflection data. The $(11\bar{1})$ data give information on the lateral registry of the alkali adatoms, which can be combined with the (111) data to triangulate the adatom position. However, as discussed above, multiple adsorption sites and multiple domains complicate the interpretation of the $(11\bar{1})$ data. To illustrate the data interpretation, we will make use of phasor diagrams (see Figures 7.5,7.8-11), following the example of Woodruff[10]. In these diagrams in complex space, each phasor represents the contribution of a specific site and domain to the overall XSW structure factor $F_{11\bar{1}}$. The length of each phasor corresponds to the fractional population f_j of that site and domain, while the angle each phasor makes with the real axis is equal to $2\pi D_{11\bar{1},j}$. The sum of all the phasors is then compared to the phasor of the measured coherent distance and fraction, whose error bars delineate a region in complex space. From the phasor diagram one also can gauge how changes in the populations and positions of each contributing phasor affects the overall sum. This is

important, as the $(11\bar{1})$ data for the room-temperature K/Si(111)3x1 surfaces changes slightly for one-domain versus two-domain structures, and the $(11\bar{1})$ data for the 3-domain Na/Si(111)3x1 surface do not change significantly when the horizontal domain has a larger fractional population than either of the other two domains. In addition, we explore the effect of deviating from equal populations of two sites, as actual site populations may be somewhat unequal at the measured alkali coverages.

We start with the model for the annealed Na/Si(111)3x1 surface. As seen above, the "500500" (Seiwatz chain) model has the best match to the Si 1s XSW data, and we will test Na adsorption sites on this surface to see if they match the Na 1s XSW data for the (111) and $(11\bar{1})$ reflections. In addition, we will test the newly proposed "560560" (honeycomb-chain channel) model for the 3x1 surface. First, the measured coherent fraction and distance rule out single-site adsorption, because of the multiple domain effect. The Na/Si(111)3x1 always exhibits a three-domain structure, although several of the samples showed increased population of the horizontal domain along the $(11\bar{2})$ direction. As discussed above, an adsorption site with lateral registry similar to the high-symmetry surface will map to the same distance $D_{11\bar{1}}$ from the $(11\bar{1})$ plane in all three domains, producing a coherent fraction $f_{11\bar{1}}$ near 1. Conversely, a site whose lateral registry is halfway between two high-symmetry sites in either the x or y direction will have destructive interference between the horizontal domain and the other two, resulting in a $D_{11\bar{1}}$ value between those for the high-symmetry site values, and a $f_{11\bar{1}}$ value of 1/3 for equally populated domains. In the destructive interference case where the horizontal domain is more heavily populated, the contribution from the horizontal domain and the sum of contributions from the other two domains are nearly equal, and $f_{11\bar{1}}$ would approach zero. As seen in Table 7.4, adatoms at the same x and y positions of the high-symmetry sites T_1, T_4, H_3 would have $(11\bar{1})$ coherent distances of $D_{11\bar{1}} = 0.222 \pm 0.009$, 0.556 ± 0.009, and 0.889 ± 0.009 respectively. These $D_{11\bar{1}}$ values were determined using equation (5) and the measured height above the diffracting plane at the Si surface corresponding to $D_{111} = 1.168 \pm 0.026$. Note that the "500500" and "560560" surface models do not have the same symmetry as the bulk-terminated surface, and we are using the bulk-terminated symmetry lateral positions purely as reference positions. The mapping of the adsorption site into three domains still produces a high coherent fraction $f_{11\bar{1}}$ near the lateral positions of the bulk-terminated high-symmetry sites, because the diffracting planes and X-ray standing wave are determined by the bulk and not the surface structure. The measured $D_{11\bar{1}}$ of 0.671 ± 0.044 is almost exactly halfway between the distances for two of the high-symmetry (T_4 and H_3) positions, and for single-site adsorption would correspond to

the destructive interference case. However, the measured $f_{11\bar{1}}$ of 0.692 ± 0.206 clearly disagrees with the value of 1/3 or less for the destructive interference case. Thus, by examining the $(11\bar{1})$ coherent distance and fraction together, a single-site adsorption case is ruled out. This is a different and more complete analysis method than that seen in many XSW papers, where single-site adsorption is assumed and the distance alone is used to determine adatom position. Unlike the Na/Si(111)3x1 case, the coherent fraction in the $(11\bar{1})$ direction is usually low in these studies, and the reduction is explained through the thermal Debye-Waller factor and disorder. As seen from the high coherent fractions in both the (111) and $(11\bar{1})$ directions for Na/Si(111)3x1, it is possible to achieve a high level of structural order upon an annealed surface, and the possibility of reduced coherent fraction due to multi-site adsorption should not be overlooked on annealed adsorbate/substrate interface in general.

A two-site model is motivated by DFT calculations of the "500500" and "560560" model surfaces. For both surfaces, nearly equivalent sites can be obtained by bonding to either side of the top layer Si chain. The reported difference in adsorption energy between the preferred site and its mirrored sites across the chain is 0.09 eV/Na atom and 0.03 eV/Na atom for the "500500" [24] and "560560" models [25]. The local bonding environment for the two sites is also very similar due to their nearly symmetric relationship to one another. Core-level Na and K photoemission spectra appear as a single peak with no apparent component or shoulder structure, which suggests that if multiple adsorption sites exist, they must have very similar energetics and chemical shifts. For these reasons, we restrict the two-site model to sites which are in close to mirrored positions across the chain structure. Different Si chain segments or patches on the surface can have one or the other adsorption geometry (L or R), while within the 3x1 unit cell, only one of two adsorption sites is occupied in order to produce the good 3x1 LEED pattern while maintaining the restriction of 1/3 monolayer coverage. This is different from the room-temperature K/Si(111)3x1 model discussed below, which has 2/3 ML coverage and therefore has two K atoms in the unit cell which are adsorbed to the same chain.

As the measured $D_{11\bar{1}}$ of 0.671 ± 0.044 is nearly halfway between the distances for the high-symmetry T_4 and H_3 positions, a good starting point for the two-site model is equal populations of adatoms at the lateral positions of the T_4 and H_3 sites. These positions would have no reduction of the coherent fraction due to consideration of multiple domains, with equal or unequal weighting. However, the difference in position between the two sites cause interference between the response of

the atoms in the two sites to the standing wave. Equation (2) relates the overall coherent fraction to the difference in position between two equally populated sites, and in this case the difference in $D_{11\bar{1}}$ values is 1/3 of a plane spacing, producing an overall coherent fraction of 1/2. Figure 7.8(c) is the phasor diagram for the two-site model in the case of equal domain populations. While this value is higher than the value of 1/3 determined for the single-site but multi-domain case, it is just within the lower limit of the measured $f_{11\bar{1}}$ of 0.692±0.206. In addition, $D_{11\bar{1}}$ would be 0.715, which again is just within the error bars of the measured value. There are two modifications to the Na adsorption sites which can bring the model coherent fraction and distance more in line with the measured values. First, the positions can be shifted slightly from the T_4 and H_3 lateral positions so that the difference in $D_{11\bar{1}}$ for the two sites is less for the horizontal domain. Summing over both sites, the coherent fraction for the horizontal domain is increased above 0.5. If contribution from the horizontal domain is given larger weight as observed in the LEED pattern, the overall coherent fraction is increased above 0.5. Second, the relative weights of the two sites can be made slightly unequal due to the calculated small difference in adsorption energy between the sites. This will shift the overall position towards position for the more populated site. Table 7.5 shows the effect of changing the weighting of the domains and sites upon the model coherent distance and fraction. A weighting of the horizontal domain to 50% of the total signal and a 60%/40% split between the two site populations was found to give closer agreement to the measured distance and fraction than the assumption of equal contributions from each of the three domains and each of the two sites. Figure 7.8(d) shows the phasor diagrams before and after changing the weighting from equal site and domain population. The measured coherent distances and fractions for the Na/Si(111)3x1 samples with equal domains and a stronger horizontal domain were found to overlap, so their values were averaged together to give the plotted result. The model results corresponding to both types of Na/Si(111)3x1 samples are within the error bars for the measured values. The similarity of the measured values for samples with equal or unequal domain weighting indicates that the lateral positions of the adsorption must be near the high-symmetry positions, as is the case for this "500500" model.

Figures 7.8(a) and (b) show the top and side views ((111) and $(1\bar{1}0)$plane projections) of our proposed "500500" model of the Na/Si(111)3x1 surface, while Figure 7.8(c) is a phasor representation of the sum of contributions from the two adsorption sites. For the "500500" model, the Si chain buckles in different directions for the two different sites, so it is expected that these two sites will not appear next to

each other along the same chain. However, longer segments of different buckling orientation along the same Si chain could be possible. The "500500" has four possible adsorption sites, corresponding to the two different sides of the Si chain and either onefold or twofold coordination to Si chain atoms. Accordingly the sites are labeled L1, L2, R1, and R2. L1 and R2 have lateral positions near the T_4 site, while L2 and R1 have lateral positions near H_3. The data can not determine whether the actual combination of sites is R1&L1 or R2&L2, but it is reasonable to assume that both sites have the same coordination in order to produce the same chemical shifts seen in photoemission spectra. DFT calculations prefer the single bond geometry[24-25]. However, these model predict bonding to the Si atom in the channel between Si chains, due to the dangling bonds protruding vertically from this atom. As discussed earlier, the measured (111) distance does not correspond to a reasonable bond length for a vertical bond to the surface. For the proposed adsorption sites, the distance from the Na atom to the channel atom is between 3.60 and 3.90 Å, clearly too long for a strong bond. The bond distance to the Si chain atoms is 2.70 Å in the model depicted (equal to the sum of covalent radii), but bond lengths up to 3.00 Å are in good agreement with the XSW data. Figure 7.9(a)-(d) is the same presentation for the "560560" model of the Na/Si(111)3x1 surface. Both of the sites bridge neighboring Si honeycomb-chain structures. The sites differ in whether the Na makes two of its three bonds to the honeycomb-chain to its right or its left. We label the two sites L and R according to which chain the Na is twofold-coordinated. The lateral position of the L site is near that of the bulk-terminated T_4 site, while the R site is near H_3.The bond length to all three Si atoms is 2.94 Å, which is in excellent agreement with the predicted value of 2.95 Å - 3.05 Å in the DFT calculation of this surface[24-25].

Comparing the phasor diagrams for the "500500" and "560560" models, we see the contributions of the two sites across the two models is very similar. Table 7.5 gives the calculated coherent distance and fraction for several values of the weighting among domains and between sites. The models assume all adatom heights are equal to the (111) distance, which is quite reasonable since the coherent distance in the (111) direction is very close to 1. Both models have the same difficulty producing a high enough coherent fraction. This is due to the consideration of three domains and to the measured $D_{11\bar{1}}$ being between the distances for high-symmetry position. In terms of matching the Na 1s XSW data for the (111) and $(11\bar{1})$ reflections, both models are reasonable. However, as determined above, the calculated coherent fraction for Si 1s emission along (111) is too high for the "560560" model, while the agreement is good for the "500500" model. As discussed in the literature, the "500500" model does not

exactly explain STM images, in particular the angle between spots corresponding to neighboring atoms in the double rows, while the "560560" model more closely matches STM data. A more important problem of the "500500" is the lack of a bond to the underlying channel. Leaving this Si atom unbound would disagree with the band structure and the passivated nature of the Na/Si(111)3x1. It is possible that the Si channel atoms could be puckered further upward towards the Na than depicted in the model; however, the atom would need to move upward by at least 0.50 Å to produce a reasonable bond length. The "560560" model does not have this problem as all dangling bonds are filled and all bond lengths are reasonable. The "560560" model also was calculated to have a considerably lower total energy (0.53 eV/Na atom) than a "500500" model with bonds to both Si chain and channel atoms[25]. Since the "500500" model agrees with both adsorbate and substrate XSW data, we believe the "500500" model to be the structure of the Na/Si(111)3x1 surface. However, a theoretical calculation of this model would help confirm its validity. An alternative model is the "560560" model, but it disagrees with Si 1s XSW data, and as we shall discuss below, this model is not correct for the annealed K/Si(111)3x1 surface.

As with the Na/Si(111)3x1 case, the structural models which match the Si 1s XSW data best for the annealed K/Si(111)3x1 surface are the missing top layer "500500" and "560560" models, with "500500" being the better match and "560560" having too high a coherent fraction. However, for K/Si(111)3x1, the "560560" model does not agree with the adsorbate XSW data using the K LMM Auger yield. In this case, the adatom height D_{111} is less than for the Na/Si(111)3x1 surface. In the "560560" model for Na/Si(111)3x1, the measured D_{111} agreed nicely with the calculated bridging site position, giving a bond length of 2.94 Å. With a shorter height by 0.13 plane spacings or 0.40 Å, the K adatoms in a "560560" model would have a bond length shorter than 2.94 Å, which is already a very short K-Si bond length relative to the sum of covalent radii 3.20 Å. Thus the "560560" model is ruled out for K/Si(111)3x1, because of the size of the K adatom relative to the channel between honeycomb-chains, coupled with the measured adatom height. This casts some doubt on the "560560" model being the correct structure for the Na/Si(111)3x1 surface as well, as the substrate structure of the Na/Si(111)3x1 and K/Si(111)3x1 surfaces should be similar, although there is yet no direct experimental comparison of the two surfaces in the literature.

As for the "500500" model of the annealed K/Si(111)3x1 surface, our preliminary analysis of K vertical height from the (111) data suggested that the K could be bound in a threefold environment with a reasonable bond length to the surface

underneath. This means that the K adatom should be bound to the channel atoms as well as the Si chain atoms, unlike the case of Na/Si(111)3x1. In addition, the lateral distribution of site is significantly different from the Na 3x1 case, as indicated by the large difference in the $(11\bar{1})$ coherent distances $D_{11\bar{1}}$ between the Na and K 3x1 surfaces. The coherent fractions in the (111) and $(11\bar{1})$ directions are also considerably lower for the annealed K/Si(111)3x1 surface. For the measured adatom height, $D_{11\bar{1}} = 0.180 \pm 0.017, 0.514 \pm 0.017, 0.847 \pm 0.017$ correspond to the lateral positions of the high-symmetry sites T_1, T_4, and H_3, respectively. The measured $D_{11\bar{1}} = 0.926 \pm 0.051$ is closer to a high symmetry site than for the Na/Si(111)3x1 case, but the error bars do overlap neither the H_3 site nor the midpoint between T_1 and H_3, so for three-domain single-site adsorption, the expected coherent fraction should be somewhere between 1/3 and 1. The low coherent fraction and intermediate position could also be due to multiple site adsorption, so we tested four possible adsorption sites for K on the "500500" surface. These are analogous to the four sites tested for Na on the "500500" surface. Figure 7.10(c) shows the phasors corresponding to the three-domain sum for each of the four sites and compares them to the measured coherent distance and fraction. All four phasors are on the same side of the line drawn through the measured value. This means that any sum of two sites would produce an overall phasor on that side of the complex plane, and would not correspond to the actual measured overall phasor. Unlike the Na 3x1 case, for the annealed K/Si(111)3x1 no evidence of unequal domain population was observed in the LEED, so there is no justification for weighting the domain contributions differently to produce different three-domain phasor sums. Therefore we can rule out a two-site adsorption geometry. On the other hand, the 3-domain coherent distance and fraction for the single site L2 are in good agreement with the measured values. We propose the single-site adsorption model of K/Si(111)3x1 shown in Figures 7.10(a)-(b), with 1/3 ML of K adsorbed in the L2 site, bound to two chain Si atoms and one channel Si atom of the "500500" structure, at bond lengths of 3.20 Å and 3.33 Å, respectively. These lengths are in excellent agreement with the sum of covalent radii 3.20 Å, and are less than the calculated distances of 3.40 Å - 3.44 Å from a DFT treatment of the K/Si(111)3x1 surface with "500500" Si surface structure[24-25]. Table 7.6 shows the good agreement between the measured $D_{11\bar{1}}$ and $f_{11\bar{1}}$ for the annealed K/Si(111)3x1 surface and the values for the proposed one-site, three-domain model.

The one discrepancy between this proposed model and the measured K LMM Auger yield XSW data is the low (111) coherent fraction. Our model assumes the K adatoms are all at the same height for ease in calculating the $D_{11\bar{1}}$ values, but the very

low (111) coherent fraction f_{111} indicates that this is not the case. In fact, f_{111} is lowest for the annealed K/Si(111)3x1 surface, out of all three 3x1 surfaces studied. As discussed above, several factors can contribute to reducing the coherent fraction. In this case, we believe f_{111} is reduced by a combination of thermal motion, height variations due to a steric effect, and a possible weak bond between K and the channel Si. While the measured (111) XSW data suggest that this is the case, a single XSW reflection is unable to describe the precise distributions of adatoms due to such effects. The measured D_{111} can be regarded as the "average" height of the adatom, with actual adatoms position in a distribution above and below this position. The steric effect results from the K adatom size being slightly larger than the Si substrate periodicity in the y or $(\bar{1}10)$ direction. This periodicity has length equal to the bulk Si-Si second nearest neighbor distance 3.84 Å, while the corresponding K-K distance, which is twice the K covalent radius, equals 4.06 Å. Since the K-K distance is too short if all the K atoms are in the same vertical plane, we expect the rows of K atoms to buckle upwards and downwards as one moves along the Seiwatz chains. If the preferred K-K distance is 4.06 Å, a vertical buckling of 1.3 Å is required to maintain this distance and still match the underlying chain structure. An alternative is to have occasional K vacancies in the row to reduce the vertical buckling. A simple two-height distribution of the K adatoms with Δz =0.90 Å does not change the coherent fraction and distance in the lateral $(11\bar{1})$ direction significantly from the values for the one-site model above, while the vertical coherent fraction along (111) reduces from 1 to 0.6. A more accurate distribution which includes a Gaussian thermal Debye-Waller factor would reduce the value further to agree better with the measured value of 0.350 ± 0.127. For the two-height distribution, the bond length to the chain varies slightly from 3.18 Å to 3.30 Å, while the bond length to the Si channel atom varies from 2.94 Å to 3.84 Å. Thus, for this model to be reasonable, we must assume a weak bond between the K and Si channel atom which can be easily stretched. This idea is supported by the case of the model of Na/Si(111)3x1 with the same "500500" model for the substrate, in which the Na adatom height is too large to bond strongly with the Si channel atom. This would be the case if the Si channel atom was lowered so that it forms a more planar sp^2-like configuration, as indicated by the arrows in Figure 7.10(b). More charge would be donated to the channel atom from its neighboring Si atoms, and the need to take charge from the alkali atom would be reduced. For the K/Si(111)3x1 surface we found the L2 site to be preferred, with two bonds to the Si chain and one bond to the channel. Since the K has more bonds to the Si chain which may also be stronger than the K-Si channel bond, the thermal motion would largely consist of a rocking of the K-Si chain bonds

around the $(\bar{1}10)$ axis. Since the equilibrium K position is to the side of the chain, the rocking motion would be mostly vertical (provided the K-Si channel bond is weak), and would be expected to reduce the vertical (111) coherent fraction more than the lateral $(11\bar{1})$ coherent fraction. The differences in binding energies of K adatoms at different distances from the channel Si atom may also explain the width of the K 3p photoemission curve, which is similar to that for the multiple-site K/Si(111) surfaces at higher coverage. It is interesting that the (111) coherent fraction for Na/Si(111)3x1 is high, even though XSW data suggest a similar adatom geometry to the annealed K/Si(111)3x1 surface. Na is a smaller atom, with twice the covalent radii equal to 3.08 Å, much less than the 3.84 Å required for the atoms to fit in neat rows along *y* on the "500500" surface. As a result, the proposed steric effect for K should not exist for Na, and Na-Na interactions should be weaker than K-K interactions. The Na-Si bonds should therefore be stronger and perhaps less prone to vibration, even though the Na is not constrained vertically by a bond to the Si channel atom. The large thermal motion of K adsorbed on Si surfaces has been seen in SEXAFS studies, in particular the work of Kendelewicz *et al.* [35] upon the K/Si(100)2x1 surface, where no EXAFS oscillations were seen for room temperature measurement, and the signal only appeared after cooling the sample with liquid nitrogen.

The room-temperature dosed K/Si(111)3x1 differs from the annealed 3x1 surfaces in its increased K coverage near 2/3 ML and in the (111) reflection XSW data results. The Si 1s XSW data best match the "567567" (extended Pandey chain) model of the Si surface, in contrast to the "500500" (Seiwatz chain) model common to both Na and K annealed 3x1 surfaces. The "567567" model has no missing Si atoms when compared to the clean Si(111)2x1 Pandey chain reconstruction, and can be readily formed from this reconstruction by rearrangement of Si bonds. The "500500" and "560560" models have a missing top layer, and the removal of 1/3 or 2/3 ML of Si atoms from the Si(111)2x1 surface to create these 3x1 surfaces is energetically prohibited at room temperature. In addition, the K adatom height, measured from the coherent distance of the K LMM yield XSW data for the (111) reflection, is lower than both annealed surfaces and produces a reasonable bond length for the threefold-coordinated adsorption sites of the bulk-terminated surface. However, the reduced Si 1s (111) coherent fraction and the single-domain nature of the 3x1 LEED pattern rule out the bulk-terminated surface as the underlying Si structure. Another difference between the room-temperature dosed and annealed 3x1 surfaces is the observation of single-domain or two-domain LEED patterns for the room-temperature phase, while the annealed 3x1 LEED pattern always has three domains. Again, the initial orientation of

the 2x1 π-bonded chain surface is maintained and the temperature is not high enough to rearrange the surface into three domains. In addition, the 2/3 ML coverage requires our surface model to have two adsorption sites within the 3x1 primitive unit cell.

Our proposed model for the room-temperature dosed surface is depicted in Figures 7.11(a)-(b), with the corresponding phasor diagrams in Figures 7.11(c)-(d). The $(11\bar{1})$ reflection data have very similar values for $D_{11\bar{1}}$ and $f_{11\bar{1}}$ for the single-domain and two-domain 3x1 surfaces, and $f_{11\bar{1}}$ is quite low. The reduced value of $f_{11\bar{1}}$ in this case mainly is caused by destructive interference between the contributions of the two sites to the XSW signal, and to a lesser extent by the multi-domain effect (for the two-domain surface). The measured $D_{11\bar{1}}$ of 0.916 ± 0.059 is in between the values of 0.81 and 1.15 for the lateral positions of the H_3 and T_1 high-symmetry sites, but is closer to the value for H_3. This indicates that the actual positions of the sites are shifted so their lateral midpoint is closer to H_3. Therefore site L was chosen near the H_3 lateral position, while the site R was chosen to be nearly half a plane spacing away from the first to reduce the overall coherent fraction, while maintaining reasonable bonding geometries to the "567567" Si surface. Upon rotation of the two sites into two equally weighted domains, the two-domain contribution from the low-symmetry site R nearly vanishes, and almost all of the total signal is from the contributions of the two domains of the high-symmetry site L. However, since this contribution represents only half of the absorbing K adatoms, the coherent fraction is also reduced below 0.5 for the two-domain surface. Figures 7.11(c) and 7.11(d) show the phasor diagrams for the $(11\bar{1})$ reflection for the single-domain and two-domain surfaces. As seen in Table 7.7, the calculated values of $D_{11\bar{1}}$ and $f_{11\bar{1}}$ for this two-site model agree well with the data for both the single-domain and two-domain surfaces.

The two proposed adsorption sites are given in Figures 7.11(a)-(b). Both sites bond to two chain Si atoms. The different sites are bonded to different sides of the buckled Pandey chain. In the case of site L, the third bond is to the Si atom atop the sixfold ring, while site R has no third K-Si bond. Site L has a K-Si distance of 3.19 Å to the chain atoms and 3.37 Å to the non-chain atom, which are in between the sum of covalent radii of 3.20 Å and the calculated distance of 3.48 Å for the K/Si(111)3x1 surface with 1/3 ML K on the "567567" surface[24]. The K-Si distance from site R to the Si chain atoms is 3.15 Å. The two sites are at different heights above the diffracting planes, which reduces the model coherent fraction along (111) while matching the measured coherent distance. The bonding environments of the two sites are not similar geometrically. The lower chain Si atoms probably will not bond to the adatom in site R as its bonds are already satisfied by neighboring Si atoms. It also is probable that the

position of site R is not as well defined as that of site L, since the bonding environment of site R is not as clear and would consist of sp^2-like bonds if any. While site L is determined by clear bonding to the dangling bonds of the π-bonded chain and the top of the sixfold ring, K adsorption near site R would be determined by keeping away from already adsorbed K in site L to avoid an energy gain due to K-K repulsion. Unlike our models of the annealed 3x1 surfaces, this model assumes that site L is preferred for adsorption over site R, and that site L is filled to 1/3 ML before site R is filled. Table 7.7 shows the variation of the model $D_{11\bar{1}}$ and $f_{11\bar{1}}$ with site and domain population, and assumption of equal site population will reduce the coherent fraction from value for site L filling first. In the case of one domain, the coherent fraction would vanish with assumption of equal site population. However, with site L preferred, one would expect to see different binding energies for K adsorbed in the two sites in the photoemission data, and the shape of the peak should vary with coverage, as the relative population of the two sites changes (see Figure 7.4(b)), which is not the case. The corresponding K photoemission spectra do not show a multi-component structure within experimental resolution, indicating that the two sites must have similar energetics. As in the case of the annealed K/Si(111)3x1 surface, vertical buckling between neighboring K adatoms along the chain may occur due to the size of the K adatom, and the resulting change in binding energy may widen the photemission curve. This model requires theoretical confirmation that the energies of the two adatom sites are similar. However, the other restrictions upon the surface model, namely 2/3 ML coverage, no missing Si layer and a Si surface reconstruction, as well as 3x1 periodicity, make this model the most favorable for the room-temperature K/Si(111)3x1 surface.

Conclusion

Using the X-ray standing waves technique to monitor alkali adatom and Si substrate atom absorption around the surface normal (111) and surface lateral $(11\bar{1})$ Bragg reflections, we have determined which of the three currently proposed models is the most correct for the annealed Na/Si(111)3x1 and K/Si(111)3x1 surfaces with 1/3 ML alkali coverage, as well as the room-temperature dosed K/Si(111)3x1 surface with 2/3 ML K. The Si 1s XSW data are most effective in differentiating between the three models, due to the differing structural features of each model, name the missing top Si layer in the "500500" and "560560" models but not the "567567" model, and the flatness of the 2/3 ML Si top layer of the "560560" model, which produces a substantially higher (111) coherent fraction than the "500500" model. Taken alone, the

Si 1s data point towards the "500500" (Seiwatz chain) model for the annealed Na and K 3x1 surfaces, and the "567567" (extended Pandey chain) model for the room-temperature dosed K/Si(111)3x1 surface. This agrees with the idea that elevated temperature is required to remove Si layers from the surface and produce the missing top layer reconstructions. Alkali absorption yield XSW data add further support to this selection of the Si substrate structure for the 3x1 surfaces. Na 1s XSW data were found to match adsorption sites on both the "500500" and "560560" model; however, in both cases two adsorption sites were required, as well as consideration of the effect of mapping the adsorption sites into the three equivalent domains upon the $(11\bar{1})$ reflection data. However, K LMM XSW data only match the "500500" model, with the K adatom being too large to produce reasonable bond lengths to neighboring Si chains in the "560560" model at the measured height taken from the (111) reflection data. If the underlying Si structure of the annealed *M*/Si(111)3x1 surface is independent of which monovalent atom *M* is adsorbed, as is suggested by LEED, STM, and angle-resolved photoemission studies, then the selection of the "500500" model for K/Si(111)3x1 forces the Na/Si(111)3x1 surface to also have the "500500" structure, which is what the Si 1s XSW data also indicate. Na is bonded to one or two Si chain atoms, while K is bound to two Si chain atoms. DFT calculations also predict alkali bonding to the Si atom in the channel between neighboring Seiwatz chains. The measured (111) distance is too large for this bond to exist for Na, and the (111) coherent fraction for K suggests that the bond to the Si channel atom may allow large thermal motion and bond length variation. A new theoretical investigation of this model, with the XSW measured adatom position as inputs, could test the validity of the "500500" structure and resolve the issue of the apparently weak bond to the channel Si atom.

The room-temperature K/Si(111)3x1 surface has an underlying "567567" Si structure, which is a natural extension of the π-bonded chain reconstruction of the clean Si(111)2x1 surface to a 3x1 periodicity. A two-site adsorption model was determined which matches the K LMM XSW data along both reflections for both single--domain and two-domain 3x1 surfaces. However, as in the case of the annealed 3x1 surfaces, the model does not agree completely with the expected bonding on the surface. The measured 2/3 ML coverage requires a two-site model; however, the model calculation has a threefold adsorption site which satisfies all dangling bonds at 1/3 ML coverage. It is possible that the second 1/3 ML adsorbs weakly to the surface in a less well-defined position. This is supported by the increased susceptibility of the room-temperature dosed K/Si(111)3x1 surface to oxygen contamination in vacuum,

compared to the observed passivation of the annealed K/Si(111)3x1 surface. In this case oxygen may attach to weakly bound K. However, among the three published models for the 3x1 surface, the "567567" model is the one that agrees best with both Si and K absorption yield XSW data. Again, a theoretical calculation of the surface with adsorbate positions taken from the XSW results would provide a more complete understanding of the surface.

XSW provides precise quantitative information on adsorbate position in the case of single-site adsorption onto a single domain structure. In the case of the multi-domain and multi-site structures of the alkali/Si(111)3x1 surfaces, the height of the adatom above the surface is still well-determined by the (111) reflection data. With reasonable assumptions about the symmetry among the domains and between the adsorption sites, the $(11\bar{1})$ reflection data can determine adatom surface lateral positions as well, although with less precision or model-independence than the (111) reflection data. In particular, low $(11\bar{1})$ coherent fractions, often previously attributed to disordered adsorption, can result from interference between multiple adatom sites and/or different distances from the $(11\bar{1})$ plane for the same site in multiple domains, even though the site geometry itself is well-defined. By combining our XSW data with theoretical calculations of structural models, a model surface could be determined whose atomic positions are confirmed by an experimental technique which measures atomic positions more directly than any of the other techniques previously used to measure the 3x1 surfaces.

References

[1] H. Daimon and S. Ino, Surf. Sci. 164 (1985) 320.

[2] W. C. Fan and A. Ignatiev, Phys. Rev. B 41 (1990) 3592.

[3] J. Quinn and F. Jona, Surf. Sci. Lett. 249 (1991) L307.

[4] K. J. Wan, X. F. Lin, and J. Nogami, Phys. Rev. B 46 (1992) 13635.

[5] D. Jeon, T. Hashizume, T. Sakurai, and R. F. Willis, Phys. Rev. Lett. 69 (1992) 1419.

[6] T. Okuda, H. Sigeoka, H. Daimon, S. Suga, T. Kinoshita, and A. Kakizaki, Surf. Sci. 321 (1994) 105.

[7] J. J. Paggel, G. Neuhold, H. Haak, and K. Horn, Phys. Rev. B 52 (1995) 5813.

[8] H. H. Weitering, X. Shi, and S. C. Erwin, Phys. Rev. B 54 (1996) 10585.

[9] K. Sakamoto, T. Okuda, H. Nishimoto, H. Daimon, S. Suga, T. Kinoshita, and A. Kakizaki, Phys. Rev. B 50 (1994) 1725.

[10] D. P. Woodruff, Prog. Surf. Sci. 57 (1998) 1.

[11] B. W. Batterman and H. Cole, Rev. Mod. Phys. 36 (1964) 681.

[12] J. C. Woicik, T. Kendelewicz, K. E. Miyano, P. L. Cowan, C. E. Bouldin, B. A. Karlin, P. Pianetta and W. E. Spicer, Phys. Rev. Lett. 68 (1992) 341.

[13] T. Kendelewicz, J. E. Klepeis, J. C. Woicik, S. H. Southworth, C. Mailhiot, M. van Schilfgaarde, M. Methfessel, A. Herrera-Gómez, and K. E. Miyano, Phys. Rev. B 51 (1995) 10774.

[14] T. Kendelewicz, P. Liu, G. E. Brown, Jr. and E. J. Nelson, Surf. Sci. 395 (1998) 229.

[15] J. C. Woicik, T. Kendelewicz, A. Herrera-Gómez, K. E. Miyano, P. L. Cowan, C. E. Bouldin, P. Pianetta, and W. E. Spicer, Phys. Rev. Lett. 71 (1993) 1204.

[16] J. C. Woicik, T. Kendelewicz, A. Herrera-Gómez, A. B. Andrews, B. S. Kim, P. L. Cowan, K. E. Miyano, C. E. Bouldin, B. A. Karlin, G. S. Herman, J. L. Erskine, P. Pianetta, and W. E. Spicer, J. Vac. Sci. Tech. A 11 (1993) 2359.

[17] J. C. Woicik, T. Kendelewicz, K. E. Miyano, P. L. Cowan, C. E. Bouldin, B. A. Karlin, P. Pianetta, and W. E. Spicer, Phys. Rev. B 44 (1991) 3475.

[18] J. Zegenhagen, Surf. Sci. Rep. 18 (1993) 199.

[19] P. L. Cowan, J. A. Golovchenko, and M. F. Robbins, Phys. Rev. Lett. 44 (1980) 1680.

[20] J. A. Golovchenko, J. R. Patel, D. R. Kaplan, P. L. Cowan, and M. J. Bedzyk, Phys. Rev. Lett. 49 (1982) 560 .

[21] J. C. Woicik, T. Kendelewicz, S. A. Yoshikawa, K. E. Miyano, G. S. Herman, P. L. Cowan, P. Pianetta and W. E. Spicer, Phys. Rev. B 53 (1996) 15425.

[22] E. Vlieg, E. Fontes, and J. R. Patel, Phys. Rev. B (1991) 7185.

[23] H. H. Weitering, N. J. DiNardo, R. Pérez-Sandoz, J. Chen, E. J. Mele, Phys. Rev. B 49 (1994) 16837.

[24] S. Jeong and M.-H. Kang, Phys. Rev. B, 54 (1996) 8196.

[25] M.-H. Kang, J.-H. Kang, and S. Jeong, Phys. Rev. B, 58 (1998) 13359.

[26] L. Lottermoser, E. Landemark, D.-M. Smilgies, M. Nielsen, R. Feidenhans, G. Falkenberg, R. L. Johnson, M. Gierer, A. P. Seitsonen, H. Kleine, H. Bludau, H. Over, S. K. Kim, and F. Jona, Phys. Rev. Lett. 80 (1998) 3980.

[27] S. C. Erwin and H. H. Weitering, Phys. Rev. Lett. 81 (1998) 2296.

[28] C. Collazo-Davila, D. Grozea, and L. D. Marks, Phys. Rev. Lett. 80 (1998) 1678.

[29] G. Le Lay, M. Manneville, and R. Kern, Surf. Sci. 72 (1978) 405.

[30] S. C. Erwin, Phys. Rev. Lett. 75 (1995) 1973.

[31] K.C. Pandey, Phys. Rev. Lett. 47 (1981) 1913.

[32] M. Tikhov, L. Surnev and M. Kiskinova, Phys. Rev. B 44 (1991) 3222.

[33] E. J. Nelson, T. Kendelewicz, P. Liu, and P. Pianetta, Surf. Sci. 380 (1997) 365.

[34] C. M. Garner, I. Lindau, C. Y. Su, P. Pianetta, and W. E. Spicer, Phys. Rev. B 19 (1979) 3944.

[35] T. Kendelewicz, P. Soukiassian, R. S. List, J. C. Woicik, P. Pianetta, I. Lindau, and W. E. Spicer, Phys. Rev. B, 37 (1988) 7115.

Table 7.1. Si 1s XSW data for the (111) Bragg reflection and comparison to simulated XSW data for Si(111) surface structural models

Surface	Reference	D_{111}	f_{111}	Model Escape Depth (Å)
Annealed Na/Si(111)3x1	2 samples	0.965 ± 0.010	0.615 ± 0.037	
Annealed K/Si(111)3x1	2 samples	0.960 ± 0.010	0.576 ± 0.035	
Room-temp. dosed K/Si(111)3x1	3 samples	0.999 ± 0.007	0.526 ± 0.025	
500500 Seiwatz chain	Ref. 24.	0.928	0.598	5.6 Å
		0.948	0.599	7.2 Å
		0.960	0.606	8.8 Å
560560 Honeycomb-chain channel	Ref. 26.	0.919	0.820	5.6 Å
		0.930	0.786	7.2 Å
		0.940	0.764	8.8 Å
567567 Extended Pandey chain	Ref. 24.	0.014	0.525	5.6 Å
		0.013	0.546	7.2 Å
		0.011	0.563	8.8 Å
1x1 Bulk-terminated		0.000	$1/\sqrt{2} = 0.707$	any

Table 7.2. Alkali Adatom X-ray Standing Wave (XSW) Results

Surface	Absorption Yield	Reflection	N	Coherent Distance D_c (plane spacings)	Coherent Fraction f_c
Annealed Na/Si(111)3x1	Na 1s	(111)	3	1.168 ± 0.026	0.908 ± 0.127
Annealed K/Si(111)3x1	K LMM	(111)	5	1.041 ± 0.079	0.346 ± 0.169
Room-temp. Dosed K/Si(111)3x1	K LMM	(111)	3	0.942 ± 0.078	0.565 ± 0.259
Annealed Na/Si(111)3x1	Na 1s	$(11\bar{1})$	5	0.671 ± 0.044	0.692 ± 0.206
Annealed K/Si(111)3x1	K LMM	$(11\bar{1})$	4	0.926 ± 0.051	0.414 ± 0.131
Room-temp. Dosed K/Si(111)3x1 One domain	K LMM	$(11\bar{1})$	1	0.935 ± 0.078	0.315 ± 0.153
Room-temp. Dosed K/Si(111)3x1 Two domains	K LMM	$(11\bar{1})$	2	0.890 ± 0.090	0.428 ± 0.227

Table 7.3. Alkali-Si bond lengths for adatoms in high-symmetry sites on the bulk-terminated Si(111) surface

Surface	D_{111}	Onefold atop T_1 bond length	Threefold filled T_4 bond length	Threefold hollow H_3 bond length	Sum of covalent radii
Annealed Na/Si(111) 3x1	1.168 ± 0.026	3.27 ± 0.08 Å	3.95 ± 0.07 Å	3.95 ± 0.07 Å	2.70 Å
Annealed Na/Si(111) 3x1	0.168 ± 0.026	0.13 ± 0.08 Å	0.92 ± 0.08 Å	2.22 ± 0.01 Å	2.70 Å
Annealed K/Si(111) 3x1	1.041 ± 0.079	2.87 ± 0.25 Å	3.62 ± 0.20 Å	3.62 ± 0.20 Å	3.20 Å
Room-temp. Dosed K/Si(111) 3x1	0.942 ± 0.078	2.56 ± 0.24 Å	3.34 ± 0.24 Å	3.39 ± 0.18 Å	3.20 Å

Table 7.4. Expected values of lateral coherent distance $D_{11\bar{1}}$ for adatoms in high-symmetry sites on the bulk-terminated Si(111) surface with height matching D_{111}

Surface	D_{111}	Measured $D_{11\bar{1}}$	Onefold atop $D_{11\bar{1}}$, T_1	Threefold filled $D_{11\bar{1}}$, T_4	Threefold hollow $D_{11\bar{1}}$, H_3
Annealed Na/Si(111) 3x1	1.168 ± 0.026	0.671 ± 0.044	0.222 ± 0.009	0.556 ± 0.009	0.889 ± 0.009
Annealed Na/Si(111) 3x1	0.168 ± 0.026	0.671 ± 0.044	0.889 ± 0.009	0.222 ± 0.009	0.556 ± 0.009
Annealed K/Si(111) 3x1	1.041 ± 0.079	0.926 ± 0.051	0.180 ± 0.017	0.514 ± 0.017	0.847 ± 0.017
Room-temp. Dosed K/Si(111) 3x1	0.942 ± 0.078	0.916 ± 0.059	0.147 ± 0.020	0.481 ± 0.020	0.814 ± 0.020

Table 7.5. Calculated $D_{11\bar{1}}$ and $f_{11\bar{1}}$ for "500500" and "560560" Two-Site, Three-Domain Models of the Annealed Na/Si(111)3x1 Surface, as a Function of Domain and Site Population

Model	% of Signal from Site L	% of Signal from horiz. domain	$D_{11\bar{1}}$	$f_{11\bar{1}}$
Measured value			0.671 ± 0.044	0.692 ± 0.206
500500 Sites L1&R1 alternate R2&L2	50%	33.3%	0.72	0.50
	50%	40%	0.73	0.52
	50%	50%	0.73	0.56
	50%	60%	0.73	0.60
	60%	33%	0.67	0.50
	60%	40%	0.67	0.53
	60%	**50%**	**0.68**	**0.58**
	60%	60%	0.69	0.62
560560 Sites L&R	50%	33.3%	0.71	0.48
	50%	40%	0.71	0.50
	50%	50%	0.70	0.54
	50%	60%	0.69	0.58
	40%	33%	0.66	0.52
	40%	40%	0.66	0.54
	40%	**50%**	**0.66**	**0.58**
	40%	60%	0.65	0.62

Table 7.6. Calculated $D_{11\bar{1}}$ and $f_{11\bar{1}}$ for "560560" Single Site, Three-Domain Model of the Annealed K/Si(111)3x1 Surface

Model	% of Signal from Site L2	% of Signal from horiz. domain	$D_{11\bar{1}}$	$f_{11\bar{1}}$
Measured value			0.926 ± 0.051	0.414 ± 0.131
560560 Site L2	100%	33.3%	0.90	0.48

Table 7.7. Calculated $D_{11\bar{1}}$ and $f_{11\bar{1}}$ for "567567" Two-Site, Three-Domain Models of the Room-Temperature Dosed K/Si(111)3x1 Surface, as a Function of Domain and Site Population

Model	K coverage (monolayers)	% of Signal from Site L	% of Signal from horiz. domain	$D_{11\bar{1}}$	$f_{11\bar{1}}$
Measured value, One-domain	0.50 ± 0.10 ML	66.7% +16.7/ -11.2 %	100%	0.935 ± 0.078	0.315 ± 0.153
Measured value, Two-domain	0.62 ± 0.12 ML	53.8 % +12.9 / -8.8 %	~50%	0.890 ± 0.090	0.428 ± 0.227
567567 Sites L&R	**0.5**	**66.7%**	**100%**	**0.92**	**0.33**
	0.6	55.6%	100%	0.90	0.11
	0.67	50%	100%	0.67	0.00
	0.5	66.7%	50%	0.86	0.56
	0.6	**55.6%**	**50%**	**0.87**	**0.45**
	0.67	50%	50%	0.88	0.39

Figure 7.1(a). Three proposed structural models of the *M*/Si(111)3x1 surface. Top (111) plane view and side $(1\bar{1}0)$ plane view of the (a) 500500 "Seiwatz chain" model. Possible adsorption sites for Na and K are shown.

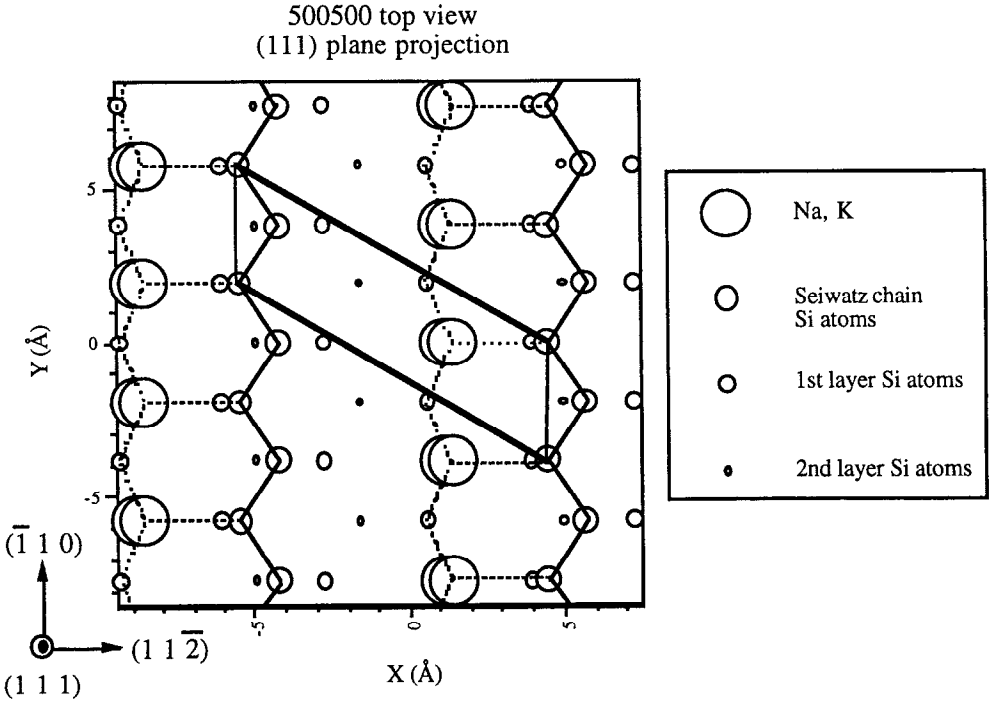

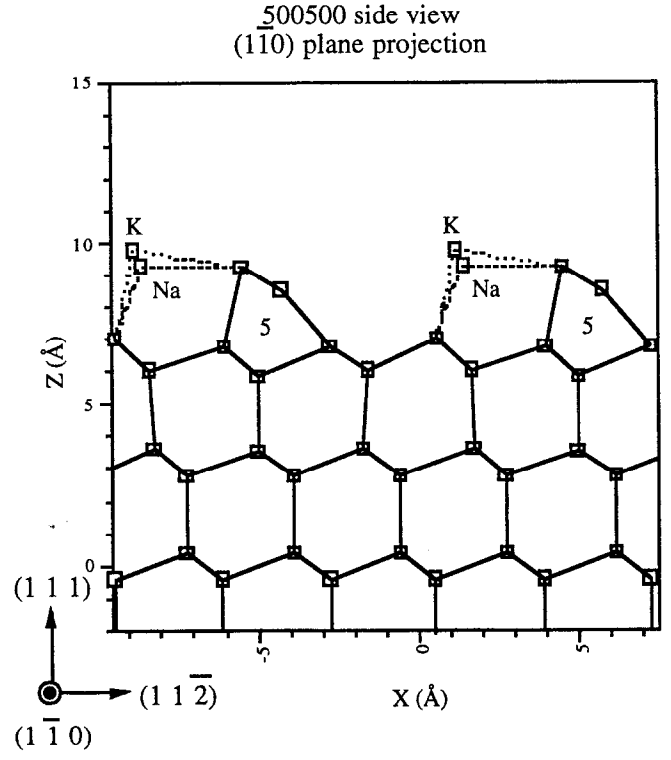

Figure 7.1(b). Three proposed structural models of the *M*/Si(111)3x1 surface. Top (111) plane view and side (1$\bar{1}$0) plane view of the (b) 560560 "Honeycomb-chain channel" model. Possible adsorption sites for Na and K are shown.

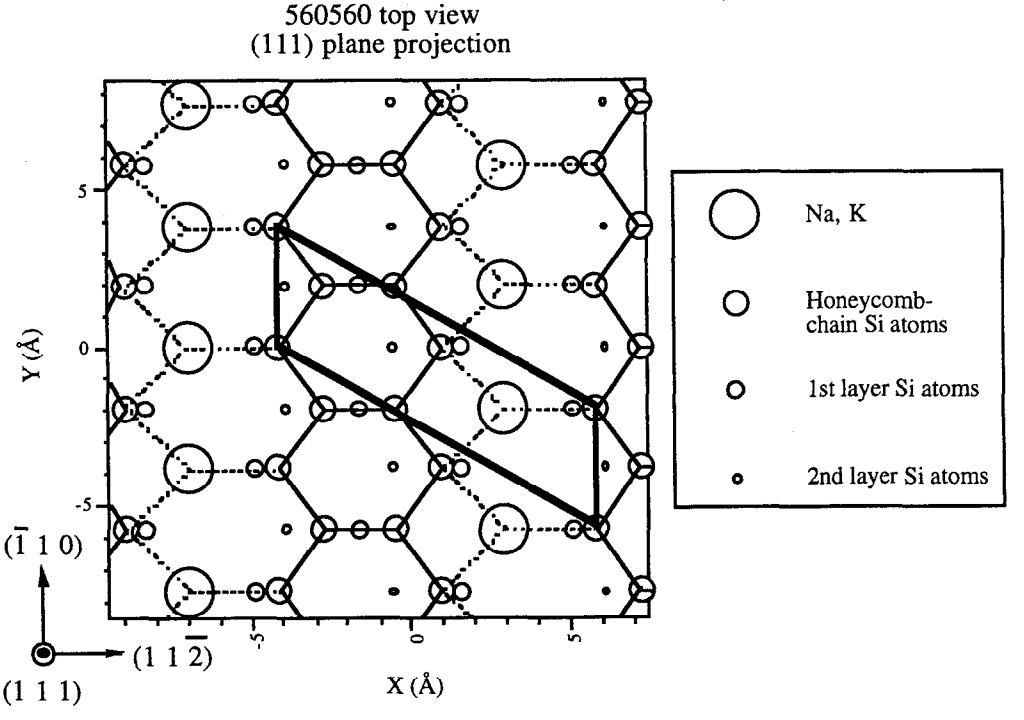

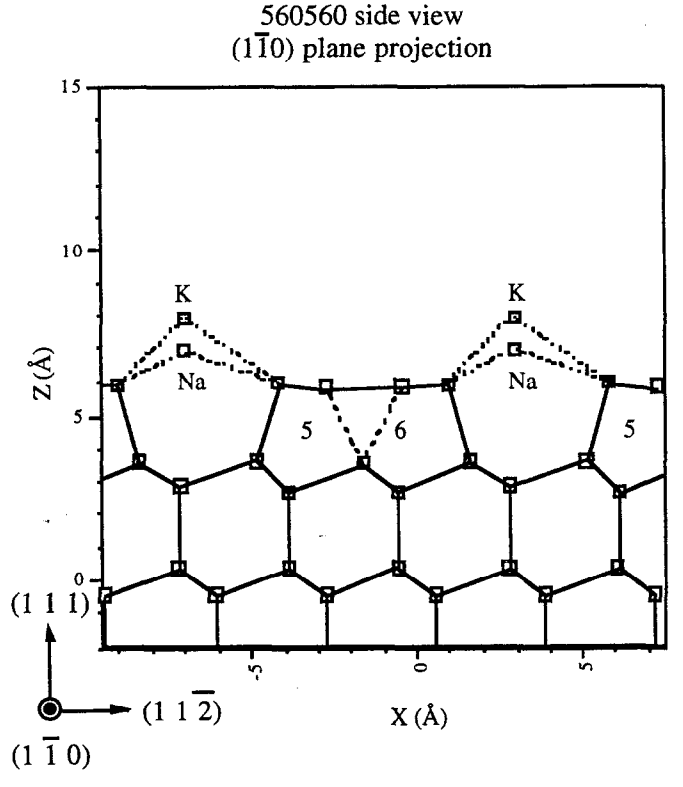

Figure 7.1(c). Three proposed structural models of the *M*/Si(111)3x1 surface. Top (111) plane view and side ($1\bar{1}0$) plane view of the (c) 567567 "Extended Pandey chain" model. Possible adsorption sites for Na and K are shown.

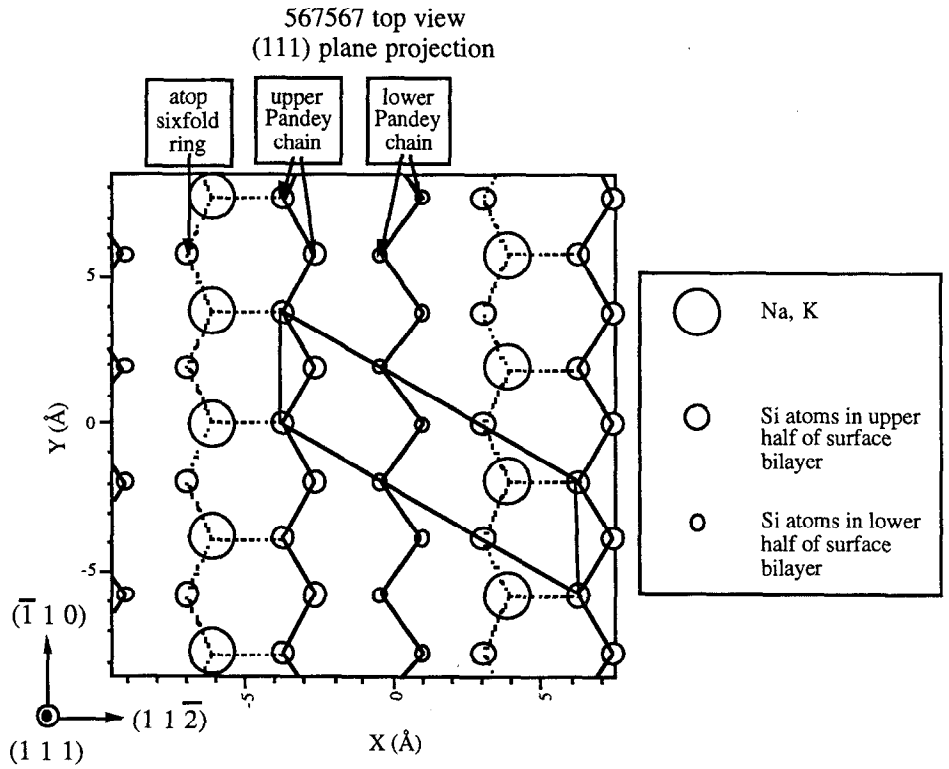

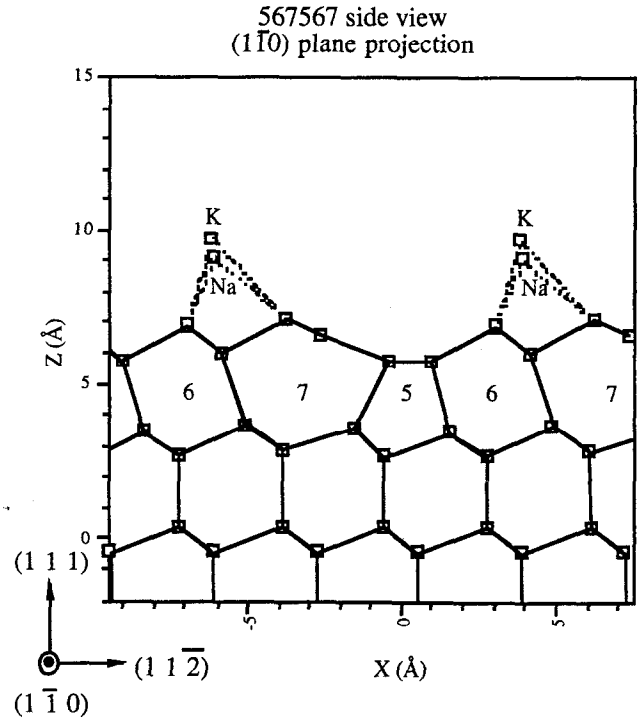

Figure 7.2. Photographs of the annealed Na/Si(111)3x1 LEED pattern for two different samples. (a) three equal domains (seen for both annealed Na/Si(111)3x1 and annealed K/Si(111)3x1) (b) stronger intensity in the horizontal domain (seen for annealed Na/Si(111)3x1 but NOT for annealed K/Si(111)3x1).

Annealed 3-domain AM/Si(111)3x1 Surfaces

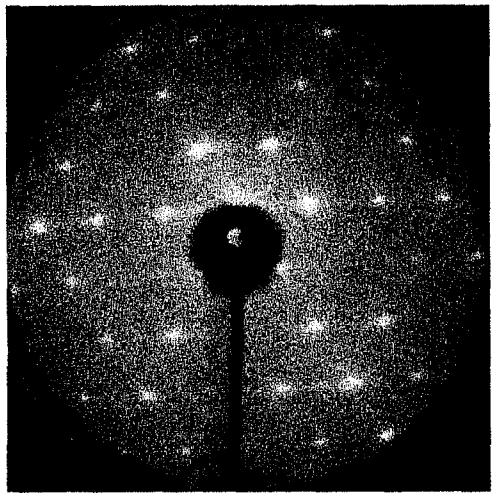

(a) Three equal domains (Both Na and K surfaces)

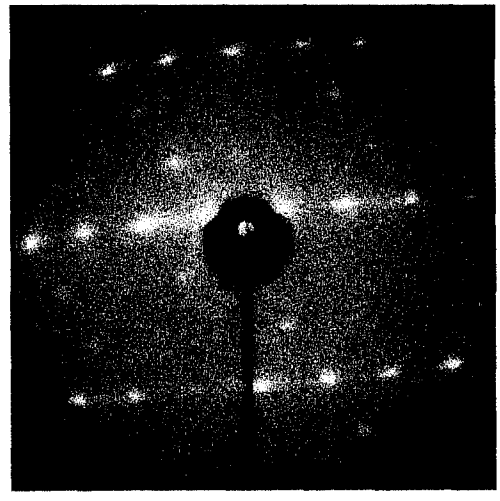

(b) Stronger horizontal domain (Na surface only)

Figure 7.3. Photographs of LEED patterns for two different samples of the room-temperature dosed K/Si(111)3x1 interface. (a) single-domain pattern (b) two-domain pattern. The direction of the 3x1 spots is the same as the direction of the 2x1 spots on the clean Si(111)2x1 surface before dosing.

Room-Temperature Dosed K/Si(111)3x1 Surfaces

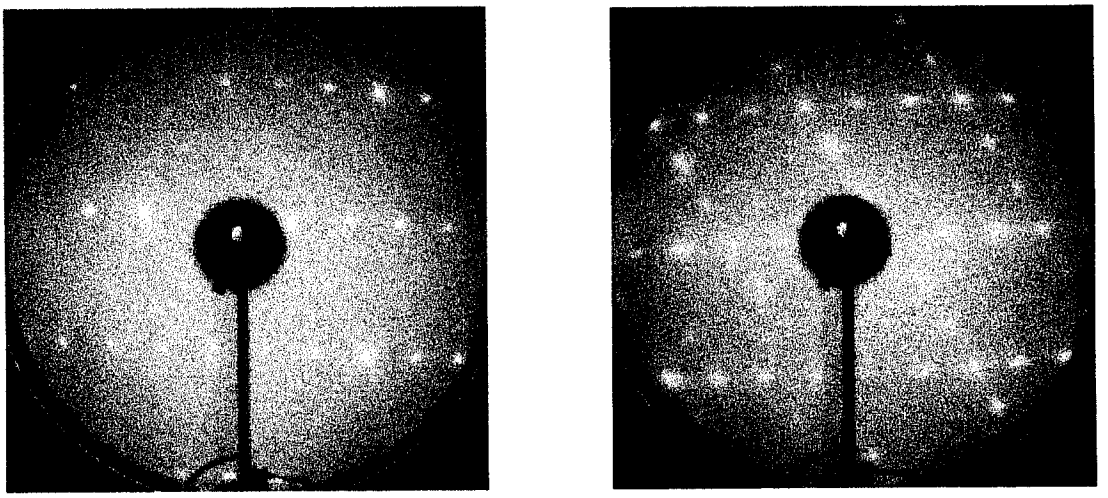

(a) Single-domain **(b) Two-domain**

Figure 7.4(a). (a) Na 2p core-level photoemission spectra comparing the Na coverages for the saturation-dosed (1 ML Na) Na/Si(111)1x1 and annealed Na/Si(111)3x1 interfaces. Photon energy 77 eV.

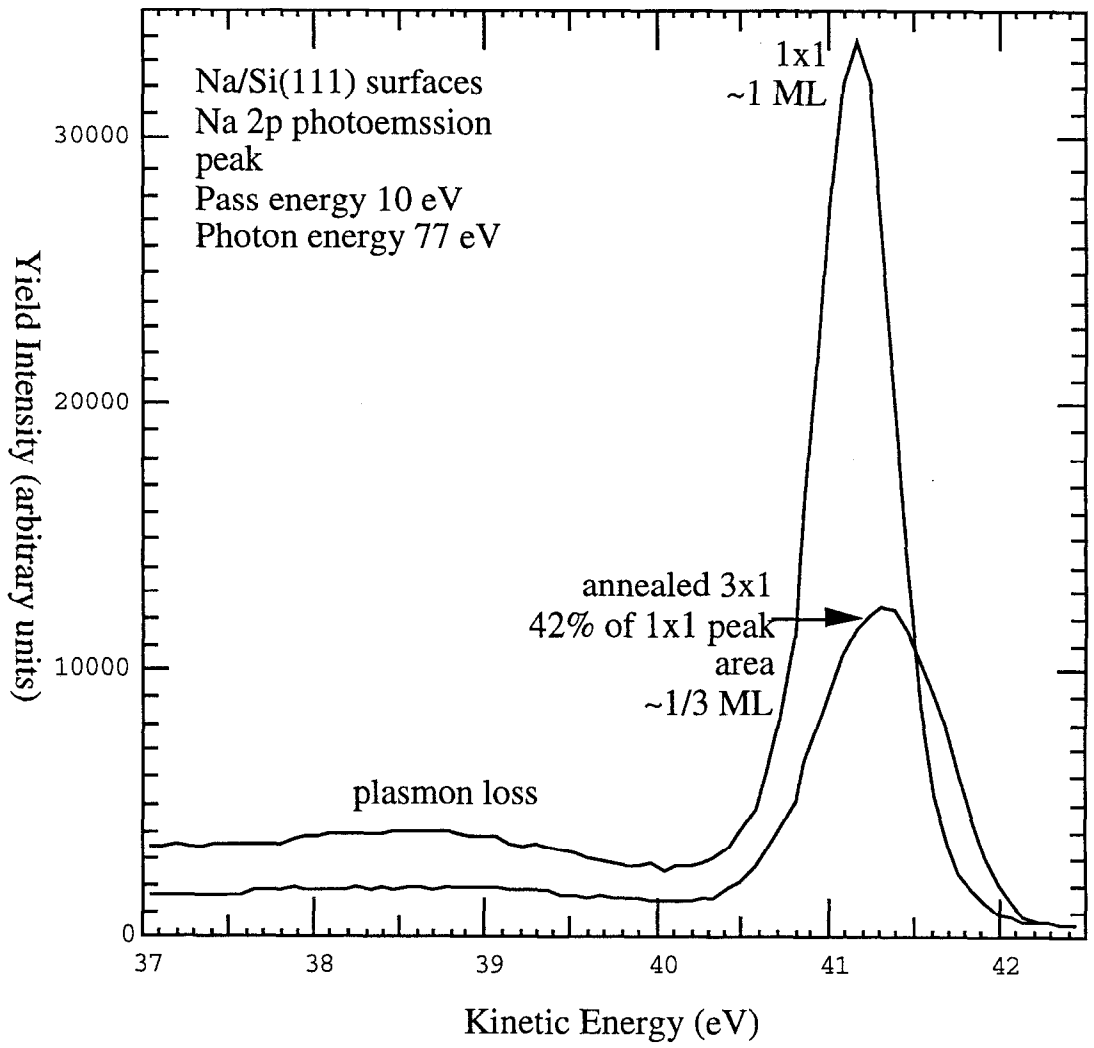

Figure 7.4(b). (b) Na 2p core-level photoemission spectra comparing the Na coverages for the saturation-dosed (1 ML Na) Na/Si(111)1x1 and annealed Na/Si(111)3x1 interfaces. Photon energy 77 eV. Spectra are expanded vertically to match peak height, in order to compare peak shapes.

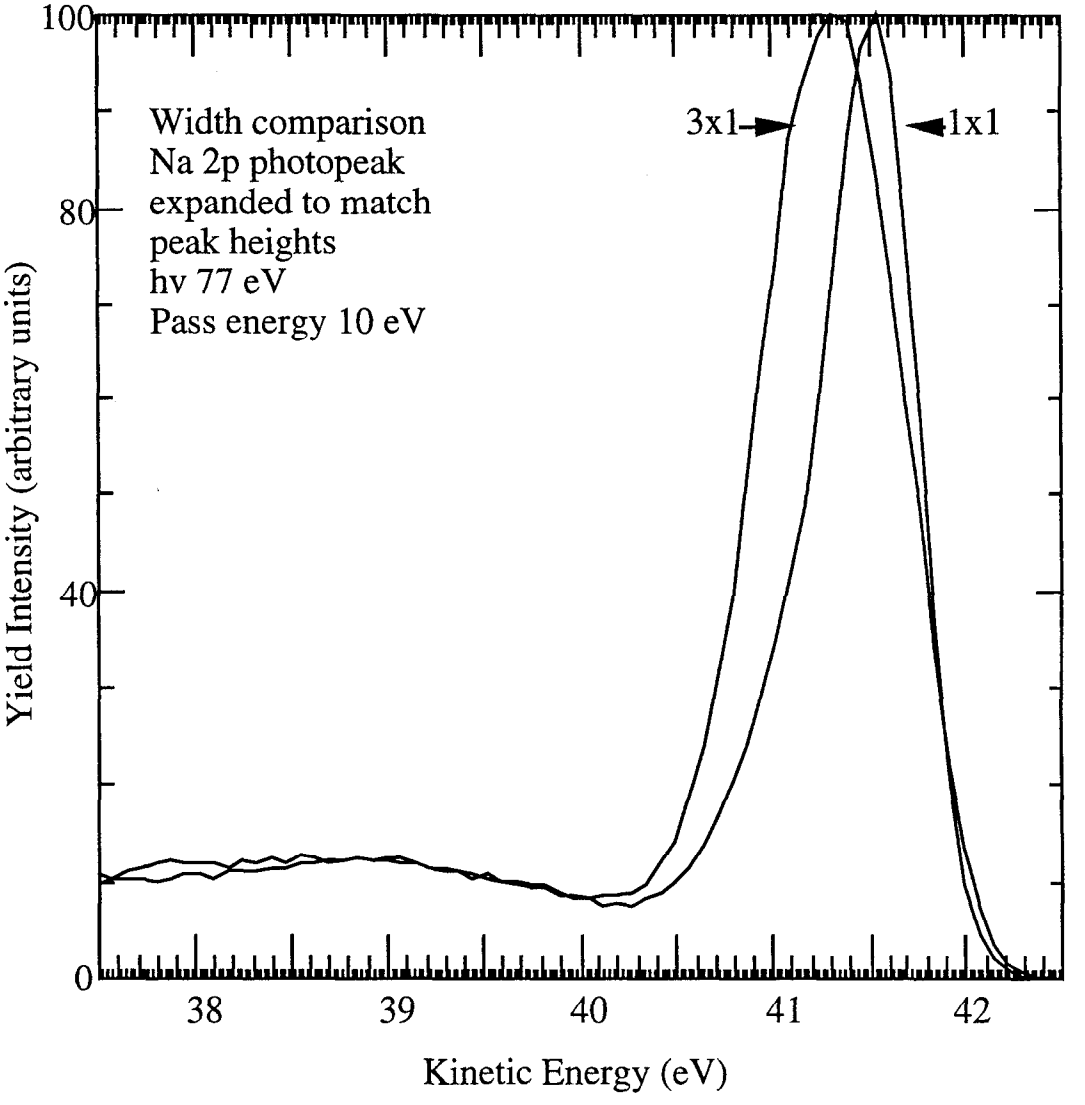

Figure 7.4(c). (c) K 3p core-level photoemission spectra comparing the K coverages for the saturation-dosed (~1 ML K) K/Si(111)1x1, annealed K/Si(111)3x1 and room-temperature dosed K/Si(111)3x1 interfaces. Photon energy 65 eV.

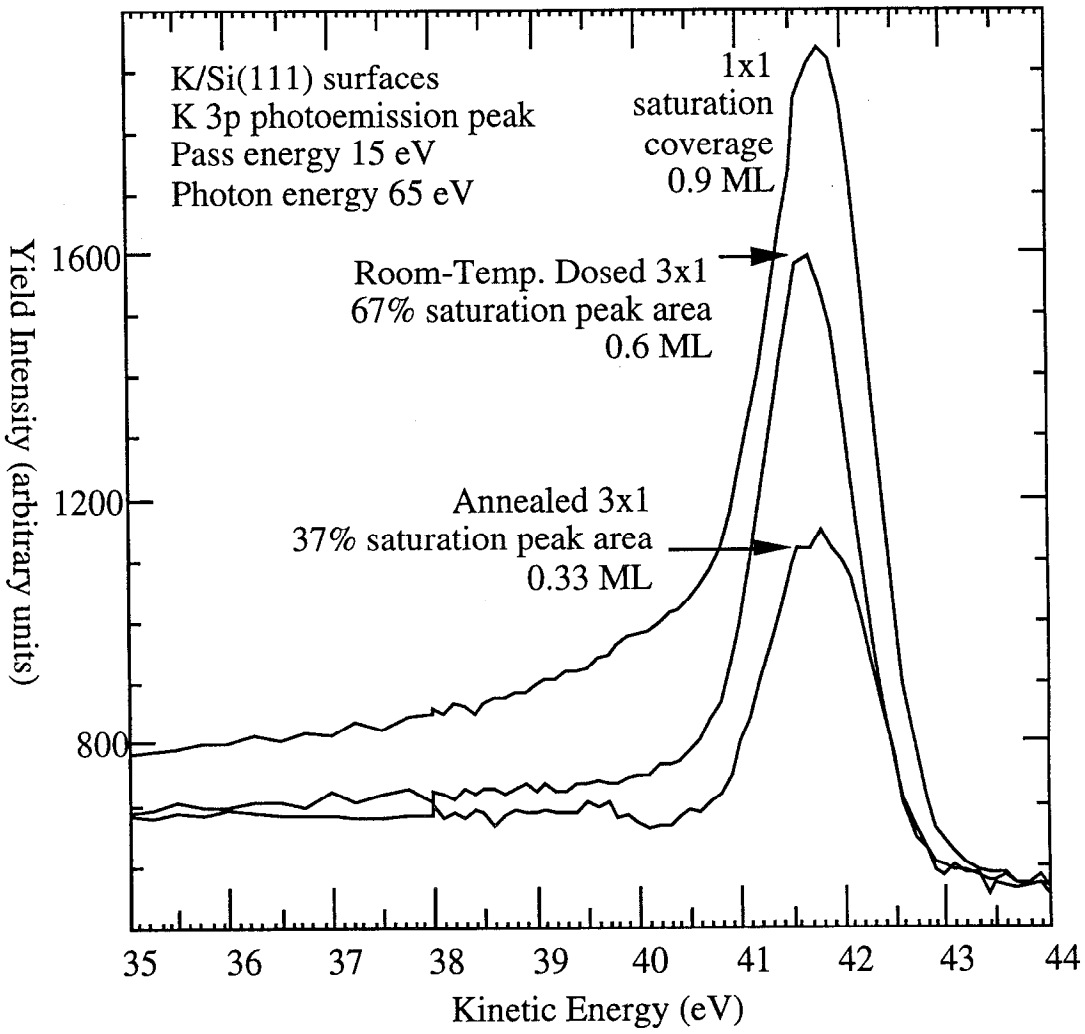

Figure 7.5(a). Effect of rotating a 3x1 geometry into the three equivalent domains on the $(11\bar{1})$ coherent distance. Top (111) plane view of a generic Si(111)3x1 surface. The shaded bar represents the center of the chain structure, with alkali adsorption sites A1 and B1. Rotating the system by 120° or -120° gives the geometries with sites (A2, B2) and (A3,B3). The distance of the adatoms from the $(11\bar{1})$ planes is the same for all three domains for site A (constructive case), while the distance in domain 1 differs from that in domains 2 and 3 for site B (destructive case).

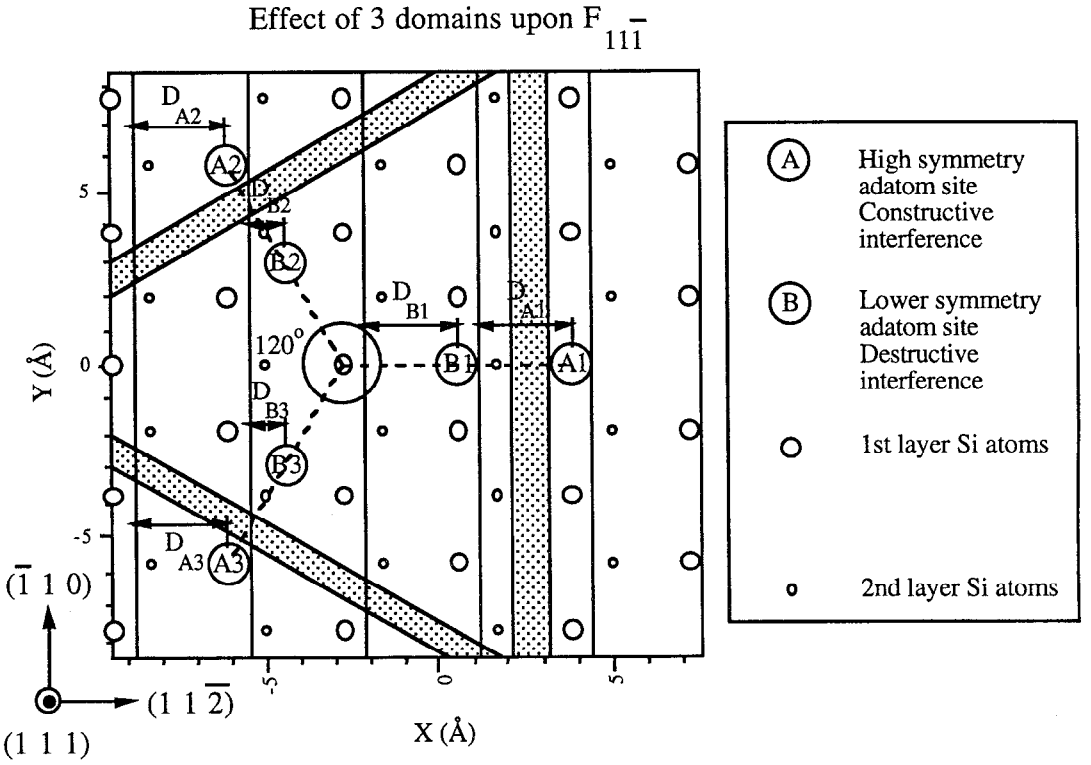

$$D_{A1} = D_{A2} = D_{A3}$$

$$D_{B1} - 0.5 = D_{B2} = D_{B3}$$

Figure 7.5(b). Phasor diagram of $F_{11\bar{1}}$ for the case of constructive interference between the three domains (site A in part (a)).

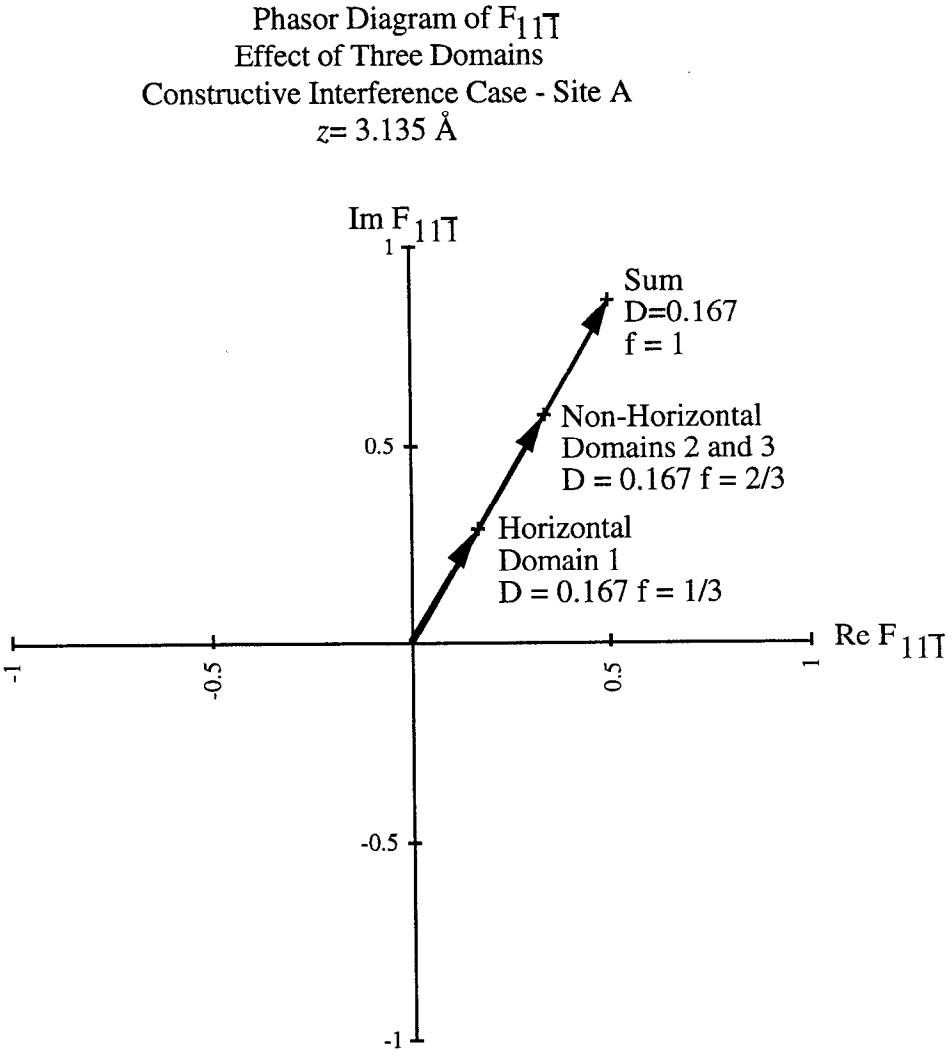

Figure 7.5(c). Phasor diagram of $F_{11\bar{1}}$ for the case of destructive interference between the three domains (site B in part (a)).

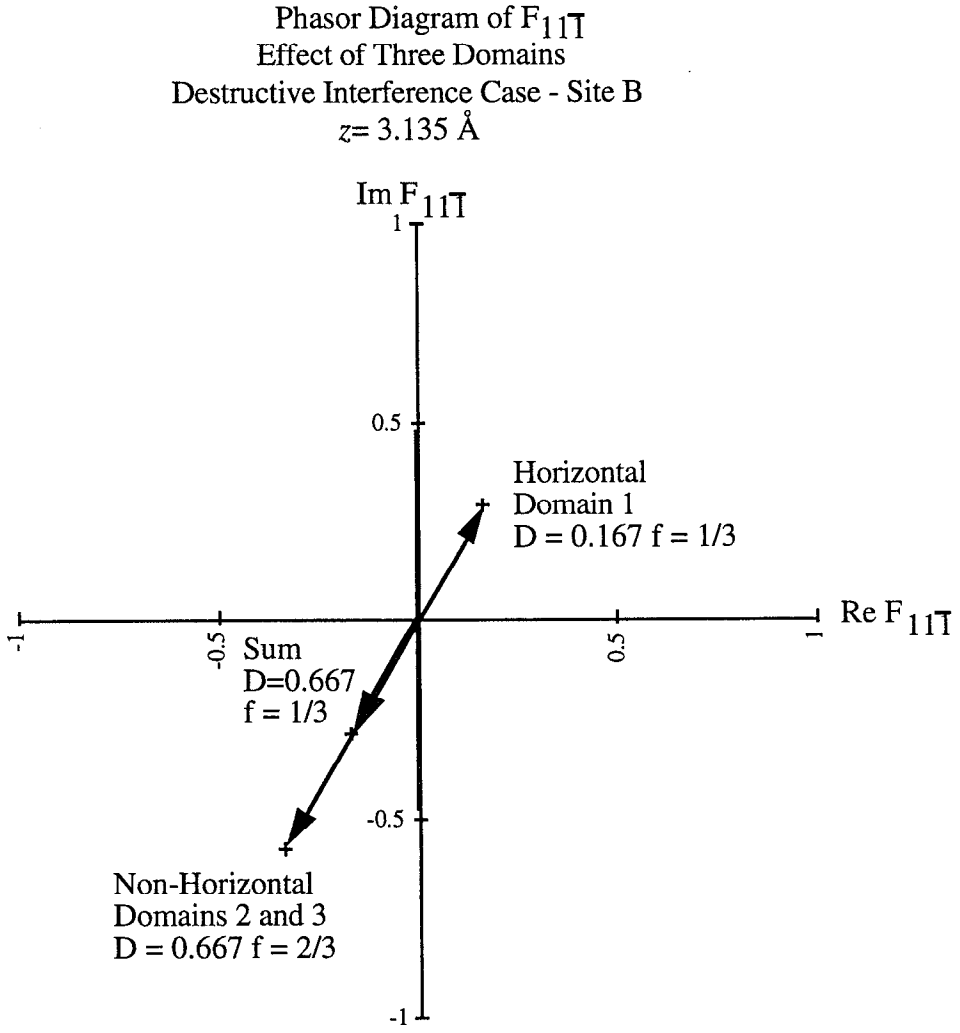

Figure 7.5(d). Phasor diagram tracing out all the possible values of $F_{11\bar{1}}$ assuming a single adsorption site and equal contributions from all three domains, and an adatom height of $D_{111} = 1.04$.

Phasor Diagram of Possible Values of $F_{11\bar{1}}$
For a Single-site, Three-domain Model
With Height $D_{111} = 1.04$

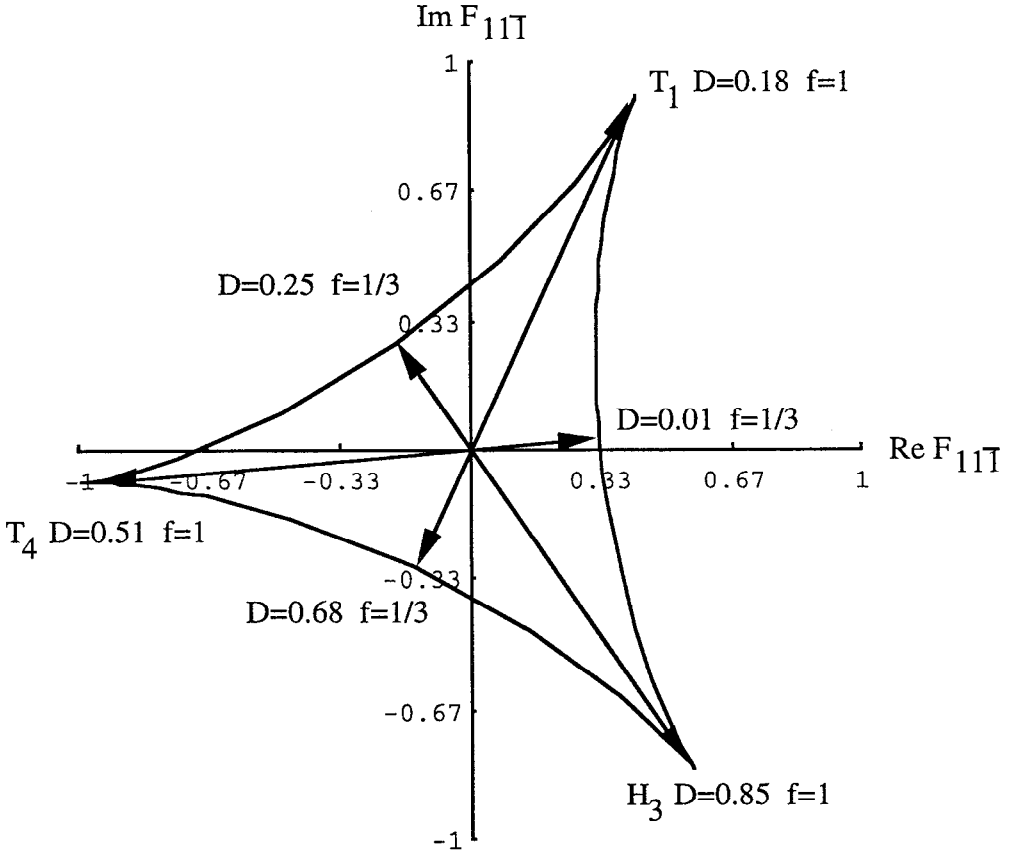

Figure 7.6. Surface-sensitive Si 1s XSW data for the (111) backreflection of Si, for the annealed Na/Si(111)3x1, annealed K/Si(111)3x1, and room-temperature dosed K/Si(111)3x1 interfaces.

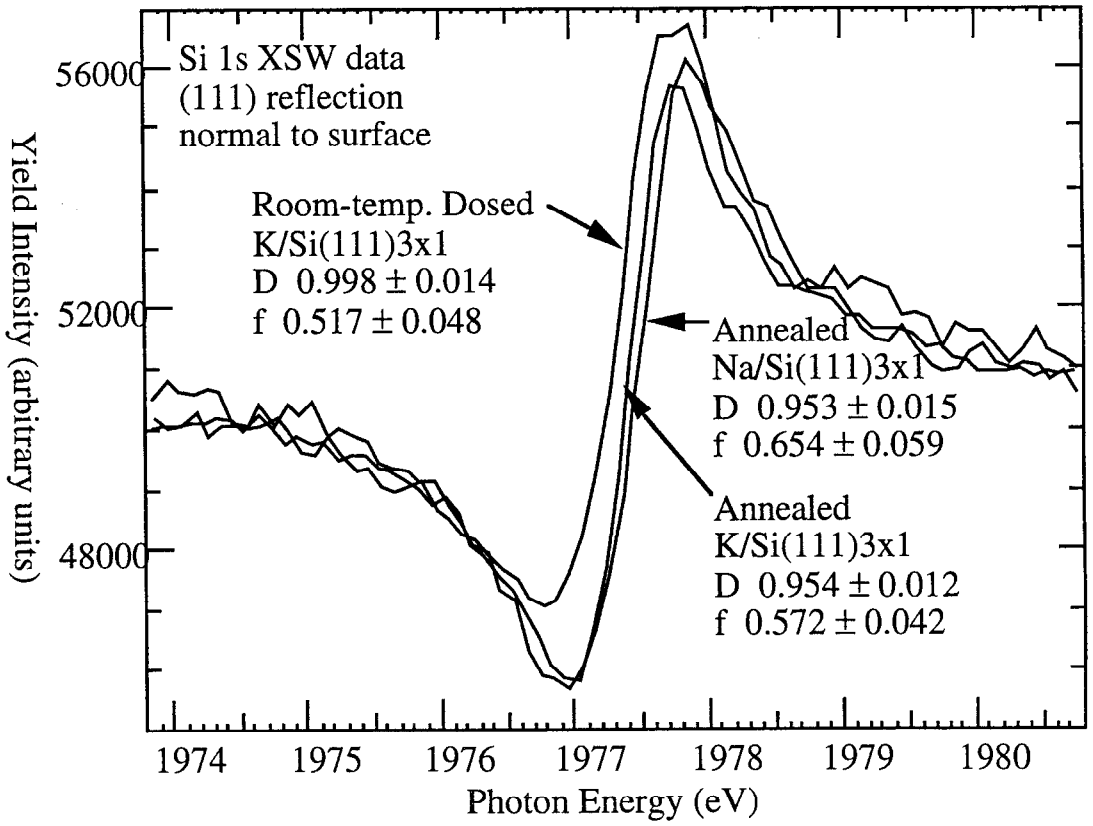

Figure 7.7(a). Alkali adsorbate XSW data for the (111) and $(11\bar{1})$ backreflections of Si for the *M*/Si(111)3x1 interfaces. (a) Annealed Na/Si(111)3x1, (111) reflection. Na 1s photoemission yield.

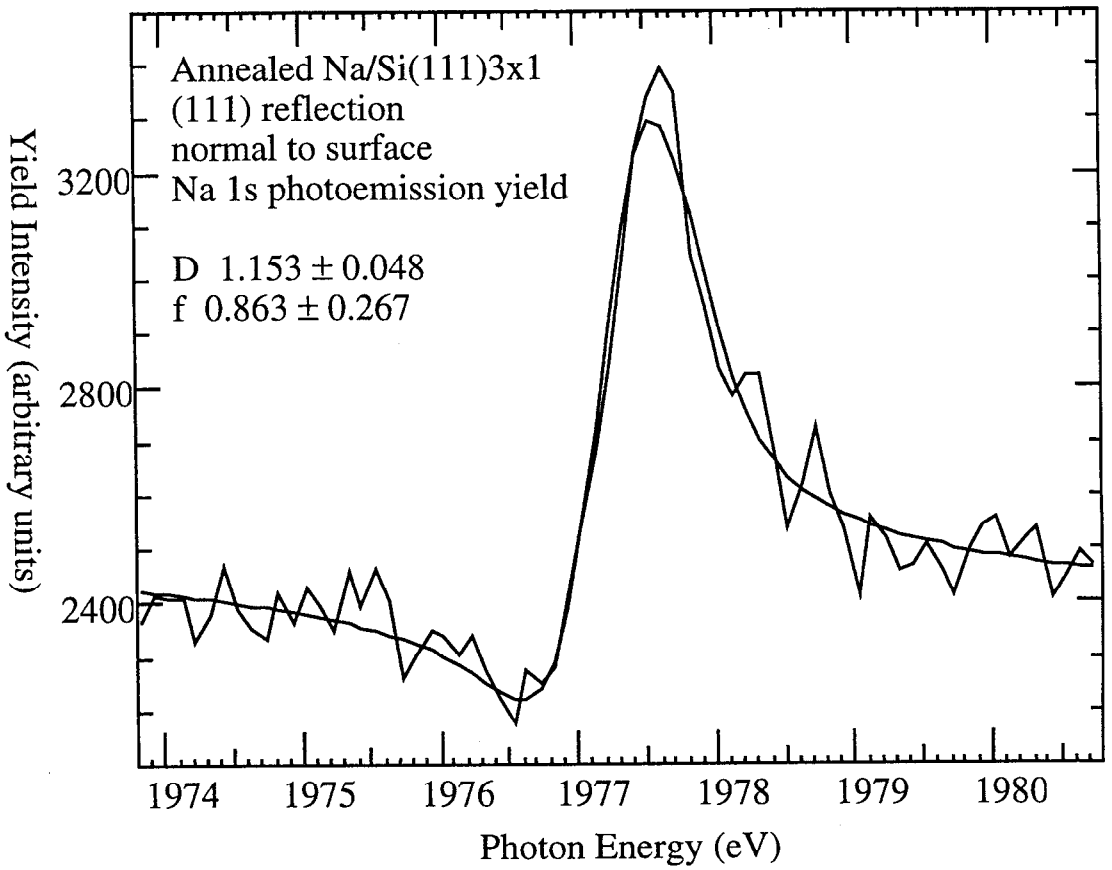

Figure 7.7(b). Alkali adsorbate XSW data for the (111) and (11$\bar{1}$) backreflections of Si for the *M*/Si(111)3x1 interfaces. (b) Annealed Na/Si(111)3x1, (11$\bar{1}$) reflection. Na 1s photoemission yield.

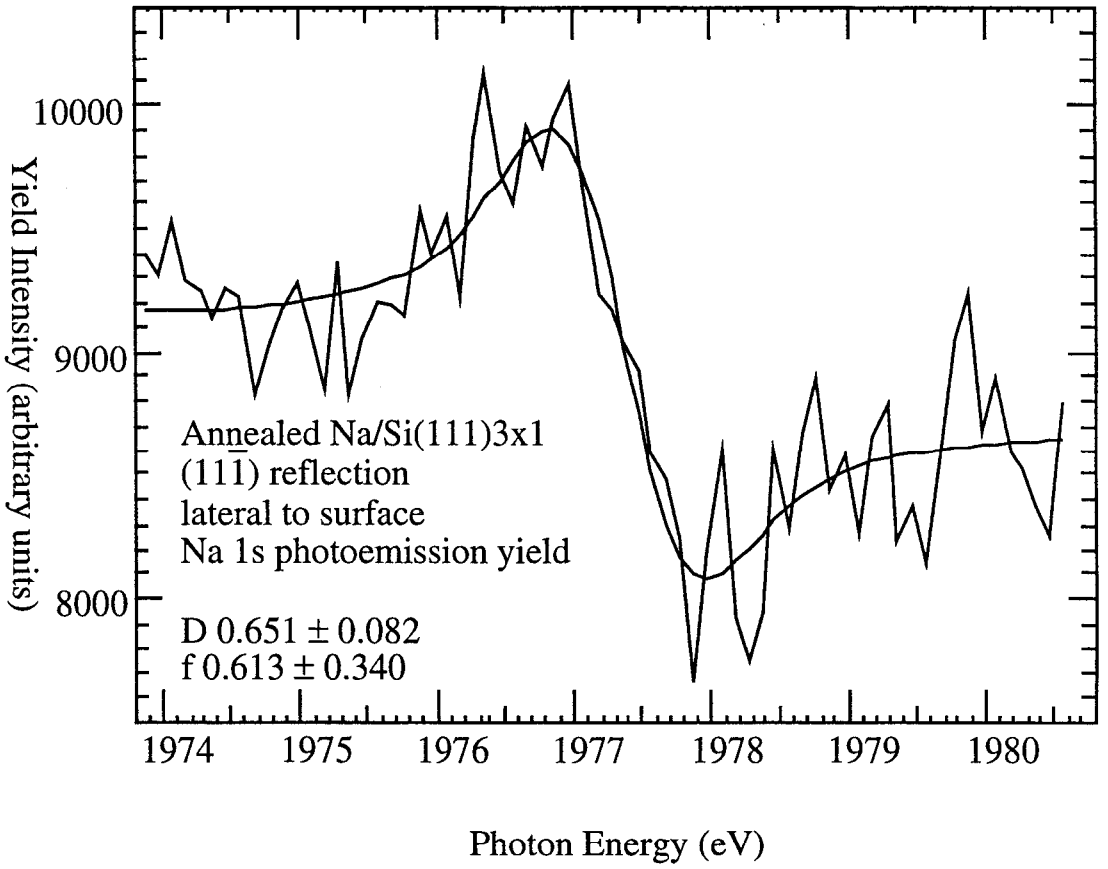

Figure 7.7(c). Alkali adsorbate XSW data for the (111) and (11$\bar{1}$) backreflections of Si for the *M*/Si(111)3x1 interfaces. (c) Annealed K/Si(111)3x1, (111) reflection. K LMM Auger yield.

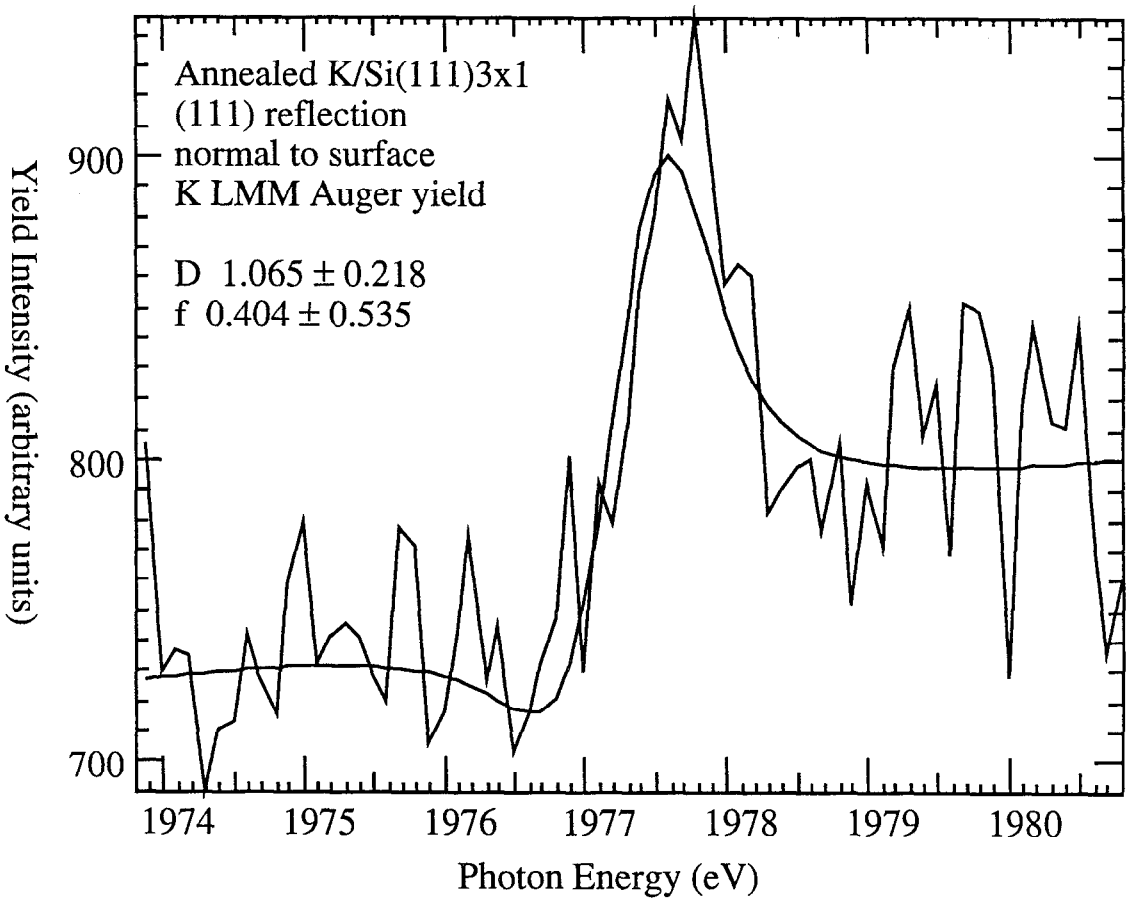

Figure 7.7(d). Alkali adsorbate XSW data for the (111) and (11$\bar{1}$) backreflections of Si for the *M*/Si(111)3x1 interfaces. (d) Annealed K/Si(111)3x1, (11$\bar{1}$) reflection. K LMM Auger yield.

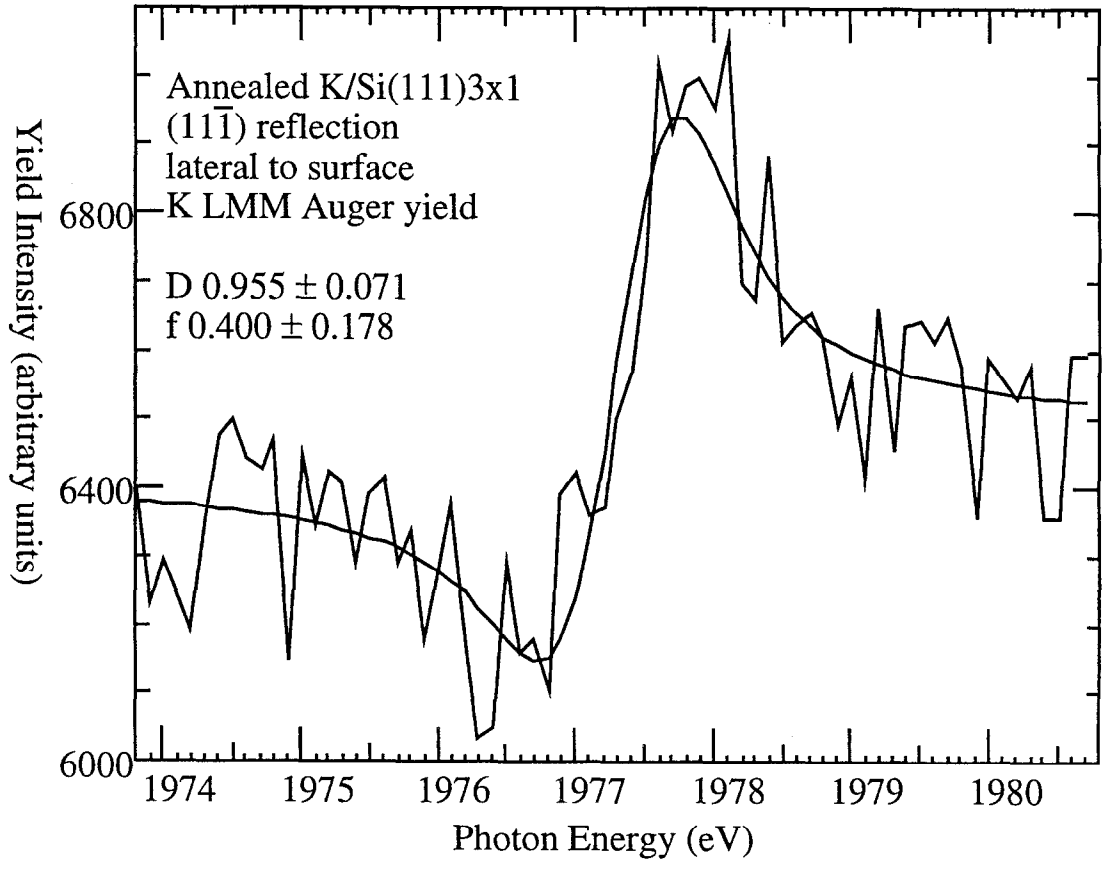

Figure 7.7(e). Alkali adsorbate XSW data for the (111) and (11$\bar{1}$) backreflections of Si for the *M*/Si(111)3x1 interfaces. (e) Room-temperature dosed K/Si(111)3x1, (111) reflection. K LMM Auger yield.

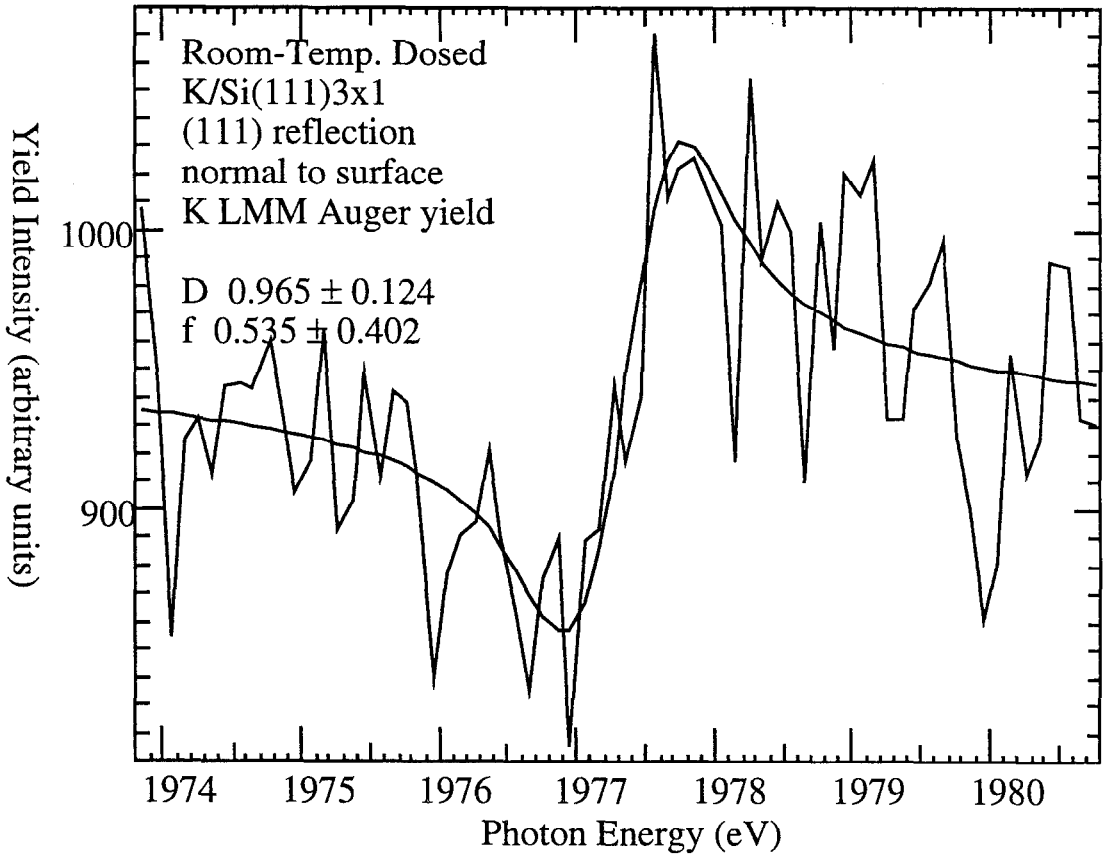

Figure 7.7(f). Alkali adsorbate XSW data for the (111) and (11$\bar{1}$) backreflections of Si for the *M*/Si(111)3x1 interfaces. (f) Room-temperature dosed K/Si(111)3x1, (11$\bar{1}$) reflection, for one-domain and two-domain surfaces. K LMM Auger yield.

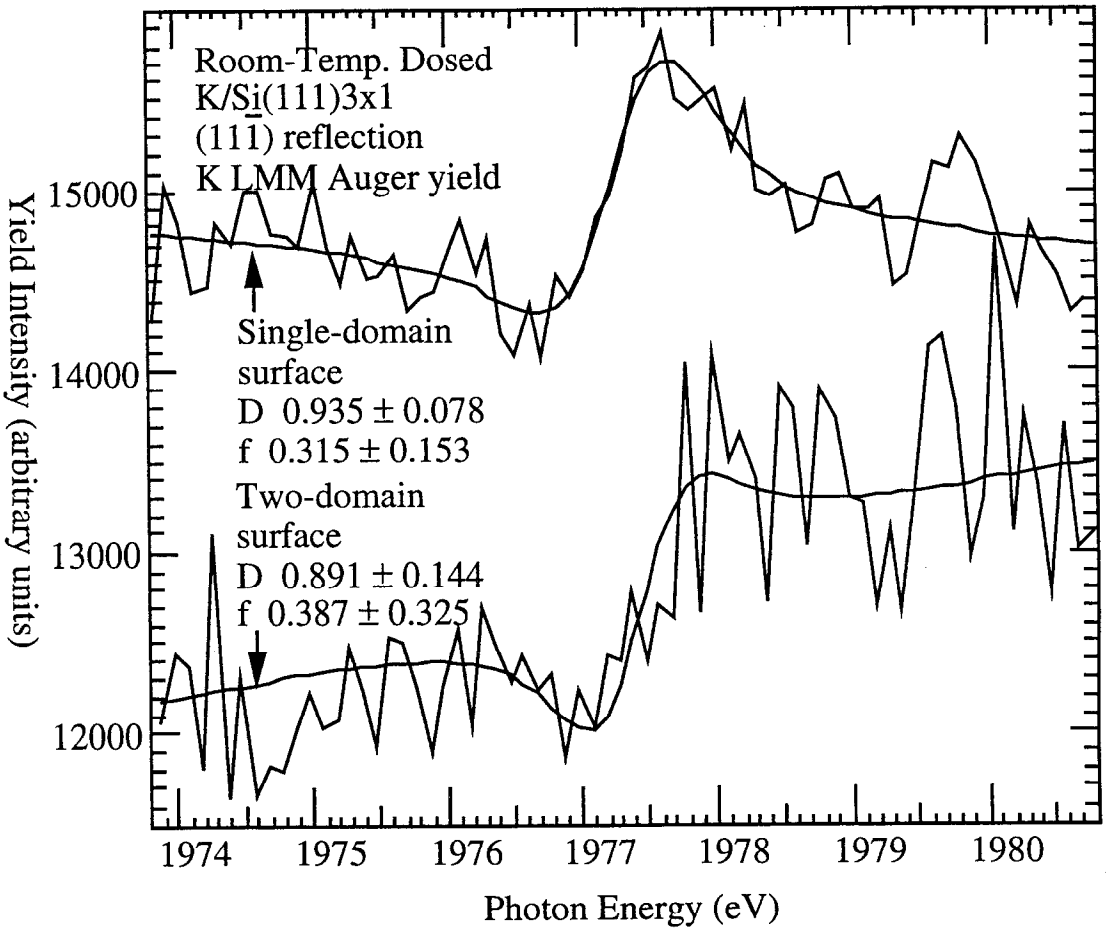

Figure 7.8(a). Our proposed "500500 Seiwatz chain" model of the annealed Na/Si(111)3x1 surface for 1/3 ML Na coverage. (a) Top view ((111) plane projection). Sites L1&L2 have the normal buckling of the surface Seiwatz chain, while the buckling is flipped for sites R1&R2.

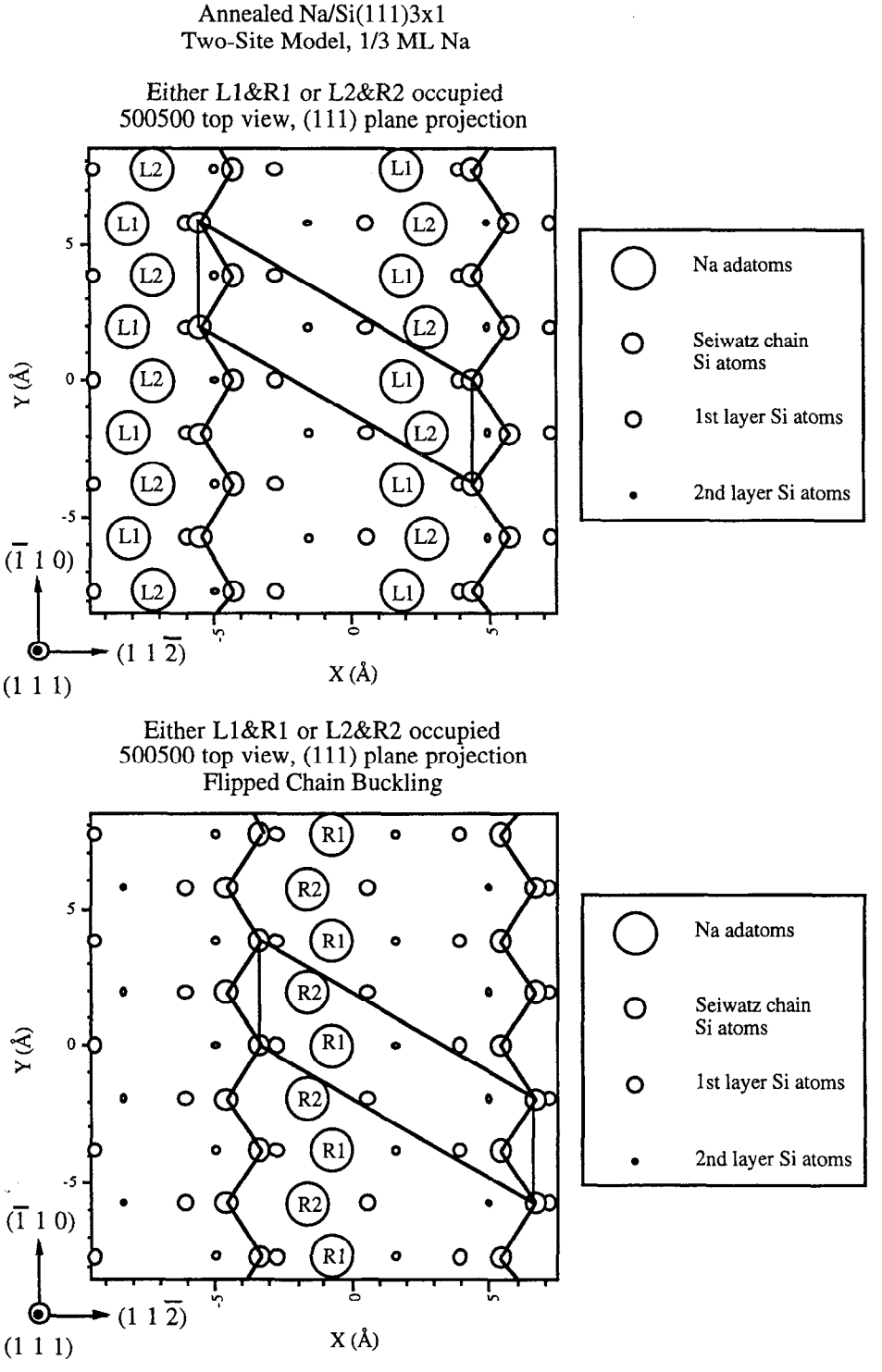

Figure 7.8(b). Our proposed "500500 Seiwatz chain" model of the annealed Na/Si(111)3x1 surface for 1/3 ML Na coverage. (b) Side view ($(1\bar{1}0)$ plane projection). Sites L1&L2 have the normal buckling of the surface Seiwatz chain, while the buckling is flipped for sites R1&R2.

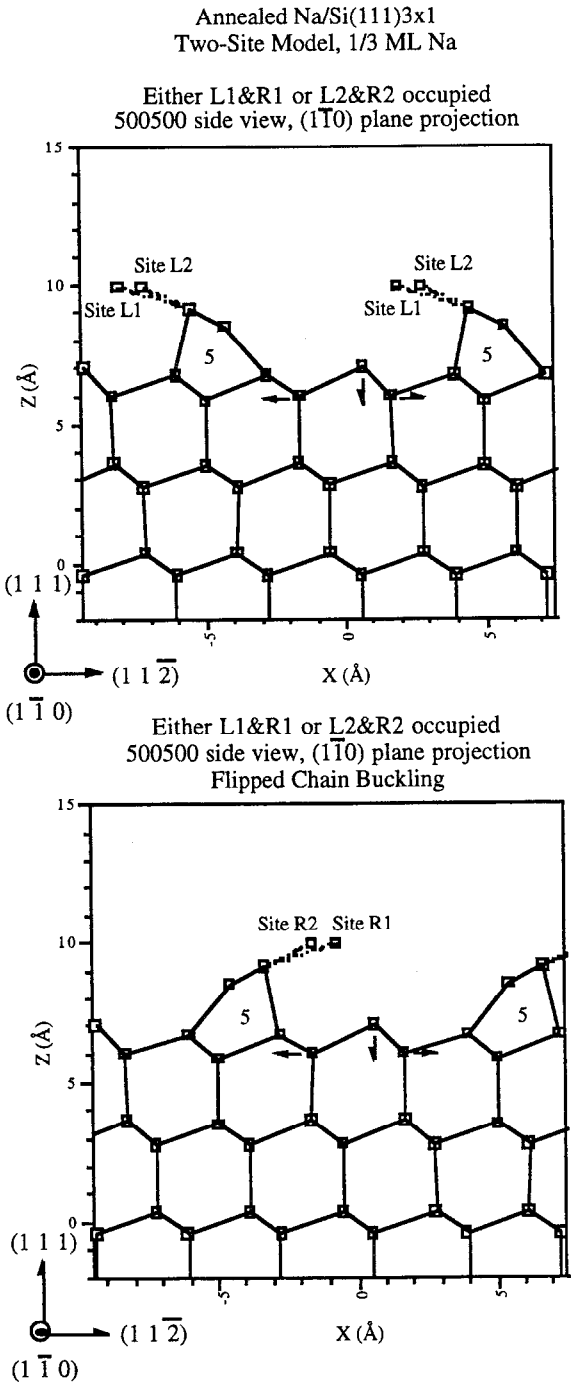

Figure 7.8(c). Our proposed "500500 Seiwatz chain" model of the annealed Na/Si(111)3x1 surface for 1/3 ML Na coverage. (c) Phasor diagram of $F_{11\bar{1}}$ showing the sum of contributions from the two adsorption sites. Pairing L1&R1 or L2&R2 gives the same result. Each site and domain is weighted equally. The shaded area represents the error bars for the measured values of $D_{11\bar{1}}$ and $f_{11\bar{1}}$.

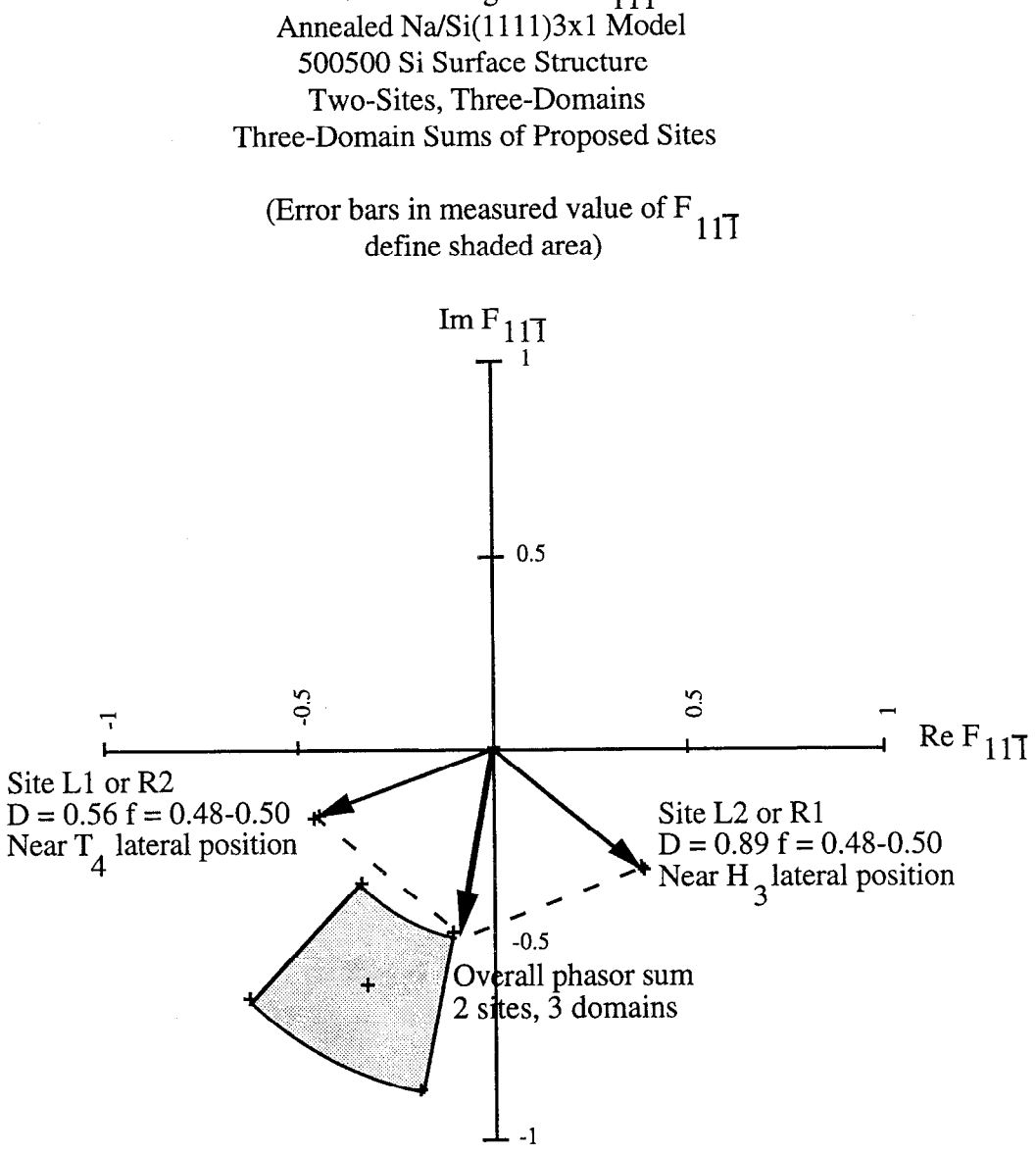

Figure 7.8(d). Our proposed "500500 Seiwatz chain" model of the annealed Na/Si(111)3x1 surface for 1/3 ML Na coverage. (d) Phasor diagram of $F_{11\bar{1}}$ before and after changing the weighting from equal site and domain population. The shaded area represents the error bars for the measured values of $D_{11\bar{1}}$ and $f_{11\bar{1}}$.

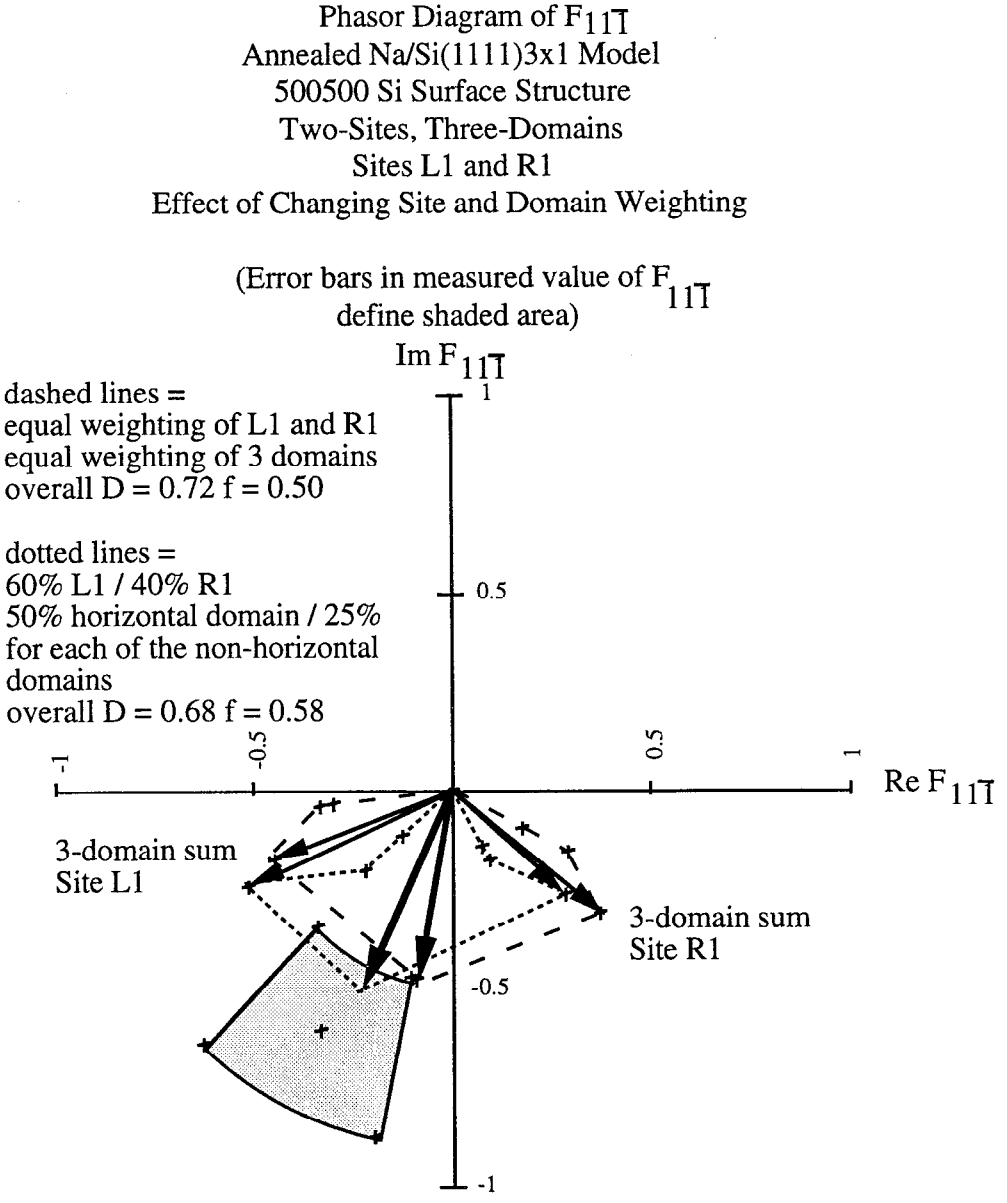

Figure 7.9(a). Our proposed "560560 honeycomb-chain channel" model of the annealed Na/Si(111)3x1 surface for 1/3 ML Na coverage. (a) Top view ((111) plane projection).

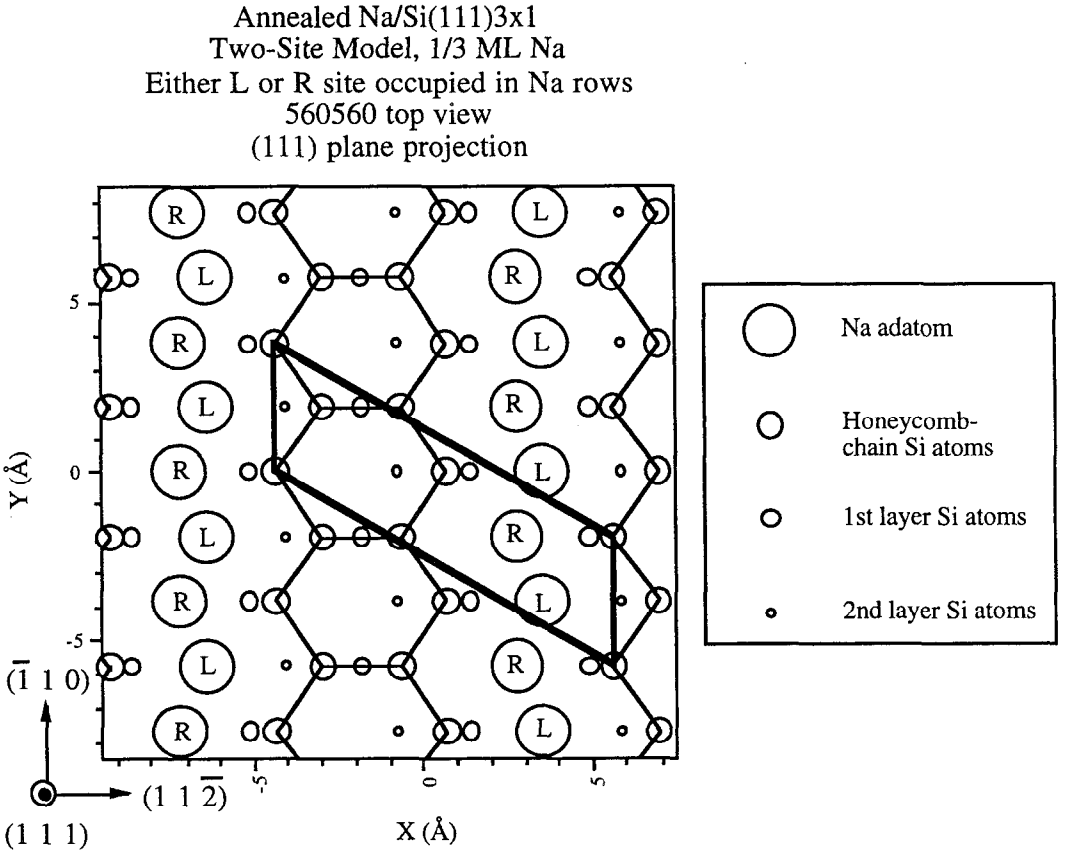

Figure 7.9(b). Our proposed "560560 honeycomb-chain channel" model of the annealed Na/Si(111)3x1 surface for 1/3 ML Na coverage. (b) Side view ($(1\bar{1}0)$ plane projection).

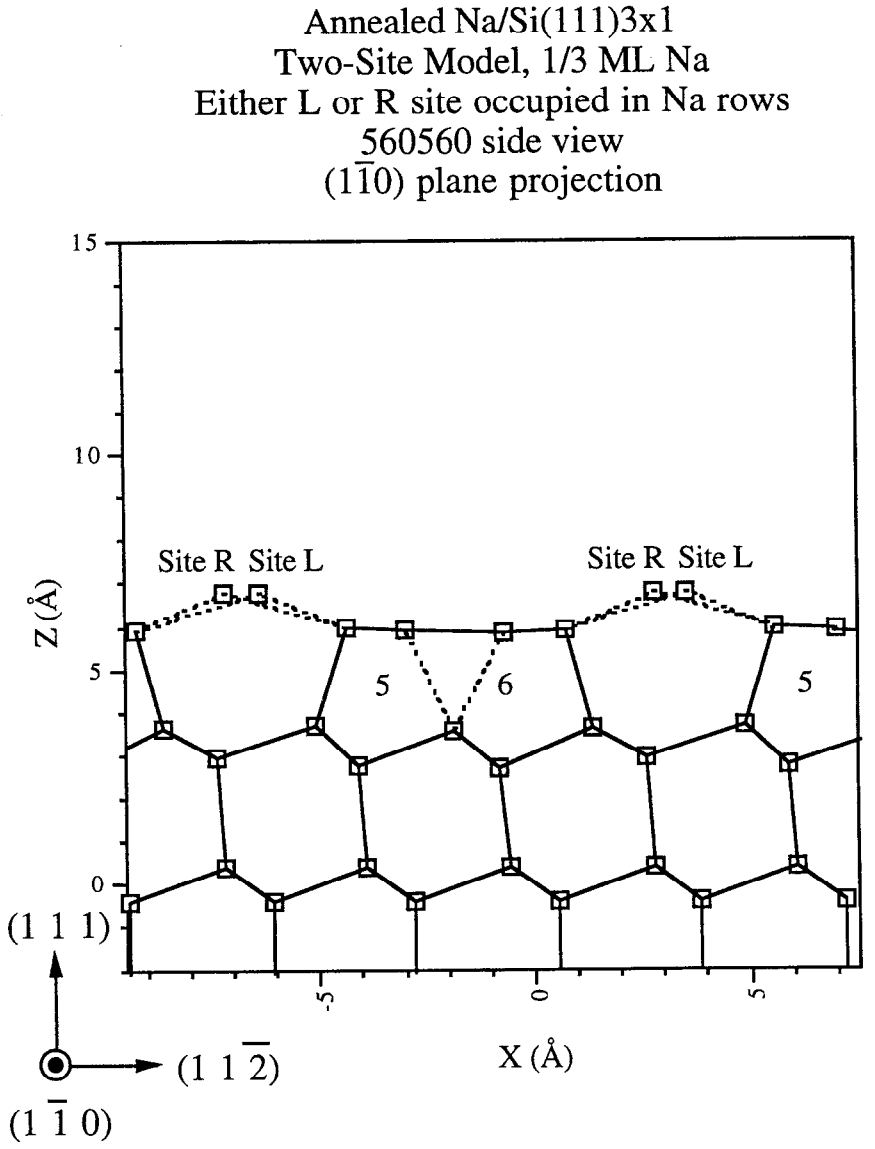

Figure 7.9(c). Our proposed "560560 honeycomb-chain channel" model of the annealed Na/Si(111)3x1 surface for 1/3 ML Na coverage. (c) Phasor diagram of $F_{11\bar{1}}$ showing the sum of contributions from the two adsorption sites L & R. The phasor sum before and after changing the weighting from equal site and domain population is shown. The shaded area represents the error bars for the measured values of $D_{11\bar{1}}$ and $f_{11\bar{1}}$.

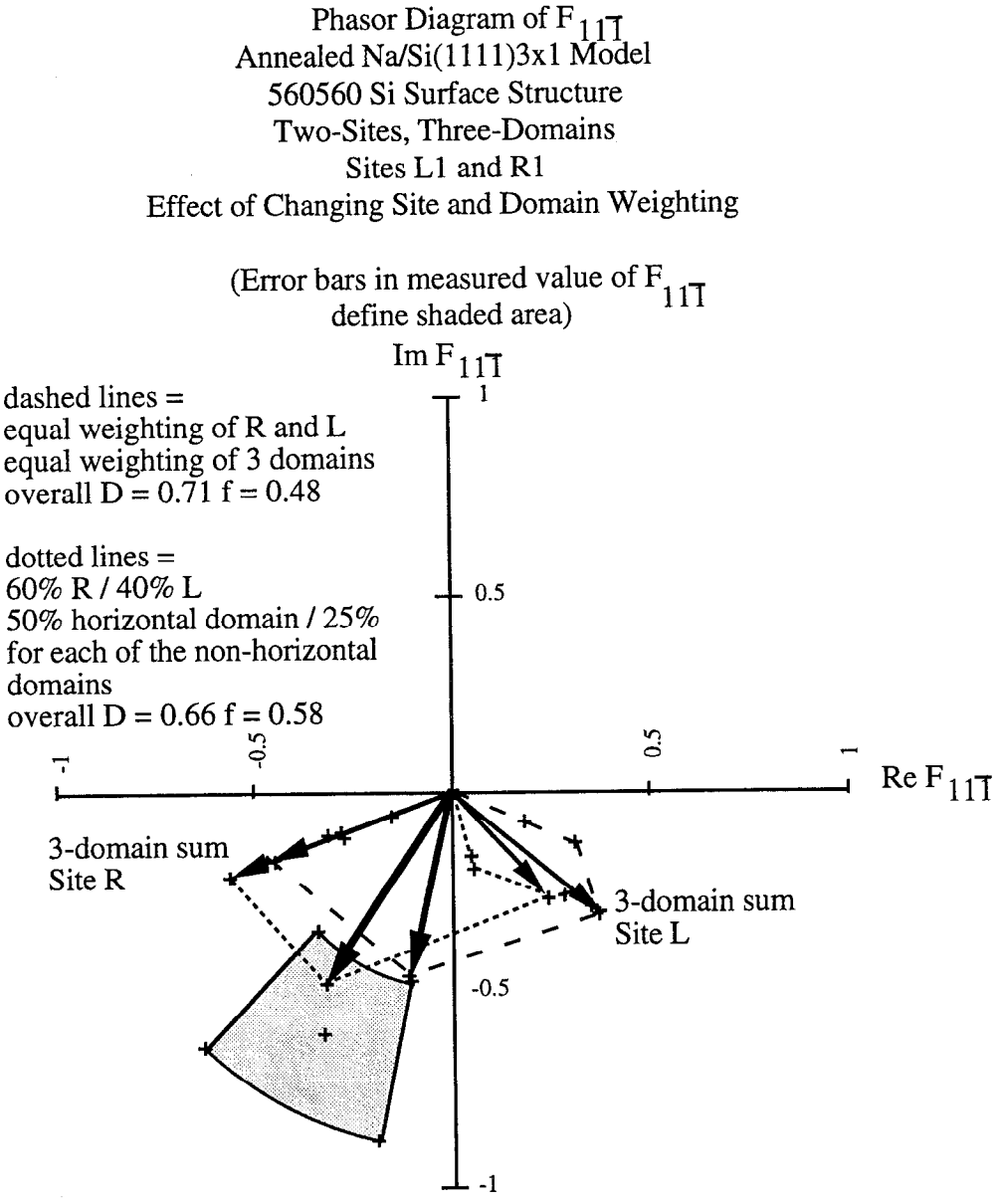

Figure 7.10(a). Our proposed "500500 Seiwatz chain" model of the annealed K/Si(111)3x1 surface for 1/3 ML K coverage. (a) Top view ((111) plane projection).

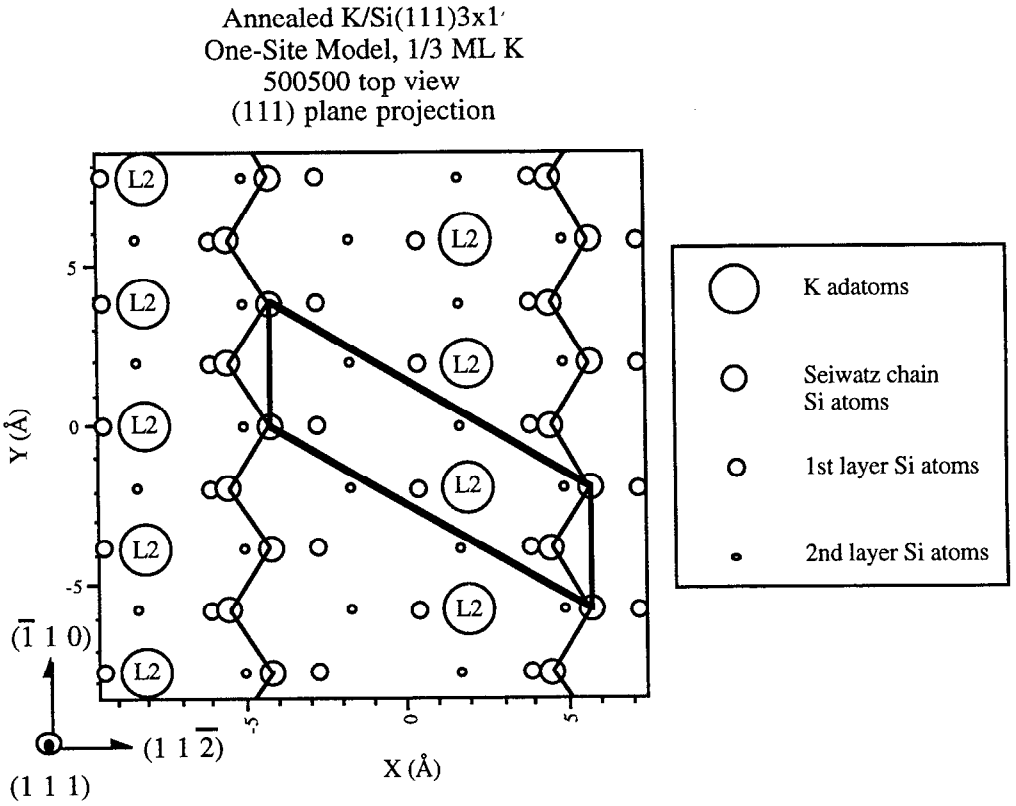

Figure 7.10(b). Our proposed "500500 Seiwatz chain" model of the annealed K/Si(111)3x1 surface for 1/3 ML K coverage. (b) Side view ($(1\bar{1}0)$ plane projection).

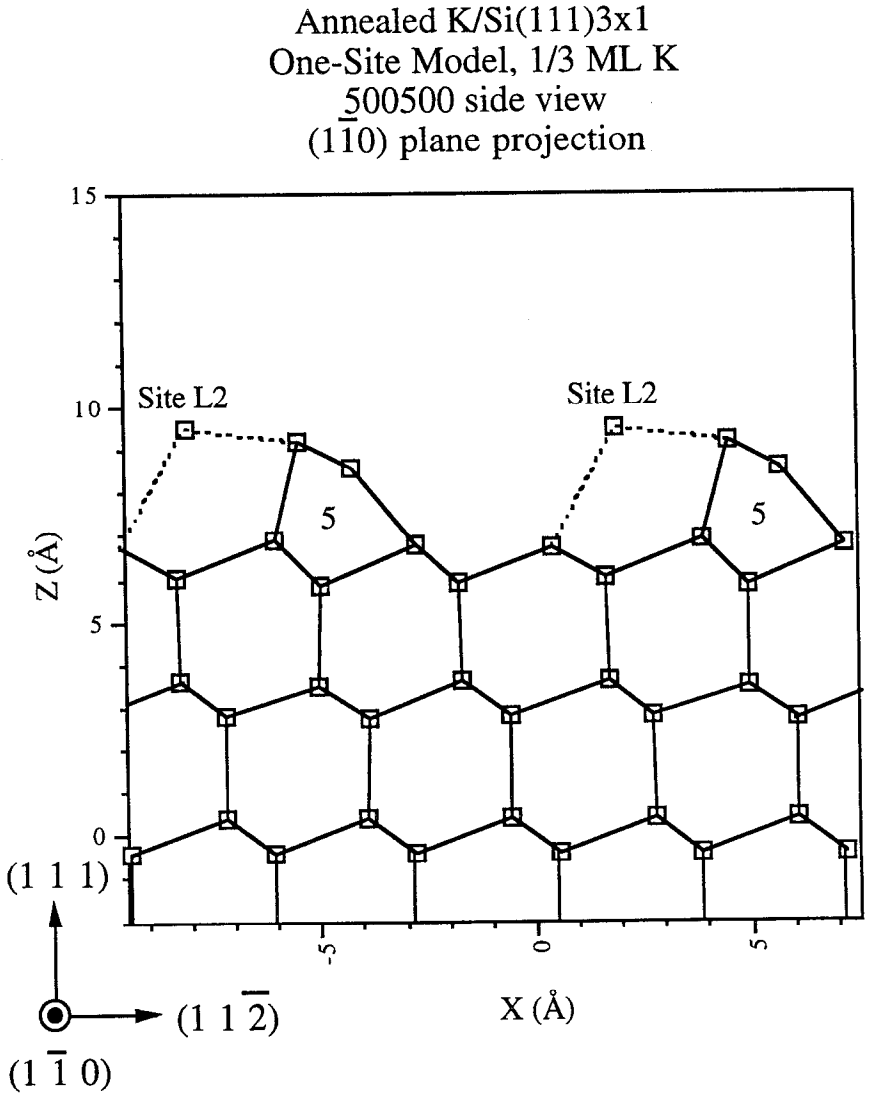

Figure 7.10(c). Our proposed "500500 Seiwatz chain" model of the annealed K/Si(111)3x1 surface for 1/3 ML K coverage. (c) Phasor diagram of $F_{11\bar{1}}$ showing the three-domain phasor sums for four proposed adsorption sites (see Figure 7.8(a)-(b) for geometry of non-L2 sites). Only site L2 matches the measured values of $D_{11\bar{1}}$ and $f_{11\bar{1}}$. The three domain contributions for site L2 are depicted. Domains are equally weighted. The shaded area represents the error bars for the measured values of $D_{11\bar{1}}$ and $f_{11\bar{1}}$.

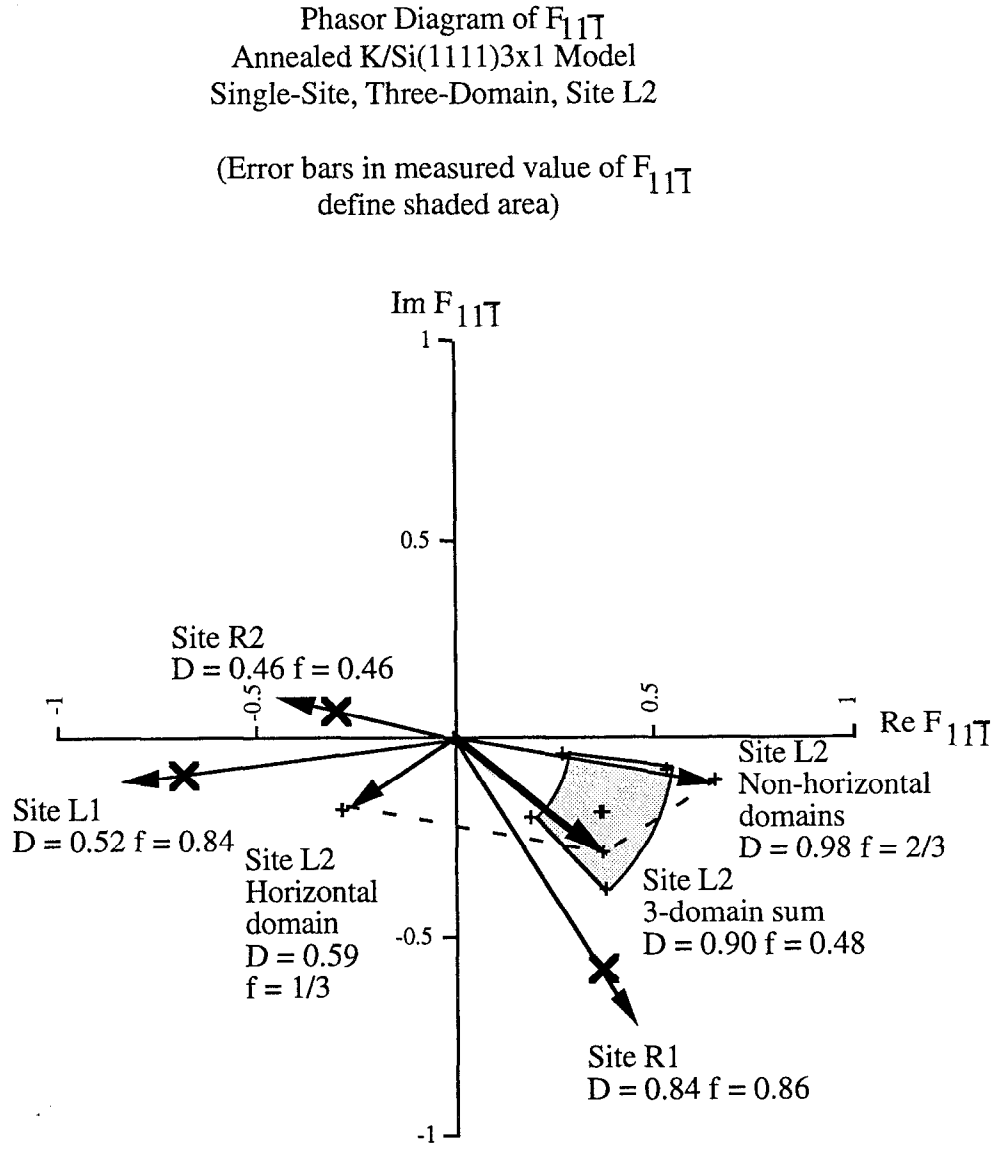

Figure 7.11(a). Our proposed "567567 extended Pandey chain" model of the room-temperature dosed K/Si(111)3x1 surface for 2/3 ML K coverage. (a) Top view ((111) plane projection).

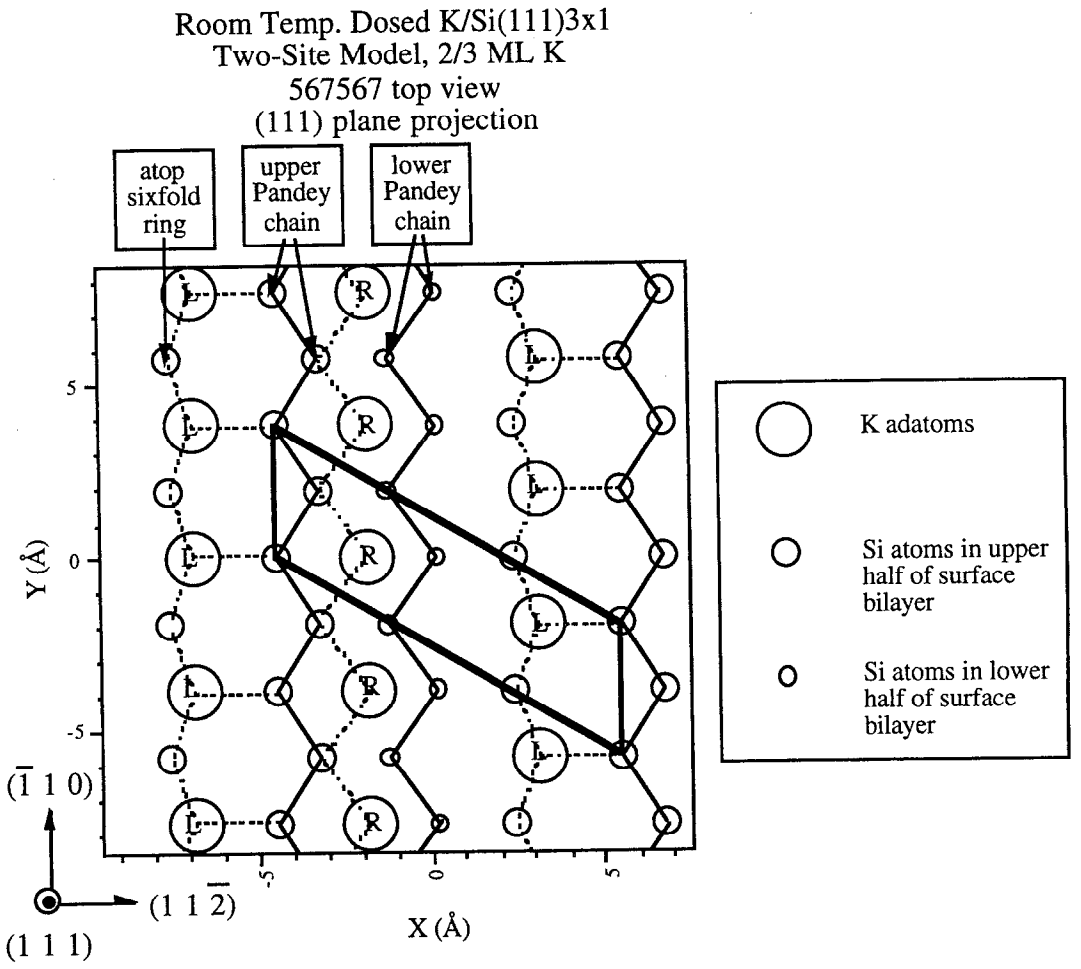

Figure 7.11(b). Our proposed "567567 extended Pandey chain" model of the room-temperature dosed K/Si(111)3x1 surface for 2/3 ML K coverage. (b) Side view ($(1\bar{1}0)$ plane projection).

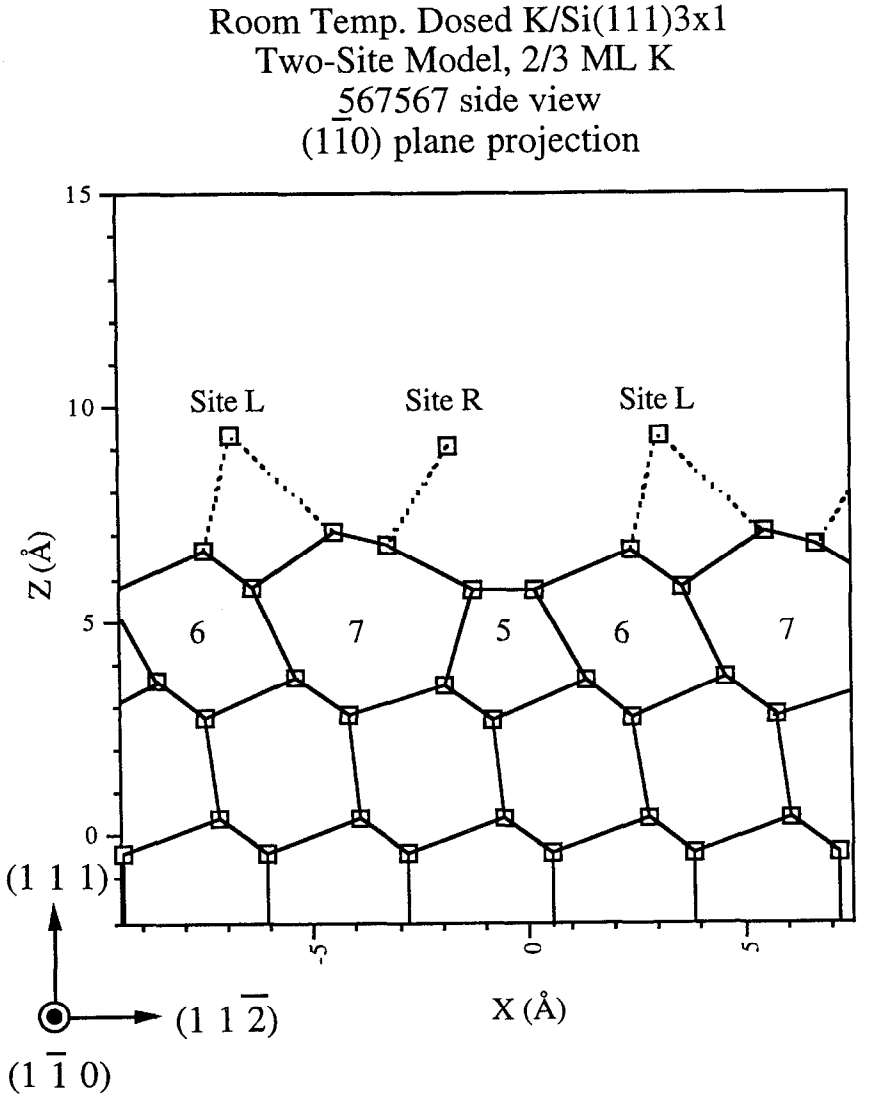

Figure 7.11(c). Our proposed "567567 extended Pandey chain" model of the room-temperature dosed K/Si(111)3x1 surface for 2/3 ML K coverage. (c) Phasor diagram of $F_{11\bar{1}}$ showing the phasor sum of sites L and R for the *single*-domain K/Si(111)3x1 surface. The shaded area represents the error bars for the measured values of $D_{11\bar{1}}$ and $f_{11\bar{1}}$.

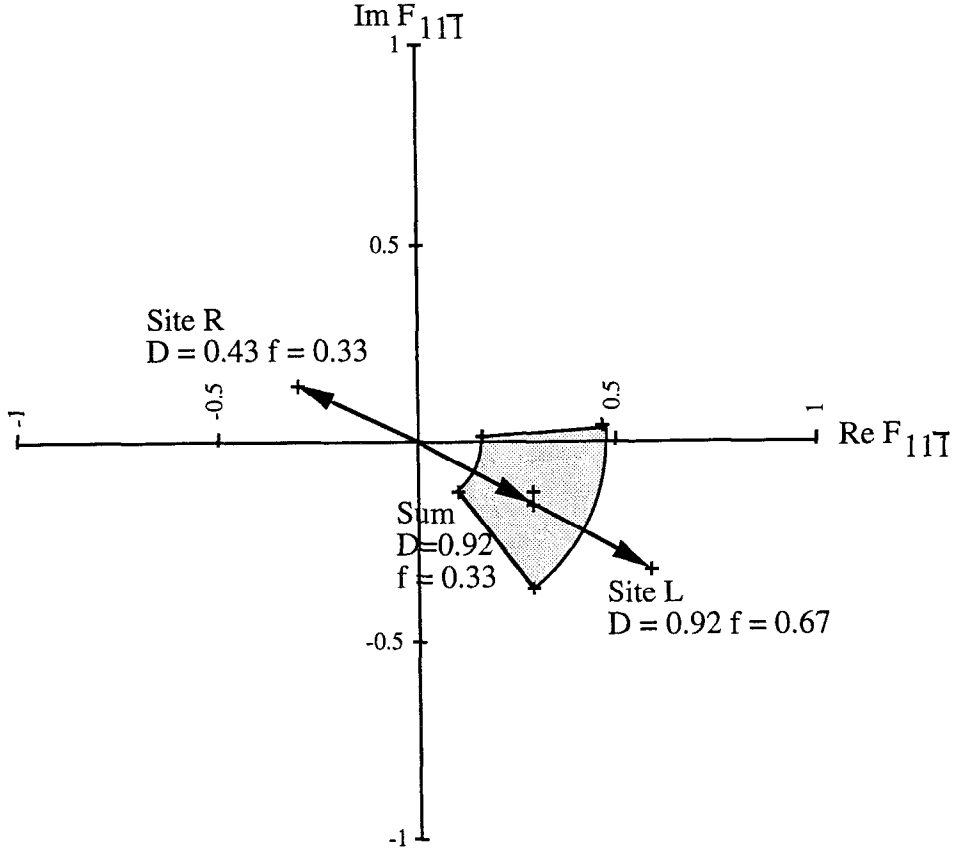

Figure 7.11(d). Our proposed "567567 extended Pandey chain" model of the room-temperature dosed K/Si(111)3x1 surface for 2/3 ML K coverage. (d) Phasor diagram of $F_{11\bar{1}}$ showing the phasor sum of sites L and R for the *two*-domain K/Si(111)3x1 surface. The shaded area represents the error bars for the measured values of $D_{11\bar{1}}$ and $f_{11\bar{1}}$.

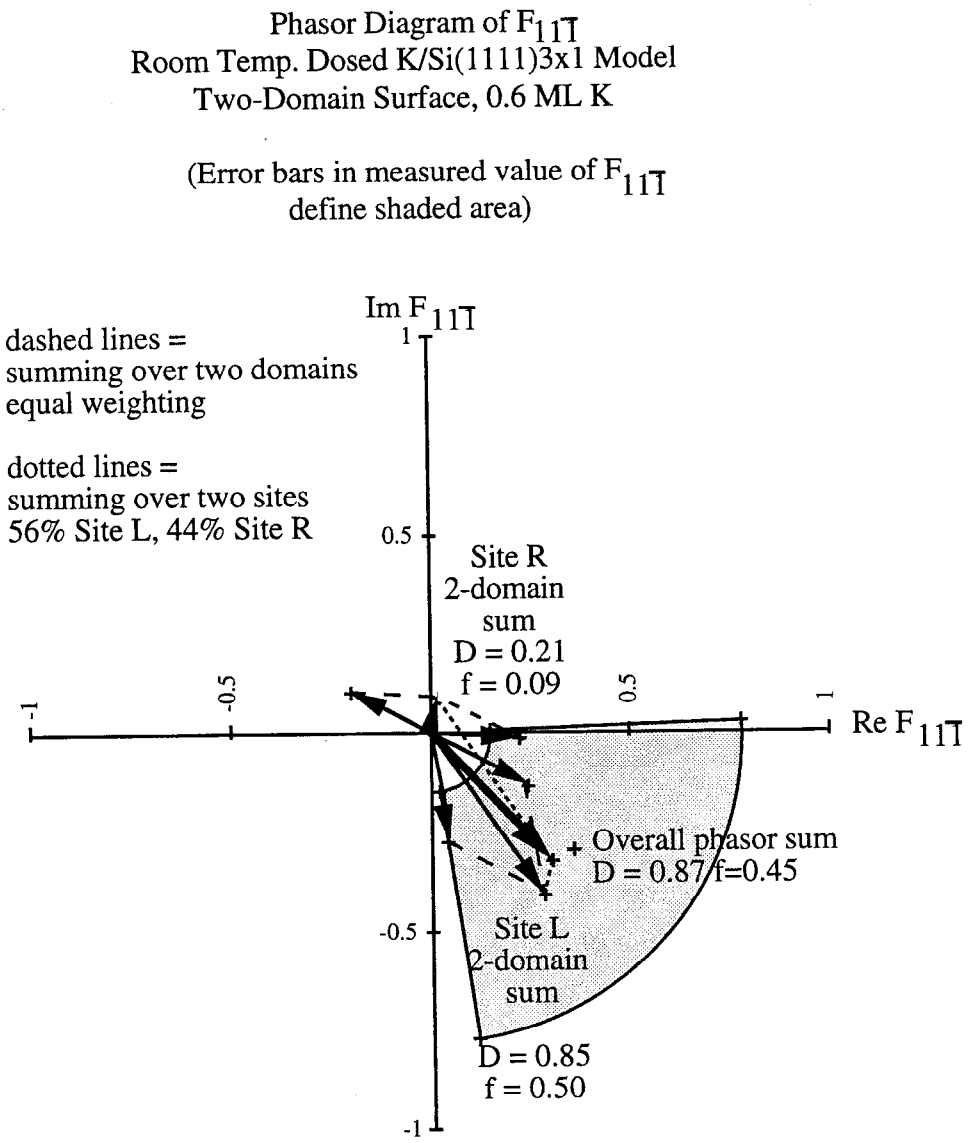

CHAPTER EIGHT

DIRECT MEASUREMENT OF VALENCE CHARGE ASYMMETRY IN BULK GAAS USING X-RAY STANDING WAVES

Abstract

Through detection of valence photoelectrons, the technique of x-ray standing waves directly measured the charge asymmetry of the GaAs valence band. Using the back-reflection geometry for the (111) and $(\bar{1}\,\bar{1}\,\bar{1})$ diffraction planes, we determine from the coherent distances of the standing waves, that a majority of the valence electrons reside on the As atoms of this heteropolar crystal. These measurements agree well with the GaAs bond polarity calculated from the values of the Hartree-Fock terms. In contrast, the valence standing waves for germanium determine the valence charge to be symmetric. The coherent fractions of the standing waves of Ge and GaAs are reduced compared to those of core-level standing waves, indicating the delocalization of valence charge. This technique using low energy x-rays together with valence photoelectron detection can be more generally applied to the study of chemical bonding,

and I plan to develop the valence band X-ray standing wave (VBXSW) technique in my future postdoctoral work.

Introduction

The traditional use of the X-ray standing wave (XSW) technique [1-4] has been to determine the atomic positions of foreign surface or impurity atoms relative to the diffracting planes of a host crystal. The first experiment on the surface applications of XSW were performed by Cowan of NIST and Golovchenko of Bell Labs [1-2]. Near the Bragg condition, incident and reflected X-rays superpose to form a standing wave whose intensity maxima move from halfway between the diffracting planes to on the diffracting planes as photon energy is moved over the finite energy width of the reflectivity. By monitoring the core-level photoabsorption through photoelectron yield as the standing wave intensity profile moves with photon energy, we can determine extremely accurately the distribution of distances of the absorbing atoms from the diffracting planes.

The atomic distribution determined from the characteristic absorption yield curves corresponds to the core-level electrons excited by the standing wave field, and since core states are highly localized, it is assumed that the core-level electron positions are at the atomic centers. In this study, we characterize the bulk valence electron distribution of Ge and GaAs using valence band photoemission yield XSW. We demonstrate that large bond polarity effects are observable in raw valence band XSW data, and the coherent distance of this valence band data is a direct determination of the bond polarity.

By monitoring the valence band photoemission yield, we use a variation of the well-established X-ray standing wave technique to probe the position distribution of bonding charge density perpendicular to the diffracting planes. With sufficient energy resolution, the valence band X-ray standing waves (VBXSW) technique will determine spatial information about specific bonding states. Recently Dr. Joseph Woicik and I performed this experiment on Beamline 3-3 (JUMBO) at SSRL, in order to test the feasibility of VBXSW. I presented our results at the Tenth International Conference on X-ray Absorption Fine Structure (XAFS X) and the results were published in the conference proceedings in the *Journal of Synchrotron Radiation*[7]. After describing the results of the GaAs and Ge bond polarity experiment, I will describe the possible applications of the valence band X-ray standing wave technique, as well as outlining future experiments to develop this technique. These future experiments will be carried

out during my two-year tenure in a NIST/NRC Postdoctoral Associateship at Brookhaven National Laboratory after completion of my Ph.D.

Experiment and Description of Technique

All XSW experiments were performed on Beam Line 3-3 (JUMBO) at Stanford Synchrotron Radiation Laboratory (SSRL) with a double-crystal InSb(111) monochrometer and a Pt-coated quartz focusing mirror upstream of the monochrometer. Samples were single-crystal cleavable bars. The front surfaces were Ge(111) and the nonpolar GaAs(110) surfaces, while the samples were oriented so the $(1\bar{1}0)$ direction was vertical. Samples were cleaved in vacuum, and the pressure throughout the experiment was less than $5\text{x}10^{-11}$ torr.

The experiments were performed in the backreflection configuration, with the incident beam normal to and reflecting off of the (111) plane of Ge and the (111) or $(\bar{1}\bar{1}\bar{1})$ planes of GaAs. The photon energy required for backreflection is approximately 1900 eV for all reflections. Near the Bragg condition, the incident and reflected X-rays superpose to form a standing wave with the spatial periodicity of the diffracting planes (~3.27 Å). The phase of the standing wave intensity changes by π as the photon energy is scanned through the Bragg condition. The intensity maxima of the standing wave move from halfway in between the diffracting planes to on the diffracting planes as the photon energy is increased from the low energy side to the high energy side of the reflectivity. By monitoring absorption through photoemission yield from a particular core level as the standing wave intensity profile moves with photon energy, we can determine the distribution of distances of the absorbing atoms from the diffracting planes in the direction perpendicular to the plane, e.g. the (111) direction. Similarly, by monitoring the variation of the valence band photoemission peak height, we can probe the position distribution of valence charge along the (111) direction.

In the dipole approximation, the x-ray standing wave absorption yield can be fit to the equation

$$Y(E) = 1 + R(E) + 2\, f_c \sqrt{R(E)} \cos(\nu(E) - 2\pi D_c) \qquad (1)$$

where the reflectivity R(E) and phase ν(E) of the standing wave are functions of the photon energy E. The fit finds the values of D_c and f_c, which are the coherent distance and fraction, respectively, and are the phase and magnitude of F_H, the Fourier

component of the electron density in the direction perpendicular to the diffracting planes, at the selected electron binding energy. The coherent distance D_c (in units normalized to the plane spacing) is the phase-averaged distance of the charge distribution from the diffraction plane. The coherent fraction f_c reflects the spread in position of the charge distribution, with increased spatial extent resulting in a decreased coherent fraction. As seen from the equation, the coherent distance D_c affects the phase and overall shape of the standing wave yield, while the amplitude of the feature is proportional to the coherent fraction f_c.

The photoelectron yield was measured using a cylindrical mirror analyzer, the axis of which was along the polarization vector of the synchrotron radiation. The constant initial state (CIS) mode was used, where the electron kinetic energy is changed with the photon energy to track the photopeak. For both Ge and GaAs we monitored the valence band and the shallow 3d core-levels so the kinetic energy of core and valence electrons are similar. The kinetic energy is 1860-1895 eV, making the measurement bulk-sensitive.

Ge Results: (111) Reflection

Figure 8.1 presents the standing wave data for the core-level Ge 3d and valence band (Ge VB) photoelectron yields, as well as a diagram of the Ge crystal atomic arrangement. The lineshapes of the Ge 3d and valence band yields are similar, indicating an identical coherent distance $D_c = 1$, which is on the (111) atomic plane. The coherent fraction of the Ge VB standing wave is 0.661±0.046, which is reduced only 5% from the Ge 3d coherent faction of 0.693±0.038, as is evident from the raw data. Because the coherent fraction reflects the spread in position of the monitored charge distribution, we anticipated a larger reduction in coherent fraction than measured due to the delocalization of the valence band initial state. One possible explanation for why the reduction is small may be due to a final state localization effect of the photoemission process at these high kinetic energies [6], as will be discussed below.

GaAs Results: (111) and $(\bar{1}\,\bar{1}\,\bar{1})$ Reflections

Contrary to the homopolar Ge case, the valence band standing wave data for the heteropolar GaAs crystal along the polar (111) and $(\bar{1}\,\bar{1}\,\bar{1})$ reflections clearly reflect the polarity of the GaAs bonds, as seen in Figures 8.2 and 8.3. For the (111) reflection, the Ga or As atoms are 1/8 of a plane spacing above or below the (111) diffraction

plane, respectively. The core-level As 3d and Ga 3d standing wave data have lineshapes and coherent distances corresponding to these atomic positions (see Figure 8.2). The valence band standing wave lineshape is at a distance between the As 3d and Ga 3d lineshapes, since the photoelectrons in this case come from both As and Ga atoms; however, the lineshape is closer to that of the As core than to that of the Ga core, indicating the valence charge distribution of the GaAs bond is weighted towards the As atom. The measured shift of the valence band coherent distance from the bilayer midplane is –0.057±0.010 plane spacings.

Flipping the sample around allows us to look at the $(\bar{1}\,\bar{1}\,\bar{1})$ reflection, for which the As and Ga atomic positions are reversed with respect to the diffraction plane (bilayer midplane) when compared to the (111) reflection. By comparing Figures 8.2 and 8.3 one can see the lineshapes of the core-level As 3d and Ga 3d standing wave data have reversed. In the $(\bar{1}\,\bar{1}\,\bar{1})$ case (Figure 8.3) the valence band standing wave data again have a lineshape between the two core-level lineshapes, being more similar to that of the As core, once again reflecting the polarity of the GaAs bond. The measured shift of the valence band coherent distance from the bilayer midplane is +0.068±0.015 plane spacings, which is equal and opposite to the shift for the (111) reflection.

Estimate of GaAs Bond Polarity

Using the measured coherent distances and a simple model of the charge distribution, we can obtain a quantitative measure of the polarity of the valence charge distribution. We assume a delta function distribution

$$f(D) = \frac{1+\alpha_p}{2}\delta(D-D_{As}) + \frac{1-\alpha_p}{2}\delta(D-D_{Ga}) \qquad (2)$$

where D is the distance of the charge from the diffracting plane, and D_{As} and D_{Ga} are the positions of the As and Ga atoms. This distribution places the valence charge at the positions of the As and Ga atomic cores and weights the fraction of charge on As or Ga with the polarity parameter α_p. Note that this model ignores the different cross sections for the Ga and As 4s and 4p orbitals and assumes that the electron emission is negligible between the atoms. (We have experimentally verified that the coherent fraction of the Ge valence band is reduced only by 5%.) This assumption of valence

emission primarily near the position of the atomic centers is discussed further in the section below. With the model distribution of equation (2), it can be shown that

$$\alpha_p = \pm \tan(2\pi D_{c,VB}) \quad (3)$$

where $D_{c,VB}$ is the experimentally observed shift of the valence band coherent distance from the bilayer midplane.

Averaging the results of the two reflections to reduce the error bar gives a measured polarity of $\alpha_p = 0.40 \pm 0.06$. This value agrees well with the value of $\alpha_p = 0.32$ calculated by Harrison [5] for GaAs using sp^3 hybrids and Hartree-Fock term values. Inclusion of cross section effects would weight the As term in equation (2) preferentially by a small amount, bringing our results into even closer agreement with theory.

Discussion and Future Work

The valence band standing wave technique has been demonstrated to provide an accurate quantitative method for measuring bond polarity. Striking polarity effects are visible in the raw data which we have explained using a simple, intuitive model, and suggests that more complicated experiments are possible. By comparing localized core level yields to valence band photoemission yields from homopolar Ge and heteropolar GaAs crystals, we verify that valence band standing wave measurements reflect the symmetry of Ge bonds and the polarity of GaAs bonds as well as a small delocalization of the valence charge.

In order to develop the technique of VBXSW, my future work will include numerous VBXSW experiments on different types of systems. Our GaAs and Ge experiments raise a number of questions about the interpretation of the data. The experiments outlined below would test the correctness of our assumptions in data analysis as well as provide a better understanding of what information VBXSW can provide about spatial distribution of bonding charge density in solid state materials.

Four areas of future research are important for the development of Valence Band X-ray Standing Waves. These are the following:

- Semiconductor polarity study - test of our simple model of polarity determination
- Delocalization study - study of how the coherent fraction f_c reflects the spatial extent of valence band states in different materials

- Spatial determination of specific valence states using resolution of electron energy
- Overall model for results and determination of usefulness of technique

1. Semiconductor polarity study. Our GaAs experiment suggests a direct, simple relationship between the VBXSW coherent distance and bond polarity. This study will test the correctness of the polarity relation of equation (3) above for bulk compound semiconductors in general. The well-established values of bond polarities α_p will be compared to the values determined from the measured VBXSW coherent distances. The model bonding charge distribution assumed for GaAs ignores the different cross sections for the constituent atomic orbitals. By performing the same polarity experiment on InP and other semiconductors, we can test the effect of differing anion and cation atomic sizes and cross sections, and span a range of polarities and bonding charge distributions. Departures of experimental results from our simple polarity relationship will be used to improve the interpretation of VBXSW data.

2. Delocalization study. In our preliminary experiment, the measured VBXSW coherent fraction f_c for Ge was much larger than expected. For core-level XSW, a reduced coherent fraction indicates disorder in the photoemitting atom positions. The meaning of the coherent fraction is less clear for VBXSW, since in this case the initial state is spatially extended. We expected that the coherent fraction would be significantly decreased for such states, because charge in different positions contribute different phases to the overall standing wave signal and will tend to cancel. However, the measured Ge valence band coherent fraction was reduced only 5% from the value for the localized Ge 3d coherent fraction. A preliminary experiment by Dr. Woicik on the delocalized valence band of copper also produced a much larger coherent fraction than expected. A possible explanation for the smallness of the reduction in f_c is an effective final state localization effect of the photoemission process at these high kinetic energies. Solterbeck *et al.* [6] calculated the angular distribution of valence photoelectrons in surface states of the GaAs(110) surface at various electron kinetic energies from 20 eV to 1500 eV. In addition, they calculated the angular distribution and relative emission strength arising from different spatial regions of an initial valence state. Above 1000 eV it was found that almost all of the valence photoemission was from valence charge density located within 0.3 Å of the atomic cores. This effective localization of the valence photoemission can be understood by looking at the matrix element between the initial and final state in the expression for the photoemission cross

section. Since the final state is highly energetic, it varies rapidly in space; for comparison, the wavelength of a free electron at 1900 eV is 0.28 Å. Therefore overlap integral between the initial and final states is only large over regions where the initial valence state also varies rapidly in space, i.e. near the atomic cores. So the resulting photoemission yield is primarily from this region. The small 5% reduction of the coherent fraction for the Ge valence band data can be explained the spread of the valence wave function around each core. This reduction is calculated by finding the average value of $\cos(2\pi r)$ over a uniform spherical distribution of radius 0.3 A, which equals 0.965. The expected coherent fraction is $(0.965)*1/\sqrt{2}*0.98 = 0.67$ (including a room-temperature Debye-Waller factor of 0.98), in good agreement with the measured value of 0.661 ± 0.046. In addition, the effective localization of the emission source at high kinetic energy justifies using the delta-function valence charge distribution used in equation (2) for interpretation of the GaAs valence band X-ray standing wave data. This distribution is used in the XSW equation (1), which describes the energy dependence of the measured photoelectron yield and would implicitly include this localization effect as it is derived from the absorption yield cross section.

By studying semiconductors (e.g. Si, Ge), metals (e.g. Cu), and ionic materials (e.g. PbS) with VBXSW, we will study how varying the initial state localization affects the observed coherent fraction. By using different Bragg reflections, we also will look at how the coherent fraction changes with incident photon and photoelectron energy. The goal of this study is to understand the sensitivity of the VBXSW coherent fraction to the delocalization of bonding charge density and in what energy regimes this sensitivity is enhanced.

3. Spatial determination of specific valence states using resolution of electron energy. By spectroscopically resolving individual features of the valence band, we will use VBXSW to study position distributions of specific bonding states. In our GaAs experiment, the electron analyzer integrated over most of the valence band so our results reflected the entire valence charge distribution. With improved electron energy resolution, we will apply VBXSW to specific bonding orbitals in bulk crystalline systems, multilayers and thin films, and to overlayer-to-surface bonds. We will test the ability of VBXSW to detect the specific atomic character of bands and bonding orbitals (e.g. which orbitals are more Ga-like or As-like in character in GaAs). We will use VBXSW to study the charge-ordered system of the lanthanum manganites, which have applications in colossal magnetoresistance (CMR). Ordered stripes of valence charge

establish the spin ordering which produces the CMR effect. X-ray diffraction determined spatial ordering of the charge, and photoemission results suggest the valence state involved in the ordering. VBXSW is a natural combination of the two techniques and would experimentally link the valence state in question to the charge spatially ordered in stripes. If successful, this experiment would greatly increase the understanding of the physics behind the electronic properties of these systems. VBXSW then will be extended to other systems where combined position and energy information is desired, such as phase transitions and bonding in thin films, multilayers, and high-T_c superconducting cuprates. We also will use an angle-resolved spectrometer for VBXSW in order to simultaneously measure both the position and momentum of valence states and Fermi edges. By looking at photoemission from shallower take off angles, we also can use VBXSW to study charge transfer in surface bonding. The simultaneous determination of energy and position data from valence band states is one of the most exciting possibilities which VBXSW offers.

4. Overall theory or model for results and determination of usefulness of technique. By modeling the VBXSW results from these experiments, we can understand how VBXSW probes the spatial distribution of bonding charge density. With this understanding we hope to develop a quantum mechanical theory for VBXSW. There are several issues to be addressed in analyzing the VBXSW data. In addition to the issues presented above, the importance of multipole effects must also be considered. Using the dipole approximation, the basic XSW yield equation (1) can be derived from the general expression for the photoemission cross section in the standing wave field. Since the dipole approximation is correct for highly localized core electrons, the coherent distances correspond to the atomic center positions for core-level XSW. The dipole approximation is not valid for bonding charge distributions, since the standing wave intensity varies over the scale of interatomic distances. For GaAs, multipole effects are not large since our simple model fits the data well. This is in part because the detector axis was parallel to the electric field polarization, and electrons were collected both in front of and behind the vertical plane of polarization, i.e. the plane normal to the photon propagation vector. Quadrupole terms exhibit a forward/backward asymmetry with respect to this plane of polarization, as seen in the expression for the angular dependence of the photoemission cross-section including quadrupole effects[8]:

$$\frac{d\sigma}{d\Omega} \propto \frac{\sigma}{4\pi}\left[1+\frac{\beta}{2}(3\cos^2\theta-1)+(\delta+\gamma\cos^2\theta)\sin\theta\cos\phi\right] \qquad (4)$$

where θ is the angle between the photoemitted electron direction and the electric field polarization, and ϕ is the angle between the photon propagation vector and photoemitted electron direction, projected into the plane perpendicular to the electric field. The forward/backward asymmetry with respect to the photon polarization plane appears through the cos ϕ dependence of the third term of equation (4). The parameter β for the angular distribution is related to dipole-dipole matrix element product terms in the cross section, and the parameters δ and γ are due to terms related to the product of electric dipole and quadrupole matrix elements. Quadrupole-quadrupole terms are the next higher order in the fine structure constant and are ignored. The parameters β, δ and γ have values dependent on the initial atomic subshell.

The corresponding cross section for a backreflected X-ray standing wave must consider the effect of both the incident and reflected X-ray which make up the standing wave. In this case the incident and reflected polarization direction are the same, but the incident and reflected propagation vectors are opposite. For the Ge(111) backreflection case, photoelectrons are detected in the "backward" half of the CMA cone only, since in this case the plane normal to the photon propagation vectors coincides with the surface plane. For the GaAs (111) backreflection, the surface is rotated with respect to the plane of polarization, and the CMA detects electrons in both the forward and backward halves of its cone, although in differing amounts. For detection backward side of the plane, cos ϕ is positive with respect to the reflected wave and negative with respected to the incident wave. The signs are switched for the forward side of the plane. For detection in the horizontal plane, Fisher *et al.* [9] define a forward/backward asymmetry parameter Q so that the ratio of photoemission intensity detected at $\phi = 0^o$ to that at 180^o is given by (1+Q)/(1-Q). This parameter is then applied to the matrix elements in the general expression for the cross section in a standing wave field,

$$\frac{d\sigma}{d\Omega} \propto \left|\begin{array}{l} < f|\exp(ik_0\cdot r)\varepsilon_0\cdot\nabla|i> \\ + \sqrt{R(E)}\exp(i(\nu(E)-2\pi(H\cdot r)))\ \times\ < f|\exp(ik_H\cdot r)\varepsilon_H\cdot\nabla|i> \end{array}\right|^2 \qquad (5)$$

to give their expression for the angular dependence of the matrix elements

$$\frac{d\sigma}{d\Omega} \propto \left|M(1-Q)^{1/2} + \sqrt{R(E)}\exp(i(\nu(E)-2\pi(H\cdot r)))M(1+Q)^{1/2}\right|^2 \qquad (6)$$

where M is the non-angular part of the matrix element, which is the same for both terms. Upon calculating the square and normalizing becomes

$$\frac{d\sigma}{d\Omega} \propto 1 + \mathrm{R(E)}\frac{1+\mathrm{Q}}{1-\mathrm{Q}} + 2\sqrt{R(E)}f_c\sqrt{\frac{1+\mathrm{Q}}{1-\mathrm{Q}}}\cos(v(E) - 2\pi D_c) \qquad (7)$$

This expression differs from the dipole standing wave expression of equation (1) only in the coefficients of the second and third terms. It is written for Q>0 for detection in the backward half of the plane, as the terms proportional to the reflectivity have an angular coefficient (1+Q)/(1-Q) greater than one in this case. This dependence can be generalized for any detection angle through the expression

$$Q = \frac{(\delta + \gamma\cos^2\theta)\sin\theta\cos\phi}{1 + \frac{\beta}{2}(3\cos^2\theta - 1)} = \frac{\text{quadrupole terms}}{\text{dipole terms}} \qquad (8)$$

where ϕ is the angle between the *reflected* photon propagation vector and photoemitted electron direction, projected into the plane perpendicular to the electric field.

This generalization allows us to integrate equation (7) over the detection cone of the CMA and determine the effect of quadrupole terms upon the standing wave adsorption profile. The detection cone covers a range of $42.3^\circ \pm 6^\circ$ about the CMA axis, which coincides with the polarization direction for backreflection. Table 8.1 lists the average value of the asymmetry factor Q for the Ge 3p, 3d, 4s, and 4p subshells, for the experimental geometries for the Ge and GaAs (111) backreflections (the surface planes were Ge(111) and GaAs(110)). The values of the angular parameters β, δ and γ were calculated for us for Ge by Cooper[10]. As expected, the asymmetry is larger for the Ge experimental geometry, as none of the electrons were detected on the "forward" side of the vertical plane of polarization. Q is largest for the Ge 3d subshell and smallest for the Ge 4s, with the Ge 3p and Ge 4p levels having nearly equal and intermediate values. This is in part due to the larger number of possible transitions for L=2 initial states, as the selection rule for quadupole transitions is $\Delta L = 0, \pm 2$.

The overall effect of the asymmetry is given in Figure 8.4, which plots the standing wave absorption profile given by equation (7) for the three values of Q corresponding to the Ge subshells for the Ge(111) reflection. These lineshapes are then fitted with the dipole standing wave equation (1) and the coherent distance and fractions are listed in Table 8.2. The predominant effect is an increase in the apparent coherent fraction of the standing wave with increasing Q. Comparing the coherent

fractions for the Ge 4p and Ge 3d lineshapes, there is a 5% decrease of the fraction for the 4p level, which should be mostly representative of the Ge valence band data lineshape, although the valence orbital also has partial 4s character. This 5% decrease matches the observed decrease in coherent fraction seen in Figure 8.1, although both the measured Ge valence band and Ge 3d coherent fraction are 90% of the predicted fraction. This suggests that multipole effects on the coherent fraction could be of similar magnitude to the delocalization effect of the initial valence band and that further study of the relative importance of the two effects is required. However, if the multipole effect is as large as predicted, this indicates the emitting source is even further effectively localized, to a radius smaller than the predicted 0.3 Å.

There also may be a problem with the Fisher *et al.*'s formalism[9] of the angular dependence in equations (6)-(7) above. The assumption that the angular coefficients $(1\pm Q)^{1/2}$ of the matrix elements M are just the real square root of the observed angular dependence of the cross section ignores possible interference between the complex matrix elements. Cooper[8] has shown that photoemission matrix elements of the form of equation (5) take the form

$$< f|\exp(ik\cdot r)\varepsilon\cdot\nabla|i> \;\propto\; \omega\langle z\rangle_{if} + \frac{i\omega^2\alpha}{2}\langle xz\rangle_{if} \qquad (9)$$

where x is the electron position along the direction of photon propagation, and z is along the photon polarization direction. $<z>_{if}$ and $<xz>_{if}$ are the matrix elements between the initial bound and final photoemitted electron state. The overall cross section will have a term like equation (9) for the incident matrix element, while the reflected matrix element undergoes the transformation

$$< xz >_{if} \;\rightarrow\; -< xz >_{if} \text{ and } < z >_{if} \;\rightarrow\; < z >_{if} \qquad (10)$$

Upon taking the complex conjugate and squaring, the cross section with this treatment becomes

$$\frac{d\sigma}{d\Omega} \propto (A-B) + (A+B)R(E) + 2A\sqrt{R(E)}f_c\cos(\nu(E)-2\pi D_c) + 2C\sqrt{R(E)}f_c\sin(\nu(E)-2\pi D_c) \qquad (11)$$

where the angular dependence is in the coefficients A, B, and C, and are proportional to the matrix elements as follows:

$$A \propto \omega^2 \langle z \rangle_{if} \langle z \rangle_{if}^*$$
$$B \propto -\omega^3 \alpha \, \mathrm{Im}\left[\langle xz \rangle_{if} \langle z \rangle_{if}^* \right] \qquad (12)$$
$$C \propto -\omega^3 \alpha \, \mathrm{Re}\left[\langle xz \rangle_{if} \langle z \rangle_{if}^* \right]$$

Cooper [8] relates the matrix elements A and B to the angular dependencies

$$A \propto 1 + \frac{\beta}{2}(3\cos^2\theta - 1) \qquad (13)$$
$$B \propto (\delta + \gamma \cos^2\theta) \sin\theta \cos\phi$$

and the angular dependence of C should be similar to that of B but with different parameter values.

The consideration of interference terms between the incident and reflected matrix elements leads to an additional term in the standing wave absorption yield equation (11) involving $\sin(\nu\text{-}2\pi D_c)$, and the usual $\cos(\nu\text{-}2\pi D_c)$ term has the dipole-only coefficient A. So at the peak or valley of the absorption lineshape, where $\cos(\nu\text{-}2\pi D_c) = \pm 1$, the last term would be close to zero. Therefore the overall size of the feature should not change dramatically, and a lesser increase of the coherent fraction with multipole effect is expected than for the profile of equation (7). In the case of equation (11) the decrease in coherent fraction from the Ge 3d to Ge valence band spectra would have a greater contribution from the delocalization of the initial state and less from multipole effects. In our future work, the correctness of either equation (7) or (11) will be determined, as well as the calculation of the angular dependence for the new coefficient C. Regardless of which equation is correct, the size of multipole effects upon the coherent fraction is less than 5% for the CMA detection geometries studied, with negligible effects on the coherent distance. Multipole considerations should not affect the polarity calculation for GaAs as the effects are nearly 3 times smaller than for the Ge experimental geometry.

In our future work, we will investigate the angular dependence of multipole effects on the VBXSW data. Using an angle-resolved analyzer instead of the CMA, one can detect in the vertical plane of polarization where the forward/backward asymmetry is removed, and compare the result to detector geometries where the asymmetry is pronounced. Also, at different photon and photoelectron energies multipole terms may become important. We expect the importance of multipole effects at high photon energies to compete with the effective final state localization of the photoemission process at high photoelectron energies[6]. The relative size of photoelectron and photon momenta will be important, and interpretation of VBXSW

data may differ in different energy regimes. We will investigate different energies by looking at different Bragg reflections for the same sample.

Through the results of multiple VBXSW experiments as well as a theoretical treatment of the standing wave photoemission problem, we hope to understand the following issues related to VBXSW data interpretation: the importance of multipole effects, the effect of photon versus photoelectron momentum, how the coherent fraction reflects delocalized bonding states, and the effect of differing anion and cation cross sections.

Conclusion

Valence Band X-ray Standing Waves (VBXSW) is a new extension of the well-established X-ray Standing Waves technique. Through detection of photoelectrons from bonding states, we successfully used VBXSW to directly measure the charge asymmetry of the GaAs bond. In addition, we observed a reduction in the coherent fraction of the Ge valence electron XSW yield relative to that for the core-levels which was less than expected from considering the extent of the initial bonding state. This result is attributed to an effective localization of the photoemitting source at high photoelectron kinetic energy. The combination of X-ray diffraction with electron energy-resolved detection can be applied to probe the spatial distribution of bonding charge density, albeit the portion near the positions of the atomic cores. The spatial extent of the initial bonding or valence states as well as high photon and photoelectron energies produce conditions which cause the interpretation of VBXSW data to differ from core-level standing wave data. The future experiments outlined in this chapter will address the interpretation of VBXSW data and its connection to the spatial distribution of bonding charge density through multiple VBXSW experiments for several materials and photon energy ranges, as well as a theoretical treatment of the standing wave photoemission problem. In addition, we will apply VBXSW to a number of systems of interest in order to assign spatial distributions to bonding states of specific energy. The success of this technique in these experiments would establish VBXSW as a new method of providing simultaneous energy and position information about bonding charge density and would have important applications in fields including the study of the electronic structure of colossal magnetoresistive (CMR) and high-T_c materials, thin films, surface science and catalysis. In the future this technique could be extended to provide further information with angular or spin resolution.

References

[1] P. L. Cowan, J. A. Golovchenko, and M. F. Robbins, Phys. Rev. Lett. 44 (1980) 1680 .

[2] J. A.Golovchenko, J. R. Patel, D. R. Kaplan, P. L. Cowan, and M. J. Bedzyk, Phys. Rev. Lett. 49 (1982) 560.

[3] D. P. Woodruff, Prog. Surf. Sci. 57 (1998) 1-60 .

[4] J. Zegenhagen, Surf. Sci. Rep. 18 (1993) 199-271 .

[5] W. A.Harrison, Electronic Structure and the Properties of Solids: The Physics of the Chemical Bond, 2nd edition, pp. 22 & 175. New York: Dover (1989).

[6] C. Solterbeck, W. Schattke, J.-W. Zahlmann-Nowitzki, K.-U. Gawlik, L. Kipp, M. Skibowski, C. S. Fadley, , and M. A. Van Hove, Phys. Rev. Lett. 79 (1997) 4681-4684 .

[7] E. Nelson, J. Woicik, and P. Pianetta, J. Synchrotron Rad., 6 (1999) 341.

[8] J. W. Cooper, Phys. Rev. A 47 (1993) 1841.

[9] C. J. Fisher, R. Ithin, R. G. Jones, G. J. Jackson, D. P. Woodruff, and B. C. C. Cowie, J. Phys. Cond. Matt. 10 (1998) L623.

[10] J. W. Cooper, private communication.

Table 8.1. Asymmetry parameters for photoemission from outer Ge subshells for the Ge and GaAs experimental geometries.

Photon Energy (eV)	Ge shell	β	δ	γ	Q Ge expt. geometry	Q GaAs expt. geometry
1900	3p	1.498	0.016	0.373	0.063	0.024
1900	3d	0.944	0.123	0.580	0.144	0.056
1900	4s	2.000	0.000	-0.035	-0.005	-0.002
1900	4p	1.488	0.016	0.362	0.062	0.024

Table 8.2. Coherent distance D_c and fraction f_c of simulated quadrupole-corrected X-ray standing wave data for outer Ge subshell photoemission near the Ge(111) Bragg condition. Coherent distance and fraction results from fit to XSW equation (1), which assumes the dipole approximation.

Ge shell	Q	Distance D_c	Fraction f_c
3p	0.06	1.009	0.729
3d	0.14	1.022	0.766
4s	0.00	1.000	0.707
4p	0.06	1.009	0.729

Figure 8.1. Top: X-ray standing wave data for Ge monitoring Ge 3d and Ge valence band (Ge VB) photoemission near the Ge(111) Bragg condition. Bottom: Atomic arrangement in bulk Ge with (111) diffraction planes indicated.

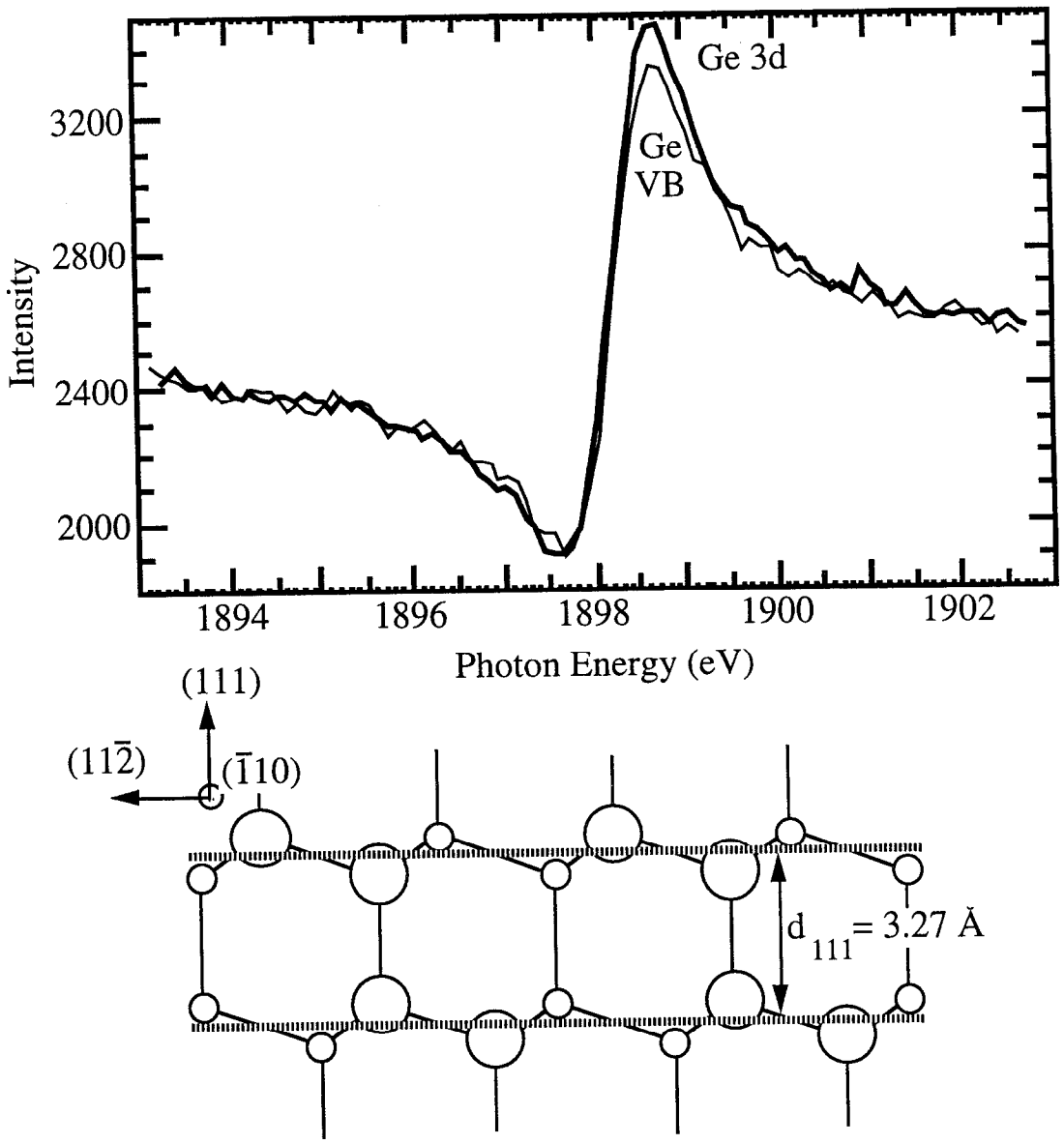

Figure 8.2. Top: X-ray standing wave data for GaAs monitoring As 3d, Ga 3d and GaAs valence band (GaAs VB) photoemission near the GaAs(111) Bragg condition for the (111) reflection. Bottom: Atomic arrangement in bulk GaAs for the (111) reflection with (111) diffraction planes indicated.

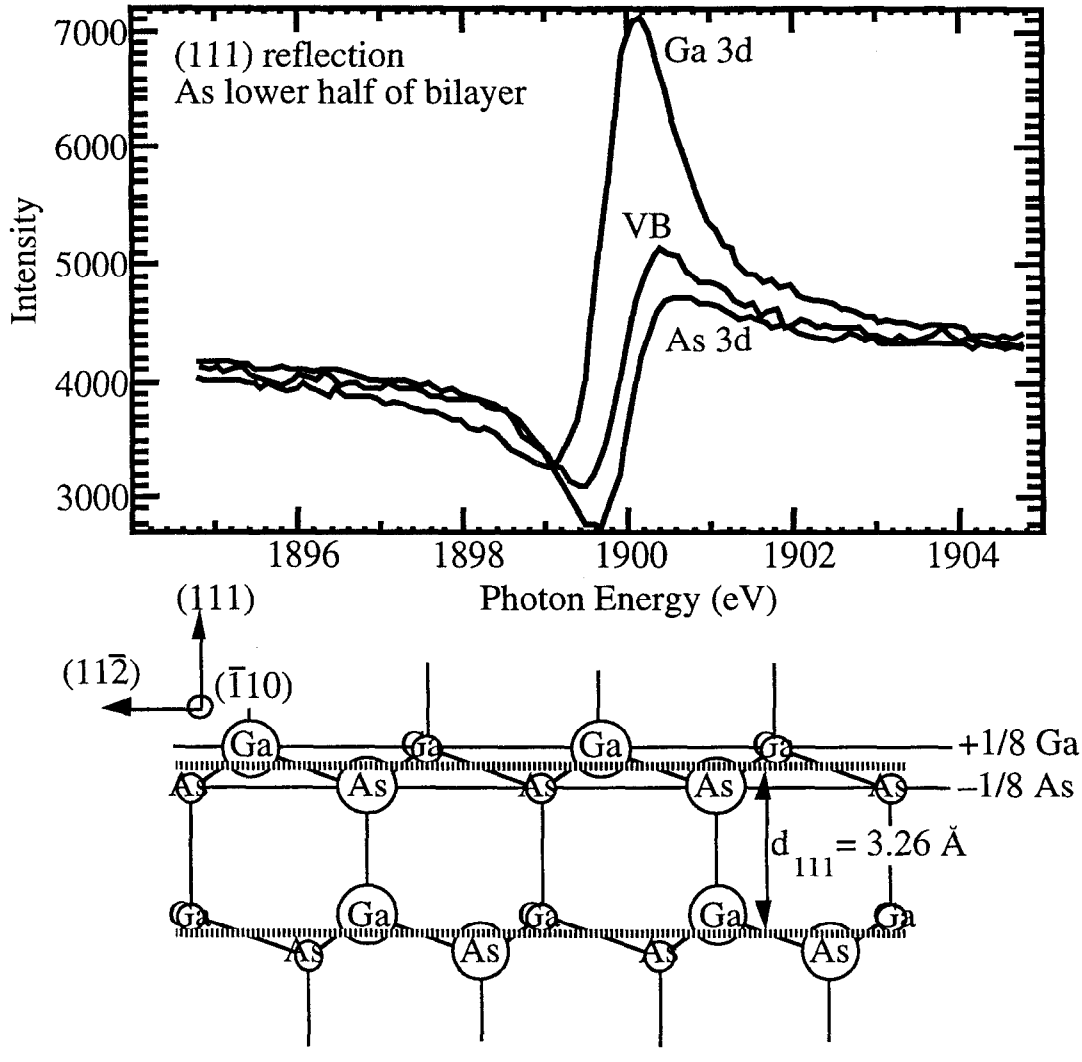

Figure 8.3. Top: X-ray standing wave data for GaAs monitoring As 3d, Ga 3d and GaAs valence band (GaAs VB) photoemission near the GaAs(111) Bragg condition for the $(\bar{1}\,\bar{1}\,\bar{1})$ reflection. Bottom: Atomic arrangement in bulk GaAs for the $(\bar{1}\,\bar{1}\,\bar{1})$ reflection with $(\bar{1}\,\bar{1}\,\bar{1})$ diffraction planes indicated.

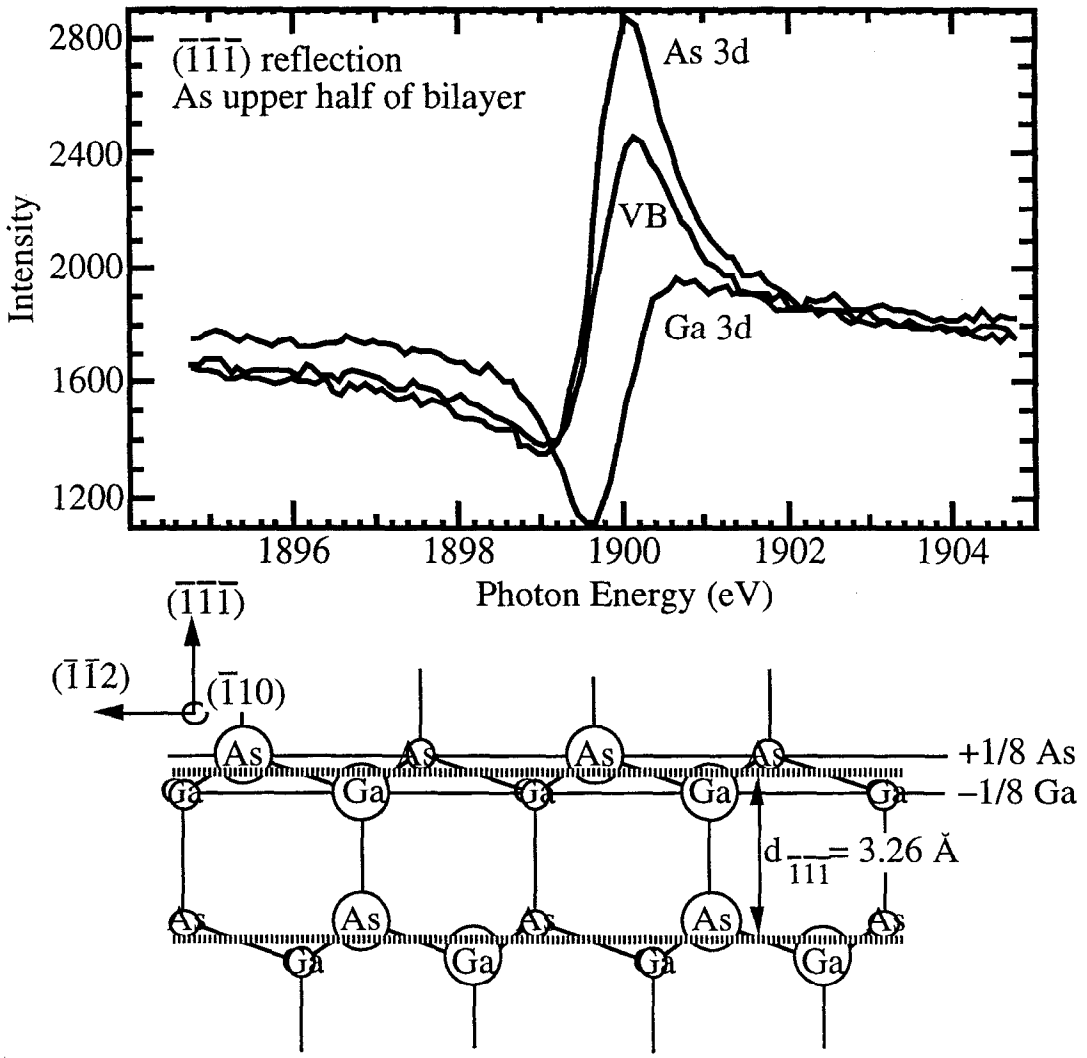

Figure 8.4. Simulated quadrupole-corrected X-ray standing wave data for outer Ge subshell photoemission near the Ge(111) Bragg condition. For each lineshape, the values of the forward/backward photoemission intensity ratio and the asymmetry parameter Q of equation (7) are indicated.

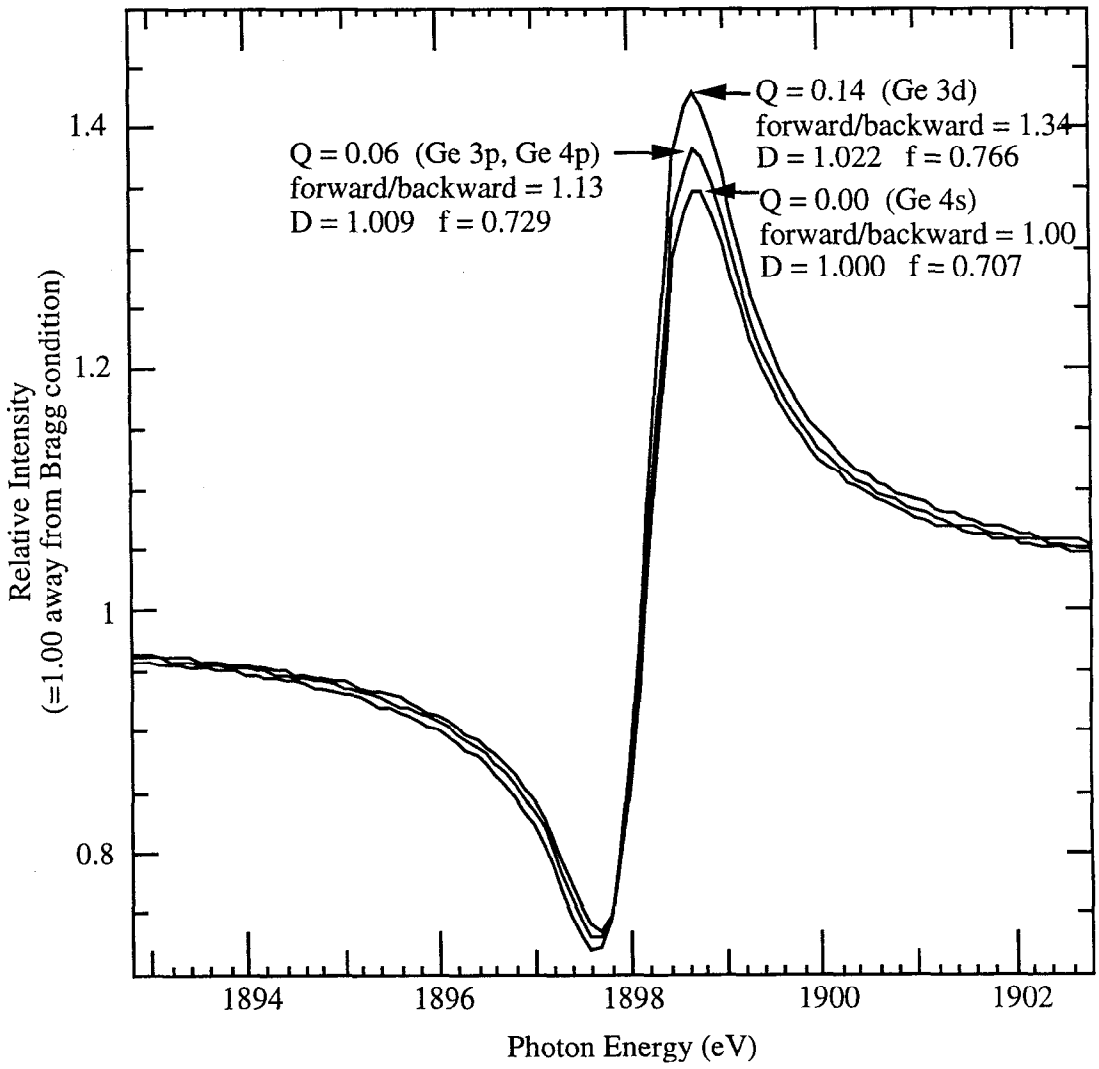

CHAPTER NINE

CONCLUSIONS

The main goal of this dissertation was to understand more completely the adsorption process of alkali metals upon the Si(111) surface. This goal was achieved both through observing changes in the electronic and atomic structure of the interfaces as AM coverage is increased from zero to one layer of alkali adatoms, and by quantitatively determining the atomic structure of several AM/Si(111) interfaces with well-defined surface periodicity. Photoemission and work function difference measurements determined changes in the electronic structure which could be correlated with changes in the atomic structure, namely adatom site positions and Si substrate reconstructions, as determined using low energy electron diffraction and X-ray standing waves. The new contributions of our work include detailed LEED phase diagrams for all three AM adsorbates upon the cleaved Si(111) surface; photoemission data for adsorbate and substrate atoms for the Na/Si(111), K/Si(111), and Cs/Si(111) interfaces at many coverages; the discovery that annealed 3x1 phases can be produced on cleaved Si(111)2x1 surfaces under similar conditions as on the Si(111)7x7 wafer surface; X-ray standing wave data on many of these surfaces which provide structural information of adsorbate and substrate atom positions; and conclusions about the

structure of these surfaces which are supported by the independent techniques of LEED, photoemission, and X-ray standing waves.

In Chapter 4 we have presented photoemission spectra of alkali metal photoemission peaks, the surface-sensitive Si 2p peak, and the valence band region as well as work function (secondary electron cutoff) data for many Na, K, and Cs coverages on the cleaved Si(111)2x1 surfaces ranging from the clean surface to 100% alkali metal saturation of the surface. In addition, spectra are presented for the annealed cleaved Na/Si(111)3x1 surface and the annealed cleaved and wafer K/Si(111)3x1 surfaces. As seen from the LEED phase diagrams in Figure 4.1, both the K/Si(111) and Cs/Si(111) phase diagrams have a sequence of many LEED patterns with increasing coverage, and several of the individual patterns for K and Cs overlayers are similar. The behavior of all the photoemission spectra also show similar trends with increasing K or Cs coverage; in particular, there is not much change in the lineshape of the alkali metal core levels, the Si 2p peak, or the valence band past the initial K or Cs dose. We conclude from the lack of change in the spectra and the directionality of the LEED patterns along the original clean 2x1 chain direction that the π-bonded chains remain underneath the K or Cs overlayer even up to saturation coverage. Si standing wave data presented below also suggest the Si remains reconstructed under the alkali overlayer for the room-temperature dosed K/Si(111)3x1, and Cs/Si(111)$\sqrt{3}$x$\sqrt{3}$–R30° surfaces.

The complexity of the K/Si(111) and Cs/Si(111) LEED phase diagrams is contrasted with the relative simplicity of the Na/Si(111) phase diagram. The photoemission data for the Na/Si(111) surface with increasing Na coverage are also qualitatively different than the behavior of the K/Si(111) and Cs/Si(111) photoemission data. Instead of a lack of change with increasing alkali coverage, for Na/Si(111) we see definite changes in the Na 2p, Si 2p, and valence band spectra corresponding to each of the three main LEED phases of the phase diagram. This indicates a stronger interaction between Na and the Si(111) surface than that for K and Cs. The reduction in the number of components of the Si 2p (and Na 2p) spectra for the 1x1 phase supports the conclusion of a conversion of the reconstructed π-bonded Si chains of the clean Si(111)2x1 and Na/Si(111)2x1 surfaces to the bulk-terminated Si(111) structure for Na/Si(111)1x1.

For room temperature dosing there are clear similarities between K and Cs adsorption upon the Si(111) surface, while Na adsorption differs. However, for the annealed AM/Si(111)3x1 surfaces, it is K and Na which are similar, with no corresponding Cs 3x1 structure. This behavior indicates the important roles of both

annealing and adatom size upon interface formation and energetics. The differing behavior of K adsorption upon room temperature and annealed surfaces can be attributed to the intermediate size of potassium, and make the K/Si(111) surfaces the most complex of the three alkalis studied, in terms of determining the nature of the adsorbate/substrate interaction.

In Chapter 5, we determined that the Na/Si(111)1x1 interface has a bulk-terminated and not a π-bonded chain or other reconstructed structure. For this saturation Na coverage interface, Na adsorbs in similar population on the threefold-hollow (H_3) and threefold-filled (T_4) symmetry sites of the bulk-terminated Si surface. The large increase in the amplitude of the surface-sensitive Si 1s XSW absorption feature for the 1x1 surface as compared to the 2x1 surface demonstrates that the 1x1 surface structure has changed from the π-bonded chain reconstruction and that the surface atoms are close to the corresponding extended bulk positions. The data for the clean Si(111)2x1 and Na-dosed Si(111) 1x1 surfaces match the predicted XSW profiles for the π-bonded chain reconstructed and bulk-terminated surface geometries, respectively. Na 1s absorption yield XSW along the (111) and (11$\bar{1}$) reflections results in a triangulated Na average lateral position between the H_3 and T_4 sites with a Na-Si bond length of 2.97 ± 0.04 Å. The reduction in the number of components of the Si 2p (and Na 2p) spectra for the 1x1 phase, as well as a large Na-Si bonding peak in the 1x1 valence band spectra, provides supporting evidence for the bulk-terminated Si(111) structure for Na/Si(111)1x1. The magnitude of the Si 2p surface component energy shift suggests covalent bonding between Na and Si at all coverages, and Na-Na overlayer interactions are weak at saturation coverage due to the localized nature of the sharp Na-Si bonding peak observed in the valence band spectra.

In Chapter 6 we investigated the coverage, bonding, and atomic structure of the Cs/Si(111)$\sqrt{3}$x$\sqrt{3}$–R30° interface, formed by room temperature dosing of 1/3 ML Cs on a cleaved Si(111)2x1 surface. The neighboring LEED patterns at higher and lower coverages exhibit a twofold symmetry and indicate retention of the π-bonded chains of the clean cleaved Si(111) surface under an ordered Cs overlayer. In addition, the lack of change in the Si 2p and Cs 4d spectral lineshapes with increasing Cs coverage as well as the retention of the π-bonding surface state at the top of the valence band further support the underlying Si structure of Cs/Si(111)$\sqrt{3}$x$\sqrt{3}$–R30° being the same as the clean Si(111)2x1 reconstruction. The retention of the chains also indicates a weak Cs-Si interaction.

X-ray standing wave data monitoring the Cs adsorption yield along the (111) and (11$\bar{1}$) reflections contradict models of a bulk-terminated Si(111) surface under a Cs

$\sqrt{3}x\sqrt{3}$–R30° overlayer with Cs in high-symmetry sites. This is because the triangulation of the coherent distance of the (111) and (11$\bar{1}$) reflections points to the atop (T_1) adsorption site of the bulk-terminated surface, but the measured Cs height and bond length to Si are too short. Our proposed model for the Cs/Si(111)$\sqrt{3}x\sqrt{3}$–R30° interface has Cs adsorption in two nearly equivalent sites on either side of the retained π-bonded chain Si(111) surface reconstruction. Using the kinematic approximation appropriate for high-Z overlayers, the LEED pattern created by the Cs atoms in this model is $\sqrt{3}x\sqrt{3}$–R30° within the observed energy range.

Unlike what one might expect from monovalent Cs, the adatoms are highly coordinated to Si atoms, yet they are weakly interacting with the Si surface, as the reconstruction is not destroyed. This is different from the case of Na/Si(111)1x1, where the Na atoms bulk-terminate the Si(111) surface upon adsorption; however, in that case the Na also are threefold-coordinated. As thermal effects at room temperature are not enough to change the Si(111) surface structure, the strength of the alkali-Si interaction and the corresponding interface geometry mainly depend on the alkali atomic size and electronegativity. Dosing further Cs upon the $\sqrt{3}x\sqrt{3}$–R30° interface causes the overlayer to metallize and further weaken the Cs-Si interaction. Thus, the Cs/Si(111)$\sqrt{3}x\sqrt{3}$–R30° interface is near a semiconductor-to-metal transition of the surface, and the lack of change in Si 2p, Cs 4d, and the surface state valence photoemission through the transition (beyond the formation of plasmon loss peaks) as well as LEED results suggest that the electronic transition is not accompanied by a corresponding structural transition in the interface.

In Chapter 7, we have used alkali and silicon absorption yield X-ray standing wave data to determine which of the three currently proposed models is the most correct for the annealed Na/Si(111)3x1 and K/Si(111)3x1 surfaces with 1/3 ML alkali coverage, as well as the room-temperature dosed K/Si(111)3x1 surface with 2/3 ML K. The surface-sensitive Si 1s XSW data are most effective in differentiating between the differing structural features of each model, and the data were compared to simulated XSW data for each model. The Si 1s XSW data point towards the "500500" (Seiwatz chain) model for the annealed Na and K 3x1 surfaces, and the "567567" (extended Pandey chain) model for the room-temperature dosed K/Si(111)3x1 surface. This agrees with the idea that elevated temperature is required to remove Si layers from the surface and produce the missing top layer reconstructions. Alkali absorption yield XSW data add further support this selection of the Si substrate structure for the 3x1 surfaces. Consideration of multiple adsorption sites as well as the effect of mapping the adsorption sites into the observed three domains was required for the (11$\bar{1}$)

reflection data. Na 1s XSW data were found to match adsorption sites on both the "500500" and "560560" model. However, K LMM XSW data only match the "500500" model, with the K adatom being too large to produce reasonable bond lengths to neighboring Si chains in the "560560" model at the measured height . If the underlying Si structure of the annealed *M*/Si(111)3x1 surface is independent of which monovalent atom *M* is adsorbed, as is suggested by LEED, STM, and angle-resolved photoemission studies, then the selection of the "500500" model for K/Si(111)3x1 forces the Na/Si(111)3x1 surface to also have the "500500" structure, which is what the Si 1s XSW data also indicate. Na is bonded to one or two Si chain atoms, while K is bound to two Si chain atoms, while the bond to the channel Si atom appears to be weak due to its long length (for Na/Si(111)3x1) or low vertical coherent fraction (for K/Si(111) 3x1).

The room-temperature K/Si(111)3x1 surface has an underlying "567567" Si structure, which is a natural extension of the π-bonded chain reconstruction of the clean Si(111)2x1 surface to a 3x1 periodicity. A two-site adsorption model was determined which matches the K LMM XSW data along both reflections for both single-domain and two-domain 3x1 surfaces. As in the case of the annealed 3x1 surfaces, the model does not agree completely with the expected bonding on the surface. The measured 2/3 ML coverage requires a two-site model; however, the model calculation has a threefold adsorption site which satisfies all dangling bonds at 1/3 ML coverage. It is possible that the second 1/3 ML adsorbs weakly to the surface in a less well-defined position. Among the three published models for the 3x1 surface, the "567567" model is the one that agrees best with both Si and K absorption yield XSW data. Theoretical calculations of the annealed and room-temperature 3x1 surfaces with adsorbate positions taken from the XSW results would provide a more complete understanding of the surface.

Through these experiments we have shown that the combination of X-Ray Standing Waves, LEED, and photoelectron spectroscopy is a powerful method to find complementary atomic and electronic structural data. Mapping the alkali metal/Si(111) interface electronic structure and surface periodicity as a function of alkali coverage provides information on the evolution of the interface from the regime of well-separated alkali-Si surface dipoles to full alkali atomic layers where alkali-alkali interactions become important. In addition, by investigating Na, K, and Cs, we emphasize the importance of the specific adatom size and electronegativity in the adsorption process. Understanding this dosing progression gives important clues as to the detailed atomic structure of specific AM/Si(111) interfaces, and X-ray standing waves is an excellent

technique for determining adatom positions. The fortunate coincidence of the (111) backreflection energy and Si 1s core-level binding energy enables Si 1s XSW to determine the surface Si reconstruction geometry. By combining our adsorbate and substrate XSW data with theoretical calculations of structural models, model surfaces were determined whose atomic positions are confirmed by an experimental technique which measures atomic positions more directly than any of the other techniques previously used to measure these surfaces. This combined method could be extended to other well-ordered adsorbates upon the Si(111) surface, as well as other substrates.

In Chapter 8, we performed preliminary experiments on a new extension of the well-established X-ray Standing Wave technique, which we call Valence Band X-ray Standing Waves (VBXSW). Through detection of photoelectrons from bonding states, we successfully used VBXSW to directly measure the charge asymmetry of the GaAs bond. In addition, we observed a reduction in the coherent fraction of the Ge valence electron XSW yield relative to that for the core-levels which was less than expected from considering the extent of the initial bonding state. This result is attributed to an effective localization of the photoemitting source at high photoelectron kinetic energy. Therefore this combination of X-ray diffraction with electron energy-resolved detection can be applied to probe the spatial distribution of bonding charge density, albeit the portion near the positions of the atomic cores. The spatial extent of the initial bonding or valence states as well as high photon and photoelectron energies produce conditions which cause the interpretation of VBXSW data to differ from core-level standing wave data.

Future Work

My future postdoctoral work with Dr. Joseph Woicik of NIST will address the interpretation of VBXSW data and its connection to the spatial distribution of bonding charge density through multiple VBXSW experiments for several materials and photon energy ranges, as well as a theoretical treatment of the standing wave photoemission problem. In addition, we will apply VBXSW to a number of systems of interest in order to assign spatial distributions to bonding states of specific energy. The success of this technique in these experiments would establish VBXSW as a new method of providing simultaneous energy and position information about bonding charge density and would have important applications in fields including the study of the electronic structure of colossal magnetoresistive (CMR) and high-T_c materials, thin films, surface

science and catalysis. In the future this technique could be extended to provide further information with angular or spin resolution.